TECHNISCHE UNIVERSITÄT MÜNCHEN

Lehrstuhl für Nukleartechnik

Development and Validation of a New Solver Based on the Interfacial Area Transport Equation for the Numerical Simulation of Sub-cooled Boiling with OpenFOAM CFD Code for Nuclear Safety Applications

Abdullah Alali

Vollständiger Abdruck der von der Fakultät für Maschinenwesen

der Technischen Universität München zur Erlangung des akademischen Grades eines

Doktor-Ingenieurs (Dr.-Ing.)

genehmigten Dissertation.

Vorsitzender: Univ.-Prof. Dr.-Ing. Thomas Sattelmayer

Prüfer der Dissertation:

1. Univ.-Prof. Rafael Macián-Juan, Ph. D.
2. Assoc. Prof. Dr.-Ing. Sergio Chiva Vicent,
   Universidad Jaume I de Castellón, Spanien

Die Dissertation wurde am 27.08.2013 bei der Technischen Universität München eingereicht und durch die Fakultät für Maschinenwesen am 21.02.2014 angenommen.

To my parents . . . my first and most influential teachers . . .

To my dear wife "Reem"... To my beloved kids . . .

"Hala and Amr"

Acknowledgements

I would like to express my sincere gratitude to my supervisor, Prof. Rafael Macián Juan, for his continuous support, guidance and encouragement. I would like also to thank him for helping me to overcome the obstacles that I faced before starting my doctoral work.

Very special thanks are also due to my colleague Joachim Herb, the OpenFOAM expert in the Gesellschaft für Anlagen- und Reaktorsicherheit (GRS) mbH for his invaluable support, without his help, this study would not have been finished on time.

I am also indebted to my colleagues Philipp Schöffel and Filippo pellacani for their comments and helpful discussions.

I would like to acknowledge the support of my parents and family during my stay in Germany, knowing that this period has been harder for them than it has been for me.

I must express my gratitude to Reem, my wife, for her continued support and encouragement. Her patience and love enabled me to complete this work.

Abdullah Alali

August 2013

Abstract

The one-group interfacial area transport equation has been coupled to a wall heat flux partitioning model in the framework of two-phase Eulerian approach using the OpenFOAM CFD code for better prediction of subcooled boiling flow.

Different models for the interfacial momentum transfer forces that govern the radial distribution of the void fraction in the adiabatic bubbly flow have been implemented in the newly generated solver. The liquid phase turbulence has been represented using the two-equation $k-\varepsilon$ turbulence model. The dispersed phase effect on the continuous phase turbulence has been modeled using the additional bubble-induced turbulent viscosity approach and the additional source term in the $k-\varepsilon$ equations approach. The performance of these models was validated against the experimental data of the MT-LOOP low void fraction test cases. Models that provide best agreement with the measured data of void fraction have been selected for the further modeling work.

For modeling flows with higher void fraction, the interfacial area transport equation has been implemented in the new solver along with different constitutive models representing bubbles coalescence and breakup processes that play a major role in the dynamic changes of the internal structure of two-phase flows. To test the validity of the interfacial area transport equation and the constitutive models, the new solver was used to simulate the air/water bubbly flow in the PUMA experiment where the simulation results showed satisfactory agreement with the measured data.

For modeling subcooled boiling, the energy equation and a wall heat flux partitioning model have been implemented and coupled to the interfacial area transport equation which was modified to include the effects of bubble nucleation at the wall and condensation in the bulk region that govern the non-uniform bubble size distribution. To validate the capability of the new solver, it has been used to simulate the upwards subcooled boiling bubbly flow in the DEBORA test facility. Predictions of the gas volume fraction, gas velocity, bubble Sauter mean diameter and liquid temperature profiles were in a good agreement with the experimental data.

Contents

Nomenclature

Latin symbols

Symbol	Unit	Description
A	m^2	Area
A_{1f}	-	Fraction of the wall area unaffected by bubbles
A_{2f}	-	Fraction of the wall area influenced by bubbles
A_w'''	m^{-1}	Area per unit volume
a_i	m^{-1}	Area density
C	-	Constant
C_{pl}	$JKg^{-1}K^{-1}$	Liquid phase heat capacity
D	m	Pipe diameter
D_e	m	Volume-equivalent diameter
D_{sm}	m	Sauter mean diameter
d_B	m	Bubble diameter
d_{BW}	m	Bubble departure diameter
d_w	m	Bubble/surface contact diameter
E	-	Aspect ratio
$\bar{E}_B$	J	Energy required for breakup
$\bar{e}$	J	Energy of a single eddy
F_b	N	Buoyancy force
F_d	N	Drag Force
F_h	N	Hydrodynamic pressure force
F_{qs}	N	Quasi-steady force
F_s	N	Surface tension force
F_{sl}	N	Shear lift force
f	-	Bubble number density function
f	s^{-1}	Interaction (coalescence or breakup) frequency
f	s^{-1}	Bubble departure frequency
G_s	-	Dimensionless shear rate
g	ms^{-2}	Gravitational acceleration
H	Jkg^{-1}	Specific enthalpy
h_c	$Wm^{-2}K^{-1}$	Single phase convection heat transfer coefficient
h_{fg}	Jkg^{-1}	Latent heat
h_i	$Wm^{-2}K^{-1}$	Interfacial heat transfer coefficient
h_q	$Wm^{-2}K^{-1}$	Quenching heat transfer coefficient
I	-	Turbulence intensity
k	m^2s^{-2}	Turbulent kinetic energy
k	$Wm^{-1}K^{-1}$	Thermal conductivity
L	m	Length
M	Nm^{-3}	Interfacial momentum transfer per unit volume
$\dot{m}$	kgs^{-1}	Mass flow rate
N''	m^{-2}	Nucleation site density
n	m^{-3}	Bubble number density
n	-	Outwardly directed normal unit vector to the interface
P	pa	Pressure
P_k	m^2s^{-3}	Shear-induced turbulence production
q''	Wm^{-2}	Heat flux

R	-	Source or sink term
R_a	-	Surface average roughness
r	m	Radius
$r(t)$	m	Bubble growth rate with respect to time
S	-	Source or sink term
S	m^2	Cross-sectional collision area
T	K	Temperature
T_b	s	Breakup time
T_{bi}	s	Breakup interaction time
T_C	s	Coalescence time
T_{ci}	s	Coalescence interaction time
T_f	s	Free travelling time
t_{ct}	s	Bubble contact time with the heated wall
t_{wait}	s	Waiting time
t_{lo}	s	Lift-off time
U	ms^{-1}	Velocity
U_r	ms^{-1}	Relative Velocity
V	m^3	Volume
X	-	Phase indicator function
y^+	-	Dimensionless distance from the wall

Greek symbols

Symbol	Unit	Description
α	-	Volume fraction
ε	m^2s^{-3}	Dissipation rate of turbulence kinetic energy
μ	$Pa.s$	Molecular dynamic viscosity
ϕ	-	Source and sink term
ψ	-	Conserved quantity
ψ	-	Shape factor of bubble
υ^t	m^2s^{-1}	Kinematic turbulent eddy viscosity
υ^{BIT}	m^2s^{-1}	Bubble-induced turbulent viscosity
τ	Nm^{-2}	Shear stress
τ_c	s	Contact time of two bubbles
ρ	kgm^{-3}	Density
σ	Nm^{-1}	Surface tension
η	-	Efficiency
Γ	$kgm^{-3}s^{-1}$	Mass transfer rate per unit volume
θ	-	Bubble contact angle at wall
γ	-	Surface liquid interaction parameter

Dimensionless numbers, coefficients and constants

Symbol	Unit	Description
β	-	Batchelor constant = 8.2
b	-	Zeng constant for the spherical effect of bubble = 1.73
C_D	-	Drag force Coefficient
C_L	-	Lift force Coefficient
C_{TD}	-	Turbulent dispersion force Coefficient
C_{WL}	-	Wall lubrication force Coefficient
C_s	-	Zeng constant = 20/3
C_t	-	Turbulence response coefficient
$E\ddot{o}$	-	Eötvos number
Ja	-	Jacob number
κ	-	Von karman constant
Mo	-	Morton number
Nu	-	Nusselt number
Pr	-	Prandtl number
Re	-	Reynolds number
We	-	Weber number

Subscripts

Symbol	Description
B	Bubble
b	Breakup
bc	Bubble critical
$be, coll$	Bubble-eddy collision
C	Coalescence
c	Convection
cr	Critical
ct	Contact
D	Drag
e	Equivalent
g	Gas phase
gl	From liquid to gas
h	Hydraulic
i	i-th component
i	Interfacial
$init$	initial
j	j-th component
k	k-th component
L	Lift
l	Liquid phase
lg	From gas to liquid
lo	Lift-off
ph	Phase change
RC	Random collision
r	Relative
sat	Saturation
sm	Sauter mean
sub	Subcooling

sup	Superheating
t	Turbulent
TI	Turbulent impact
w	Wall condition
WE	Wake entrainment
$wait$	Waiting

Abbreviations

Abbreviation	Description
BIT	Bubble Induced Turbulence
BWR	Boiling Water Reactor
CFD	Computational Fluid Dynamics
CHF	Critical Heat Flux
DNS	Direct Numerical Simulation
IATE	Interfacial Area Transport Equation
LOCA	Loss Of Coolant Accident
MUSIG	MUltiple SIze Group
PWR	Pressurized Water Reactor
SST	Shear Stress Transport

Chapter One

Introduction

The rapid increase of the world population and the accelerated economic growth rates lead to an increasing demand for electricity generation in a time where fossil fuel witnesses a big shortage in its resources and faces increasing global concerns about climate changes due to greenhouse gas emissions. These constraints must be satisfied by an energy source that is sustainable, safe, reliable, and has no or little environmental impact. Renewable sources such as wind and solar energy can produce electricity with no greenhouse gas emissions but with a cost of electricity higher than other forms of generation. It is also associated with less reliability of supply, because renewable electric power often relies on the weather for its source of energy, which makes it very difficult to generate a steady supply of electricity. Nuclear power represents the most reliable source for electricity generation in comparison with renewable energy sources, since nuclear power plants are designed to operate for longer periods of time without interruption, thus ensuring a stable energy supply. Moreover, nuclear energy can produce electricity without greenhouse gas emissions and, therefore, does not contribute significantly to global warming. Furthermore, nuclear energy is, by far, the most concentrated form of energy available today, and the high energy density of the nuclear fuel makes it possible to generate a large amount of electricity with one single nuclear power plant, thus reducing the need for large extensions of land dedicated to the production of energy, e.g. wind and solar power, or to the production of the fuels needed in the case of, for instance, biofuels.

For all these reasons described above, nuclear energy can contribute decisively, today and in future, to meet the challenges facing the increase demand for power around the world. It will, most likely, remain an important part of the energy mix in many countries for years to come, and the absolute need to do so under the most strict safety requirements will foster advanced research in order to better understand the physical behaviour of current and future plant designs, as well, as the complex systems interactions taking place in them. Such knowledge will also contribute to more advanced reactor designs that can make other uses of nuclear power feasible, e.g. hydrogen production, desalination, very high temperature chemical processes, etc.

Research in nuclear safety can also very importantly contribute to addressing the concerns associated to the use of nuclear power, such as nuclear waste management and the achievement of better public acceptance. The development of better, more accurate models, supported by well-designed experiments, can clearly improve the performance and safety of nuclear systems, while reducing the likelihood of potentially serious accidents, and offering better procedures to handle them, were they to occur.

1.2 Research Motivation

The thermal-hydraulic design of light water reactors (LWR), including Pressurized Water Reactor (PWR) and Boiling Water Reactor (BWR), requires a very good understanding of gas-liquid two phase flow and its associated phenomena, which are essential for the safety analysis of nuclear reactors under normal and accident conditions.

In PWRs, the heat generated by the fuel rods is removed by single phase forced convection and, in the hottest fuel assemblies, by an efficient heat transfer process called sub-cooled boiling. Sub-cooled boiling designates the process of evaporation of liquid flowing near a heated solid (also known as “wall”), while the bulk liquid temperature is lower than local saturation temperature. When the wall temperature exceeds the local liquid saturation temperature, micro-cavities distributed over the heated solid surface called *nucleation sites* activate the formation of vapor bubbles by becoming centers around which steam accumulates forming bubbles that start to grow until they reach a critical size. At this point, the bubbles slide along the heated surface while continuing to grow until they become large enough that buoyancy forces overcome surface tension forces and the bubbles can leave the wall migrating laterally towards the sub-cooled bulk liquid where they condensate, releasing their energy and heat the bulk liquid.

There are several important safety related effects of the sub-cooled boiling process during normal operation of PWR is relate to how the presence of bubbles affect the local neutron moderation characteristics, which is reflected in changes on the reactivity of the nuclear reactor (Koncar et al., 2005)

Another effect is caused by the enhancement, driven by sub-cooled boiling on the surface, of the formation of corrosion products and boron deposition (“crud”) on the cladding surface of the fuel rods leading to the so called Axial Offset Anomaly (AOA) that refers to a neutron flux depression at the top of the PWR cores. AOA leads to operational difficulties for the reactor (Joshua M. Hawkes 2004). Furthermore, sub-cooled

boiling takes place in the downcomer during the reflood phase of a Large Break Loss-of–Coolant Accident (LBLOCA) reducing the mass flow rate of emergency core coolant flowing to reduce core temperature (Bae et al., 2007,Song et al., 2007).

Sub-cooled boiling is characterized by a larger heat transfer capability than forced convection and contributes to a more efficient cooling of the nuclear fuel rods located in high power density regions. Unfortunately, there is a limit for the heat flux that can be transferred from the rods to the coolant by this means. The maximum value of heat flux which can be exchanged with the fluid is called Critical Heat Flux (CHF) (see Figure 1.1). When the wall heat flux increases beyond the critical heat flux (CHF), the phenomenon known as *boiling crisis* occurs. This phenomenon can be described by the formation of a vapor blanket that prevents the liquid from reaching the heated surface, thus causing a sudden degradation of the heat transfer capability and a reduction of the heat transfer coefficient which changes abruptly from that of a boiling process to one for single phase gas (the steam). With a constant power delivered by nuclear fission to the clad surface, the clad temperature will exhibit a sharp increase leading to the breaking of the safety barrier isolating the fuel from the coolant, allowing the release of some radioactive fission products into the primary coolant circuit and it may lead finally to fuel failure. For such a reason, the nuclear reactor must be operated with a maximum heat flux at the clad surface always within a regulated safe margin below the CHF.

Sub-cooled boiling modeling is considered as a preliminary state towards numerical simulation of CHF and the precise prediction of the boiling crisis in computational fluid dynamics (CFD) codes. Therefore, accurate estimation of the radial profiles of two-phase flow parameters in the sub-cooled boiling region: gas volume fraction, interfacial area concentration, bubble Sauter mean diameter, gas velocity and liquid temperature is fundamental in order to establish the use of CFD codes to nuclear safety, with the important advantages that such a step can bring by allowing a detailed and accurate description of phenomena with global impact on reactor safety.

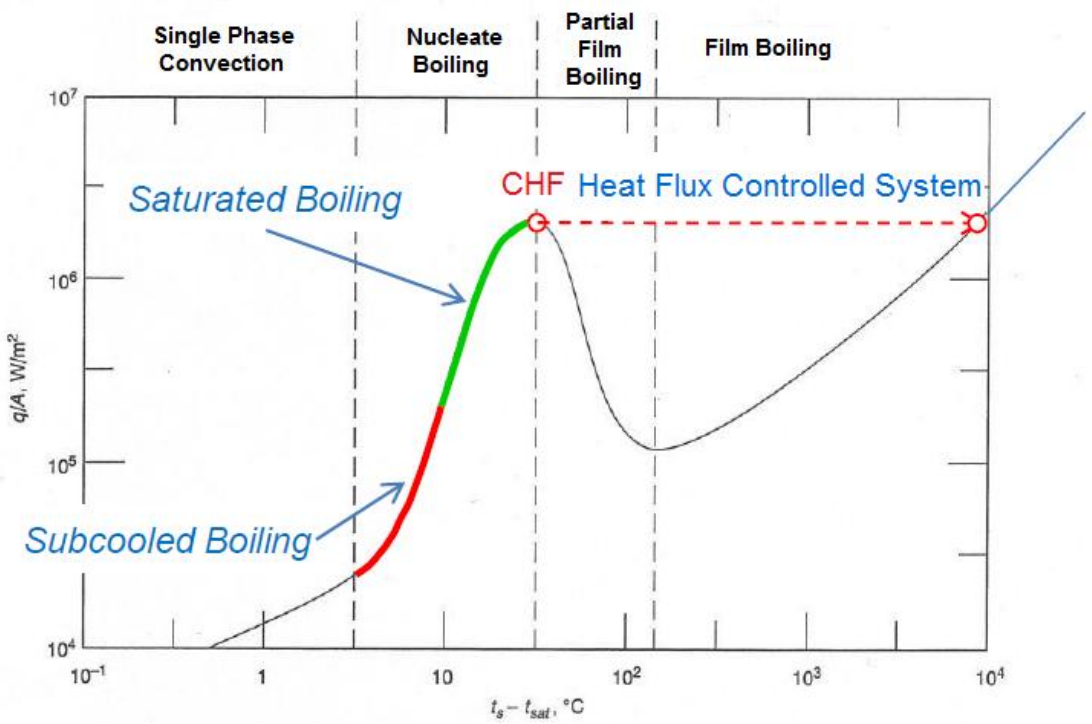

Figure 1.1. Boiling Curve and Critical Heat Flux (CHF).

1.3 Computational Fluid Dynamics (CFD)

Since actual measurements of gas-liquid flow conditions in real nuclear facility experiment is too expensive, not free of hazards and sometimes, difficult or even impossible to measure the relevant data, numerical simulation by CFD codes can provide more economical, time efficient alternative that can also yield the values of a larger quantity of flow defining variables. It is clear, however, that for CFD codes to “replace” experiments, especially when nuclear safety issues are at stake, will require extensive, thorough and rigorous validation and assessment of their integral results and that of the modes implemented in them to address the different physical processes of interest. Nevertheless, such a procedure has been followed with success by simpler systems analysis codes in the past, and still continues today. For this reason, there should not be in principle major concerns and hindrances to a similar procedure, and with similar results, being carried out with CFD codes in future.

CFD simulations are based on the solution of the partial differential equations which describe the two-phase flow. Because analytical solution is only feasible for very simplified applications, for real flow systems a numerical solutions of the equations is necessary. The discretization, and sometimes also linearization, of these equations is the first step for their numerical solution. The original partial differential equations (PDE) are converted into a system of algebraic equations for the flow variables at a number of

discrete points in space and time. These discrete points are locations at which the variables are calculated and, according to the discretization method used, they are called control volumes, finite differences, finite elements, etc.. The approach used in this thesis is based in the discretization of the flow domain into a finite number of control volumes into which the equations are numerically integrated to produce the algebraic approximation. Practically, the creation of the control volumes is carried out by using a so-called mesh generating tool, which divides the fluid domain into a mesh of control volumes interconnected at their surfaces with the adjacent ones. This interconnection will allow the fluxes of flow variables to enter or leave the volumes and create a mathematically space and time coupled system of equations that can be solved by appropriate numerical techniques. Before the solution procedure can begin, the initial and the boundary conditions of the specific problem must be specified according to the physical characteristics of the flow field. The convergence and accuracy of the solution procedure is controlled by reviewing the evolution of several flow-determining variables, e.g. pressure, velocity, void fraction, etc., as the solution progresses.

In the numerical simulation of two-phase flow, there are three approaches that are mainly applied in CFD codes regarding how the movement and interaction between the two different phases are dealt with:

- **Direct Numerical Simulation (DNS) approach:** it aims to describe the full physics of the flow under consideration at a smallest length scale. DNS is "*model free*" in the sense that no turbulence and interfacial exchange models are needed. The computational cost of DNS is very high and, with the current state of efficiency of numerical algorithms and computer power, it is suitable only for low Reynolds numbers and to follow the evolution of localized small number of bubbles, which is not the case of most of real industrial applications, including nuclear power plants.
- **Eulerian-Lagrangian approach**: a certain number of individual particles or bubbles is tracked and its interaction with the continuous phase is modeled with single particle models (Lagrangian). The continuous phase is solved by phase-averaged equations integrated on an Eulerian mesh (fixed in space) covering the flow domain. The problem with this approach is that in dense flows the number of particles required for a reasonable accuracy is high, and thus the number of equations needed to be solved (every particle is "moved" by its own equation) and computational cost are correspondingly high.

- **Eulerian-Eulerian approach**: the dispersed and continuous phases are solved by phase-averaged equations integrated on an Eulerian mesh, and the all inter-actions between both phases are volume averaged within a control volume. The major advantage of this approach is that the number of equations only depends on the number phases, instead on the number of particles, as in the Eulrtian-Lagrangian approach.

1.3.1 OpenFOAM

OpenFOAM (Open Field Operation and Manipulation) is an open-source and free CFD code written in the C++ programming language. It gives the user full access to the source code, where he can add new or modify existing equations in order to create new equation solvers.

OpenFOAM uses the Finite Volume Method (FVM) for the discretization of the partial differential equations into a linear algebraic system of equations where the differential operators can be treated as finite volume calculus (fvc) or finite volume method (fvm) depending on the time discretization followed (OpenFOAM user guide). The first function calculates *explicit* derivatives while the second is used to discretize *implicit* derivatives resulting in a linear system of matrix coefficients.

An important feature of OpenFOAM is the capability to represent equations in their natural language. As an example, the momentum conservation equation

$$\frac{\partial \rho \vec{U}}{\partial t} + \nabla . \left(\rho \vec{U} \vec{U} \right) - \nabla . \left(\mu \nabla \vec{U} \right) = -\nabla p$$

Is implemented in OpenFOAM as

```
solve
(
  fvm::ddt(rho, U)
+ fvm::div(phi, U)
- fvm::laplacian(mu, U)
==
- fvc::grad(p)
);
```

The OpenFOAM structure (see Figure 1.2) includes pre-processing environment including mesh generating tools; solvers that are used to create executables representing the implemented set of equations and their discretization; and post-processing tools including ParaView that is a visualization application supplied in OpenFOAM and any other third party visualization tool like EnSight.

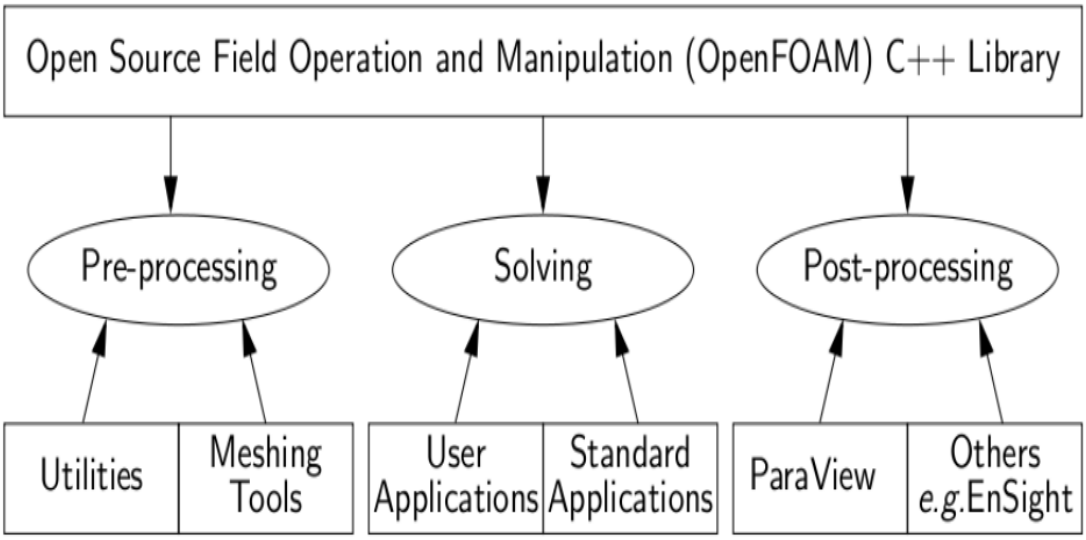

Figure 1.2. OpenFOAM structure (according to OpenFOAM user guide)

1.4 Goal and Plan of the Thesis

The main goal of this thesis is to enhance the applicability of OpenFOAM CFD for subcooled boiling two-phase flow simulations, which are very important for nuclear reactor safety.

The techniques developed and insights gained in the process of the implementation and assessment in OpenFOAM can certainly be generalized to other CFD codes using a similar solution approach, such as ANSYS-CFX, FLUENT, etc.

In order to fulfill this goal, the following plan has been followed to complete the research work:

1. Implementation of different models for interfacial drag and non-drag forces that govern the radial distribution of the gas phase in adiabatic bubbly flow.
2. Implementation of different bubble-induced turbulence models.
3. Validation of the implemented models against the low-void fraction test cases of the air-water MT-LOOP experiment to select the best combination of these closure models to be used in the further modeling work. During this part of the work, bubble diameter will be assumed constant.

4. Implementation of the one-group interfacial area transport equation coupled with the two-fluid model conservation equations along with different bubble coalescence and breakup constitutive models.
5. Validation of the applicability of the one-group interfacial area transport equation to describe the non-uniform distribution of bubble size, and testing the validity of the implemented constitutive models against the PUMA experimental data.
6. Implementation of a wall heat flux partitioning model and the energy equation which is not available in the adiabatic solver and then coupling these models with one-group interfacial area transport equation that is modified by the inclusion of new source terms representing bubble nucleation at the wall and bubble condensation by sub-cooled liquid in the fluid bulk.
7. Examining the performance of the implemented models by comparison with the experimental data of sub-cooled boiling flow of DEBORA facility and further comparison with predicted results using MUSIG (Multiple Size Group) model implemented in CFX.

1.5 Thesis Outline

The thesis is organized as follows:

Chapter 2 describes the formulation of two-fluid model for adiabatic flow and the averaging techniques along with the closure models including interfacial momentum exchange and two phase turbulence. Different models for the interfacial drag and non-drag forces coefficients are proposed and discussed including drag, lift, wall lubrication and turbulent dispersion forces. Different approaches for modeling bubble-induced turbulence are also presented in this chapter.

In chapter 3, the implemented closure models in the developed solver are used to simulate the air-water adiabatic bubbly flow in the MT-LOOP experiment to test the performance of these models in the prediction of the radial distribution of void fraction.

The derivation of the one-group interfacial area transport equation and the constitutive models for bubble coalescence and breakup are presented in chapter 4.

Next, in chapter 5, the performance of the one-group interfacial area transport equation and the performance of the different coalescence and breakup models in predicting the geometrical structure of two-phase bubbly flow is tested against the PUMA experiment.
Chapter 6 discusses the sub-cooled boiling phenomena and explains the wall heat flux partitioning model and the associated boiling closure models. It also describes the manner of modeling the extra source terms of the one-group interfacial area transport equation, which takes into account bubble nucleation at the heated wall and bubble condensation in the sub-cooled bulk region for better estimation of bubble size distribution in sub-cooled boiling flow.

The performance of the implemented models in predicting sub-cooled boiling flow parameters are discussed in chapter 7 by the simulation of DEBORA boiling experiment. Where further comparisons of the simulation results are conducted against another predicted data using empirical correlations for calculating bubble size in the bulk region and also using the population balance approach of MUSIG (Multiple Size Group) model.
In chapter 8, conclusions and recommendations for further research work are given.

Chapter Two

Two-phase Flow Methodology

Two phase flow is very important in a wide range of engineering applications including power generation systems such as nuclear reactors. In this last field, the accurate prediction of the dynamical behavior of two-phase flow is essential for safety analysis under normal and accident conditions (Ishii 1984). In general, the optimum design, the prediction of operational limits and the safe control of the reactor depend all upon the availability of realistic and accurate mathematical models of two-phase flow.

The most important characteristic of two-phase flow systems is the presence of interfaces separating the phases. Two-phase flows are classified depending on the thermodynamical state of the two phases as well as on their interface structures (Ishii1975). For instance, a two-phase flow can be categorized as gas-solid, gas-liquid, solid-liquid, and liquid-liquid and, based on its interface geometry it can be classified into separated, transitional or dispersed flow (Wallis 1969).

This thesis is dedicated to modelling the gas-liquid dispersed bubbly flow. The liquid phase is treated as a continuum while the gas bubbles are considered as the dispersed phase embedded, transported and interacting with the continuum.

The treatment of two phase flow is done through various models in terms of the flow field equations and of the constitutive relations that couple their terms. The level of accuracy of the models dependes on their ability to capture relevant non-equilibrium phenomena. Such models must account for the interactions between the phases and of their interactions with the solid structures in contact. The number of constitutive relationships necessary, also known as closure relationships, increases with the complexity and detail of the models. For instance, two-phase flow models can be distinguished according to the level of non-equilibrium introduced in the field equations:

- **The Homogeneous Equilibrium Model (HEM)**: assumes that the two phases have equal velocities (mechanical equilibrium) and equal temperatures (thermal equilibrium) and the two phases are treated as a single fluid mixture.

- **The Drift Flux Model**: assumes that the two phases are in thermal equilibrium. This model is different from the (HEM) model only in allowing the two phases to have different velocities (mechanical non-equilibrium).
- **The Two-Fluid Model**: is formulated by considering each phase separately in terms of two sets of conservation equations governing the balance of mass, momentum and energy of each phase. This model allows the phases to have thermal non-equilibrium as well as unequal velocities.

The numerical simulation of the models mentioned above, is carried out with the use of computer programs that provide the time-space evolution of the two-phase structure and thermodynamic state. The degree of mathematical detail in the numerical solution of the flow equations and of physical detail in their associated closure relationships determine their accuracy, but they also adds to the complexity of the solution methodology and increases the computing power needed to achieve an acceptable solution (in terms of accuracy and stability). The increase in the power of computers and the development of faster, more stable numerical solution techniques has progressively allowed for the use of increasingly complex and more sophisticated mathematical and physical models to predict the behavior of two-phase flows.

The latest most advanced approach is the use of Computational Fluid Dynamics (CFD) based codes, especially after showing the feasibility of solving the Navier–Stokes equations that govern the motion of multiple phases (Yeoh and Tu, 2010). In order to be solved, these equations have to be simplified by averaging them in time and space. The averaging procedure creates additional fluctuation terms e.g.; Reynolds Stresses that require special modeling, and add an additional set of averaged equations known as Reynolds Averaged Navier-Stokes (RANS) equations. Turbulence effects are intended to be described by them.

In the CFD two-fluid modelling, both phases are commonly described by using Eulerian conservation equations. Hence, the model is also referred to as the Euler-Euler model. Each phase is treated as a continuum, each one inter-penetrating the other one, and is represented by averaged conservation equations.

The Euler-Euler framework is selected for the presented two-phase CFD simulations carried out in this work.

2.1 Formulation of Two-Fluid Models and Averaging Technique

This section is based on the description of averaging procedures found in Enwald et al.,(1996).

Modeling two-phase flow is difficult because of the difficulty in the formulation of two single phases with moving boundaries and the modeling of the interaction between the phases at the interface. If the number of particles suspended in a gas-liquid flow is large, an averaging operator acting on the local instantaneous equations is needed (the alternative would be to solve one ordinary differential transport equation for each particle in a statistically significant ensemble of them by using a Lagrangian approach).

In the Eulerian approach, the local instantaneous equations must be averaged in space, in time or as an ensemble. But the averaging process will introduce more unknowns than the number of equations, which creates the need for closure equations in order to obtain a closed system of equations to solve.

A general procedure for developing a two-fluid averaged mathematical model is shown in Figure (2.1).

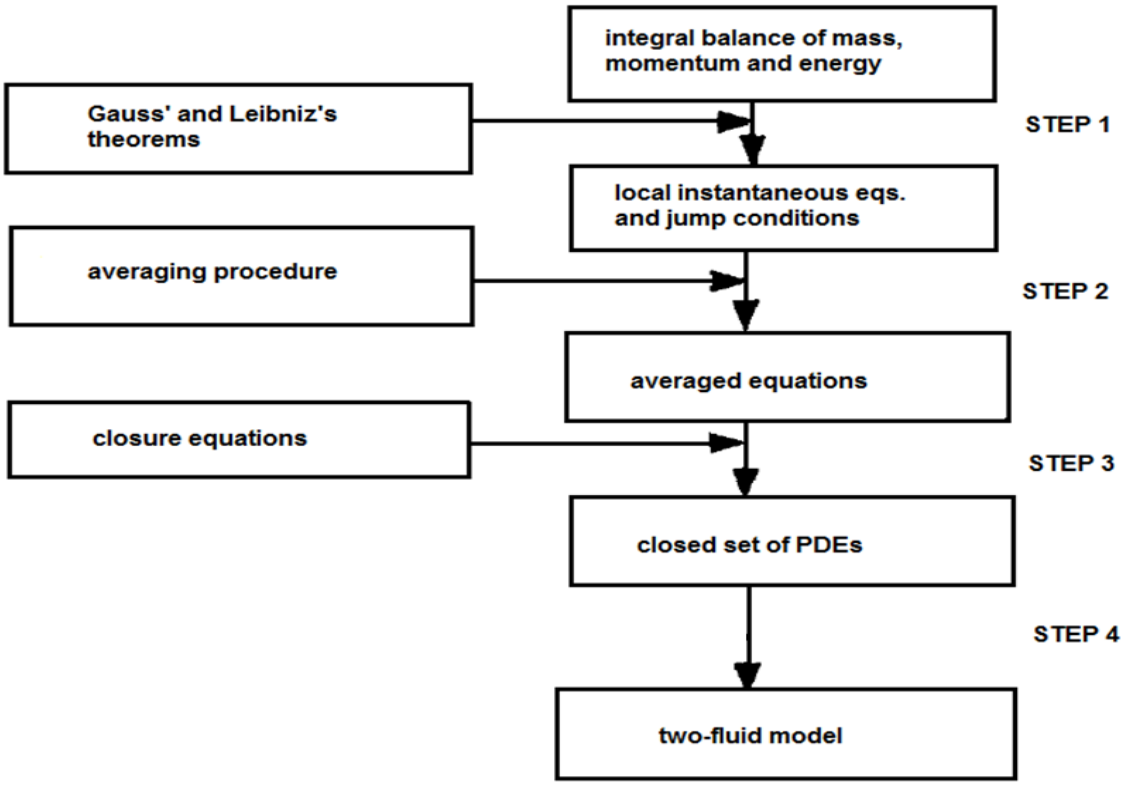

Figure 2.1. General procedure for formulating a two-fluid model (Enwald 1997)

For complete modeling of two-phase flow, the instantaneous conservation equations of mass, momentum and energy must be averaged. In the following sub-sections, only the averaging procedure of the momentum equation will be described in detail.

2.1.1 The local instantaneous Momentum Equation

When a vector or scalar variable ψ_k belonging to phase k is to be transported through the control volume using a coordinate system which is fixed (Eulerian approach), the general integral balance can be written

$$\sum_{k=1}^{2}\left(\frac{d}{dt}\int_{V_k(t)}\rho_k\psi_k dV\right)=\int_{A_I(t)}\phi_I dA$$
$$+\sum_{k=1}^{2}\left(-\int_{A_k(t)}\rho_k\psi_k(U_k.n_k)dA+\int_{V_k(t)}\rho_k\phi_k dV\quad-\int_{A_k(t)}J_k.n_k dA\right), \tag{2.1}$$

In this notation, n_k is the outwardly directed normal unit vector to the interface of the volume occupied by phase k, $^{d}/_{dt}$ is the ordinary time derivative, U_k is the velocity of phase k, ρ_k is the density, ψ_k is the conserved quantity, J_k is the molecular flux, ϕ_k is the source term and ϕ_I is the interfacial source term.

The time derivative term in Eq. (2.1) can be transformed into a sum of volume and surface integrals using Leibniz's theorem, (see appendix A for details). The convective and diffusion terms can also be transformed into a sum of volume and surface integrals using Gauss' theorem, (see appendix A).

The general integral balance equation can be written now as a sum of volume integral for the volumes occupied by the two phases and surface integral for the jump conditions (the ones coupling the phases by modelling the interchange of momentum) across the interface.

$$\sum_{k=1}^{2}\int_{V_k(t)}\left(\frac{\partial}{\partial t}(\rho_k\psi_k)+\nabla.(\rho_k\psi_k U_k)+\nabla.J_k-\rho_k\phi_k\right)dV$$
$$-\int_{A_I(t)}\left(\sum_{k=1}(\dot{m}_k\psi_k+J_k.n_k)+\phi_I\right)dA=0, \tag{2.2}$$

Where $\dot{m}_k$ is the mass transfer per unit area of interface and unit time defined as

$$\dot{m}_k = \rho_k\left(\vec{U}_k - \vec{U}_I\right).\vec{n}_k, \tag{2.3}$$

The general local instantaneous equation can be then written as

$$\frac{\partial}{\partial t}(\rho_k\psi_k) + \nabla.\left(\rho_k\psi_k\vec{U}_k\right) + \nabla.J_k - \rho_k\phi_k = 0, \tag{2.4}$$

with the local instantaneous jump condition

$$\sum_{k=1}^{2}(\dot{m}_k\psi_k + J_k.\vec{n}_k) = -\phi_I, \tag{2.5}$$

From Eq. (2.4), the local instantaneous momentum equation and jump condition, after applying $\psi_k = U_k,\ J_k = -\bar{\bar{R}}_k$, $\phi_k = g$, and $\phi_I = 0$, are

$$\frac{\partial}{\partial t}\left(\rho_k\vec{U}_k\right) + \nabla.\left(\rho_k\vec{U}_k\vec{U}_k\right) - \nabla.\bar{\bar{R}}_k - \rho_k\vec{g} = 0, \tag{2.6}$$

$$\sum_{k=1}^{2}\left(\dot{m}_k\vec{U}_k - \bar{\bar{R}}_k.\vec{n}_k\right) = 0, \tag{2.7}$$

where $\bar{\bar{R}}_k$ is the stress tensor.

2.1.2 Averaging Procedure

The phase indicator function, X_k, for phase k is a step function defined in the following way

$$\mathrm{X}_k(r,t) = \begin{cases} 1, & if\ r \in k \\ 0, & otherwise \end{cases}, \tag{2.8}$$

The average of the phase indicator function is equivalent to the average occurrence of phase k, i.e. $\alpha_k = \langle X_k \rangle$

where

$$\sum_{k=1}^{2}\alpha_k = 1, \tag{2.9}$$

The averaging procedure is assumed to have the following properties

$$\langle f + g\rangle = \langle f\rangle + \langle g\rangle, \tag{2.10}$$

$$\langle\langle f\rangle g\rangle = \langle f\rangle\langle g\rangle, \tag{2.11}$$

$$\langle constant \rangle = constant, \tag{2.12}$$

$$\left\langle \frac{\partial f}{\partial t} \right\rangle = \frac{\partial \langle f \rangle}{\partial t}, \tag{2.13}$$

$$\langle \nabla f \rangle = \nabla \langle f \rangle, \tag{2.14}$$

$$\langle \nabla . f \rangle = \nabla . \langle f \rangle, \tag{2.15}$$

$$\frac{\partial \langle \mathrm{X}_k f_k \rangle}{\partial t} = \left\langle \mathrm{X}_k \frac{\partial f_k}{\partial t} \right\rangle + \left\langle f_k \frac{\partial \mathrm{X}_k}{\partial t} \right\rangle, \tag{2.16}$$

$$\nabla \langle \mathrm{X}_k f_k \rangle = \langle \mathrm{X}_k \nabla f_k \rangle + \langle f_k \nabla \mathrm{X}_k \rangle, \tag{2.17}$$

$$\nabla . \langle \mathrm{X}_k f_k \rangle = \langle \mathrm{X}_k \nabla . f_k \rangle + \langle f_k . \nabla \mathrm{X}_k \rangle, \tag{2.18}$$

The first step in the averaging procedure is to multiply the local instantaneous momentum equation by the phase indicator function and form the average of the resulting equation.

The averaged momentum equation with no mass transfer between the phases will be

$$\frac{\partial}{\partial t} \langle \mathrm{X}_k \rho_k \vec{U}_k \rangle + \nabla . \langle \mathrm{X}_k \rho_k \vec{U}_k \vec{U}_k \rangle - \nabla . \langle \mathrm{X}_k \bar{\bar{R}}_k \rangle - \langle \mathrm{X}_k \rho_k \vec{g} \rangle = \langle -\bar{\bar{R}}_k . \nabla \mathrm{X}_k \rangle = \vec{M}_k, \tag{2.19}$$

where M_k represents the interfacial momentum transfer.

The averaged momentum jump condition in this case is

$$\sum_{k=1}^{2} \langle -\bar{\bar{R}}_k . \nabla \mathrm{X}_k \rangle = \sum_{k=1}^{2} \vec{M}_k, \tag{2.20}$$

Since the averaged momentum equation contains averages of products of the dependent variables it cannot be solved directly and needs to be rewritten in the form of products of the averaged variables. This can be done by applying the Reynolds decomposition and a weighting procedure.

The Reynolds decomposition is a mathematical technique to separate the average and fluctuating parts of a quantity. For example, for a quantity Q the decomposition would be

$$Q = \langle Q \rangle^W + Q', \tag{2.21}$$

with Q' representing the fluctuating part.

Regarding the weighting process there are two procedures:

- **Phasic average**: the variable is weighted with the phase indicator function

$$\langle Q\rangle^{X_k} = \frac{\langle X_k Q\rangle}{\langle X_k\rangle} = \frac{\alpha_k Q^{X_k}}{\alpha_k} = Q^{X_k}, \tag{2.22}$$

- **Mass-weighted or Favre average**: the variable is weighted with the phase indicator function times the density.

$$\langle Q\rangle^{X_k\rho_k} = \frac{\langle X_k\rho_k Q\rangle}{\langle X_k\rho_k\rangle} = Q^{X_k\rho_k}, \tag{2.23}$$

The Reynolds decomposition of the velocity is then

$$\vec{U}_k = \langle\vec{U}_k\rangle^W + \vec{u}_k{}', \tag{2.24}$$

Introducing the Reynolds decomposition of the velocity in the averaged momentum Eq. (2.19) we obtain

$$\begin{aligned}\frac{\partial}{\partial t}\left(\langle X_k\rho_k\left(\vec{U}_k + \vec{u}_k{}'\right)\rangle\right) + \nabla.\left(\langle X_k\rho_k\left(\vec{U}_k + \vec{u}_k{}'\right)\left(\vec{U}_k + \vec{u}_k{}'\right)\rangle\right)\\ -\nabla.\left(\langle X_k\bar{\bar{R}}_k\rangle\right) - \langle X_k\rho_k\vec{g}\rangle = \vec{M}_k,\end{aligned} \tag{2.25}$$

The transient term is formulated using the mass weighted average of the velocity $\langle\vec{U}_k\rangle^{X_k\rho_k} = \vec{U}_k$, and the fluctuating velocity $\langle\vec{u}_k{}'\rangle^{X_k\rho_k} = 0$, and the phasic average of the density $\langle\rho_k\rangle^{X_k} = \rho_k^{X_k}$, in the following way

$$\frac{\partial}{\partial t}\left(\langle X_k\rho_k\left(\vec{U}_k + \vec{u}_k{}'\right)\rangle\right) = \frac{\partial}{\partial t}\left(\alpha_k\rho_k^{X_k}\left(\vec{U}_k + \underbrace{\langle\vec{u}_k{}'\rangle^{X_k\rho_k}}_{=0}\right)\right) = \frac{\partial}{\partial t}\left(\alpha_k\rho_k^{X_k}\vec{U}_k\right), \tag{2.26}$$

The convective term is treated as follows

$$\begin{aligned}&\nabla.\left(\langle X_k\rho_k\left(\vec{U}_k + \vec{u}_k{}'\right)\left(\vec{U}_k + \vec{u}_k{}'\right)\rangle\right)\\ &\quad= \nabla.\left(\langle X_k\rho_k\vec{U}_k\vec{U}_k\rangle + \langle 2X_k\rho_k\vec{U}_k\vec{u}_k{}'\rangle + \langle X_k\rho_k\vec{u}_k{}'\vec{u}_k{}'\rangle\right)\\ &\quad= \nabla.\left(\langle X_k\rho_k\rangle\vec{U}_k\vec{U}_k + 2\langle X_k\rho_k\rangle\vec{U}_k\underbrace{\langle\vec{u}_k{}'\rangle^{X_k\rho_k}}_{=0} - \alpha_k\bar{\bar{R}}_k^{Re}\right)\\ &\quad= \nabla.\left(\alpha_k\rho_k^{X_k}\vec{U}_k\vec{U}_k - \alpha_k\bar{\bar{R}}_k^{Re}\right),\end{aligned} \tag{2.27}$$

The stress tensor of phase k is weighted using the phasic average

$$\langle X_k \bar{\bar{R}}_k \rangle^{X_k} = \alpha_k \bar{\bar{R}}_k^{X_k}, \tag{2.28}$$

The gravity term is also weighted using the phasic average

$$\langle X_k \rho_k \vec{g} \rangle = \alpha_k \rho_k^{X_k} \vec{g}, \tag{2.29}$$

Reynolds-decomposed and averaged momentum equation is obtained as

$$\frac{\partial}{\partial t}\left(\alpha_k \rho_k^{X_k} \vec{U}_k\right) + \nabla.\left(\alpha_k \rho_k^{X_k} \vec{U}_k \vec{U}_k\right) = \nabla.\left(\alpha_k\left(\bar{\bar{R}}_k^{X_k} + \bar{\bar{R}}_k^{Re}\right)\right) + \alpha_k \rho_k^{X_k} \vec{g} + \vec{M}_k, \tag{2.30}$$

The stress tensor term $\nabla.\left(\alpha_k \bar{\bar{R}}_k^{X_k}\right)$ can be split up into a pressure term and a shear stress term as

$$\nabla.\left(\alpha_k \bar{\bar{R}}_k^{X_k}\right) = \nabla.\left(\alpha_k\left(-P_k \bar{\bar{I}} + \bar{\bar{\tau}}_k\right)\right) = -\nabla(\alpha_k P_k) + \nabla.\left(\alpha_k \bar{\bar{\tau}}_k\right), \tag{2.31}$$

And the final form of the averaged momentum equation is

$$\frac{\partial}{\partial t}\left(\alpha_k \rho_k \vec{U}_k\right) + \nabla.\left(\alpha_k \rho_k \vec{U}_k \vec{U}_k\right) = -\alpha_k \nabla P_k + \nabla.\left(\alpha_k\left(\bar{\bar{\tau}}_k + \bar{\bar{\tau}}_k^{Re}\right)\right) + \alpha_k \rho_k \vec{g} + \vec{M}_k, \tag{2.32}$$

2.2 The Eulerian Two-Fluid Model

The averaged Eulerian conservation equations for mass and momentum for incompressible two-phase system with no interfacial heat and mass transfer are presented in this subsection together with a full description of the dynamics of the interaction between the two phases by the closure laws or constitutive equations.

2.2.1 Governing Equations

Mass conservation

The continuity equation of the two-fluid model according to Ishii (1975) and Drew and Lahey (1979) can be written as

$$\frac{\partial}{\partial t}(\alpha_k \rho_k) + \nabla.\left(\alpha_k \rho_k \vec{U}_k\right) = 0, \tag{2.33}$$

Momentum conservation

The momentum equation for the two-phases reads

$$\frac{\partial}{\partial t}\left(\alpha_k \rho_k \vec{U}_k\right) + \nabla.\left(\alpha_k \rho_k \vec{U}_k \vec{U}_k\right) = -\alpha_k \nabla P_k + \nabla.\left(\alpha_k\left(\bar{\bar{\tau}}_k + \bar{\bar{\tau}}_k^{Re}\right)\right) + \alpha_k \rho_k \vec{g} + \vec{M}_k, \quad (2.34)$$

where $\alpha_k,\ \rho_k, \vec{U}_k$ are the void fraction, density and velocity of phase k, respectively. $\bar{\bar{\tau}}_k, \bar{\bar{\tau}}_k^{Re}$ are the viscous and Reynolds (turbulent) stresses, respectively. $\vec{M}_k$ is the averaged inter-phase momentum transfer term.

The Reynolds and viscous stress tensors are modeled using Boussinesq hypothesis which uses the Newtonian strain-stress relation. It is given by

$$\bar{\bar{\tau}}_k + \bar{\bar{\tau}}_k^{Re} = -(\mu_k + \mu_k^t)\left(\nabla \vec{U}_k + \nabla \vec{U}_k{}^T - \frac{2}{3} I \nabla.\vec{U}_k\right) + \frac{2}{3} I k_k, \quad (2.35)$$

where I, μ_k^t, k_k, are the identity tensor, turbulent dynamic viscosity and turbulent kinetic energy of phase k.

2.2.2 Constitutive Equations

The interfacial momentum transfer term $\vec{M}_k$, and the Reynolds stress tensor $\bar{\bar{\tau}}_k^{Re}$ term that arise from the averaging process need to be modeled and thus a set of closure laws are required.

2.2.2.1 Interfacial Momentum Transfer

As stated by Frank et al., (2004), in adiabatic bubbly flow the interfacial momentum transfer has a large effect on the two-phase momentum transfer and the distribution of the gas and liquid phases are effectively governed by the interfacial forces in the flow volume . The interfacial force can be partitioned into four main terms: drag, lift, wall lubrication and turbulent dispersion force. The last three forces are lumped together as non-drag forces.

$$\vec{M}_g = \vec{M}_g^D + \vec{M}_g^l + \vec{M}_g^{WL} + \vec{M}_g^{TD}, \quad (2.36)$$

- **Drag Force**

In dispersed flows (bubbly, slug or churn-turbulent), the interfacial drag force acts in the opposite direction of the flow as a result of the shear and form drag of the fluid flow. A bubble that moves relative to the liquid accelerates part of the surrounding liquid and decelerates itself. The drag force has a significant effect on the hydrodynamics of the system, especially on the velocity fields. It can be modeled according to the following equation

$$\vec{M}_g^D = -\frac{3}{4}\frac{C_D}{d_B}\rho_l \alpha_g \left|\vec{U}_g - \vec{U}_l\right|\left(\vec{U}_g - \vec{U}_l\right), \tag{2.37}$$

where C_D is the drag coefficient which is modeled differently for various flow and bubble shape regimes (see Figure 2.2). It depends strongly on the Reynolds number Re in the viscous regime. For deformable or distorted bubble regime, in which the effect of the surface tension becomes important (ANSYS 2009) and the dispersed bubbles are initially ellipsoidal and can reach a capped shape, $C_D$depends on the Eötvös number Eo, which measures the ratio between gravitational and surface tension forces. According to Ishii and Zuber (1979) C_D is given as

$$C_D = max\left(C_{D,sphere}, min\left(C_{D,ellipse}, C_{D,cap}\right)\right), \tag{2.38}$$

where

$$\begin{aligned} C_{D,sphere} &= \frac{24}{Re}(1 + 0.1Re^{0.75}), \\ C_{D,ellipse} &= \frac{2}{3}\sqrt{Eo}, \\ C_{D,cap} &= \frac{8}{3}, \end{aligned} \tag{2.39}$$

with the Reynolds Re and Eötvös Eo numbers are defined respectively as

$$Re = \frac{\rho_l \left|\vec{U}_r\right| d_B}{\mu_l}, \tag{2.40}$$

$$Eo = \frac{g\Delta\rho d_B^2}{\sigma}, \tag{2.41}$$

where σ is the surface tension and μ_l is the molecular viscosity of the liquid phase.

Another drag force coefficient model was proposed by Tomiyama (1998a) for slightly-contaminated air-water two-phase flow based on the Reynolds Re and Eötvös Eo numbers, which is considered as an extension of the model of Schiller and Naumann (1933)

$$C_D = max\left\{min\left[\frac{24}{Re}(1 + 0.15Re^{0.687}), \frac{72}{Re}\right], \frac{8}{3}\frac{Eo}{Eo + 4}\right\}, \tag{2.42}$$

The original Schiller-Naumann model for drag force coefficient depends only on the Reynolds number when Re < 1000, and for Re > 1000 the drag coefficient is constant and equal to **0.44** according to

$$C_D = max\left(\frac{24}{Re}(1 + 0.15Re^{0.687}), 0.44\right), \tag{2.43}$$

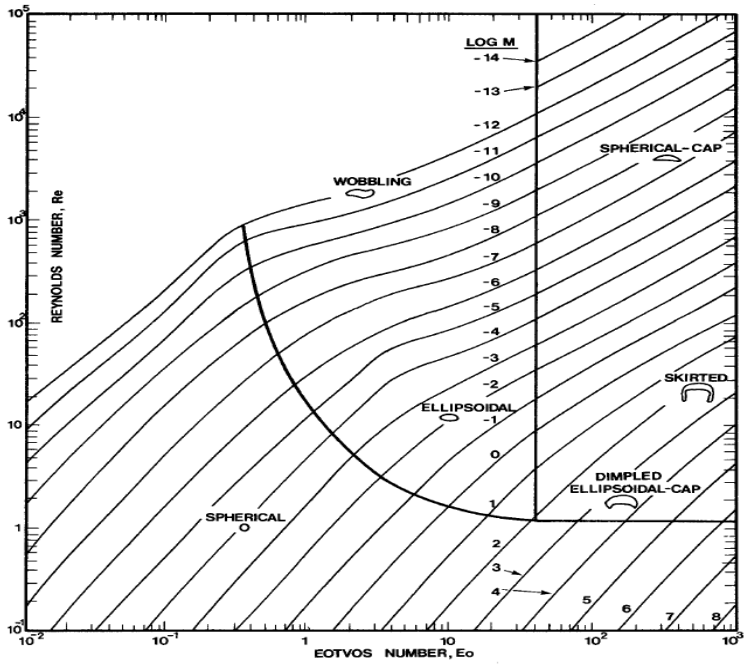

Figure 2.2. Shape regimes of fluid particles in unhindered gravitational motion through liquids (Rusche 2002)

- **Lift Force**

The lift force acts in the perpendicular direction to the relative motion of the two phases as a result of the interaction between the bubbles and the shear field of the liquid phase. It is formulated in terms of the slip velocity between the phases and the local *vorticity* of the continuous phase by Zun (1980) as

$$\vec{M}_g^l = -C_L\rho_l\alpha_g\left(\vec{U}_g - \vec{U}_l\right) \times \left(\nabla \times \vec{U}_l\right), \tag{2.44}$$

where C_L is the lift force coefficient. Lopez de Bertodano (1992) suggested a value of $C_L = 0.1$ to fit a set of experimental data for bubbly flow in ducts. Drew and Lahey (1979) recommended a value of $C_L = 0.5$ for inviscid flow where bubbles have infinite Reynolds number Re because it makes no sense when calculating the lift force

coefficient based on an infinite Reynolds number. Wang et al., (1987) found that a value of $C_L = 0.01$ could be satisfactory for viscous flows.

All suggested coefficients are positive, hence the associated lift forces acts in the direction of the ***decreasing*** liquid velocity, i.e., towards the pipe wall in case of upward co-current flow in pipes. On the other hand, for deformed bubbles, the lift force may changes its direction, towards ***higher*** liquid velocity (in the direction of the pipe center) (see Figure 2.3). This finding was a result of numerical (Schmidtke 2008) and experimental (Tomiyama et al., 2002) investigations.

Tomiyama observed the trajectories of single bubbles in a well-defined shear field flow of a glycerol water solution under the conditions $-5.5 \leq logMo \leq -2.8$ and $1.39 \leq Eo \leq 5.74$, and derived a correlation for the lift force coefficient as

$$C_L = \begin{cases} min[0.288tanh(0.121Re), f(Eo_d)] & Eo_d < 4 \\ f(Eo_d) & 4 < Eo_d < 10, \\ -0.27 & Eo_d > 10 \end{cases} \quad (2.45)$$

where Mo is a dimensionless number that is used to characterize the shape of bubbles moving in a surrounding fluid or continuous phase, defined as

$$Mo = \frac{g\mu_l^4 \Delta\rho}{\rho_l^2 \sigma^3},$$

$f(Eo_d) = 0.00105Eo_d^3 - 0.0159Eo_d^2 - 0.0204Eo_d + 0.474$, is a function of the modified Eötvös number Eo_ddefined as

$$Eo_d = \frac{g\Delta\rho d_H^2}{\sigma}, \quad (2.46)$$

in which d_H is the maximum bubble horizontal dimension that is calculated using the aspect ratio in order to account for the influences caused by the deformation of the bubbles. The aspect ratio is the ratio between the spherical bubble diameter $d_B$and the maximum horizontal dimension of a spheroidal bubble of equal mass d_H (Politano et al., 2003), and is defined as

$$E = \left(\frac{d_B}{d_H}\right)^3, \quad (2.47)$$

In this relationship, E is calculated by the correlation of Wellek et al., (1966) for the aspect ratio as

$$E = \frac{1}{1 + 0.163Eo^{0.757}}, \tag{2.48}$$

and then d_H is given by

$$d_H = d_B \sqrt[3]{1 + 0.163Eo^{0.757}}, \tag{2.49}$$

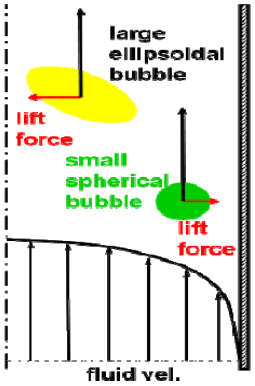

Figure 2.3. Illustration of lift force

According to Tomiyama´s correlation, for the air-water system at normal conditions (atmospheric pressure and 25°C temperature), the lift force coefficient C_L changes its sign at a bubble diameter of **5.8 mm** (see Figure 2.4).

Because smaller bubbles tend to migrate towards the pipe wall, this lead to "*wall peak*" void fraction distribution. On the other hand, larger bubbles accumulate in the center of the pipe ("*core peak*" distribution).

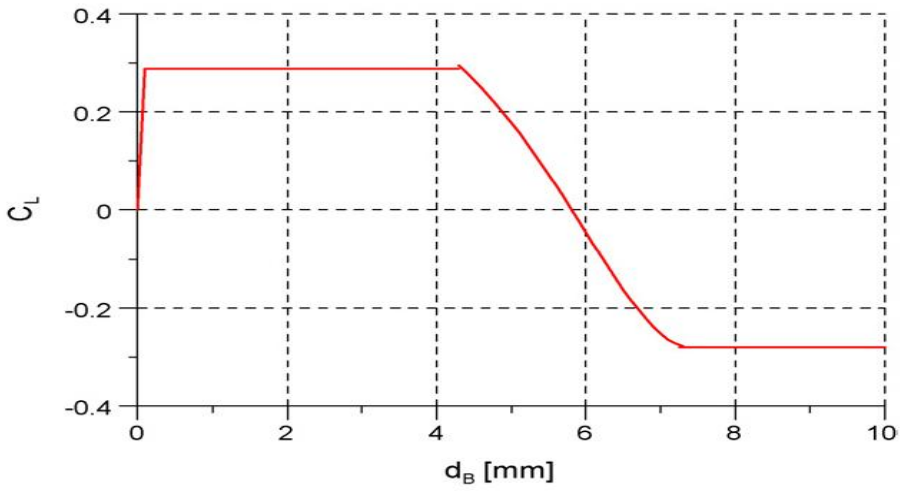

Figure 2.4. Lift coefficient for air-water bubbly flow (E. krepper et al. 2008)

- **Wall Lubrication Force**

Translating bubbles near the wall experience a repulsive force pushing it away from the wall (see Figure 2.5). This force is due to the velocity profile change near the wall region where the liquid phase has a velocity close to zero, and this will slow the drainage rate of liquid around the bubble in the wall region and increase it in the other side causing "asymmetric drainage" (Wang 2010), and then a pressure difference around the bubble surface resulting in a hydrodynamic force called wall lubrication force, that prevent the bubbles attaching the wall. According to Antal et al., (1991), this force can be modeled as

$$\vec{M}_g^{WL} = C_W \alpha_g \rho_l \left|\vec{U}_g - \vec{U}_l\right|^2 \vec{n}_w, \tag{2.50}$$

where $\vec{n}_w$is the outward vector normal to the wall, C_W is the wall lubrication force coefficient given as

$$C_W = max\left\{0, \frac{C_{W1}}{d_B} + \frac{C_{W2}}{y_w}\right\}, \tag{2.51}$$

where y_w is the distance from the wall boundary. And the coefficients are set to $C_{W1} = -0.01$ and $C_{W2} = 0.05$.

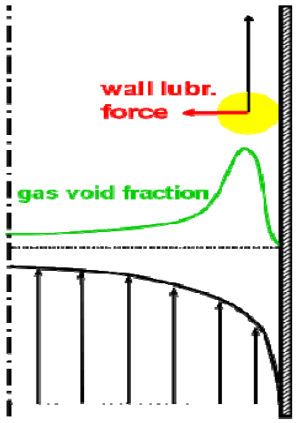

Figure 2.5. Illustration of wall lubrication force

The model constants have been modified by Krepper et al., (2005) to be $C_{W1} = -0.0064$ and $C_{W2} = 0.016$. According to this model the wall lubrication force is set to **zero** if the wall distance satisfies the condition: $y_w > \frac{C_{W2}}{C_{W1}} d_B$.

Tomiyama (1998) proposed another correlation (modified by Frank et al., (2008)) based on the observation of single bubble trajectories in a simple shear flow of a glycerol water solution at a single value of Morton number $\log_{10} Mo = -2.8$ as follow

$$C_W = C_{W3} \frac{d_B}{2} \left(\frac{1}{y_w^2} - \frac{1}{(D - y_w)^2} \right), \tag{2.52}$$

where D is the pipe diameter and C_{W3} is an Eötvös number dependent coefficient modeled as

$$C_{W3} = \begin{cases} 0.47 & Eo < 1 \\ e^{(-0.933Eo + 0.179)} & 1 \leq Eo \leq 5 \\ 0.00599Eo - 0.0187 & 5 < Eo \leq 33 \\ 0.179 & Eo > 33 \end{cases}, \tag{2.53}$$

Hosokawa et al., (2002) has investigated a large range of Morton numbers $\log_{10} Mo = -2.5 \ \ to \ -6$ in different glycerol water solutions. By extrapolating their results of the dependence of C_W on Eo to vanishing Morton number the following correlations were found (Rzehak et al., 2012)

$$C_W = C_{W3} \left(\frac{d_B}{2y} \right)^2, \tag{2.54}$$

$$C_{W3} = 0.0217Eo, \tag{2.55}$$

Turbulent Dispersion Force

The turbulent dispersion force accounts for the dispersion of the bubbles due the turbulent eddies in the liquid phase (Lahey et al., 1993; Koncar et al., 2005). It is driven by the void fraction gradient and determines the sharpness of the wall peak and influences the radial void fraction profile (Lucas et al., 2007). Lopez de Bertodano (1992) from the Rensselear Polytechnic Institute (RPI) proposed a simple formulation for the turbulent dispersion force as follows

$$\vec{M}_g^{TD} = -C_{TD} \rho_l k_l \nabla \alpha_g, \tag{2.56}$$

where k_l is the total turbulent kinetic energy of the liquid phase, and C_{TD} is the turbulent dispersion force coefficient with different values proposed by many authors ranging from $0.1 \ \ to \ 0.5$. This model referenced as RPI TD model.

Since the physical mechanism responsible for the turbulent dispersion force is the action of turbulent eddies via interphase drag, Burns et al.,(2004) derived an alternative

model based on the Favre average of the interfacial drag force. According to this model the turbulent dispersion force coefficient is set to

$$C_{TD} = \frac{3}{4} C_D \frac{v_l^t}{Pr_l^t} \frac{\left|\vec{U}_g - \vec{U}_l\right|}{d_B k_l} \frac{1}{1-\alpha_g}, \tag{2.57}$$

where Pr_l^t is the turbulent Prandtl number for the liquid phase and a value of 0.9 is used in this work. C_D is the drag force coefficient. This model referenced as FAD TD model.

2.2.2.2 Two-Phase Turbulence Modelling

The Reynolds stress tensor considered one of the terms that are resulting from the conditional averaging process of the momentum conservation equation, it represents the effect of turbulence on the average phase momentum, it relates to the effect of velocity fluctuations (which are a result of the shear induced turbulence) on the mean transport of the phases (Hill 1998), and in gas-liquid flows turbulence has a strong influence on the void fraction distribution, and the mechanistic models of the bubble interactions such as bubble coalescence and breakup rely strongly on the turbulence parameters.

The task of Reynolds averaged turbulence is to express the Reynolds stress tensor in terms of the known quantities. The turbulence stresses are modeled only for the liquid phase, whereas the vapor phase is modeled by a simple zero equation model. The most popular approach in the continuous phase turbulence modeling is prescribing a relationship between the Reynolds stress and mean velocity gradient using the eddy viscosity concept of Boussinesq as

$$\overline{\vec{U}_l{}' \vec{U}_l{}'} = -v_l^t \left(\nabla \vec{U}_l + \nabla \vec{U}_l{}^T - \frac{2}{3} I \nabla . \vec{U}_l \right) + \frac{2}{3} Ik, \tag{2.58}$$

where k is the turbulent kinetic energy in the continuous phase, and v_l^t is the kinematic eddy viscosity which is evaluated with the following formula

$$v_l^t = C_\mu \frac{k^2}{\varepsilon}, \tag{2.59}$$

where ε is the turbulent energy dissipation rate and C_μ is a dimensionless coefficient. The dispersed gas phase turbulence is related to the turbulence in the continuous phase by setting the viscosity to be proportional to the continuous phase turbulent viscosity through the turbulent response coefficient C_t which is relating the dispersed

phase velocity fluctuations u_g' to those of the continuous phase u_l' (Politis 1989) as follows

$$C_t = \frac{u_g'}{u_l'}, \tag{2.60}$$

and the dispersed phase turbulent viscosity can be expressed (Rusche 2002) as

$$v_g^t = C_t^2 v_l^t, \tag{2.61}$$

- **The $k-\varepsilon$ Turbulence Model**

The values of k and ε in Eq. (2.59) are obtained from the solution of their respective transport equations, which are generally called the standard "$k-\varepsilon$" model by Launder and Spalding (1972). The general governing equations of the $k-\varepsilon$ model are (Rusche 2002)

$$\frac{\partial(k_l)}{\partial t} + (\vec{U}_l \cdot \nabla) k_l - \nabla \cdot \left(\frac{v_l^{eff}}{\sigma_k} \nabla k_l \right) = P_k - \varepsilon, \tag{2.62}$$

$$\frac{\partial(\varepsilon_l)}{\partial t} + (\vec{U}_l \cdot \nabla) \varepsilon_l - \nabla \cdot \left(\frac{v_l^{eff}}{\sigma_\varepsilon} \nabla \varepsilon_l \right) = \frac{\varepsilon_l}{k_l} (C_{\varepsilon 1} P_k - C_{\varepsilon 2} \varepsilon), \tag{2.63}$$

where v_l^{eff} is the effective viscosity of the liquid phase calculated from

$$v_l^{eff} = v_l + v_l^t, \tag{2.64}$$

Where v_l^t is the turbulent viscosity calculated from Eq. (2.59) applied to the liquid phase

$$v_l^t = C_\mu \frac{k_l^2}{\varepsilon_l}, \tag{2.65}$$

$C_{\varepsilon 1}$, $C_{\varepsilon 2}$, σ_k, σ_ε, C_μ are model coefficients summarized in Table (2.1), and P_k is the shear-induced turbulence production given by

$$P_k = v_l^{eff} \nabla \vec{U}_l \cdot \left(\nabla \vec{U}_l + (\nabla \vec{U}_l)^T \right) - \frac{2}{3} \nabla \cdot \vec{U}_l (v_l^{eff} \nabla \cdot \vec{U}_l + k_l), \tag{2.66}$$

which can be rewritten as

$$P_k = 2\upsilon_l^{eff}\left(\nabla\vec{U}_l \bullet dev\left(\nabla\vec{U}_l + \left(\nabla\vec{U}_l\right)^T\right)\right) - \frac{2}{3}k_l\nabla\cdot\vec{U}_l, \quad (2.67)$$

The second term in the right-hand side does not make a significant contribution to the turbulence production because for incompressible flow, which is the situation in the current work, the divergence of the liquid velocity $\nabla\cdot\vec{U}_l$ approaches **zero** (ANSYS 2009).

Table 2.1. Coefficients of $k-\varepsilon$ model

$C_{\varepsilon 1}$	$C_{\varepsilon 2}$	C_μ	σ_k	σ_ε
1.44	1.92	0.09	1.00	1.30

- **Bubble-Induced Turbulence (BIT)**

In bubbly two-phase flow, another source of liquid turbulence is generated in the wake of the large moving bubbles called bubble-induced turbulence.

Modeling bubble-induced turbulence is a key element in order to achieve a complete physical model that allows predictive CFD based simulations for multiphase flow. The BIT can be taken into account by using the two different approaches described next.

Sato's approach

According to Sato et al.(1980) the bubble-induced and shear-induced turbulence effects are *decoupled* from each other and, therefore, they can be modeled separately and then linearly composed together. The shear-induced turbulent viscosity is calculated from the two-equation $k-\varepsilon$ model, while the bubble-induced turbulent viscosity is derived by analogy to the potential flow around a sphere. Hence, the effective kinematic viscosity of the liquid phase is

$$\upsilon_l^{eff} = \upsilon_l + \upsilon_l^t + \upsilon_l^{BIT}, \quad (2.68)$$

Where υ_l^{BIT} is the BIT viscosity defined as

$$\upsilon_l^{BIT} = C_{\mu b}\alpha_g d_B\left|\vec{U}_g - \vec{U}_l\right|, \quad (2.69)$$

with a $C_{\mu b}$ constant value of **0.6** as recommended by Sato et al.(1980).

Additional source terms in the $k-\varepsilon$ equations approach

The bubble-induced turbulence is taken into account *directly* as additional source terms in the turbulent transport Eqs. (2.62) and (2.63). The modified transport equations are

$$\frac{\partial(k_l)}{\partial t}+\left(\vec{U}_l\cdot\nabla\right)k_l-\nabla\cdot\left(\frac{\upsilon_l^{eff}}{\sigma_k}\nabla k_l\right)=P_k-\varepsilon+S_l^k, \tag{2.70}$$

$$\frac{\partial(\varepsilon_l)}{\partial t}+\left(\vec{U}_l\cdot\nabla\right)\varepsilon_l-\nabla\cdot\left(\frac{\upsilon_l^{eff}}{\sigma_\varepsilon}\nabla\varepsilon_l\right)=\frac{\varepsilon_l}{k_l}\left(C_{\varepsilon1}P_k-C_{\varepsilon2}\varepsilon\right)+S_l^\varepsilon, \tag{2.71}$$

S_l^k is the source term describing the bubble induced turbulence effect in the k-equation and it is modeled by assuming that all the energy loss by the bubble caused because of the drag with the liquid phase is converted to turbulent kinetic energy in the wake of the bubble. Therefore, S_l^k can be written as a function of the relative velocity in the following manner

$$S_l^k=-\vec{M}_g^D.\left(\vec{U}_g-\vec{U}_l\right), \tag{2.72}$$

with $\vec{M}_g^D$ as the interfacial drag force.

For the ε-source S_l^ε modeling, a similar approach as that followed in the case of single phase turbulence is used, that is, the k-source is divided by a characteristic turbulence time scale τ

$$S_l^\varepsilon=C_\varepsilon\frac{S_l^k}{\tau}, \tag{2.73}$$

Several models are available in the literature for the calculation of the time scale τ based on a dimensional analysis background. These models and the values of C_ε as recommended by their authors are summarized in Table (2.2).

Table 2.2. Summary of BIT time scale models

	Morel *Morel (1997)*	*Pfleger* *Pfleger & Becker (2001)*	*Rzehak* *Rzehak & Krepper (2012)*	*Troshko* *Troshko & Hassan (2001)*
τ	$\left(\frac{d_B^2}{\varepsilon}\right)^{1/3}$	$\frac{k}{\varepsilon}$	$\frac{d_B}{\sqrt{k}}$	$\frac{2C_{VM}d_B}{3C_D\lvert\vec{U}_r\rvert}$
C_ε	1.0	1.92	1.0	0.45

C_D in Troshko´s model is the drag force coefficient, and C_{VM} is the virtual mass force coefficient.

- **Near-Wall Treatment**

In a fully developed turbulent velocity profile, as shown in Figure (2.6), the velocity gradient at the wall, and hence the wall shear stress τ_w, are very large. The latter is defined as

$$\tau_w = \mu \left.\frac{\partial u}{\partial y}\right|_w, \tag{2.74}$$

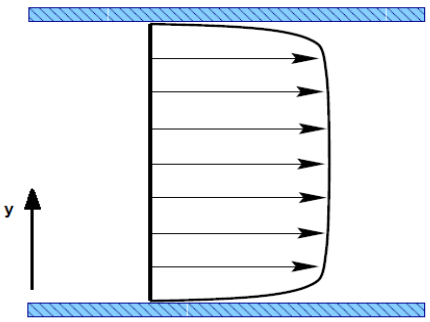

Figure 2.6. Turbulent velocity profile

According to the Figure (2.6) there must be at least two length scales (McDonough 2007) associated with this flow: one is related to the region adjacent to the wall with a

non-uniform velocity profile and a large gradient, and the other, farther from the wall, with nearly uniform velocity profile.

In the region *very close* to the wall, the velocity varies *linearly* with distance from the wall and the flow is completely dominated by the viscous (laminar) effect: the viscous sub-layer. In the region where the velocity is nearly uniform, this cannot satisfy the no-slip conditions at the wall, and the inner (linear) profile, which satisfies the no-slip condition, will not tend asymptotically to the near uniform profile region (turbulent). This creates the need for a third transition region to continuously connect both profiles. It is formally known as the method of matched asymptotic expansion (McDonough 2007). This method will generate an *intermediate* region called buffer layer or overlapping region, in which the flow is turbulent and the velocity is changing quickly.

The laminar and turbulent layers are characterized by different velocity profile curves, as depicted in Figure (2.7)

$$U^+ = \begin{cases} y^+ & y+ < 11.6 \\ \frac{1}{\kappa}\ln\left(Ey^+\right) & y^+ > 11.6' \end{cases} \tag{2.75}$$

where y^+ is the dimensionless distance from the wall derived from the actual distance y by the relation

$$y^+ = \frac{C_\mu^{1/4} k^{1/4}}{\upsilon_l}.y, \tag{2.76}$$

The second part of Eq. (2.75) is the well-known “log-law” that matches the inner to the outer layer (see Figure 2.7).

A value of **11.6** for y^+signals the distance at which the flow changes from laminar to turbulent, and it is calculated by the intersection between the two curves by solving the following equation

$$y^+ = \frac{1}{\kappa}\ln(Ey^+), \tag{2.77}$$

with κ is the von Karman constant equal to **0.42** and E is the so-called log-law constant equal to **9.793**.

The turbulent kinetic energy in Eq. (2.76) is calculated by the solution of the k-equation over the entire calculation domain, even for near-wall computational cells, which is not

the case for the dissipation of turbulence kinetic energy ε, which is calculated for the near wall region according to the formula

$$\varepsilon = \frac{C_\mu^{3/4} k^{3/2}}{\kappa y}, \tag{2.78}$$

Bases on the derivation above the shear-induced turbulent viscosity for the liquid phase in the near wall region v_l^t can be finally calculated as follow

$$v_l^t = \begin{cases} 0 & y+ < 11.6 \\ v_l \left(\frac{y\kappa}{ln(Ey^+)} - 1 \right) & y^+ > 11.6 \end{cases}, \tag{2.79}$$

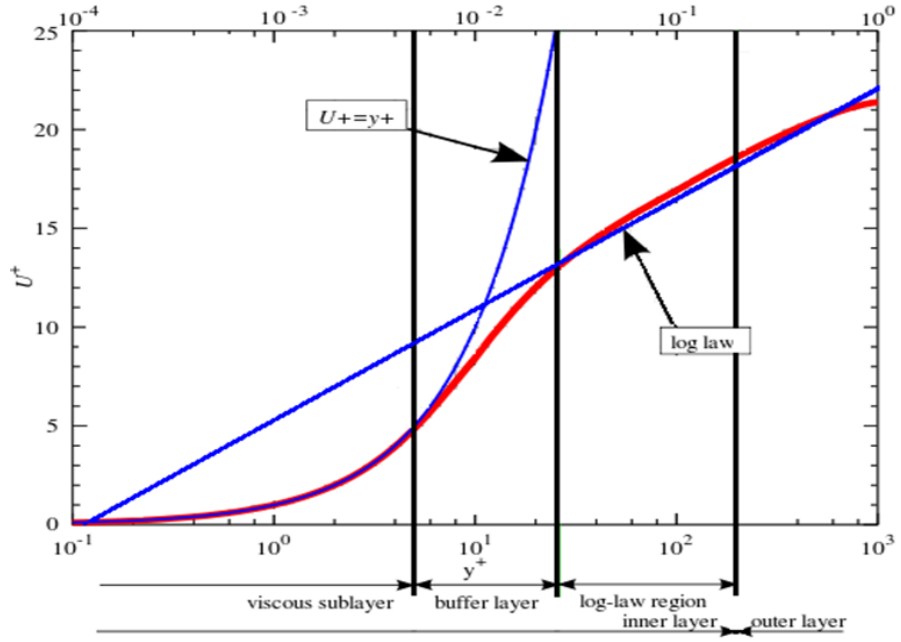

Figure 2.7. Transition in the buffer layer for the non-dimensional velocity profiles

Chapter Three

Monodispersed Adiabatic Bubbly Flow Simulation with OpenFOAM

This chapter is dedicated to the validation of the capability of different interfacial drag and non-drag forces to predict the gas void fraction distributions in disperse bubbly flows. It aims also at studying the effect of bubble-induced turbulence through the application of different models found in the literature to calculate the overall liquid phase turbulence. Liquid turbulence determines the *radial profile* of the mean liquid velocity, which appears in all the expressions for the interfacial forces, except in the turbulent dispersion force which depends on the turbulent viscosity directly.

The applicability of the numerical models discussed in the previous chapter has been validated against the air-water MT-LOOP test facility of the Forschungszentrum Rossendorf (FZR) in the bubbly flow regime. In the simulation, a fixed mono-dispersed bubble size distribution is assumed with the average bubble size taken from the experimental measurements for each test. In the study reported in this chapter bubble interaction mechanisms, such as bubble coalescence and breakup, which are very important for the determination of the bubble size distribution, are not taken into consideration during the simulations presented. In any case, these processes are relatively rare events when the void fraction is very low.

3.1 The MT-LOOP Test Facility

The MT-LOOP facility (Prasser et al., 2003, Lucas et al., 2005) was designed and operated to study upward vertical flow of air and water at atmospheric pressure and 30°C. The test section consisted of a circular pipe with an inner diameter, $\mathrm{D} = 51.2\ \mathrm{mm}$ (Figure 3.1). Air bubbles were injected into an upward water flow using a sparger with 19 capillaries equally distributed over the pipe cross section. The distance between the gas injector and the measurement location was varied between $\mathrm{L} = 0.03\ \mathrm{m}$ and $\mathrm{L} = 3.03\ \mathrm{m}$, but in the present work only the measurements at the largest distance will be considered, so that fully developed flow is observed.

A large number of tests with different ratios of air and water superficial velocities were performed; the test matrix is shown in Figure (3.2). Radial profiles of gas volume fraction and gas velocity as well as distribution of bubble size were measured using a fast wire-mesh sensor developed at FZR with 24x24 electrodes.

For the current study, which is the validation of the closure models of the interfacial forces and turbulence models by numerical simulation of mono-dispersed bubbly flow, Experiments 17, 19, 39, 41, 61, 63 have been selected as assessment data for the implemented models because, according to Figure 3.2 their conditions are such that they are all placed well into the bubbly flow region and they cover a range of superficial air and liquid velocities that are most appropriate for the range of validity of the models used. In addition the size of the bubbles in these cases are small enough so that it is not expected that effects due to bubble deformation will have an impact on the forces acting on the bubbles. The relevant parameters of the selected cases are summarized in Table (3.1).

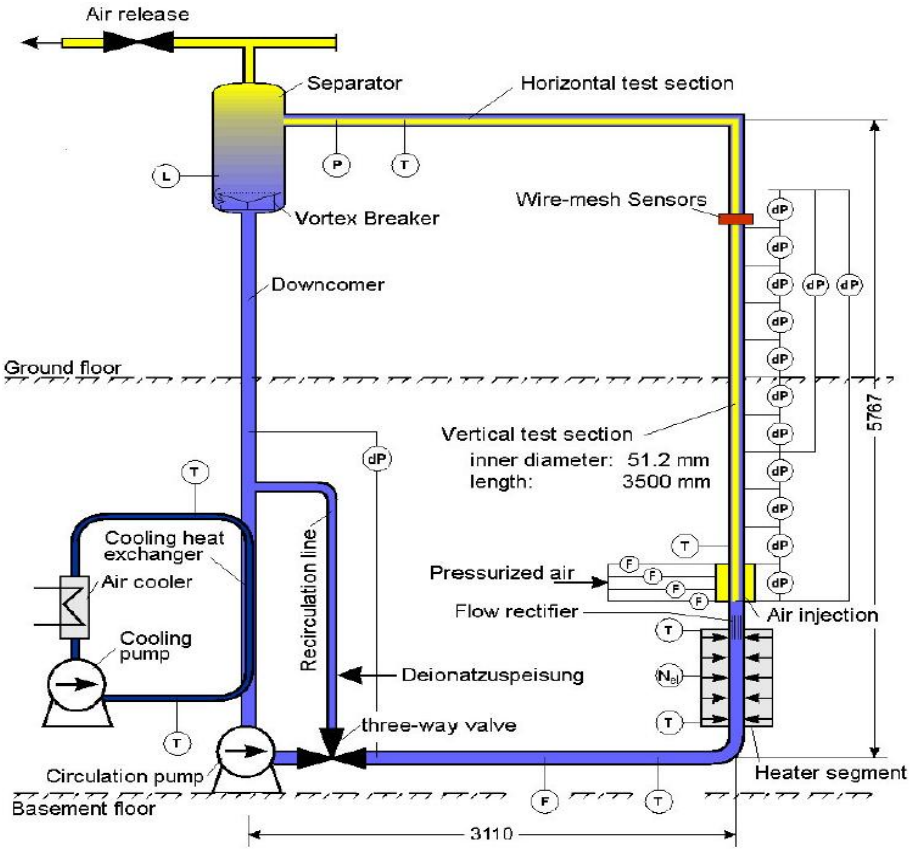

Figure 3.1. MT-LOOP test facility for vertical pipe flow investigation (FZR/Germany)

Table 3.1. Selected test cases conditions for experimental investigations at the MT-LOOP test facility

Test	J_L*(m/s)*	J_G*(nominal)(m/s)*	J_G*(adjust.)(m/s)*	$\langle d_b \rangle$*(mm)*	$\langle \alpha_G \rangle$*(%)*
MT017	0.405	0.004	0.0033	4.25	0.6
MT019	1.0167	0.004	0.0029	4.0	0.28
MT039	0.4050	0.0096	0.0111	4.5	1.89
MT041	1.0167	0.0096	0.0115	4.5	1.00
MT061	0.4050	0.0235	0.0309	4.5	5.03
MT063	1.0167	0.0235	0.0316	4.5	2.64

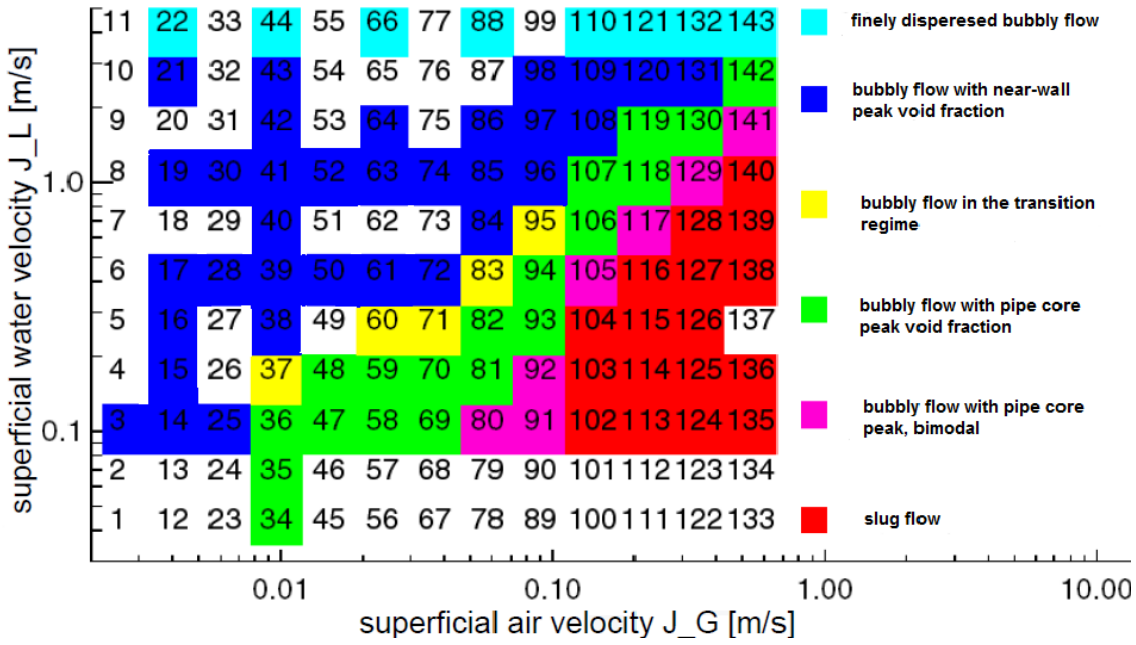

Figure 3.2. Test Matrix of the MT-LOOP experiments with the combinations of superficial gas and liquid velocities

3.2 Numerical Simulation Model

After the implementation of the different interfacial forces and bubble-induced turbulence models in the twoPhaseEulerFoam solver of the OpenFOAM CFD code which serves as a platform for two-phase flow simulation based on the solution of two sets of equations governing the conservation of mass and momentum, an extensive numerical simulations for the different test cases were carried out in a quasi-2D cylindrical geometry (see Figure 3.3), i.e. a 5° cylindrical sector. A 3D-simulation with 45° sector of the pipe has shown a good agreement with the simplified geometry. The simulation was performed in accordance to the Best Practice Guidelines for the use of CFD in Nuclear Reactor Safety Application (2007).

The computational domain boundaries of the geometry consist of: INLET, OUTLET, SYMMETRY PLANE1, SYMMETRY PLANE2 and WALL. With the following boundary conditions imposed at these boundaries:

INLET

The profile of the liquid velocity was set according to a typical single phase turbulent flow profile in a pipe. While the gas velocity and volume fraction are set to a uniform profile at the inlet.

OUTLET

Atmospheric pressure was set as a boundary condition at the outlet.

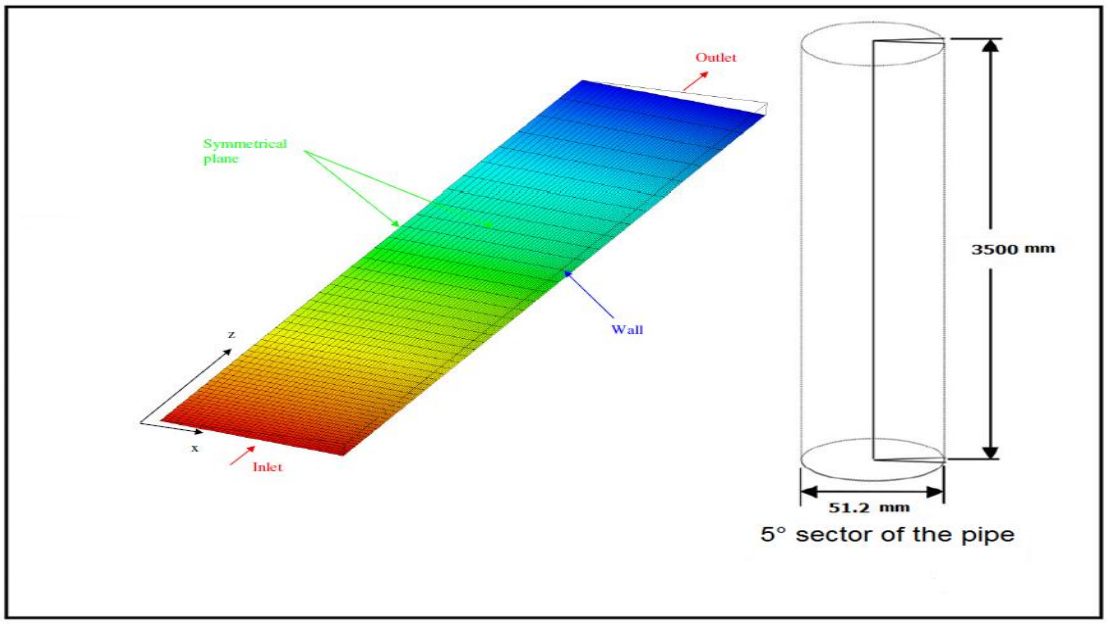

Figure 3.3. Quasi-2D cylindrical geometry and 3D view of the mesh (Liao 2011)

WALL

A no slip condition ($U_l = 0.0\ \mathrm{m}/s$) for the liquid phase and a *free* slip condition for the gas phase were used at the wall.

SYMMETRY PLANE 1&2

Symmetry boundary conditions were imposed on the side faces of the geometry.

For the purpose of mono-dispersed bubbly flow simulation, the *mean bubble diameter* was specified as the one determined from the experimental data for each test case.

As reported by Rzehak et al., (2012), in order to keep the computational advantage of an incompressible calculation with constant material properties, the gas velocity has been adjusted from the measured velocity profile and the value of the constant gas density used in the simulation. The adjusted velocities are given in Table (3.1). The gas velocity adjustment takes into account the effect of the pressure reduction along the pipe that leads to higher void fractions due to the gas expansion. Because the pressure reduction effect is not represented in the simulation due to the constant density assumption, then the same void fraction at a higher elevation can be produced by higher gas velocity.

For all flow conditions, reliable convergence was achieved when the RMS residuals for all variables fell below the residual convergence criteria set to 10^{-4}.

3.3 Grid Sensitivity Analysis

For the study of the grid independence of the numerical results, five mesh structures (Table 3.2) have been tested. The numerical meshes used local refinement towards the outer pipe wall where for the first cell adjacent to the wall (y^+) value is kept at less than 30 for all numerical grids. Test MT-LOOP 41 was selected among other cases for the grid independence study.

In the grid sensitivity study, the drag force is modeled according to Ishii-Zuber, the Tomiyama correlation based on Eötvos number is adopted for the lift force modelling, the wall lubrication force is modeled based on Hosokawa, Favre-averaged expression for the turbulent dispersion force is employed, and the Sato bubble-induced turbulence model has been used.

Table 3.2. Hierarchy of numerical meshes

Grid level	*No. of grid elements in pipe cross-section*	*No. of grid elements along pipe axis*	*No. of grid elements*
1	20	300	6000
2	25	300	7500
3	32	300	9600
4	40	300	12000
5	50	300	15000

Figure (3.4) of the gas volume fraction profile for grid levels 1 to 5, shows that numerical simulations give almost grid independent results starting from the first grid level.

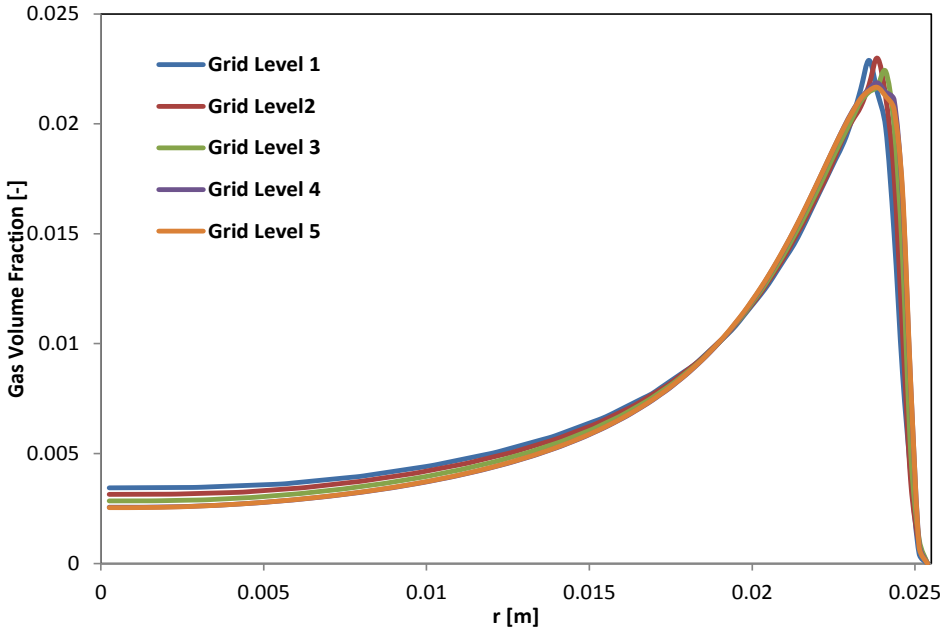

Figure 3.4. Grid independence of numerical results for test case MTLOOP 41

3.4 Investigations on Interfacial Forces Models

For the accurate prediction of void fraction profiles in multiphase bubbly flow, suitable closure models for the momentum exchange between liquid and gas phases must be identified. A number of interfacial drag and non-drag forces models have been proposed in the literature and implemented in the solver. Simulations using a selection of

these models are compared with the experimental data from the selected MT-LOOP test points described in Table (3.1).

Based on previous experience, the set of models that has been selected as a basis for the differential analysis are:

- Drag force:Ishii and Zuber (1979).
- Lift force: Tomiyama et al., (2002).
- Wall lubrication force: Hosokawa et al., (2002).
- Turbulent dispersion force: FAD/Burns et al., (2004).
- Turbulence model: $k-\varepsilon$.
- Bubble-induced turbulence: Morel (1997).

The analysis will then proceed by systematically changing the force models with those we want to evaluate. The following sections are discussing the influence of the different models.

3.4.1 Drag Force

The drag force acts in the opposite direction of the fluid flow and it has a significant effect on the gas, liquid and relative velocity fields. Because the relative velocity appears in all interfacial forces, then drag force plays also a role in the radial distribution of the void fraction. Three models have been implemented in the code to calculate the drag force coefficient which are Ishii-Zuber (1979), Tomiyama (1998a), and Schiller-Naumann (1933). The numerical simulation results have been validated against the experimental data of point MTLOOP 41.

Figure (3.5) depicts that Ishii-Zuber and Tomiyama models predict a much larger drag force than the Schiller-Naumann model as a consequence of higher prediction of drag coefficient, because the first two models depend strongly on the Eötvos number, which takes into account the deformation of the bubbles.

A larger drag force means more deceleration of the gas bubbles and a smaller gas velocity, which explains the higher gas velocity predicted by Schiller-Naumann (see Figure 3.6).

As a result of the good prediction of drag force and gas velocity by Ishii-Zuber and Tomiyama models, this leads to a better prediction of the void fraction as shown in Figure (3.7). Indeed, the void fraction distribution in gas-liquid two-phase flows is not de-

termined only by the drag force but is mainly influenced by other interfacial forces like lift and wall lubrication forces.

Accordingly, the drag force coefficient calculated by the Ishii-Zuber model is selected for further simulations in the rest of this thesis work. The better performance is related to its taking into account the effect of bubble distortion and deformation from spherical to ellipsoidal and cap shape bubbles on the drag coefficient through the inclusion of the Eötvös model.

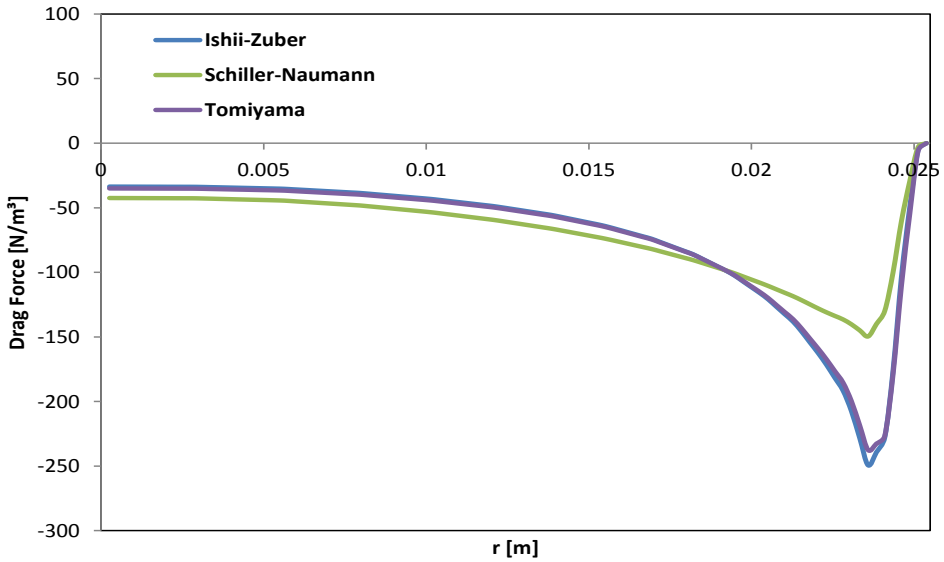

Figure 3.5. Drag force value calculated with different drag coefficient models of MT-LOOP 41

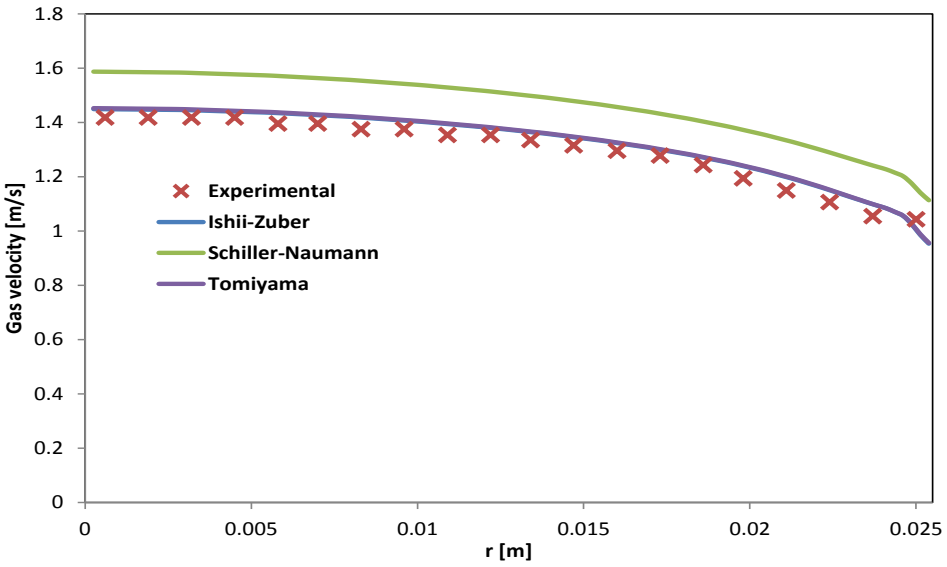

Figure 3.6. Gas velocity profiles calculated with different drag coefficient models of MT-LOOP 41

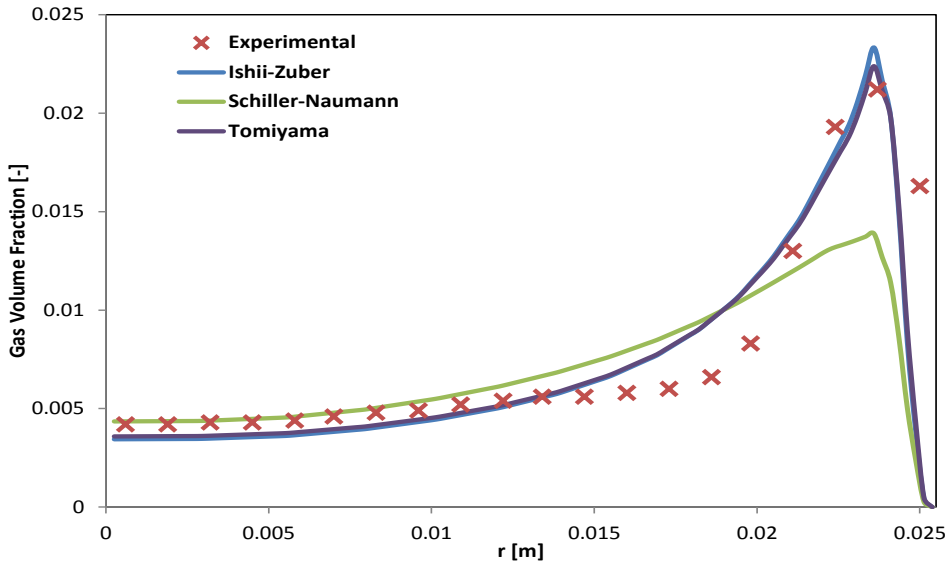

Figure 3.7. Void fraction profiles using different drag coefficient models of MT-LOOP 41

3.4.2 Lift Force

The effect of the lift force on the radial distribution of the gas volume fraction has been studied by using different lift force coefficient models, which determine the migration of bubbles in the radial direction as introduced by Zun (1980). A constant value $C_L = 0.1$ suggested by Lopez de Bertodano (1992) has been implemented and compared to another value $C_L = 0.5$ recommended by Drew and Lahey (1979). According to these models the lift coefficient is always positive and the associated lift force acts perpendicular to the flow in the direction of the lower liquid velocity, i.e., towards the pipe wall in case of upward co-current flow in pipes, which mean that it is valid only for small spherical bubbles. The results of the simulations of Test MT-LOOP 39 using the previous models, have been compared to another simulation results using the model of Tomiyama (2002) which takes into account the deformation that is shown by larger bubbles, leading to a sign change in the lift force acting towards higher liquid velocity, i.e., towards the pipe center.

The results of the previous investigations are shown in Figure (3.8). Where $C_L = 0.1$ can reproduce the gas volume fraction at the wall as the Tomiyama model does, contrary to $C_L = 0.5$ which is over-predicting the peak of the void fraction near the wall.

Because one of the main targets of this work is the simulation of poly-dispersed bubbly flow with variable bubble diameter, bubbles with larger diameters (> 5.8 mm) could be encountered, that, according to lift force definition should reside in the central region of

the pipe (negative lift coefficient), then Tomiyama correlation is used in all the following simulations. To prove the superiority of Tomiyama model over the constant value of $C_L = 0.1$ for bubbles with larger diameters, the same test case MT-LOOP 39 has been simulated again using a bubble diameter larger than 5.8 mm (i.e. 8 mm), the result of the simulations depicted in Figure (3.9) shows that the usage of the Tomiyama lift force coefficient model predicts higher void fraction values in the core region rather than with the use of a constant coefficient $C_L = 0.1$, because of the negative lift coefficient associated with large bubbles captured by Tomiyama model. This results prove the migration of large bubbles toward the pipe core.

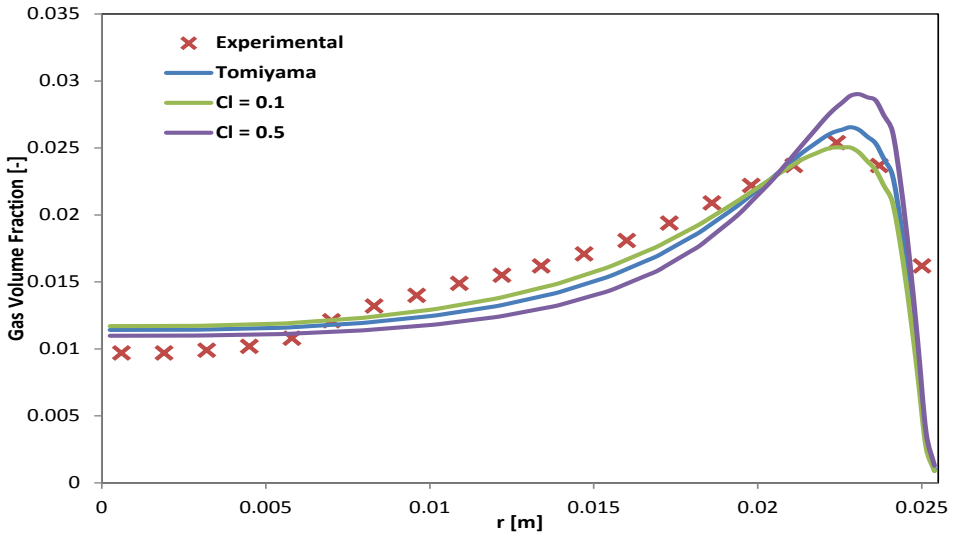

Figure 3.8. Void fraction profiles using different lift force coefficient models of MT-LOOP 39.

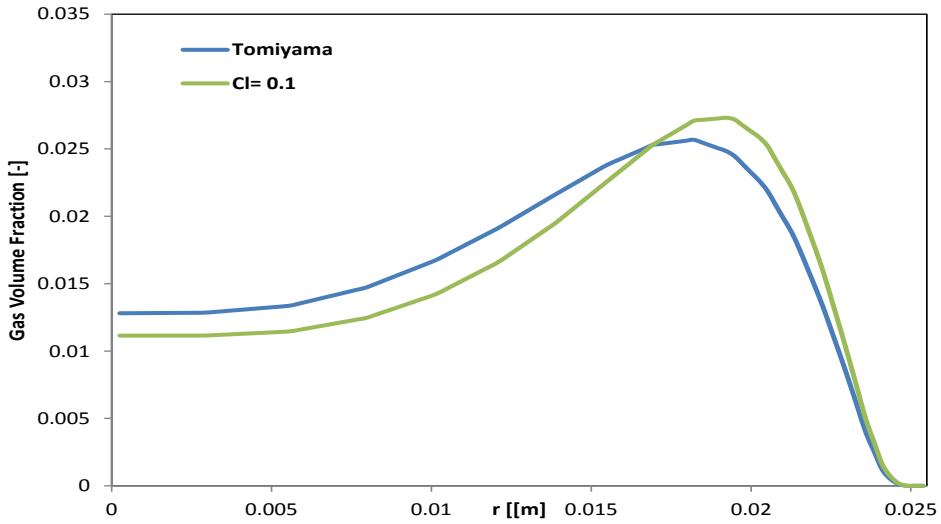

Figure 3.9. The effect of different lift force coefficient models for large bubble diameters (>5.8mm) of MT-LOOP 39.

2.4.3 Wall Lubrication Force

The wall lubrication force is the second force acting perpendicular to the flow direction which determines the radial distribution of the gas volume fraction profile. It acts on the bubbles in the vicinity of the wall and it is caused by the surface tension preventing them from attaching the solid wall.

Of the different wall lubrication force models available in the literature, three of them have been chosen because of their superior applicability in the widely-used CFD codes and implemented in OpenFOAM for assessment. Then a comparison is made between them to asses which model provides the best prediction of the void fraction radial profile across the flow channel. The implemented models are Antal et al., (1991), Tomiyama et al., (1998) and Hosokawa et al., (2002). According to the three of them, the wall force coefficient C_W depends on the distance to the wall and is expected to be positive so the bubble is driven away from it. The results of the comparison are shown in Figure (3.10) for the MT-LOOP test 61 with lower liquid velocity and test 63 with higher one.

For test MT-LOOP 61, the height of the void fraction peak is underestimated by both Antal and Tomiyama models. In addition, the position of the peak predicted by Tomiyama is far away from the wall. Prediction by Hosokawa model is in good agreement with the data. For test MT-LOOP 63, the models of Antal and Hosokawa tend to overestimate the height of the void peak, the model of Tomiyama again underestimating the peak height with a shifted position far away from the wall because of a higher wall force coefficient. A radial shift of the void fraction peak towards the wall can also be observed with Antal model, which indicates that the wall force by Antal seems too weak to balance the lift force at a given radial position (Frank et al., 2004). The Hosokawa model predicts better the position of the void peak and, therefore, it will be used in the rest of this thesis.

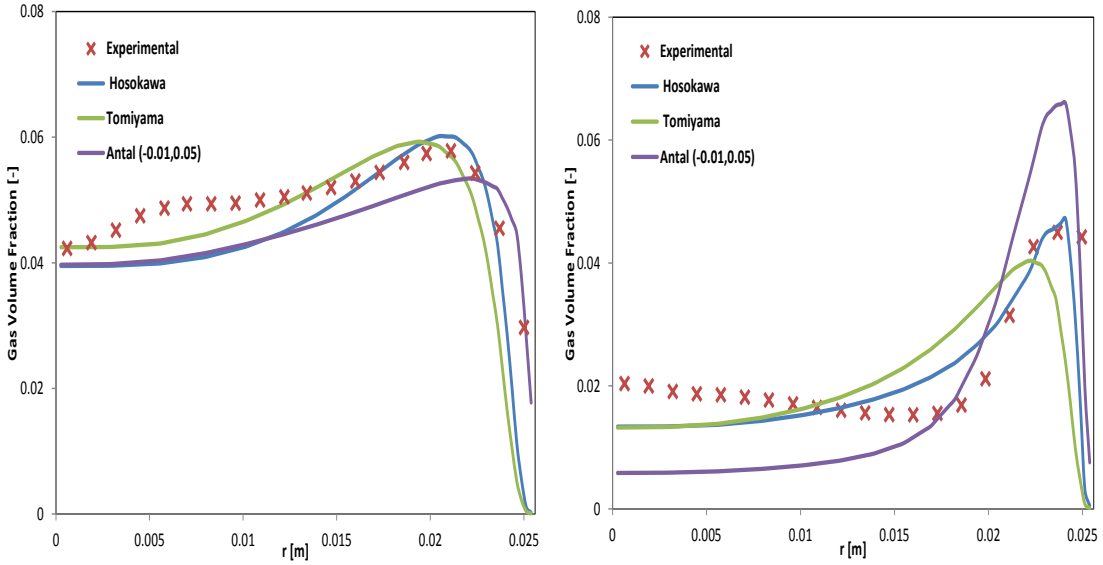

Figure 3.10. Comparison of measured and calculated radial gas volume fraction profile of Tests MT-LOOP 61 (left) and MT-LOOP 63 (right)

3.4.4 Turbulent Dispersion Force

The turbulent dispersion force describes the effect of the turbulent fluctuations of the liquid velocity on the bubbles, it is driven by the void fraction gradient and result in additional dispersion of bubbles from high gas volume fraction regions to those with lower gas fraction.

Two models describing the turbulent dispersion force coefficient have been investigated through studying their effects on the void fraction radial profile. The results are shown in Figure (3.11) for the simulation of MT-LOOP Test 39. According to the FAD model described in section (2.2.2.1), the turbulent dispersion force coefficient C_{TD} is large and variable along the pipe cross section when compared to the constant value of 0.1 – 0.5 proposed by Lopez de Bertodano from RPI. The higher value of the turbulent dispersion force by FAD leads to a better prediction of the void fraction profile peak within the wall region in comparison with the over-predicted peak calculated by the constant coefficient C_{TD} by RPI due to a reduced turbulent dispersion force.

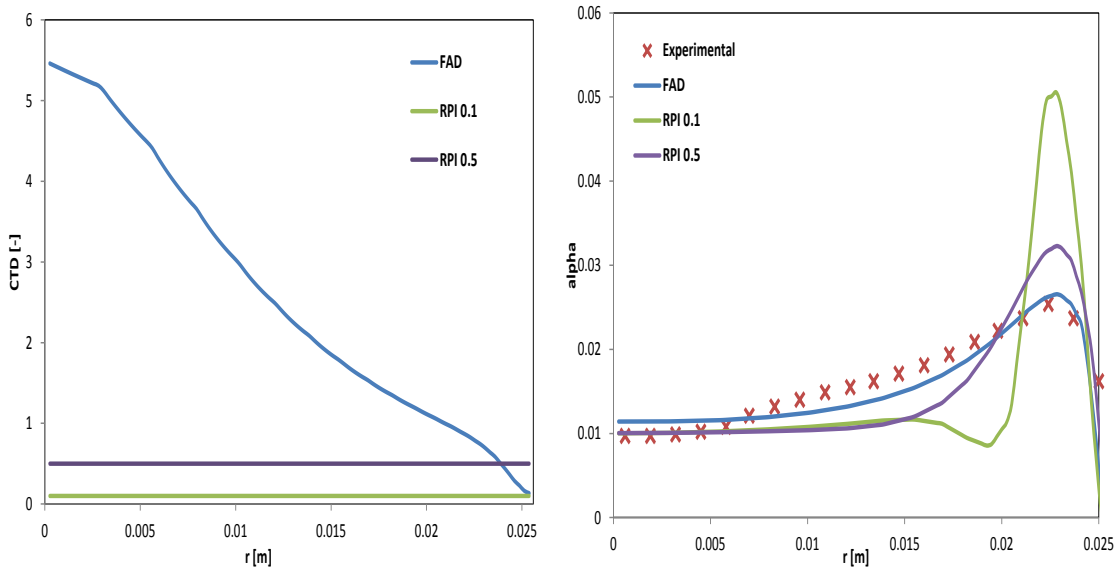

Figure 3.11. Comparison of C_{TD} (left), and void fraction profile (right) using FAD and PRI models for MT-LOOP Test 39

In conclusion, the radial void fraction profile is assumed to correspond to the equilibrium of the non-drag forces lift, wall lubrication and turbulent dispersion that are depicted in Figure (3.12).

Considering the results of the different model evaluations, a combination of the following interfacial force models: Ishii and Zuber (1979) drag force, Tomiyama et al., (2002) lift force**,** Hosokawa et al., (2002) wall lubrication force and FAD/Burns et al., (2004) turbulent dispersion force will be used for further simulations that will come in the rest work of this thesis.

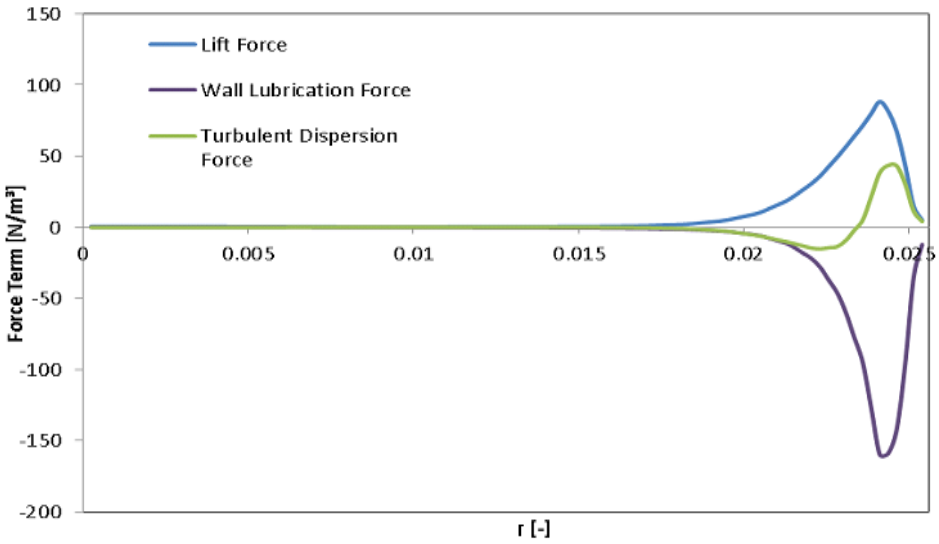

Figure 3.12. Radial profiles of the non-drag forces for MT39

3.5 Investigations on Bubble-Induced Turbulence Models

The accurate prediction of turbulence parameters is very important, because bubble interaction mechanisms such as bubble coalescence and breakup rely strongly on these parameters, i.e. the turbulent energy dissipation rate. In this section the effect of the bubbles on the turbulence production and destruction has been investigated by studying the contribution of BIT and the effect of different models.

The effect of BIT is considered by following two approaches, either by adding an additional viscosity term or source terms to the turbulent transport equations ($k-\varepsilon$). In the second approach the difference between various models lies in the calculation of the turbulence time scale τ. Four BIT source term models that reflect the last approach have been implemented and tested, namely, Rzehak et al., (2012), Morel (1997), Troshko et al., (2001) and Pfleger et al., (2001), (see Bubble-Induced Turbulence in section 2.2.2.2).

According to Eq. (2.73) for each of the previous models, different values have been proposed for the parameter C_ε that are summarized in Table (2.2).

The effect of the bubble-induced turbulence on the turbulence parameters is shown in Figure (3.14) for the cases MT-LOOP39 and 61. A combination of the interfacial forces that provided better results during the evaluation that was conducted in section 3.4 are also used during the current simulations for the assessment of the different BIT mod-

els. The results show that including BIT can improve the void fraction radial profile considerably (see Figure 3.13), where the exclusion of BIT from the turbulence modeling leads to an extreme over-prediction of the void fraction peak near the wall as a result of a lower predicted value of the liquid eddy viscosity in the near wall region, thus increasing the velocity gradient, since it is inversely proportional to the eddy viscosity μ_l^t (Liao et al., 2012) according to the equation

$$\frac{dU_l}{dr} = \frac{\tau_{shear}}{(1-\alpha_g)(\mu_l + \mu_l^t)}, \tag{3.1}$$

where τ_{shear} represents the shear stress.

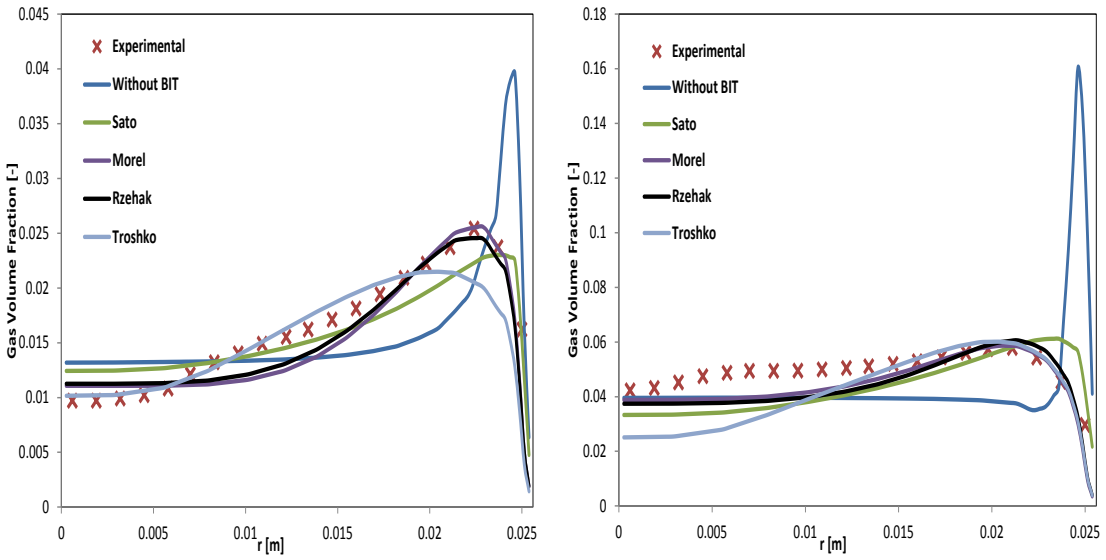

Figure 3.13. Influence of the BIT models on the void fraction for MT39 (left) and MT61 (right)

The large liquid velocity gradient leads to a too strong lift force that pushes small bubbles (with positive lift coefficient according to Tomiyama et al., 2002) towards the pipe wall. This explains the higher predicted void fraction peak in that region without using BIT. Other reason for the over-prediction of the void fraction in that region is the lower turbulent dispersion force associated with lower eddy viscosity, this force which has an equalizing effect on the bubble distribution, and, therefore, its under-prediction will result in a higher void fraction gradient.

The Sato model, which considers the BIT contribution by an additional viscosity term, gives a maximum eddy viscosity in the central core region if compared with other BIT models, which show a suppression of the viscosity in that region. Regarding the turbulent dissipation rate, the Sato model yields an under-prediction in the core region which

is where some important processes such as turbulent dispersion and bubble coalescence and breakup take place, especially in cases with high void fractions and larger bubble diameters. These processes are highly dependent on the turbulent dissipation rate. The turbulent dissipation increases with the increase in the gas velocity, which yields a higher void fraction with small bubbles. These bubbles accumulate near the wall and increase the turbulence intensity and, therefore, the liquid velocity gradient. A larger velocity gradient leads to an increase in the shear-induced dissipation.

For the additional source term models in the $(k-\varepsilon)$ equations, as stated before, the BIT models differ in the calculation of the time scale τ and the value of C_{ε}. For them the time scale is dependent on a combination of two of the variables: k, ε or bubble diameter, except for Troshko in which τ has a strong dependence on the bubble diameter. It decreases with the increase in the gas superfacial velocity (Liao et al., 2012). Furthermore, the Pfleger model provides the largest time scale value along the radial direction except for the near wall region where Rzehak provides a larger value (see Figure 3.14).

The differences in the calculation of the time scale amongst the models will necessarily reflect a difference in the calculated dissipation rate and eddy viscosity values. The time scale calculated by Troshko is the smallest of all, leading to a very low liquid eddy viscosity in the pipe center region and, hence, a lower turbulent dispersion force. This means an unreasonable void wall peak because of the effect of the lift force that pushes small bubbles effectively towards the wall in the case of the insufficient smoothing effect of the turbulent dispersion force due to low liquid viscosity. Therefore, C_{ε} has been adjusted to a smaller value equal to 0.1 to achieve reasonable results.

The models of Morel and Rzehak behave similarly when predicting the eddy viscosity and the turbulent dissipation rate as shown in Figure (3.14), and even the void fraction profile shows a good agreement with the experimental void fraction profile, especially in the wall region. The results obtained with Pfleger´s model have been excluded from the comparison due to the difficulty in achieving a converged solution, which affects the accuracy of the obtained results.

In conclusion, the BIT can improve the void fraction profile prediction, because it has a strong and indirect effect through the coupling between the turbulence parameters calculated by the BIT and the lift force from on one side, and the strong coupling between the turbulent viscosity and the turbulent dispersion force, on the other side. Both mechanisms have a strong effect on the bubble distribution in the radial direction.

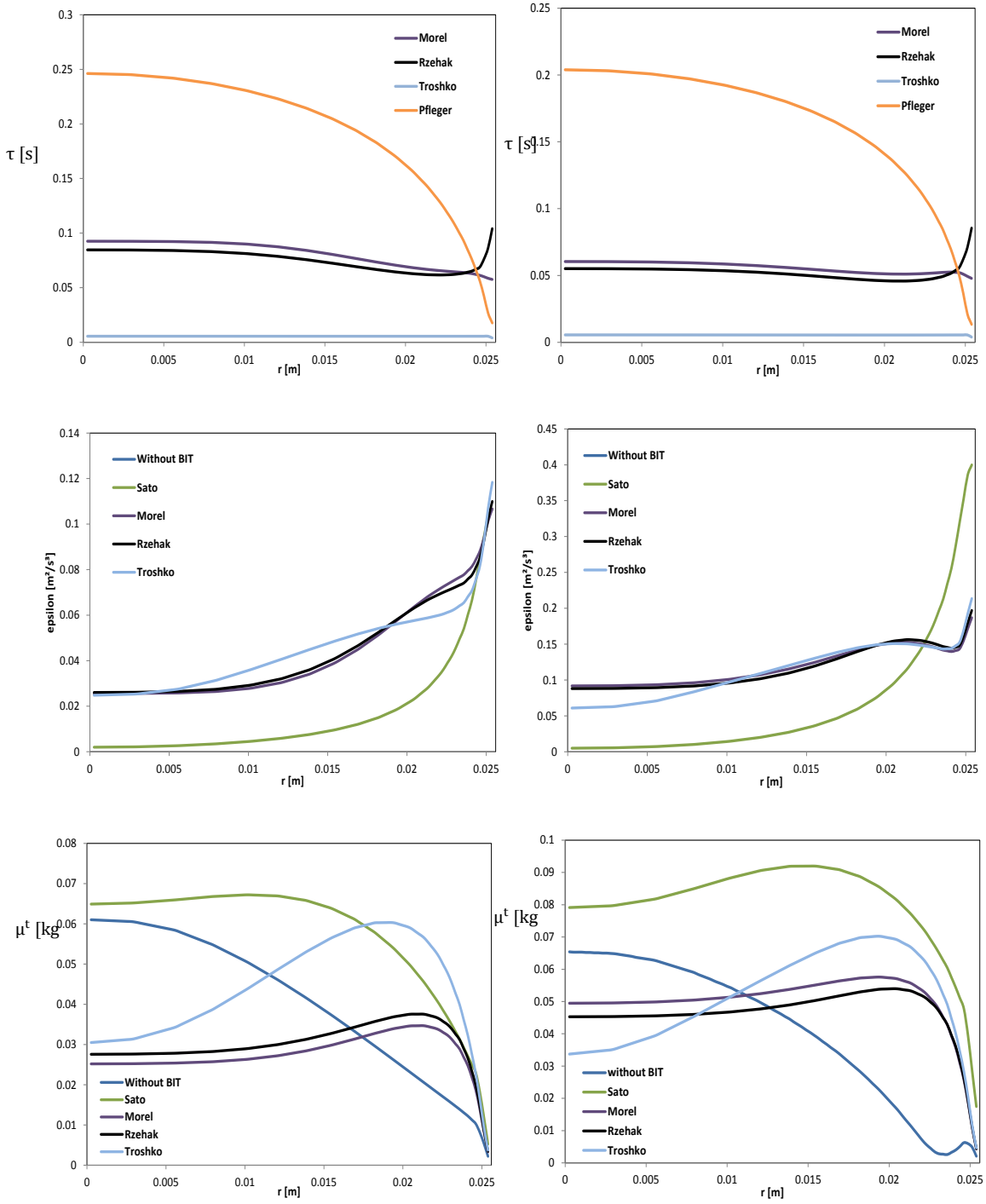

Figure 3.14: Turbulent parameters calculated by different BIT models for MT39 (left) and MT61(right)

3.6. Conclusion

In this chapter the ground work needed for the rest of the thesis has been performed, The chapter has focused on the modeling of bubbly two phase flow with different inter-facial drag and non-drag forces models as closure relations for the Euler-Euler two-fluid model which adopted in the thesis. The models have been implemented in the new solver that is developed in the framework of this thesis work for OpenFOAM (the solver is briefly described in APPENDIX B) in order to obtain the best combination of these forces to predict the radial gas volume fraction distribution as accurately as possible. Furthermore, the effect of the bubble-induced turbulence on the radial void fraction distribution has been investigated through the implementation of different models found in the literature to assess their performance in describing the effect of the bubbles on the turbulence production and destruction.

In order to examine the relative merits of the aforementioned closure models, the developed solver has been used to simulate the bubbly flow of some steady state experiments carried out at the air-water MT-LOOP test facility. During the simulation, the bubble diameter has been assumed to be constant with an average bubble size taken from the experimental data for each test simulated. The bubble interaction mechanisms like bubble coalescence and breakup, which play a major role in the determination of the bubble size distribution, have not been taken into account, because these processes are rare to occur in low void fraction system flows such as those observed in the experimental tests analyzed. This has facilitated the assessment of the bubble force and turbulence models by eliminating the more complex bubble interactions.

A good agreement between the measured and the predicted radial void fraction profiles of different MT-LOOP test cases can be seen in Figure (3.15) when using the best combination of reference closure models that was identified as an outcome of the analysis performed in this chapter, namely

- **Drag force**:Ishii and Zuber (1979).
- **Lift force**: Tomiyama et al., (2002).
- **Wall lubrication force**: Hosokawa et al., (2002).
- **Turbulent dispersion force**: FAD/Burns et al., (2004).
- **Bubble-induced turbulence**: Morel (1997).

As we can see, the accuracy of the results is reduced as the gas content as measured by its superficial velocity increases. For high void fractions, it is clear that the bubble

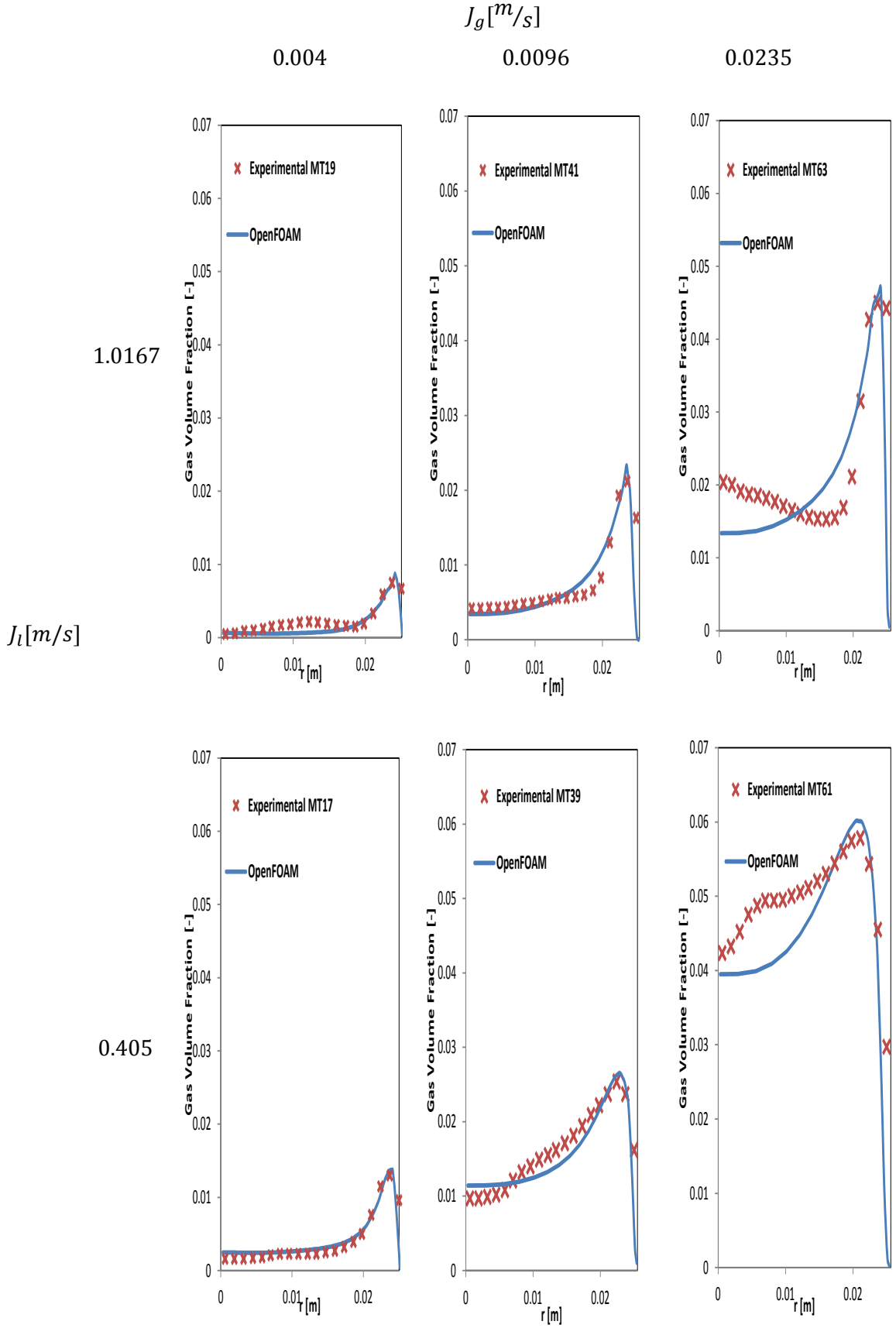

Figure 3.15. Simulation of different MT-LOOP Tests by using the reference closure models.

interaction mechanisms are necessary and the assumption of a single bubble size is not appropriate. Further developments in the direction of taking these mechanisms into consideration is shown in the following chapters.

Chapter Four

Interfacial Area Transport and Mechanistic Models for Bubble Coalescence and Breakup

In the safety analysis of nuclear reactors the flow field is complex and involves two-phase flow which can be represented by field equations and constitutive relations. In the two-fluid model approach adopted in this work, each phase is considered separately in terms of two sets of conservation equations that govern the balance of mass, momentum and energy in each phase (Talley 2011). The constitutive relations representing the phasic interaction terms, the most important characteristics of the two-fluid model formulation, express the transport of mass, momentum and energy through the interface between the phases in term of the interfacial area concentration (IAC) which is related to the geometrical effects of the interfacial structure, and the driving force that characterizes the local transport mechanism of the inter-phase transport (Cheung 2006). Therefore, an accurate estimation of the interfacial area concentration is essential.

In gas-liquid two-phase vertical flow, the interfacial structure distribution, known as flow regimes, is traditionally classified into five different categories, namely, bubbly, cap, slug, churn-turbulent and annular flow (shown in Figure 4.1). In most of thermal-hydraulic system analysis codes, the interfacial area concentration is calculated by using an empirical approach based on the two-phase flow regimes and several empirically based regime transition criteria (Mishima and Ishii, 1984; Hibiki and Mishima, 2001). Since these transition criteria are empirical relations, they cannot describe the dynamic nature of the structural changes occurring at the interface and the gradual transition between regimes. Therefore, they are only applicable for steady state and fully developed flow, and only valid for a limited set of flow conditions and geometries (Hibiki and Ishii 2001).

The internal structure of two-phase flow can be described by the interfacial area concentration that changes with the evolution of the flow due to bubble coalescence and breakup resulting from the interactions among the bubbles and between the bubbles and the turbulent eddies. Therefore, the dynamic change of the interfacial structure could, in principle, be adequately described by a transport equation (Ishii, 1975;

Kocamustafaogullari and Ishii, 1995), analogous to the Boltzmann transport equation, that describes the transport of the interfacial area density by an integro-differential equation. Its solution can provide the time and space evolution of the interfacial area concentration, and eliminate the need of using empirical correlation to determine the flow regime transitions. This dynamic approach eliminates the artificial discontinuities that appear at flow regime transition.

In the previous chapter three, for the purpose of the assessment of the momentum closure models, the gas bubbles were assumed to have an equal size and shape, which might be correct for low gas fraction flows. But for a real poly-dispersed flow, a wider spectrum of bubble sizes and shapes may exist due to bubble coalescence and breakup, and the interfacial area concentration has to be solved together in a coupled manner with the set of conservation equations provided by the two-fluid model for gas-liquid flow.

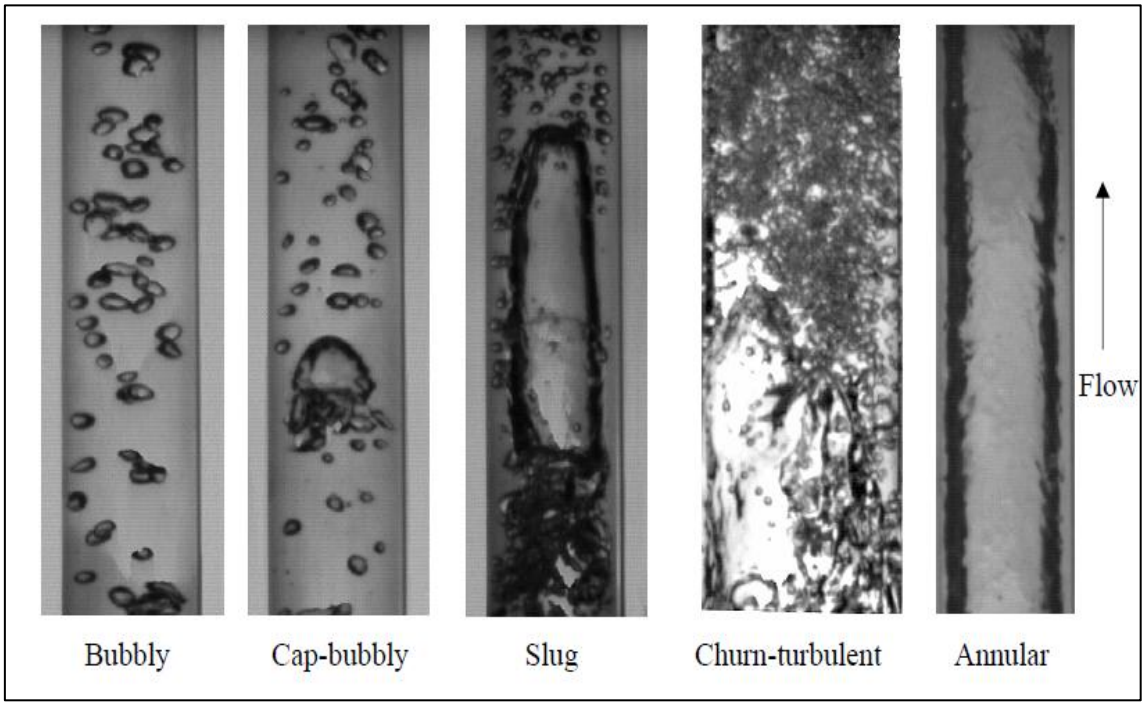

Figure 4.1. Typical flow regimes for air-water in a vertical pipe (Sun 2007)

4.1 The Transport Equation for the Interfacial Area Concentration

The interfacial area transport equation is based on the Boltzmann transport equation for particles whose distribution is specified by the particle number density distribution function $f(V,x,t)$ per volume of the two-phase mixture, and written as

$$\frac{\partial f}{\partial t}+\nabla(f\vec{v})+\frac{\partial}{\partial V}\left(f\frac{dV}{dt}\right)=\sum_j S_j+S_{Ph}\,, \tag{4.1}$$

where v is the particle velocity. The S_j and S_{Ph} are the particle source/sink rates per unit mixture volume due to jth particle interactions such as breakup or coalescence and the source rate due to phase change caused by nucleation, evaporation, or condensation, respectively.

The interfacial area transport equation is derived by multiplying Eq. (4.1) by the interfacial area of a particle with volume V and integrating it over the volume of all particle sizes (Kim et al., 2002) in order to get

$$\frac{\partial a_i}{\partial t}+\nabla(a_i\vec{v}_i)-\left(\frac{\dot{V}}{V}\right)\int_{V_{min}}^{V_{max}} fV\,dA_i=\int_{V_{min}}^{V_{max}}\left[\sum_j S_j+S_{ph}\right]A_i\,dV\,, \tag{4.2}$$

where a_i is the average interfacial area given by

$$a_i(x,t)=\int_{V_{min}}^{V_{max}} f(V,x,t)\,A_i(V)\,dV\,, \tag{4.3}$$

The variable $\vec{v}_i$ is the interfacial area-weighted velocity of the fluid particle defined as

$$\vec{v}_i(x,t)=\frac{\int_{V_{min}}^{V_{max}} f(V,x,t)A_i(V)\vec{v}(V,x,t)dV}{\int_{V_{min}}^{V_{max}} f(V,x,t)A_i(V)dV}\,, \tag{4.4}$$

For the purpose of modeling the source and sink terms in Eq. (4.2) resulting from bubble coalescence and breakup, the bubbles are treated in two groups: the spherical/distorted bubble group and the cap/slug bubble group (Wu et al., 1997) yielding two interfacial area transport equations that involve the inner and inter-group interactions. Since this work is dedicated to the modeling of two-phase bubbly flow, where all bubbles can be categorized as one group and they remain similar in shape after their inter-

actions, their characteristic transport phenomena are similar and can be described by one single transport equation (Ishii and Hibiki 2006). Therefore, only the one-group interfacial area transport equation will be studied and described in more details.

4.2 The one-group Interfacial Area Transport Equation

Based on the derivation of the one-group interfacial area transport equation by Wu et al., (1998b), Kim (1999) and Ishii and Hibiki (2006), it can be written as

$$\frac{\partial a_i}{\partial t} + \nabla.(a_i \vec{v}_i) = \frac{2}{3}\left(\frac{a_i}{\alpha}\right)\left(\frac{\partial \alpha}{\partial t} + \nabla.\left(\alpha \vec{v}_g\right) - \eta_{ph}\right) + \frac{1}{3\psi}\left(\frac{\alpha}{a_i}\right)^2 \sum_j R_j + \pi D_{bc}^2 R_{ph}\,, \quad (4.5)$$

with the variables η_{ph}, R_j, R_{ph} and D_{bc} being the interfacial area density change rate due to phase change, change rate due to bubble interaction, change rate due to nucleation and the bubble critical size, respectively. ψ is the bubble shape factor defined as

$$\psi = \frac{1}{36\pi}\left(\frac{D_{sm}}{D_e}\right)^3, \quad (4.6)$$

in which D_{sm} is the Sauter mean diameter given by

$$D_{sm} = \frac{6\alpha}{a_i}, \quad (4.7)$$

and D_e is the volume-equivalent diameter. For small spherical shape bubbles, D_{sm} and D_e are equal.

In Eq. (4.5) the left-hand side represents the time rate of change and convection of the interfacial area concentration. The first term on the right-hand side represent the rate of change of the interfacial area concentration due to particle volume change. The second term account for the rate of change due to bubble interaction mechanisms, and the third term due to phase change by nucleation at the wall.

For spherical bubbly flow *without phase change*, Eq. (4.5) can be simplified as

$$\frac{\partial a_i}{\partial t} + \nabla.(a_i \vec{v}_i) = \frac{2}{3}\left(\frac{a_i}{\alpha}\right)\left(\frac{\partial \alpha}{\partial t} + \nabla.\left(\alpha \vec{v}_g\right)\right) + 12\pi\left(\frac{\alpha}{a_i}\right)^2 \sum_j R_j\,, \quad (4.8)$$

The bubble interaction term R_j appearing in Eq. (4.8), should be modeled independently by a mechanistic models expressing the interaction mechanisms including bubble coalescence and breakup. In the case of boiling-condensing flow, bubble nucleation

and condensation phenomena need also to be modeled, which will be done in another place in this thesis.

4.3 Bubble Coalescence and Breakup

Bubble coalescence and breakup are important processes characterizing the gas-liquid dispersion, they govern the bubble size distribution and directly affect the interfacial mass transfer by the renewal of bubble surfaces. The bubble size distribution is controlled by the balance between rates of coalescence and breakup (Luo 1993). The modeling of bubble coalescence and breakup rates is complex and depends mainly on the knowledge of collision and breakup frequencies as well as the probabilities of coalescence and breakup. Both phenomena are depicted in Figure (4.2) and (4.3).

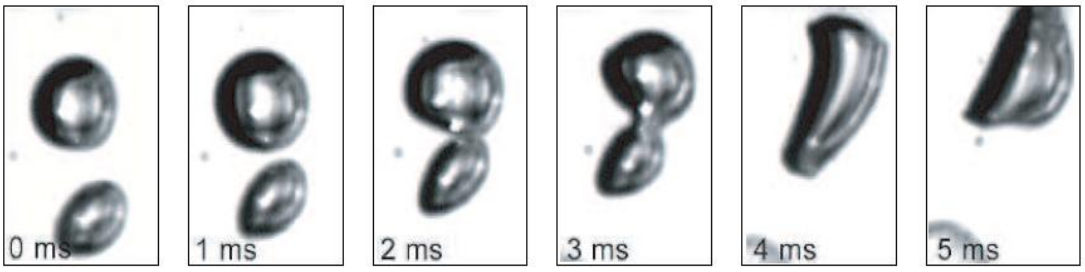

Figure 4.2. Coalescence of two air bubbles in liquid phase (Gharaibah 2008)

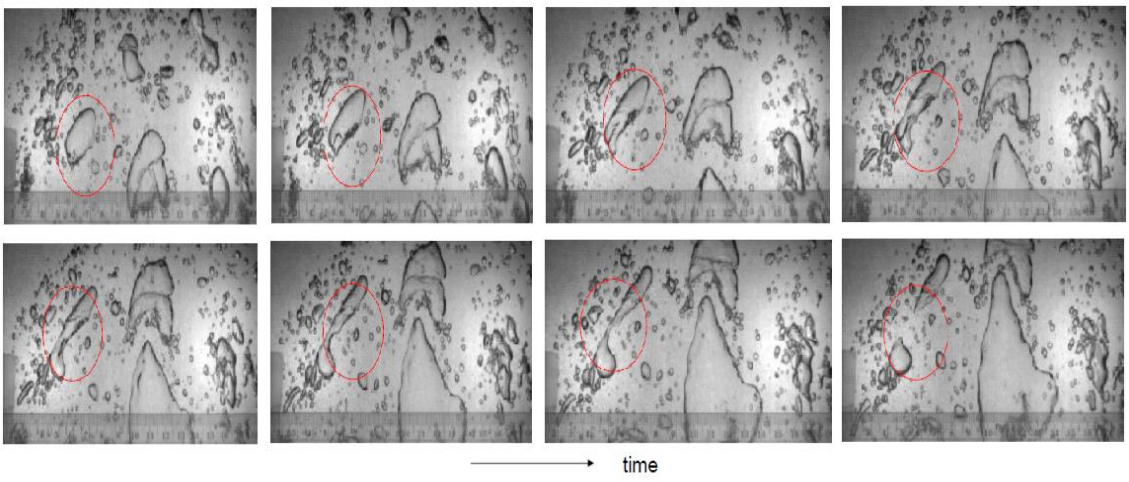

Figure 4.3. Breakup of air bubble (Sun 2007)

Three major interaction mechanisms that occur in bubbly flow conditions were identified and mechanistic models of theses mechanisms have been established (Ishii et al., 2002). They include

- Coalescence through random collision driven by turbulent eddies (RC).
- Coalescence due to the acceleration of the following bubble in the wake of the preceding bubble (WE).
- Breakup due to the impact of turbulent eddies (TI).

Schematic illustrations of these mechanisms are shown in Figure (4.4).

Modeling bubble coalescence and breakup depends on the estimation of the breakup frequency, breakup efficiency, collision frequency, and coalescence efficiency. The breakup efficiency is not explicitly modeled but it is considered by different authors included in the breakup frequency term. The breakup frequency could be expressed as the collision frequency of the turbulent eddies against the bubble multiplied by a collision efficiency (Pellacani 2012), many models for breakup have been published in the literature based on the determination of the breakup frequency in terms of turbulent fluctuation and collisions, viscous shear stresses, shearing off, and surface instability (Liao and Lucas 2009, DEJU et al., 2012). Only the turbulent collision mechanism is considered in this work.

Various models describing the coalescence process have been proposed in the literature such as the critical velocity model proposed by Lehr et al., (2002), the energy model, and the film drainage model (Shinnar and Church 1960). The film drainage model is the most used one; it states that collision of two bubbles will trap a thin film of liquid between them. The attractive force between the bubbles will drive the film to drain out to a critical thickness, where it ruptures resulting in coalescence (see Figure 4.5). The coalescence process can be analyzed by examining the collision events (frequency) and the probability of collision resulting in coalescence (coalescence efficiency) (Luo 1993). Since the collision of two or more bubbles at the same time has a very small probability, only binary collision or binary coalescence is usually considered. For the estimation of bubble-bubble collision frequency, it is assumed that the movement of bubbles behaves like ideal gas molecules (Coulaloglou and Tavlarides 1977), following the kinetic theory of gases (Loeb 1927). For the derivation of the collision frequency expression, Prince and Blanch (1990) suggested the effects of turbulence, buoyancy

and laminar shear. They postulated that the fluctuating turbulent velocity is the primary cause of bubble collision.

The numerical simulation of breakup processes is based on some simplifying assumptions that reduce the complexity of the problem to be solved (Jo and Revankar, 2010a; Pellacani 2012). These assumptions are

- Binary breakup: the bubble splits into *two* bubbles of equal or unequal size.
- The liquid phase turbulence can be regarded as locally homogeneous and isotropic.
- The bubble diameter D lies in the inertial sub-range ($L > D > \eta$), where L is the large eddy scale and η is the Kolomogrov scale. Therefore, the characteristics of bubble and eddy motion can be expressed as a function of the kinetic energy dissipation ε only.

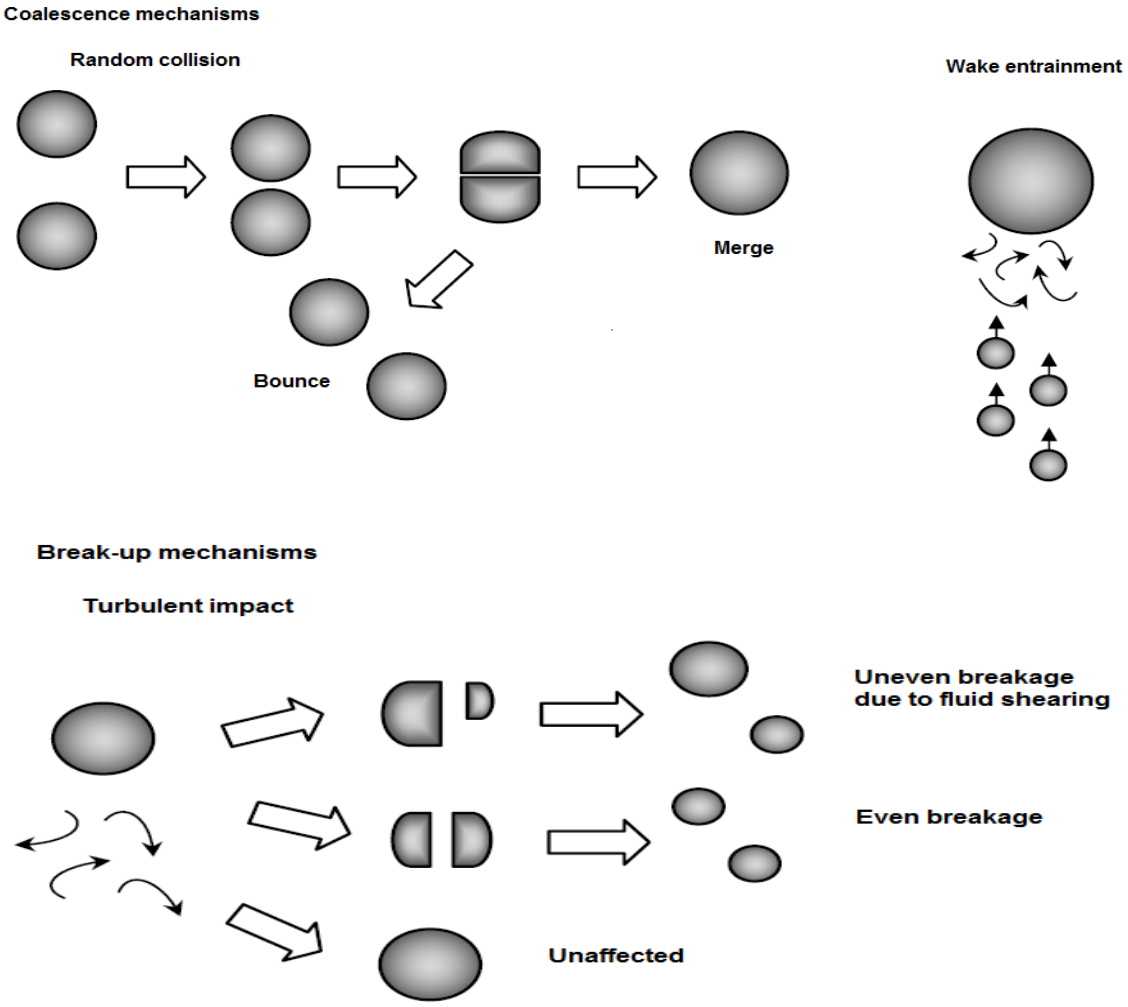

Figure 4.4. Major bubble interaction mechanisms in bubbly flow conditions (Yeoh and Tu 2010)

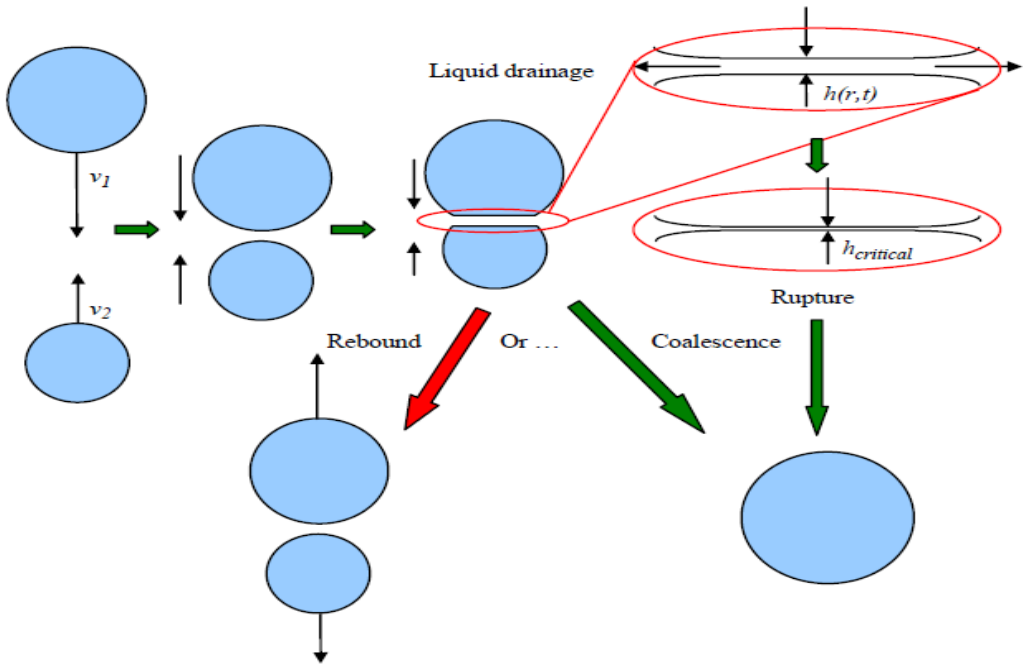

Figure 4.5. Film drainage model (Chen et al., 2005)

4.4 Mechanistic Models for Bubble Coalescence and Breakup

In the following subsections the most used models describing the coalescence and breakup effects for the one-group interfacial area transport equation are presented in detail. For the purpose of identifying the different bubble interaction terms in the adiabatic bubbly flow, the one-group interfacial area transport equation can be written as

$$\frac{\partial a_i}{\partial t} + \nabla.(a_i \vec{v}_i) = \frac{2}{3}\left(\frac{a_i}{\alpha}\right)\left(\frac{\partial \alpha}{\partial t} + \nabla.(\alpha \vec{v}_g)\right) + (\phi_{RC} + \phi_{WE} + \phi_{TI}), \qquad (4.9)$$

4.4.1 Wu et al. (1998) Model

- **Bubble Coalescence Due to Random Collisions**

The bubble coalescence rate caused by random collision, ϕ_{RC}, is given by

$$\phi_{RC} = -12\pi\left(\frac{\alpha}{a_i}\right)^2 f_{RC} n \eta_C, \qquad (4.10)$$

where, f_{RC} is the bubble collision frequency, η_C is the coalescence efficiency and n is the bubble number density. The bubble collision induced by turbulence is assumed to occur between *neighboring* bubbles only. The time interval for one collision, Δt_C, is defined as

$$\Delta t_C = \frac{L_T}{u_t}, \tag{4.11}$$

where, u_t is the root-mean-square approaching velocity of the two bubbles given by $\varepsilon^{1/3} D_{sm}^{1/3}$, and L_T is the mean travelling distance between the two bubbles for one collision given by

$$L_T \propto \frac{D_{sm}}{\alpha^{1/3}} \left(1 - \left(\frac{\alpha}{\alpha_{max}}\right)^{1/3}\right), \tag{4.12}$$

with α represeting the void fraction. The collision frequency for two bubbles moving toward each other, f_{RC}, is given by (the symbol $\propto$ represents proportionality)

$$f_{RC} = \frac{1}{\Delta t_C} \propto \frac{u_t}{D_{sm}} \alpha^{1/3} \left(\frac{\alpha_{max}^{1/3}}{\alpha_{max}^{1/3} - \alpha^{1/3}}\right), \tag{4.13}$$

The collision frequency is modified by the introduction of a probability function, P_C, that characterizes the probability that a bubble move toward a neighboring bubble; because the bubbles do not always move toward each other. This probability is given by

$$P_C \propto \left(\frac{\alpha}{\alpha_{max}}\right)^{2/3}, \tag{4.14}$$

Another modification factor is suggested for the situations in which the mean distance between the bubbles is very large, and hence; no collision can be accounted for because the range of the relative motion for collisions between neighboring bubbles is limited by an eddy size comparable to the bubble size. To consider this effect, the following modification factor is suggested

$$\left(1 - exp\left(-C \ \frac{\alpha_{max}^{1/3} \alpha^{1/3}}{\alpha_{max}^{1/3} - \alpha^{1/3}}\right)\right), \tag{4.15}$$

The final form of the bubble collision frequency is given by

$$f_{RC} \approx (u_t n D_{sm}^2)\left(\frac{1}{\alpha_{max}^{1/3}\left(\alpha_{max}^{1/3}-\alpha^{1/3}\right)}\right)\left(1-exp\left(-C\frac{\alpha_{max}^{1/3}\alpha^{1/3}}{\alpha_{max}^{1/3}-\alpha^{1/3}}\right)\right), \quad (4.16)$$

Since not all collisions will lead to coalescence, a collision efficiency was suggested (Oolman and Blanch, 1986b; Kirkpatrik and Lockett, 1974). According to the film drainage or thinning model, the coalescence rate decreases exponentially as the turbulent fluctuation velocity increases, because when the bubbles approach faster, they tend to bounce back without coalescence (see Figure 4.5). A constant coalescence efficiency, η_C, is employed in this model to depict the randomness of the coalescence phenomenon after each collision. Thus, the final form of the bubble coalescence due to random collision, is given by

$$\begin{aligned}\phi_{RC} &= -12\pi\left(\frac{\alpha}{a_i}\right)^2 f_{RC} n \eta_C \\ &= -12\pi\left(\frac{\alpha}{a_i}\right)^2 \frac{C_{RC}\alpha^2\varepsilon^{1/3}}{D_{sm}^{11/3}}\left(\frac{1}{\alpha_{max}^{1/3}\left(\alpha_{max}^{1/3}-\alpha^{1/3}\right)}\right)\left(1-exp\left(-C\frac{\alpha_{max}^{1/3}\alpha^{1/3}}{\alpha_{max}^{1/3}-\alpha^{1/3}}\right)\right)\end{aligned} \quad (4.17)$$

where, $C_{RC} = 0.021$ and $C = 3.0$ are the adjustable model constants that are determined experimentally and also include other proportionality constants presented in the model. The maximum allowable void fraction $\boldsymbol{\alpha_{max}} = \mathbf{0.8}$ was chosen considering the transition point from slug to annular flow (Cheung et al., 2007).

- **Bubble Coalescence Due to Wake Entrainment**

The bubble coalescence rate caused by wake entrainment, ϕ_{WE}, is given by

$$\phi_{WE} = -12\pi\left(\frac{\alpha}{a_i}\right)^2 f_{WE} n \eta_{WE}\,, \quad (4.18)$$

For a spherical air bubble with an attached wake region in the liquid medium, the number of bubbles inside the effective volume, V_w, in which the following bubbles may collide with the leading one is given by

$$N_w = V_w n \approx \frac{1}{4}\pi D_{sm}^2\left(L_w - \frac{D_{sm}}{2}\right)n\,, \quad (4.19)$$

where L_w is the wake region length. The collision frequency then can be written as

$$f_{we} = \frac{1}{2}\frac{N_w}{\Delta t} = \frac{1}{8}\pi D_{sm}^2 \frac{\left(L_w - \frac{D_{sm}}{2}\right)}{\Delta t} n = \frac{1}{8}\pi D_{sm}^2 \bar{u}_{rw} n\,, \tag{4.20}$$

with Δt as the average time interval for a bubble in the wake region to catch up the preceding bubble, and $\bar{u}_{rw}$ as the relative velocity between the leading bubble and the bubble in the wake region. This variable is given by

$$\bar{u}_{rw} = u_r F\left(\frac{D_{sm}}{L_w}\right), \tag{4.21}$$

in which u_r is the bubble terminal velocity relative to the liquid motion, defined based on the balance between the buoyancy force and drag force in a two-phase bubbly flow (Ishii and Chawla, 1979)

$$u_r = \left(\frac{D_{sm}}{3C_D}\frac{\Delta\rho}{\rho_l}\right)^{1/2}, \tag{4.22}$$

with C_D as the interfacial drag coefficient.

The ratio function, $F\left(\frac{D_{sm}}{L_w}\right)$ was determined by Tsuchiya et al.,(1989), where the wake length is defined to be 5 to 7 times the bubble size in air-water systems. Therefore $F\left(\frac{D_{sm}}{L_w}\right)$ is treated as a constant depending on the fluid properties.

The final form of the bubble coalescence due to wake entrainment is

$$\phi_{WE} = -12\pi\left(\frac{\alpha}{a_i}\right)^2 f_{WE} n \eta_{WE} = -12\pi\left(\frac{\alpha}{a_i}\right)^2 C_{WE} u_r \frac{\alpha^2}{D_{sm}^2}, \tag{4.23}$$

where, C_{WE}= 0.0073 is the model constant determined experimentally by the ratio of the effective wake length to the bubble size and coalescence efficiency.

- **Bubble Breakup Due to Turbulent Impact**

The bubble breakup rate caused by turbulent impact, ϕ_{TI}, is given by

$$\phi_{TI} = 12\pi\left(\frac{\alpha}{a_i}\right)^2 f_{be,coll} n \eta_{TI}\,, \tag{4.24}$$

where $f_{be,coll}$ is the bubble-eddies collision frequency, that depends on the Weber number We, defined as the ratio of the turbulent inertial energy to surface energy

$$We = \frac{\rho_l u_t^2 D_{sm}}{\sigma}, \tag{4.25}$$

The velocity u_t is the *root-mean-square* velocity difference between two points separated by a length D_{sm}. The critical value of Weber number We_{cr} describes the balance between the cohesive and disruptive forces (Wang 2010). Therefore, bubble breakup caused by turbulent eddies impact occurs when the turbulent eddies have enough energy to overcome the surface tension of the bubble, i.e., $We \gg We_{cr}$.

Based on a momentum balance approach between the inertial force of the turbulent eddies and the bubble surface tension force, (Wu et al., 1998) derived the bubble-eddies collision frequency as

$$f_{be,coll} \propto \frac{u_t}{D_{sm}}\left(1 - \frac{We_{cr}}{We}\right)^{1/2}, We > We_{cr}\,, \tag{4.26}$$

The break up efficiency η_{TI}, defined as the probability for a bubble to collide with an eddy that has sufficient energy to break the bubble, is given by (Coulaloglou and Tavlarrides 1976) as

$$\eta_{TI} \propto exp\left(-\frac{u_{t,cr}^2}{u_t^2}\right) = exp\left(-\frac{We_{cr}}{We}\right), We > We_{cr}\,, \tag{4.27}$$

Finally, the increase of the interfacial area due to the bubble breakup caused by turbulent impact can be expressed as

$$\begin{aligned}\phi_{TI} &= 12\pi\left(\frac{\alpha}{a_i}\right)^2 f_{be,coll} n \eta_{TI} \\ &= 12\pi\left(\frac{\alpha}{a_i}\right)^2 C_{TI}\frac{\alpha\varepsilon^{1/3}}{D_{sm}^{11/3}}\left(1 - \frac{We_{cr}}{We}\right) exp\left(-\frac{We_{cr}}{We}\right), We > We_{cr}\,,\end{aligned} \tag{4.28}$$

The adjustable parameters, C_{TI}= 0.0945 and We_{cr}= 2.0 are determined experimentally.

4.4.2 Hibiki and Ishii (2000a) Model

Hibiki and Ishii (2000a) proposed that bubble coalescence due to wake entrainment is unlikely to occur in bubbly flow, and it plays an important role between pairs of large cap bubbles when the flow regime is near the bubbly to slug flow transition boundary, and in the slug flow regime when the fluid is sufficiently viscous to maintain a laminar bubble wake (Yeoh and Tu 2010). For highly turbulent flows, the bubble captured in the wake region will easily leave it before any coalescence can take place. Hence, Hibiki

and Ishii (2000a) focused on the development of models for breakup due to turbulent impact and for coalescence due to random collisions driven by the liquid turbulence.

- **Bubble Coalescence Due to Random Collision**

The bubble coalescence rate caused by random collision, ϕ_{RC}, is given by

$$\phi_{RC} = -12\pi\left(\frac{\alpha}{a_i}\right)^2 f_{RC} n \eta_C \,, \tag{4.29}$$

The bubble random collision frequency f_{RC} is estimated by assuming that the movement of the bubbles behaves like ideal gases molecules (Coulaloglou and Tavlarides, 1977) following the kinetic theory of gases (Loeb, 1927; Prince and Blanch, 1990). f_{RC} is then expressed as a function of the surface available for the collision to take place and of the volume available to the collision, By taking into account the excluded volume for the colliding bubbles and the overlap of the excluded volume for high void fraction situations (Hibiki and Ishii 2000a) the collision frequency is obtained from

$$f_{RC} = C_{RC}\frac{\alpha\varepsilon^{1/3}}{D_{sm}^{2/3}(\alpha_{max}-\alpha)}, \tag{4.30}$$

where C_{RC} is an adjustable variable determined experimentally to be **0.005** for bubbly flow. The maximum allowable void fraction α_{max} is determined to be **0.52** (Taitel et al., 1980), representing the transition boundary from finely dispersed to slug flow.

In contrast to using a constant value for the coalescence efficiency η_C, as Wu et al., (1998) did, Hibiki and Ishii (2000a) used the expression of Coulaloglou and Tavlarides (1977) for η_C as a function of a time required for coalescence of bubbles t_C and a contact time for two bubbles τ_C which led to

$$\eta_C = exp\left(-\frac{t_C}{\tau_C}\right), \tag{4.31}$$

Coulaloglou and Tavlarides (1977) believed that coalescence occurs if the contact time between two intervening bubbles exceeds the time required for the complete film drainage and rupture (Deju et al., 2012).

The time t_C is derived from the liquid-film-thinning assumption (Oolman and Blanch, 1986a, 1986b), as

$$t_C = \frac{1}{8}\sqrt{\frac{\rho_l D_{sm}^3}{2\sigma}}\ln\frac{h_{init}}{h_{crit}}, \tag{4.32}$$

h_{init} is the initial film thickness given by Kirkapatrick and Locket (1974) to be 10^{-4} m, and h_{crit}, is the critical film thickness were rupture occur proposed by Kim and Lee (1987) to be 10^{-8} m.

Levich (1962) used a dimensional consideration for turbulent flow to derive the contact time τ_C

$$\tau_C = \frac{D_{sm}^{2/3}}{2^{2/3}\varepsilon^{1/3}}, \tag{4.33}$$

Finally, the expression for the coalescence efficiency is

$$\eta_C = exp\left(-\frac{\frac{1}{8}\sqrt{\frac{\rho_l D_{sm}^3}{2\sigma}}\ln\frac{h_{init}}{h_{crit}}}{\frac{D_{sm}^{2/3}}{2^{2/3}\varepsilon^{1/3}}}\right) = exp\left(-K_C\frac{\varepsilon^{1/3}\rho_l^{1/2}D_{sm}^{5/6}}{\sigma^{1/2}}\right), \tag{4.34}$$

$$K_C = \frac{2^{2/3}}{8\times 2^{1/2}}\ln\frac{h_{init}}{h_{crit}} = 1.29, \tag{4.35}$$

The final form of the rate of change in the interfacial area due to coalescence induced by random collision ϕ_{RC} is obtained from

$$\begin{aligned}\phi_{RC} &= -12\pi\left(\frac{\alpha}{a_i}\right)^2 f_{RC} n\eta_C \\ &= -12\pi\left(\frac{\alpha}{a_i}\right)^2 C_{RC}\frac{\alpha^2\varepsilon^{1/3}}{D_{sm}^{11/3}(\alpha_{max}-\alpha)}exp\left(-K_C\frac{\varepsilon^{1/3}\rho_l^{1/2}D_{sm}^{5/6}}{\sigma^{1/2}}\right),\end{aligned} \tag{4.36}$$

- **Bubble Breakup Due to Turbulent Impact**

The bubble breakup rate caused by turbulent impact ϕ_{TI}, is given by

$$\phi_{TI} = 12\pi\left(\frac{\alpha}{a_i}\right)^2 f_{be,coll} n\eta_{TI}, \tag{4.37}$$

The bubble-eddy collision frequency $f_{be,coll}$ is calculated based on the assumption that eddies and bubbles behave like ideal gas molecules. Only an eddy with a size comparable to the bubble diameter can break the bubble, since larger eddies transport the

bubbles rather than breaking it, and smaller eddies do not have enough energy for the breakage. Following this idea, Prince and Blanch (1990) set the minimum eddy size which could not cause bubble breakup at eddies smaller than 20% of the bubble size. As for random collision between bubbles, the bubble-eddy collision frequency can be expressed as a function of the surface available to the collision and of the volume available for the collision. One must also take into account the excluded volume occupied by bubbles and eddies and the overlap of the excluded volume for high void fraction. With this considerations, the collision frequency can be written as

$$f_{be,coll} = C_{TI} \frac{\alpha \varepsilon^{1/3}}{D_{sm}^{2/3}(\alpha_{max} - \alpha)} \,, \tag{4.38}$$

where C_{TI} is an adjustable variable determined experimentally to be **0.007** for a bubbly flow. The maximum allowable void fraction α_{max} is determined to be **0.52**.

The break up efficiency η_{TI} is given in terms of the average energy of a single eddy $\overline{e}$ and the average energy required for bubble breakup $\overline{E}_B$,(Prince and Blanch, 1990; Coulaloglou and Tavlarides, 1977; Tsouris and Tavlarides, 1994) as

$$\eta_{TI} = exp\left(-\frac{\overline{E}_B}{\overline{e}}\right), \tag{4.39}$$

The average energy of a single eddy acting on the bubble breakup is given by

$$\overline{e} = 0.43\pi\rho_l D_{sm}^{11/3} \varepsilon^{2/3} \,, \tag{4.40}$$

and the energy required for breakup is calculated from the formula (Hibiki and Ishii 2002)

$$\overline{E}_B = 0.587\pi\sigma D_{sm}^2 \,, \tag{4.41}$$

The final form of the breakup efficiency is then given by

$$\eta_{TI} = exp\left(-\frac{\overline{E}_B}{\overline{e}}\right) = exp\left(-\frac{0.587\pi\sigma D_{sm}^2}{0.43\pi\rho_l D_{sm}^{11/3}\varepsilon^{2/3}}\right) = exp\left(-K_B \frac{\sigma}{\rho_l D_{sm}^{5/3}\varepsilon^{2/3}}\right), \tag{4.42}$$

where K_B is a constant set to **1.37** (i.e. 0.587/0.43).

Finally, the increase of the interfacial area due to the bubble breakup caused by the turbulent impact is obtained as

$$\phi_{TI} = 12\pi\left(\frac{\alpha}{a_i}\right)^2 f_{be,coll} n \eta_{TI}$$
$$= 12\pi\left(\frac{\alpha}{a_i}\right)^2 C_{TI} \frac{\alpha(1-\alpha)\varepsilon^{1/3}}{D_{sm}^{11/3}(\alpha_{max}-\alpha)} exp\left(-K_B \frac{\sigma}{\rho_l D_{sm}^{5/3}\varepsilon^{2/3}}\right), \quad (4.43)$$

4.4.3 Yao and Morel (2004) Model

Yao and Morel (2004) indicated that Wu et al., (1998) evaluated the breakup time by considering only the interaction of a breaking bubble with a turbulent eddy of the same size, which is called the 'interaction time'. While Hibiki and Ishii (2000a) evaluated the breakup time as the time necessary for a given bubble to collide with a turbulent eddy, the so-called called 'free travelling time'. As a combination of both approaches, Yao and Morel (2004) proposed a new model taking into account the free travelling time and the interaction time separately for both coalescence and bubble breakup.

- **Bubble Coalescence Due to Random Collision**

The bubble coalescence rate caused by random collisions ϕ_{RC} is given by

$$\phi_{RC} = -12\pi\left(\frac{\alpha}{a_i}\right)^2 \frac{1}{2}\frac{n\eta_C}{T_c}, \quad (4.44)$$

where T_c is the coalescence time for a single bubble and η_C is the coalescence efficiency. The 1/2 factor included in the definition of the rate is used to avoid double counting of the same coalescence event happening between the same bubble pairs.

The coalescence time T_c is given by

$$T_c = T_{cf} + T_{ci}, \quad (4.45)$$

as the sum of the interaction time T_{ci} and the free travelling time T_{cf} estimated by

$$T_{cf} = \frac{n}{2f_c}, \quad (4.46)$$

Yao and Morel (2004) used the expression of Prince and Blanch (1990) for the calculation of the collision frequency f_c between two bubbles of different groups *(i,j)* induced by turbulence

$$f_{ij}^c = n_i n_j S_{ij}\left(u_i^2 + u_j^2\right)^{1/2}, \quad (4.47)$$

The effective cross sectional area S_{ij}, is given by

$$S_{ij} = \frac{\pi}{4}\left(r_i + r_j\right)^2 , \tag{4.48}$$

and the bubble velocity is a function of the bubble Suter mean diameter and the dissipation rate of turbulent kinetic energy

$$u^2 = 2(\varepsilon D_{sm})^{2/3} , \tag{4.49}$$

Accordingly, the collision frequency is

$$f_c = C_{RC1} \frac{\varepsilon^{1/3}}{D_{sm}^{11/3}} \alpha^2 , \tag{4.50}$$

C_{RC1} = 2.86.

A modification factor has been introduced to take into account the effect of the void fraction on the free travelling time

$$g(\alpha) = \frac{\left(\alpha_{max}^{1/3} - \alpha^{1/3}\right)}{\alpha_{max}^{1/3}}, \tag{4.51}$$

α_{max} is the maximum packing limit equal to 0.52.

The final form of the free traveling time has the following expression

$$T_{cf} = \frac{n}{2f_c} g(\alpha) = \frac{1}{3} \frac{D_{sm}^{2/3}}{\alpha \varepsilon^{1/3}} \frac{\left(\alpha_{max}^{1/3} - \alpha^{1/3}\right)}{\alpha_{max}^{1/3}}, \tag{4.52}$$

The film drainage model has been adopted for the calculation of the interaction time, according to the following formula

$$T_{ci} = t_c = \frac{1}{8}\sqrt{\frac{\rho_l D_{sm}^3}{2\sigma}} \ln \frac{h_{init}}{h_{crit}} = 0.814 \sqrt{\frac{\rho_l D_{sm}^3}{\sigma}}, \tag{4.53}$$

With these two definitions for the interaction time and the free travelling time, the coalescence time T_c is now

$$T_c = T_{cf} + T_{ci} = \frac{1}{3}\frac{D_{sm}^{2/3}}{\alpha\varepsilon^{1/3}}\frac{\left(\alpha_{max}^{1/3} - \alpha^{1/3}\right)}{\alpha_{max}^{1/3}} + 0.814\sqrt{\frac{\rho_l D_{sm}^3}{\sigma}}, \quad (4.54)$$

For the calculation of the coalescence efficiency, an exponential relation between the bubble contact time τ_C (Eq. 4.33), and the coalescence time has been used, yielding

$$\eta_C = exp\left(-\frac{T_c}{\tau_C}\right) = exp\left(-\frac{0.814\sqrt{\frac{\rho_l D_{sm}^3}{\sigma}}}{\frac{D_{sm}^{2/3}}{2^{2/3}\varepsilon^{1/3}}}\right), \quad (4.55)$$

Finally, the decrease in the interfacial area due to the bubble coalescence due to random collision is estimated by

$$\phi_{RC} = -12\pi\left(\frac{\alpha}{a_i}\right)^2\frac{1}{2}\frac{n\eta_C}{T_c}$$

$$= -12\pi\left(\frac{\alpha}{a_i}\right)^2 C_{RC1}\frac{\varepsilon^{1/3}\alpha^2}{D_{sm}^{11/3}}\frac{1}{\frac{\left(\alpha_{max}^{1/3} - \alpha^{1/3}\right)}{\alpha_{max}^{1/3}} + C_{RC2}\alpha\sqrt{We/We_{cr}}}exp\left(-C_{RC3}\sqrt{\frac{We}{We_{cr}}}\right), \quad (4.56)$$

Where the derived constants are C_{RC1}= 2.86, C_{RC2}= 1.922, C_{RC3}= 1.017, and We_{cr}= 1.247.

- **Bubble Breakup Due to Turbulent Impact**

The bubble breakup rate caused by turbulent impact ϕ_{TI} is given by

$$\phi_{TI} = 12\pi\left(\frac{\alpha}{a_i}\right)^2\frac{n\eta_{TI}}{T_b}, \quad (4.57)$$

where T_b is the breakup time and η_{TI} is the breakup efficiency.

The breakup time T_b is given by

$$T_b = T_{bf} + T_{bi}, \quad (4.58)$$

with T_{bi} as the breakup characteristic interaction time and T_{bf} is the free bubble travelling time given by

$$T_{bf} = \frac{n}{f_b}, \tag{4.59}$$

Based on the assumption that only the eddies with a size comparable to the bubble diameter can break the bubbles ($\mathbf{0.65}D_{sm} \leq d_e \leq D_{sm}$) Yao and Morel (2004) choose a value of **0.65** to get a good agreement of the bubble diameter profile in comparison to the DEBORA experiment, the breakup frequency f_b is

$$f_b = 1.6\frac{\varepsilon^{1/3}}{D_{sm}^{11/3}}\alpha(1-\alpha), \tag{4.60}$$

and the free traveling time

$$T_{bf} = \frac{n}{f_b} = 1.194\frac{D_{sm}^{2/3}}{\varepsilon^{1/3}(1-\alpha)}, \tag{4.61}$$

The breakup characteristic interaction time T_{bi} is derived from the assumption that the breakup mechanism is due to the resonance of bubble oscillations with turbulent eddies, and given as

$$T_{bi} = 0.64\sqrt{\frac{\rho_l D_{sm}^3}{\sigma}}, \tag{4.62}$$

The breakup time T_b is now

$$T_b = T_{bf} + T_{bi} = 1.194\frac{D_{sm}^{2/3}}{\varepsilon^{1/3}(1-\alpha)} + 0.64\sqrt{\frac{\rho_l D_{sm}^3}{\sigma}}, \tag{4.63}$$

The breakup efficiency is expressed similarly to Wu et al., (1998) as

$$\eta_{TI} = exp\left(-\frac{We_{cr}}{We}\right), \tag{4.64}$$

The final form of the interfacial area change rate due to the bubble breakup caused by the turbulent impact, is

$$\begin{aligned}\phi_{TI} &= 12\pi\left(\frac{\alpha}{a_i}\right)^2\frac{n\eta_{TI}}{T_b} \\ &= 12\pi\left(\frac{\alpha}{a_i}\right)^2 K_{B1}\frac{\varepsilon^{1/3}\alpha(1-\alpha)}{D_{sm}^{11/3}}\frac{1}{1+K_{B2}(1-\alpha)\sqrt{We/We_{cr}}}exp\left(-\frac{We_{cr}}{We}\right),\end{aligned} \tag{4.65}$$

and the derived constants are K_{B1}= **1.6**, and K_{B2}= **0.42**.

4.4.4 Other Coalescence and Breakup Models

- **Prince and Blanch (1990) and Chesters (1991) Coalescence Models**

For the calculation of the collision frequency, Prince and Blanch (1990) proposed a model based on the summation of the turbulent collision rate, buoyancy-driven collision rate, and laminar shear collision rate (Chen at al., 2005). Only the turbulence collision rate between two bubbles of different groups *(i,j)* is considered here

$$f_c = 0.089\pi n_i n_j \left(D_{sm,i} + D_{sm,j}\right)^2 \varepsilon^{1/3} \left(D_{sm,i}^{2/3} + D_{sm,j}^{2/3}\right)^{1/2}, \tag{4.66}$$

For bubbly flow group only, $i = j$, and

$$f_c = 5.76 \frac{\alpha^2 \varepsilon^{1/3}}{D_{sm}^{11/3}}, \tag{4.67}$$

Chesters (1991) proposed an expression for the coalescence efficiency

$$\eta_C = exp\left[-c\left(\frac{We}{2}\right)^{1/2}\right], \tag{4.68}$$

Where the term c is a constant of order unity including the ratio of the fluctuating bubble to the continuous phase velocities.

- **Martinez-Bazan et al. (1999a) Breakup Model**

Martinez-Bazan et al., (1999a), proposed a model for breakup frequency based on the balance between the turbulent stresses and the surface tension. In this model for a bubble to break, its surface has to deform, and this deformation energy must be provided by the turbulent stresses produced by the surrounding fluid. The confinement stress of the bubble surface τ_s is given by geometric considerations as

$$\tau_s = 6\frac{\sigma}{D_{sm}}, \tag{4.69}$$

and the average deformation stress can be estimated as

$$\tau_t = \frac{1}{2}\rho_l \overline{\Delta u}^2, \tag{4.70}$$

Based on the Kolomogrov's universal turbulence theory, in homogeneous and isotropic turbulent conditions, the mean value of the velocity fluctuations between two points separated by a characteristics distance that is assumed to be of the order of magnitude of the bubble Sauter mean diameter D_{sm} can be estimated as

$$\overline{\Delta u}^2 = \left|\overline{u(x+D,t) - u(x,t)}\right|^2 = \beta(\varepsilon D_{sm})^{2/3}, \tag{4.71}$$

with the constant β = **8.2** given by (Batchelor, 1956).

When $\tau_t > \tau_s$, the bubble deforms and eventually breaks up. The equality $\tau_t = \tau_s$, is used to define the critical bubble diameter D_c by the crossing point of the curves of the two stresses as shown in Figure (4.6). Therefore, bubbles with $D_{sm} < D_c$, are stable and will never break. And bubbles with $D_{sm} > D_c$, have a surface energy smaller than the deformation energy and, thus, they will break.

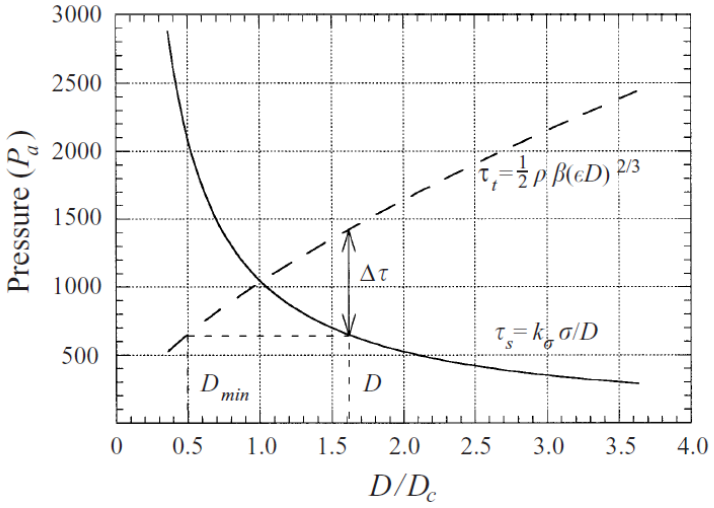

Figure 4.6. (Solid line) is the confining force provided by surface tension. (broken line) is the one given by the turbulent stresses. k_σ= 6.0 (Martinez-Bazan et al.1999a)

Based on all the above considerations, the breakup frequency can be written as

$$f_b = K_g \frac{\sqrt{\beta(\varepsilon D_{sm})^{2/3} - 12\frac{\sigma}{\rho_l D_{sm}}}}{D_{sm}}, \tag{4.72}$$

The breakup efficiency is included in the coefficient K_g which was found experimentally by (Martinez-Bazan et al.,1999a) to be **0.25**.

Chapter Five

Adiabatic Bubbly Two-Phase Flow Simulation using IATE

In Chapter 3 simulations for low void fraction cases of the MT-LOOP experiment have been conducted considering a fixed mono-disperse bubble size distribution with a constant bubble diameter during the simulations. For higher void fraction flow conditions, however, this is not true; because bubble interactions such as coalescence and breakup take place. As already pointed out, these interaction mechanisms are very important for the determination of the bubble size distribution and the interfacial area concentration appearing in all constitutive relations representing the mass, momentum and energy transfer through the interface between the phases.

For the validation of the developed OpenFOAM solver that describes the geometrical structure of the two-phase flow using the interfacial area transport equation coupled with the two-fluid model Euler-Euler approach, and for the purpose of validating the different mechanistic models for bubble breakup and coalescence, experimental data for the radial gas volume fraction, interfacial area density, bubble diameter and gas phase velocity profiles at different axial profiles are needed. The experimental data of PUMA test facility (Santos Mendez 2008) is used for the validation work. These data have been collected with the main goal of making available experimental data for the validation of interfacial area density models.

5.1 The PUMA Test Facility

The PUMA experimental facility (Santos Mendez 2008) was built and operated at the University of Valencia. Its set-up is shown in Figure (5.1). The test section consisted of a vertical circular pipe with an internal diameter $D = 52\mathrm{mm}$ and a length of L= $3000\mathrm{mm}$ long used for upwards adiabatic flows of an air/water system. The supply of the water is done from the bottom of the pipe at atmospheric pressure and a constant 20°C temperature due to the sensitivity of the coalescence and breakup models to the temperature because of its effect on the surface tension (Liao 2011). The transport properties of air and water under these conditions are shown in Table (5.1). The flow

conditions cover most of the bubbly flow region, including finely dispersed bubbly flow and bubbly-to-slug transition flow.

Four sensor conductivity probes were used for the measurement of the average radial profiles of the void fraction, gas velocity and the interfacial area density, at 15 radial locations ($r/R=0$ to 0.95) and at three axial locations ($z/D=2$, $z/D=36$, $z/D=56$) to follow the evolution of the flow along the test section. From these quantities, radial profiles of the Sauter mean diameter were derived (Pellacani 2012).

An extensive range of flow conditions with superficial gas velocities from 0.035 m/s to 1.315 m/s and superficial liquid velocity from 0.51 m/s to 4.074 m/s was covered in the measurement. The flow conditions of tests related to bubbly flow which are the scope of the present work are summarized in Figure (5.2).

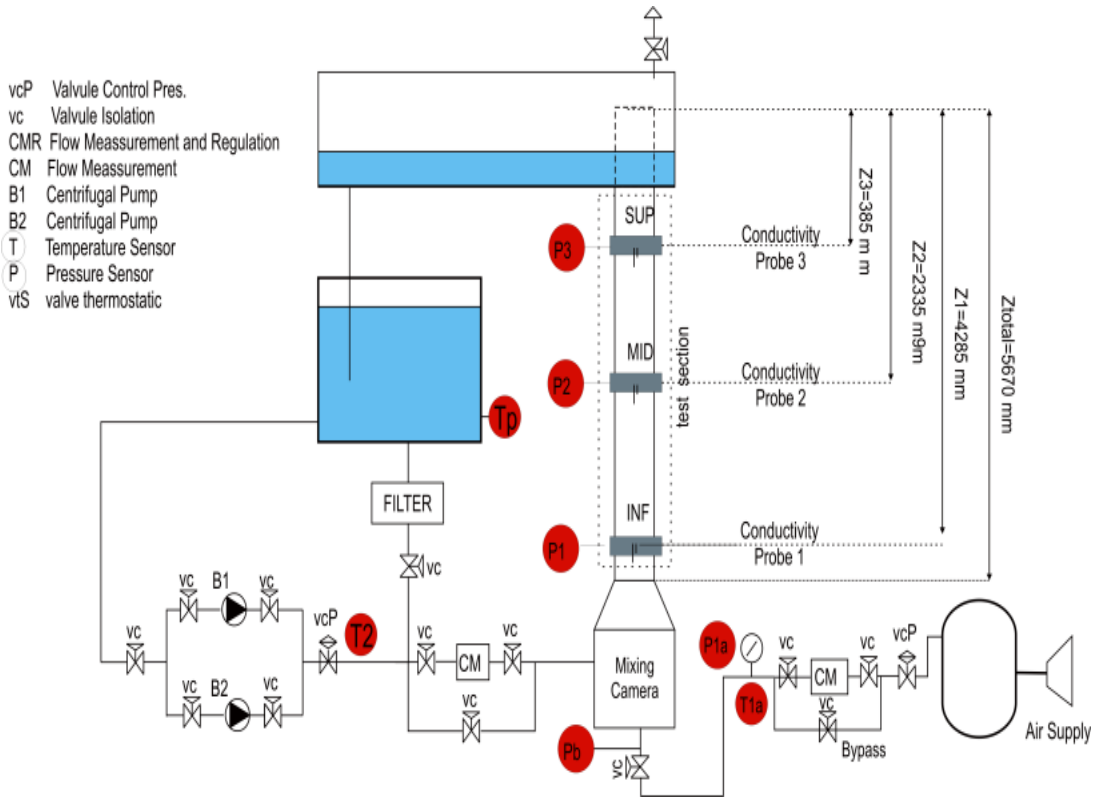

Figure 5.1. Setup of the PUMA experiment (Santos Mendez, 2008; Pellacani ,2012)

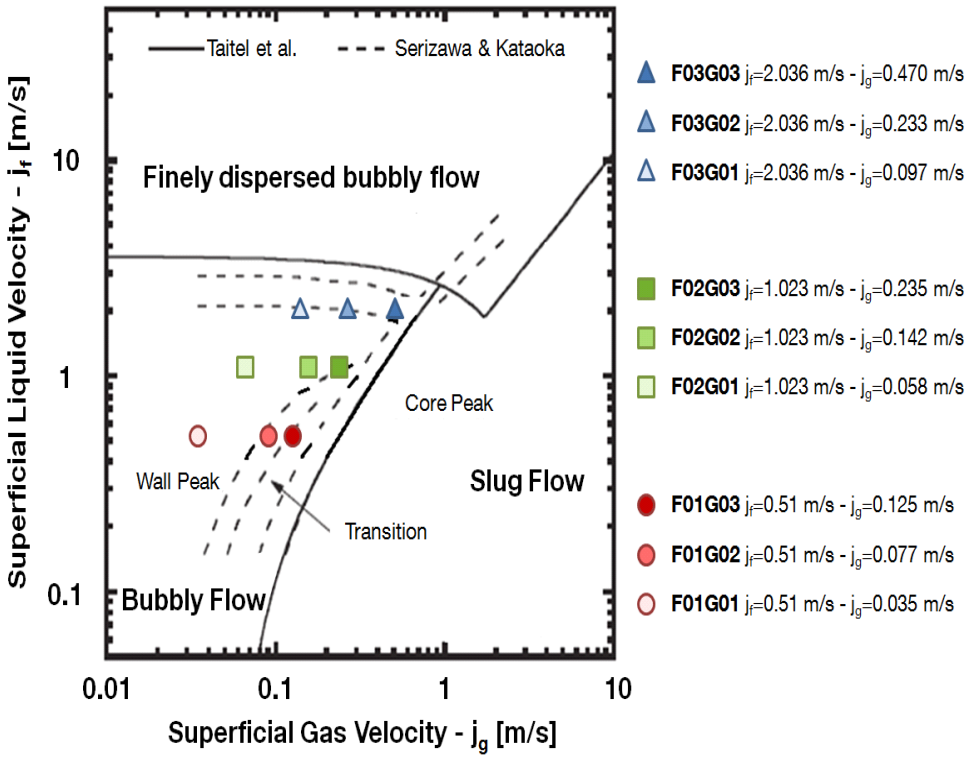

Figure 5.2. Map of phase distribution patterns (Pellacani 2012)

Table 5.1. Transport properties of water and air in the PUMA experiment

Property	*Value*
p	1.013 bar
ρ_l	997 kgm^{-3}
ρ_g	1.185 kgm^{-3}
ν_l	8.9× $10^{-7} m^2 s^{-1}$
ν_g	1.54× $10^{-5} m^2 s^{-1}$
σ	0.072 Nm^{-1}

5.2 Numerical Details

For the modeling of adiabatic bubbly two-phase flow, the one-group interfacial area transport equation with appropriate sink and source terms representing the bubble coalescence and breakup has been implemented and solved in the open source code OpenFOAM, along with the two-fluid model Euler-Euler conservation equations. The coalescence and breakup models that have been implemented include: Wu et al., (1998), Hibiki and Ishii (2000a), Yao and Morel (2004), Prince and Blanch (1990) and Chesters (1991), and Martinez-Bazan et al., (1999a).

Based on the simulation results of MTLOOP in Chapter 3 that aims at validating the capability of different interfacial drag and non-drag forces models, a combination of the following models will represent the momentum exchange term in the momentum equation:

- **Drag force**: Ishii and Zuber (1979).
- **Lift force**: Tomiyama et al., (2002).
- **Wall lubrication force**: Hosokawa et al., (2002).
- **Turbulent dispersion force**: FAD/Burns et al., (2004).

For two-phase turbulence modeling, the standard $k-\varepsilon$ model and the standard wall function that bridges the near-wall region between the wall and the turbulent core are employed for the calculation of the turbulent kinetic energy and its dissipation rate for the liquid phase. In addition, the effect of the bubbles on the turbulence in the liquid phase (BIT) is taken into account by introducing appropriate source term in the $k-\varepsilon$ equations according to Morel (1997). For the gas phase the dispersed phase *zero-equation* OpenFOAM model is utilized.

Radial symmetry was assumed in the experimental geometry, which allows the simplification of the domain to be modeled as a quasi-2D-cylindrical geometry, i.e. a 5° slice of the pipe, with symmetry boundary conditions imposed on both sides. The use of such a geometry has been validated against a 3D-geometry (45° wedge section), the results showed no difference between the two geometries, and hence the quasi-2D has been used for the purpose of reducing the computational cost and simulation time.

At the inlet of the test section, a liquid velocity profile was set according to a typical single phase turbulent flow profile in a pipe, while the gas velocity, void fraction and bubble size were specified uniformly in accordance with the flow condition described in Ta-

ble (5.2). A constant fixed value equal to the atmospheric pressure was specified at the outlet. On the wall a no-slip condition was used for the liquid phase and a free-slip condition for the gas phase assuming that direct contacts between the bubbles and the walls are negligible (Rzehak et al., 2012).

A mesh sensitivity study with three mesh structures corresponding to a coarse, medium and fine mesh covering the range of 2040 – 8160 elements, showed that no significant differences were observed in the results, and grid independent results can be achieved starting from the coarser mesh.

The distance of the first cell adjacent to the wall was set to 0.7 mm, in order to keep the value of y^+ less than ~ 30, selecting such a high value when compared to the single phase simulation, is due to a stability matters for the simulation of two-phase flow.

For all flow conditions, reliable convergence was achieved when the RMS residuals for all variables go below the residual convergence criteria which was set to 10^{-4}.

Table 5.2. Selected test cases conditions for experimental investigations at the PUMA test facility

Test	J_L*(m/s)*	J_G*(m/s)*	$\langle d_b \rangle$*(m)*	$\langle \alpha_G \rangle$*(%)*	$\langle IAC \rangle$*(1/m)*
F01G01	0.51	0.035	0.003	5.56	111
F01G02	0.51	0.077	0.0032	10.39	194
F01G03	0.51	0.125	0.0025	15.73	377
F03G01	2.036	0.097	0.003	3.7	74
F03G02	2.036	0.233	0.003	8.18	164
F03G03	2.036	0.47	0.0035	14.93	256

5.3 Analysis of the Contribution of Interfacial Area Transport and Bubble Coalescence and Breakup Models on Two-Phase Flow Parameters

In order to evaluate the feasibility of including the one-group interfacial area transport equation in OpenFOAM, the validity of the different coalescence and breakup models described in the previous chapter will be examined in this chapter and the flow parameters measured in PUMA experiment and predicted by OpenFOAM will be compared.

5.3.1 Evaluation of the Coalescence and Breakup Sub-models

The different coalescence and breakup frequency and efficiency sub-models are evaluated in terms of the eddy turbulent dissipation rate ε which is one of the main driving parameters of bubble breakup and coalescence. The comparison is done based on the PUMA test point F01G01 at an average void fraction equal to 5.56%.

- **Coalescence due to Random Collision**

The coalescence model suggested by (Wu et al., 1998) is not considering the coalescence frequency separately but coupled to the coalescence efficiency through a constant coefficient that represents the constant coalescence efficiency and the proportionality term in the coalescence frequency model, for this reason the model of Wu et al., (1998) will not be included in the comparison. On the other hand, Hibiki and Ishii (2000a), Yao and Morel (2004), Prince and Blanch (1990) and Chesters (1991) are treating the coalescence frequency and efficiency separately. Comparison of the values estimated for the random collision frequency for a range of turbulent kinetic energy dissipation rate of the different coalescence models is shown in Figure (5.3).

For the same dissipation rate, Yao and Morel (2004) model delivers the highest collision frequency, because it takes into account the contribution of both the free travelling time and the interaction time in the calculation of collision frequency, while Prince and Blanch (1990) use the free travelling time only. The Hibiki and Ishii (2000a) model provides the lowest frequency value. Creating more resolution of the plot in Figure (5.3) to show the behavior of the random collision frequency in term of dissipation rate calculated by Hibiki and Ishii (2000a) model (see Figure 5.4), shows the same shape as the other two models do but with two orders of magnitude smaller values.

An inverse relationship is observed between the turbulent dissipation rate and the coalescence efficiency, as shown in Figure (5.5), because, physically, it should be expected that the increase in the turbulent fluctuations represented by higher values of ε leads to a shorter bubble contact time, resulting in a lower coalescence efficiency. Higher values of coalescence efficiency are provided by Chesters (1991) model. The models of Yao and Morel (2004), and Hibiki and Ishii (2000a) are delivering similar results.

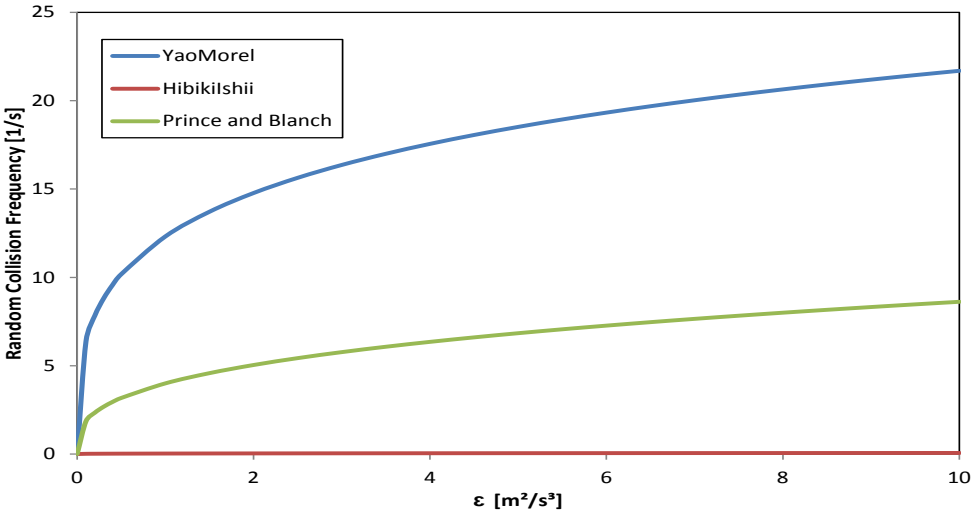

Figure 5.3. Effect of turbulent dissipation on collision frequency by different models

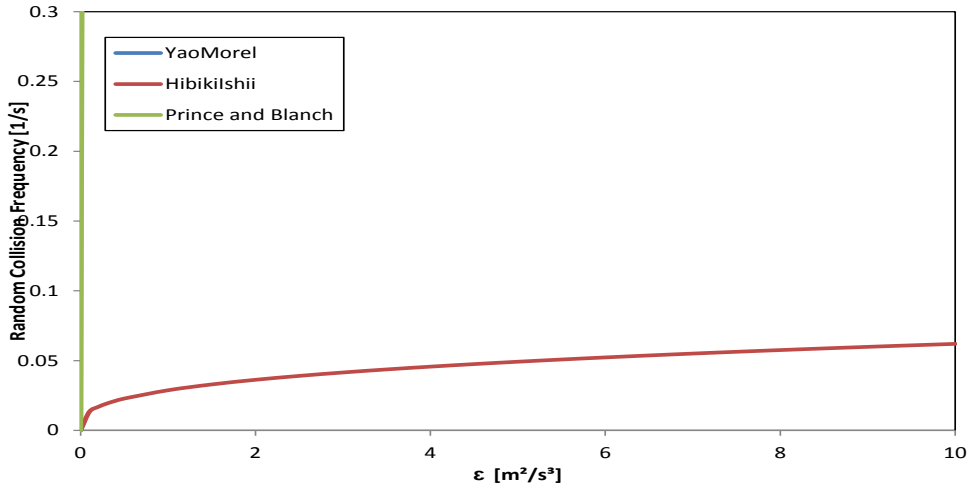

Figure 5.4. Resolution of Figure 5.3 to see the Hibiki and Ishii (2000a) behavior

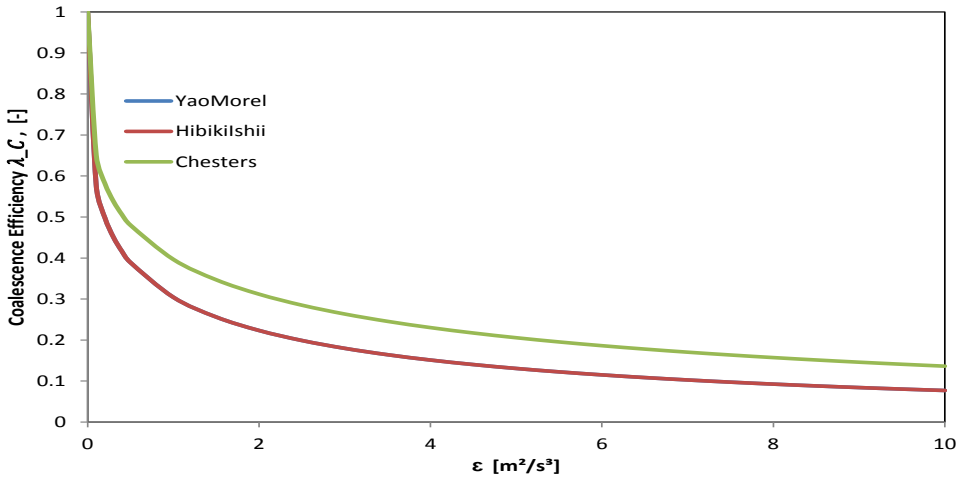

Figure 5.5. Effect of turbulent dissipation on coalescence efficiency by different models

The effect of the turbulent fluctuations on the coalescence efficiency can be clearly noticed along the flow direction as illustrated in Figure (5.6), where the Test F01G01 with a lower liquid velocity yields a higher coalescence efficiency due to a larger bubble contact time. On the other hand, F03G02 with higher liquid velocity tends to reduce the contact time, and yields a lower coalescence efficiency.

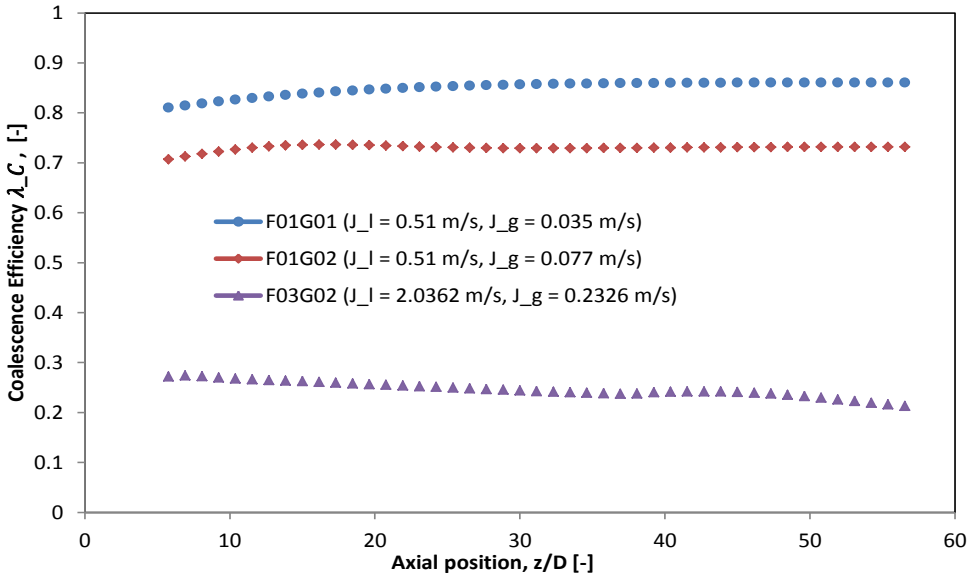

Figure 5.6. Numerical simulation of different PUMA test cases showing the dependence of the coalescence efficiency on gas and liquid velocities

For cases of the same low liquid velocity, i.e. F01G01 and F01G02, the increase in gas velocity, which yields a higher void fraction for the same gas mass content, reduces the coalescence efficiency, because of a reduced contact time that is inversely proportional to the turbulent dissipation rate (see Eq. 4.33). This trend increases with higher void fraction values as the data for F03G02 shows.

- **Breakup Due to Turbulent Impact**

The comparison of the turbulent impact frequency delivered by different models is depicted in Figure (5.7). At a lower values of turbulent dissipation, the Yao and Morel (2004) model yields higher values for the frequency than Wu et al.,(1998) model, because the first model includes the effect of free travelling time and interaction time together, while the latter uses only the interaction time for the calculation of breakup frequency.

According to Wu et al.,(1998) and Martinez-Bazan et al.,(1999a), the breakup event will not be initiated until the turbulent eddies achieve a threshold energy value. The model of Hibiki and Ishii (2000a) delivers the lowest values for turbulent impact frequency. The same strategy as in random collision frequency by increasing the resolution of the plot in Figure (5.7) to show the behavior of the turbulent impact frequency in term of dissipation rate calculated by Hibiki and Ishii (2000a) model (see Figure 5.8), shows the same shape as the other two models do but with two orders of magnitude smaller values.

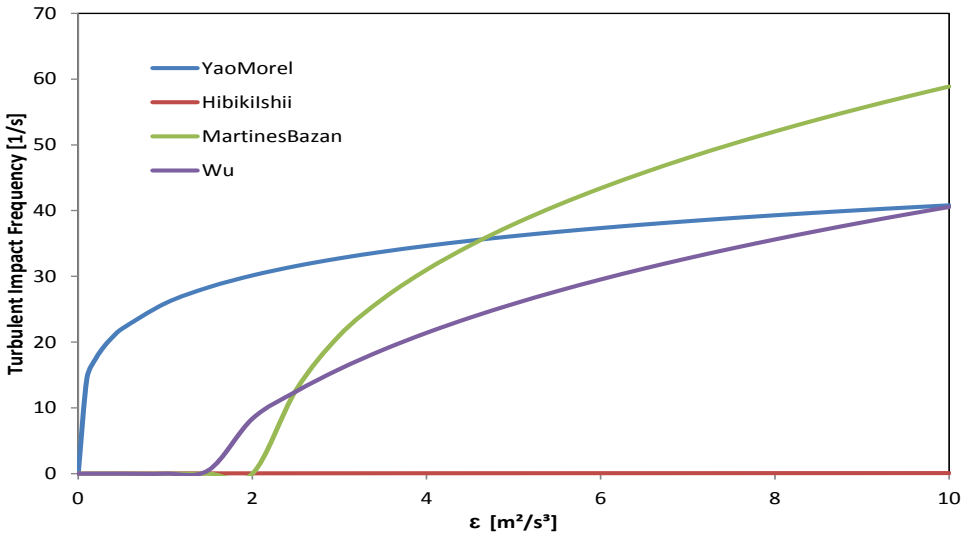

Figure 5.7. Effect of turbulent dissipation on turbulent impact frequency by different models

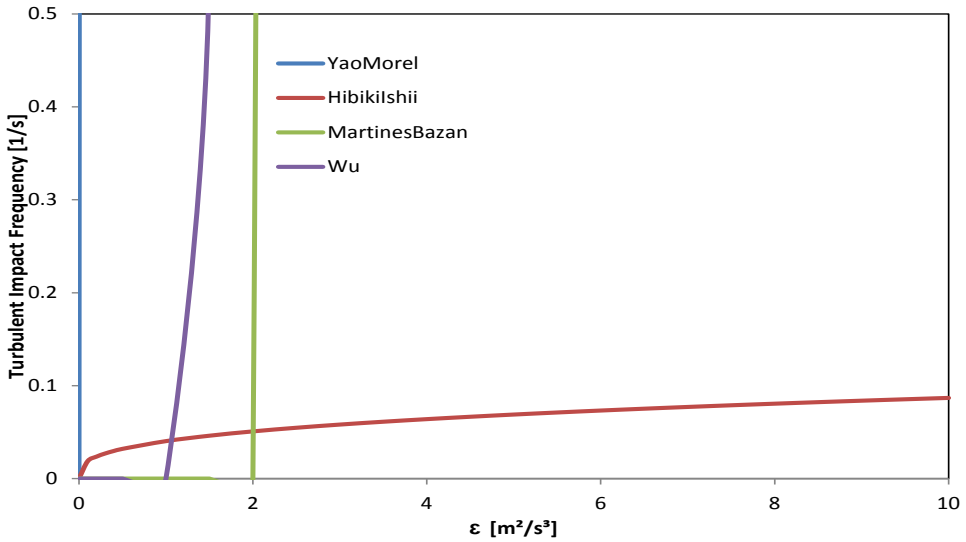

Figure 5.8. Resolution of Figure 5.8 to see the Hibiki and Ishii (2000a) behavior

In Martinez-Bazan et al.,(1999a) model, the bubble will not break until the turbulent stresses provide the minimum energy required for the bubble deformation. As already explained in section (4.4.4), when the turbulent and bubble confining stresses are equal, then a critical bubble diameter D_c can be defined so that bubbles with $D < D_c$ are stable and have zero breakup frequency. For bubbles with diameter $D > D_c$, the breakup frequency starts to increase rapidly until it reaches a maximum value at bubble diameter D_{max}, and then starts to decrease monotonically with the bubble diameter (J.C.Lasheras et al., 2002), as shown in Figure (5.9).

It has been noted that Hibiki and Ishii (2000a) model provides the lowest values for both bubble coalescence and breakup frequencies. However, this is not considered as a shortcoming of the model, because the accuracy of each model is estimated by its capability to capture the evolution of the interfacial area by the balance between the coalescence and breakup mechanisms.

Contrary to the inverse relationship between coalescence efficiency and turbulent dissipation, the breakup efficiency increases with increased dissipation, because of stronger turbulent eddies providing enough energy for bubble deformation, thus increasing the bubble breakup efficiency, as illustrated in Figure (5.10). Because Martinez-Bazan et al.,(1999a) model considers the breakup efficiency as a constant value, it is not included in the comparison.

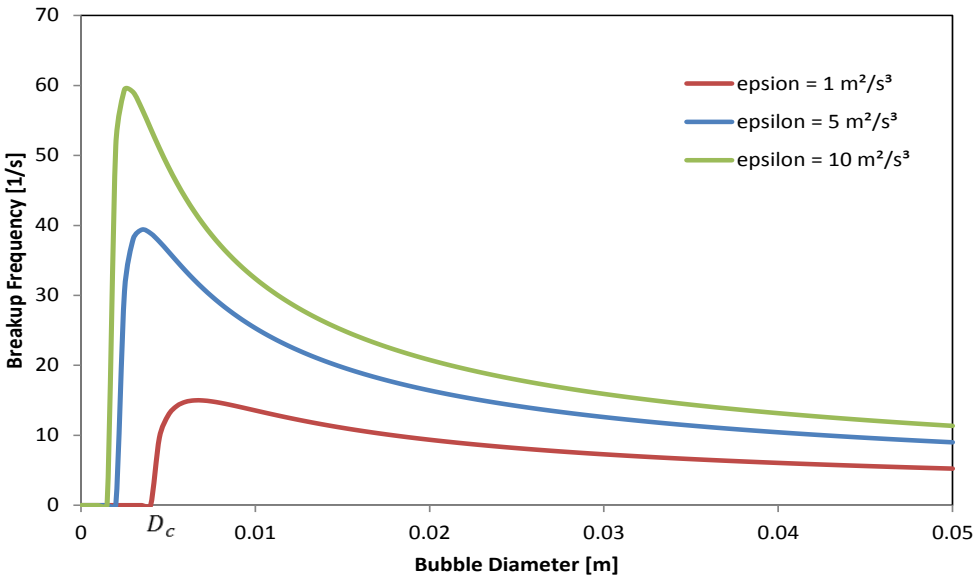

Figure 5.9. Evolution of breakup frequency with bubble diameter in Martinez-Bazan et al.,(1999a) model

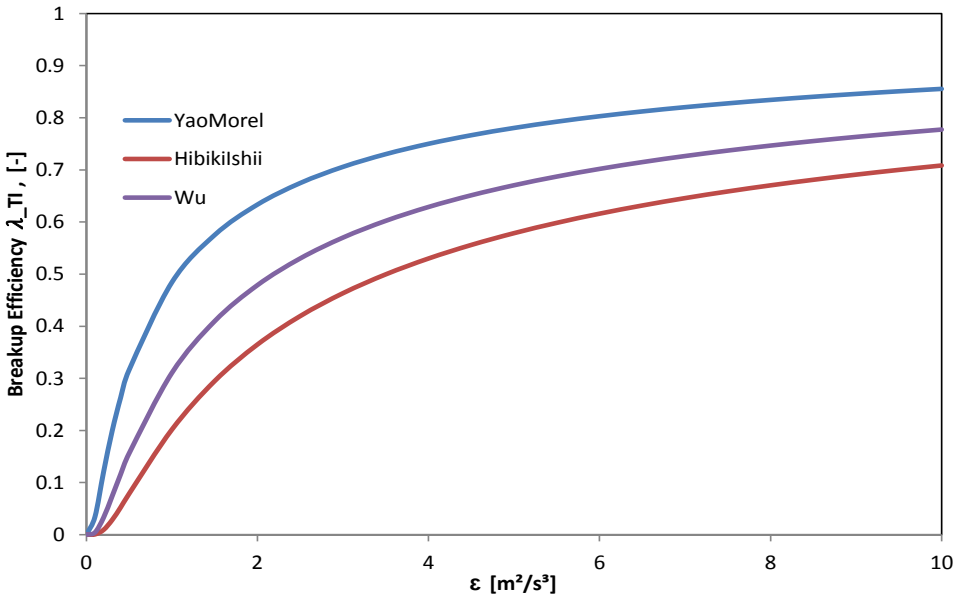

Figure 5.10. Effect of turbulent dissipation on breakup efficiency by different models

The influence of bubble size on the breakup efficiency is depicted in Figure (5.11). In the results one can see that an increase of the bubble diameter leads to higher breakup efficiencies due to the low surface tension larger bubbles have, making it easy to break them.

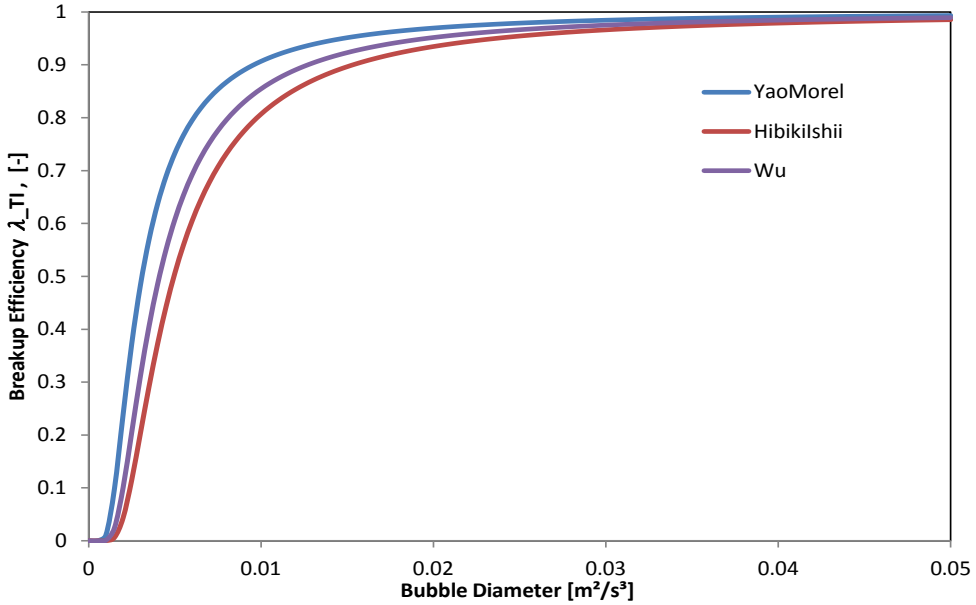

Figure 5.11. Dependency of breakup efficiency on the bubble diameter $(\varepsilon = 1\ m^2 s^{-3})$

The effect of liquid velocity on the breakup efficiency can be captured along the axial flow direction as shown in Figure (5.12). For low liquid velocities, inducing smaller tur-

bulence fluctuation, i.e. F01G01 and F01G02 test cases, the turbulent eddies may not have enough energy to disintegrate the bubbles (breakup efficiency, $\lambda_{TI} = 0$).

For test case F03G02, the higher liquid velocity that yields a strong turbulence will increase the bubble breakup significantly.

To obtain a clearer picture about interaction efficiencies, Figure (5.6) and (5.12) are coupled together as shown in Figure (5.13). For test case F01G01, with low liquid velocity and low void fraction, the small turbulence fluctuation increase the contact time between bubbles yielding a high coalescence efficiency ($\lambda_C \sim 0.8$), and because the turbulent eddies do not have enough energy to break the bubbles, the breakup efficiency is negligible ($\lambda_{TI} \sim 0$). However, even with a higher coalescence efficiency the interfacial area concentration increases along the axial direction (see Figure 5.13), due to the effect of bubble volume expansion resulting from the pressure reduction along the axial direction of the flow (Hibiki and Ishii, 2000).

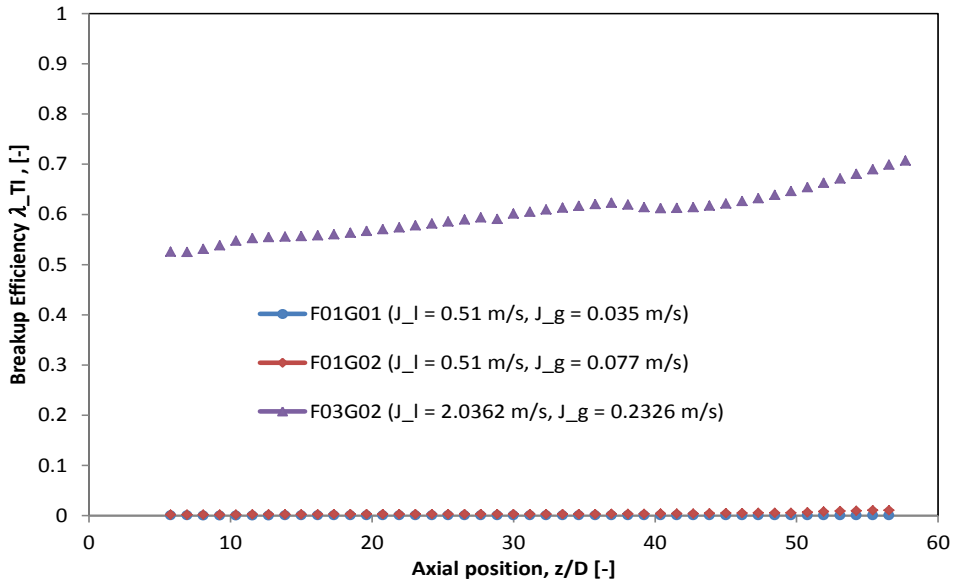

Figure 5.12. Numerical simulation of different PUMA test cases showing the dependence of the breakup efficiency on gas and liquid velocities

For test case F01G02, with low liquid velocity and high void fraction, the increase in void fraction can reduce the coalescence efficiency slightly ($\lambda_C \sim 0.7$), but at the same time it increases the collision frequency, which in turn enhances the coalescence rate. Furthermore, the increase in void fraction reduces the breakup efficiency ($\lambda_{TI} \sim 0$), which is a result of the decreased number of turbulent eddies. The bubble expansion

due to pressure reduction and bubble coalescence are both playing a role in the governing of the interfacial area concentration along the axial direction for this test case, the pressure reduction leads to interfacial area increase from the pipe inlet up to $z/D=25$, where the effect of the bubble coalescence starts to become important, resulting in interfacial area reduction again (see Figure 5.14).

For test case F03G02, with high liquid velocity and high void fraction, the strong turbulence increases the breakup efficiency ($\lambda_{TI}\sim0.6$) and reduces the bubble coalescence efficiency ($\lambda_C\sim0.25$) due to the reduced bubble contact time. In turn, the bubble breakup rate exceeds the bubble coalescence rate leading to significant interfacial area increase along the flow direction.

According to Hibiki and Ishii (2002), bubble expansion due to pressure reduction plays a major role in governing the interfacial area at low liquid velocities and void fractions, where bubble-bubble and bubble-eddy interactions are weak. At higher void fractions, the coalescence process is the dominant mechanism in the interfacial area transport due to the short distance between bubbles. On the other hand, breakup effect on the interfacial area evolution starts at relatively high liquid velocity; where turbulence eddies have enough energy to break bubbles.

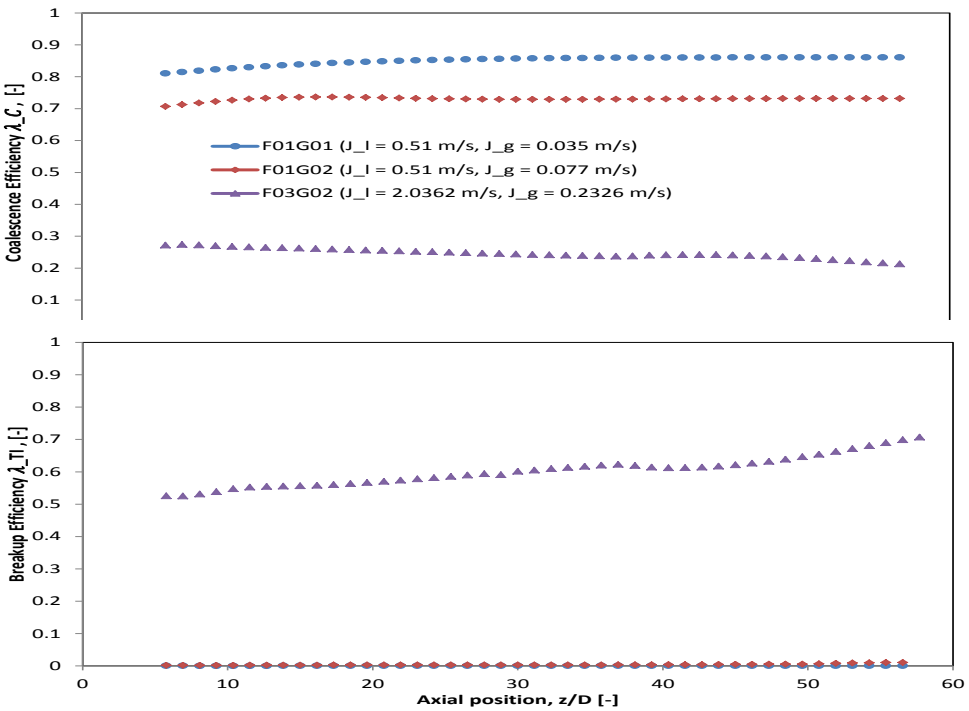

Figure 5.13. Dependence of the coalescence and breakup efficiencies on gas and liquid velocities

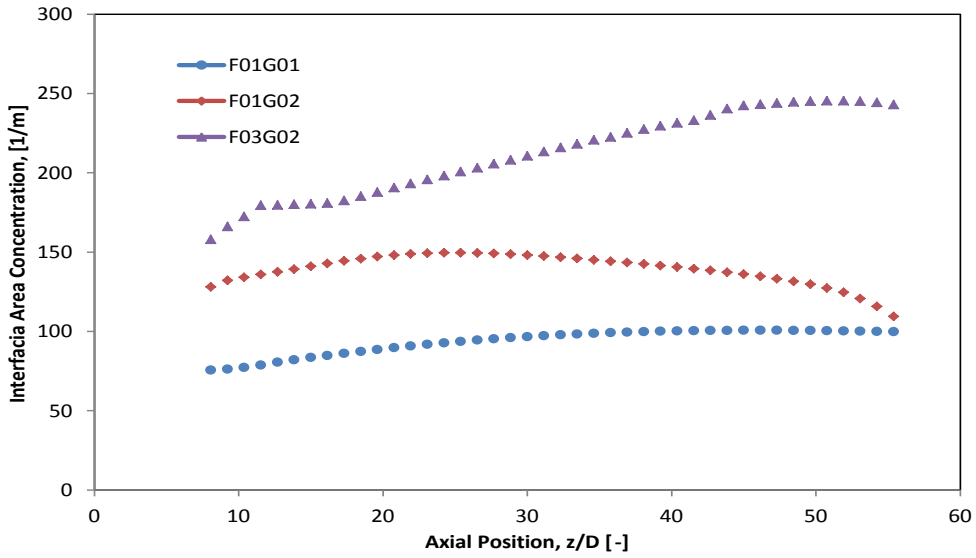

Figure 5.14. Numerical simulation of different PUMA test cases showing the axial evolution of the interfacial area concentration with different liquid velocities

5.3.2 Radial Predictions of Flow Parameters

The radial profiles of void fraction, interfacial area concentration, bubble Sauter mean diameter and gas velocity have been calculated at two axial locations ($z/D=36$, $z/D=56$) by the simulation of the test cases described in Table (5.1) using the newly developed solver that employs the interfacial area transport equation along with different bubble coalescence and breakup models described in Chapter 4 and the forces acting on the bubbles in Chapter 3. The calculated flow parameters are compared against the experimental data of PUMA, to examine the relative merits of the implemented models.

- **Void fraction distribution**

The comparison of the predicted gas void fraction profile by the four implemented models with the measured data for several bubbly flow conditions is depicted in Figure (5.15). The comparison indicates a good agreement with the measurements, where the four models are able to reproduce the radial profile of the void fraction. The wall peak behavior can be observed in all test cases for both experimental and predicted profiles. In the low liquid velocity cases, i.e., F01G01 and F01G02, the wall peak profile is well established from the first measuring station of $z/D=36$, this behavior is captured by the implemented models except the Chesters (1991) – Bazan (1999a) models that predicts void fraction peak far from the wall, because at such a low liquid velocity flow condi-

tions, the bubbles coalescence is the dominant process, and the Chesters (1991) coalescence efficiency model is implemented along with the classical model of Prince and Blanch (1990) for collision frequency without any modification factors that can reduce the collision rate. According to Wu et al., (1998), these modification factors are suggested due to the fact that bubbles do not always move toward each other. It is also necessary for the situations in which the mean distance between bubbles is very large and, therefore, no collisions should be expected, because the range of the relative motion to enable collisions between neighboring bubbles is limited by an eddy size comparable to the bubble size. Therefore, the overestimation of the coalescence rate yields bubbles with large sizes, which results in a negative lift force coefficient that pushes large bubbles away from the wall.

In the high liquid velocity cases, i.e., F03G01 and F03G02, the wall-peak void fraction profile becomes well developed near the pipe outlet (i.e. $z/D=56$), this behavior of void fraction profile evolution was reproduced by the four models with a good agreement with the experimental results. A slight over-prediction of the void fraction is shown in the near-wall region for test case F03G02 by Martinez-Bazan et al., (1999a) breakup model, which is the dominant process for high liquid velocity cases, this model is expected to provide the highest breakup rate amongst other breakup models at the same turbulent dissipation value specially in the near wall region as shown in Figure (5.7).

For the low liquid velocity case F01G01, the void fraction profile in the core region is slightly under-estimated by all models. Moreover, for case F03G02 with high gas and liquid velocities, the void fraction profile is slightly over-predicted in the core region, this under/over-prediction of void fraction in the core region could be attributed to the uncertainty in the bubble-induced turbulence models, because no theoretical derivation is available for the time scale involved (Krepper et al., 2013). This time scale appears in the bubble-induced source term of the turbulent energy dissipation transport equation. The uncertainty on its true value leads to a lower accuracy in the predicted turbulent dissipation rate, which is a basic driving parameter for both the bubble coalescence and breakup processes.

In general, the newly developed solver can reproduce acceptably well the wall peak profile of the void fraction at the two axial measurement locations when the correlations from Wu et al., (1998), Hibiki and Ishii (2000a) and Yao and Morel (2004) are used.

- **Interfacial area concentration**

The radial interfacial area concentration calculated by the four models and the experimental data at the two axial measurement locations are shown in Figure (5.16). For all test cases, the interfacial area concentration profile is evolving along the pipe flow direction, where at low liquid velocity cases, i.e., F01G01 and F01G02 a slight reduction in the interfacial area values along the pipe is observed due to the coalescence process considered as the dominant process at such a low liquid velocity cases. The evolution of the interfacial area is captured by all models with slight under- prediction at the first measurement station (i.e. $z/D=36$) by Wu et al. (1998), Hibiki and Ishii (2000a) and Yao and Morel (2004) models and a clear under-prediction by Chesters (1991) – Bazan (1999a) models, because of the inclusion of the Prince and Blanch (1990) for the calculation of the collision frequency without any modification factors that can reduce the predicted coalescence rate. Hence, the over-prediction in the coalescence rate yields an under-prediction in the interfacial area concentration. Near the pipe outlet (i.e. $z/D=56$), the interfacial area radial profile predicted by Wu et al. (1998), Hibiki and Ishii (2000a), is in good agreement with the experimental results, while the Chesters (1991) – Bazan (1999a) model under-predicts the profile once more. The Yao and Morel (2004) model over-predicts the interfacial area concentration in the near wall region in all cases.

For high liquid velocity cases, i.e., F03G01 and F03G02, the interfacial area concentration increases along the pipe, because at a high liquid velocity the breakup process plays a major role in the evolution of the interfacial area concentration. This evolution can be captured by all models, with slight under-prediction by Chetsers (1991) – Bazan (1999a) model in the near-wall region at the first axial measurement station. At the second measurement station of case F03G01, the Chetsers (1991) – Bazan (1999a) model predicts the interfacial area concentration profile very well, even with the over-prediction of the coalescence rate by Prince and Blanch (1990) model. This happened due to the ability of the Martinez-Bazan (1999a) breakup model to overcome the reduction rate of the interfacial area concentration due to the Prince and Blanch (1990) model, which means that Martinez-Bazan (1999a) model also over-predicts the breakup rate. This behavior is clearly seen in the F03G02 case, for which the coalescence process plays a minor role in the evolution of the interfacial area concentration, and the breakup process has the large effect, yielding a clear over-prediction in the interfacial area concentration at the near wall region by the Martinez-Bazan (1999a).

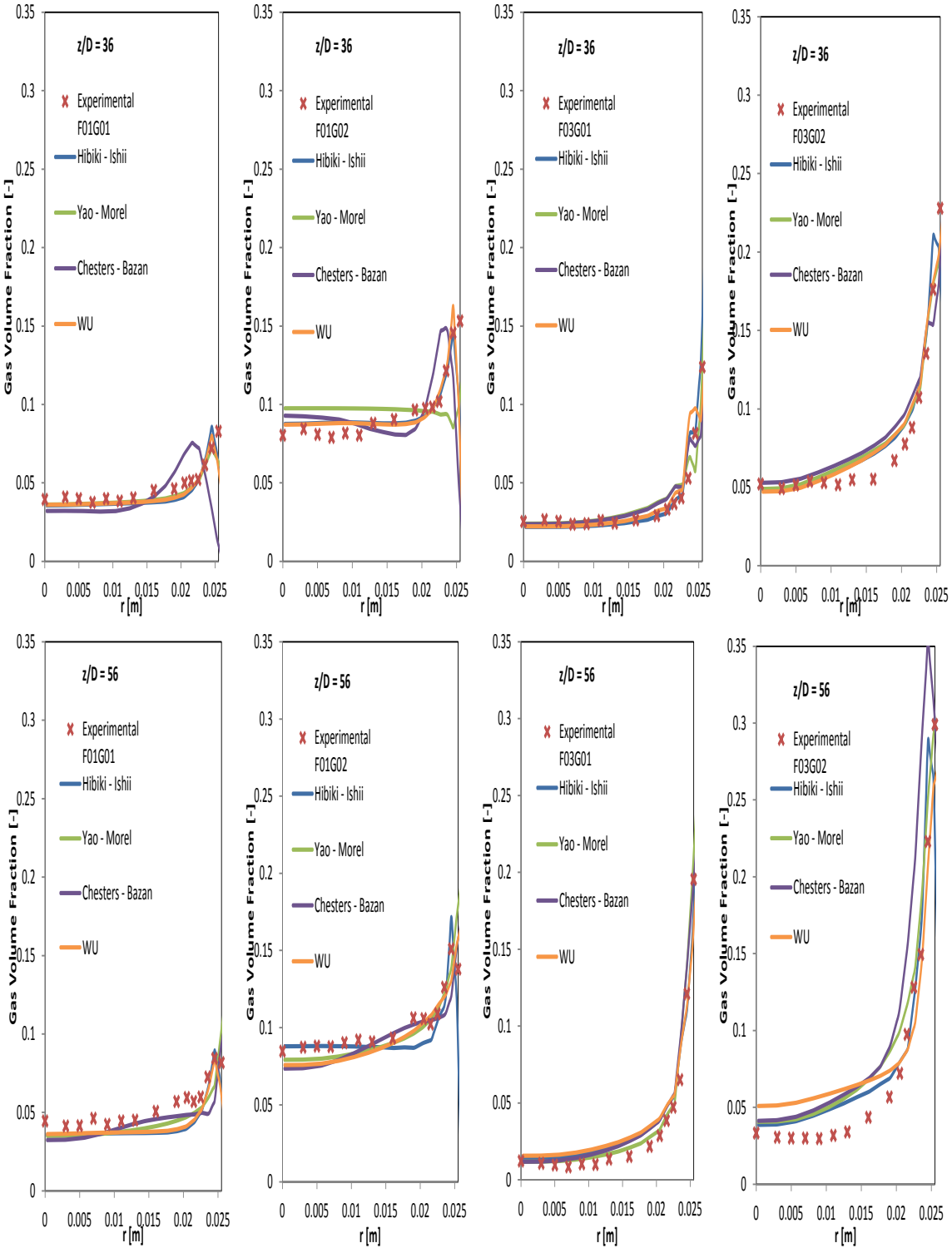

Figure 5.15. Radial gas volume fraction profiles for different test points at z/D: 36 and 56

The Yao and Morel (2004) over-predicts the interfacial area in the near wall region. One reason for this result could be that their model used for the calculation of the bubbles-eddies collision frequency has been tuned to obtain a good agreement with the bubble diameter profile measured in the boiling bubbly flow experiment (DEBORA). Therefore, its usage for the simulation of adiabatic bubbly flow could create some discrepancies.

In general, Wu et al., (1998), Hibiki and Ishii (2000a) models are able to reproduce with a good agreement the interfacial area concentration radial profile and their differences with the experimental measurements are small. These differences stem from the adjustable parameters present in the models that have been tuned by the authors to better approximate the upward turbulent bubbly flow in pipes, by fitting a large set of experimental data. Moreover, these parameters are suggested for *one-dimensional* simulations and their application to the three-dimensional simulations can create some discrepancies in the predictions of the lateral phase distributions under pipe bubbly flow conditions.

The prediction of the interfacial area concentration by Yao and Morel (2004) and Chetsers (1991) – Bazan (1999a) models is in relative good agreement with the experimental data in the central region of the pipe, while in the near wall region, the discrepancies are much larger.

- **Bubble Sauter mean diameter**

The predicted and measured radial distributions of the bubble mean Sauter diameter are illustrated in Figure (5.17). Comparing the experimental values of the bubble diameter at the two measurement elevations shows a slight increase in the bubble diameter along the pipe for low liquid velocity cases, due to the dominant effect of bubble coalescence and gas expansion in such conditions. On the other hand, for high liquid velocity cases and especially case F03G02 where bubble breakup plays a major role, a slight reduction in the bubble diameter is observed along the pipe.

In the radial direction, the bubble size distribution shows a uniform profile with a small peak in the near wall region, where according to the lift force effect, small bubbles will be pushed towards the wall that increases the possibility of its coalescence there, forming slightly larger bubbles (Cheung et al.,2007).

The prediction of the bubble diameter depends on the calculated void fraction and interfacial area concentration values. Without a well-predicted void fraction profile, the Sauter mean bubble diameter cannot be accurately predicted because the void fraction is needed for the breakup and coalescence closure (Chen et al., 2005). In all test cases, the bubble diameter profile estimated by the Chetsers (1991) – Bazan (1999a) model is over-predicted due to the under-estimation of interfacial area concentration caused by the higher coalescence rate calculated by the included Prince and Blanch (1990) model. In the cases where the breakup process is dominant, a higher bubble diameter is also observed because according to the work of Chen et al. (2005), Martinez-Bazan (1999a) breakup model produces significantly fewer smallest bubbles and more largest bubbles.

Due to the over-prediction of the interfacial area concentration in the near wall region, Yao and Morel (2004) model tends to estimate smaller bubbles in that region. The Sauter mean bubble diameter profile estimated by Wu et al., (1998) and Hibiki and Ishii (2000a) models is in a good agreement with the experimental data with some discrepancies in the near wall region especially for high liquid velocity cases , due to the discrepancies in the interfacial area concentration prediction because of the reasons addressed in the previous section.

- **Time-averaged gas velocity**

The radial gas velocity profiles from the four models and the experimental data at the two measurement elevations are shown in Figure (5.18). At the first measurement station, the gas velocity is over-predicted by all models due to the over-estimation of the bubble Sauter mean diameter at the same axial location by all models. The bubble diameter appears in all constitutive closure relations for the interfacial drag and non-drag forces that play a role in the determination of the radial gas velocity profile.

At the second elevation near the test section outlet, the radial gas velocity profiles predicted by all models compare favorably with the experimental data, with some discrepancies when using Chetsers (1991) – Bazan (1999a) model, due to the *clear over-estimation of the bubble diameter* by the combination of these two models.

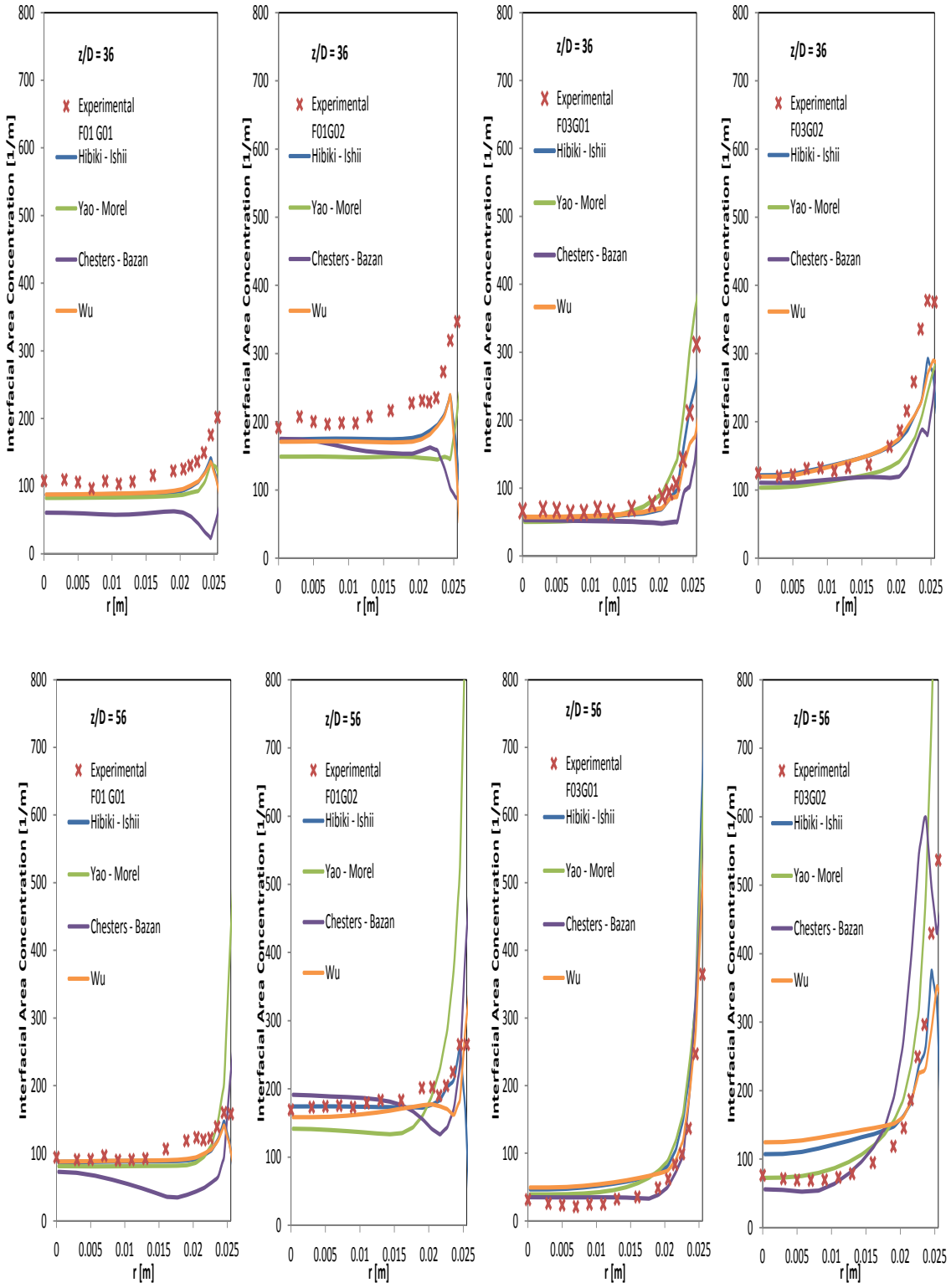

Figure 5.16. Radial interfacial area concentration profiles for different test points at z/D: 36 and 56

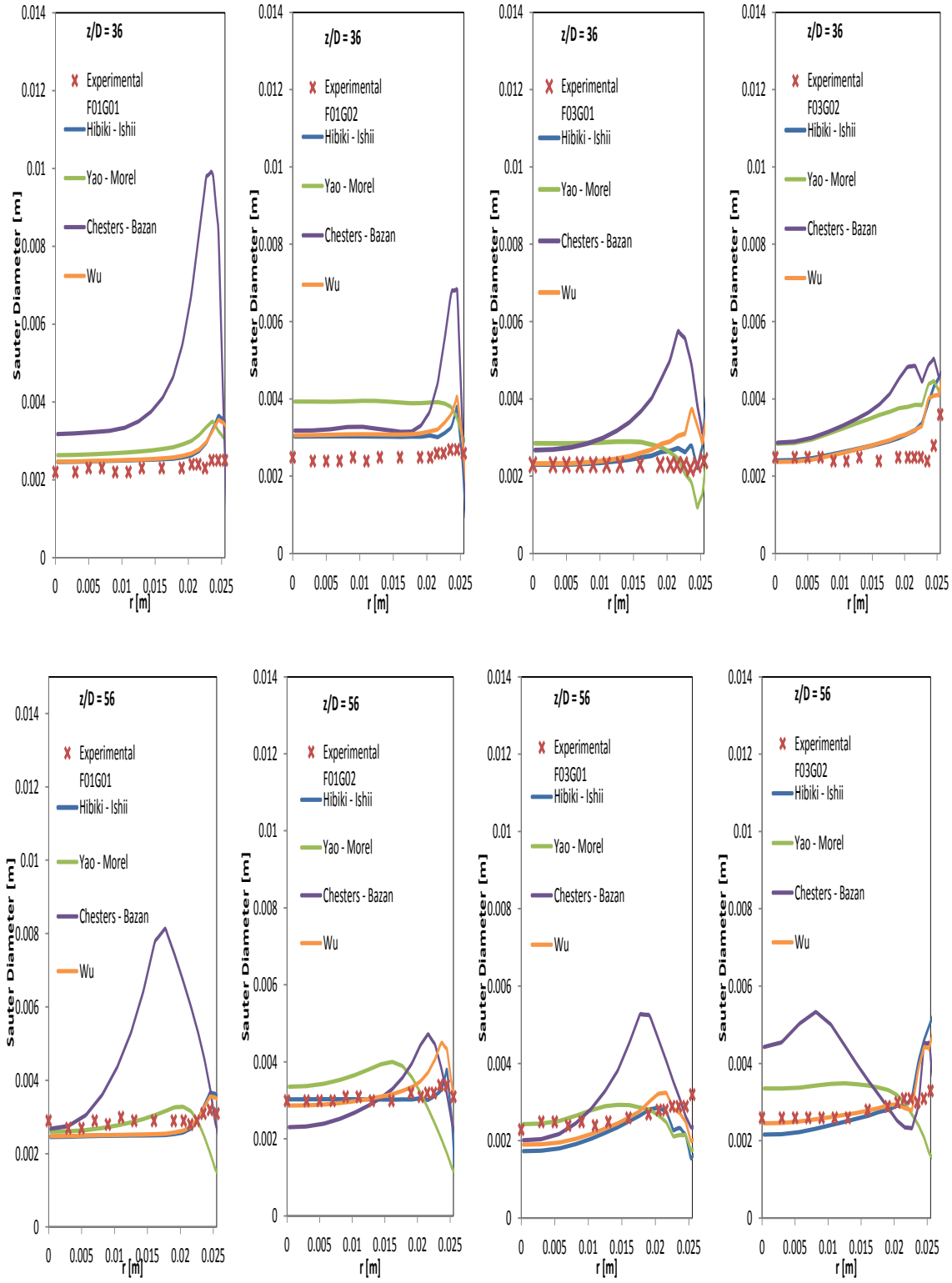

Figure 5.17. Radial Sauter mean bubble diameter profiles for different test points at z/D: 36 and 56

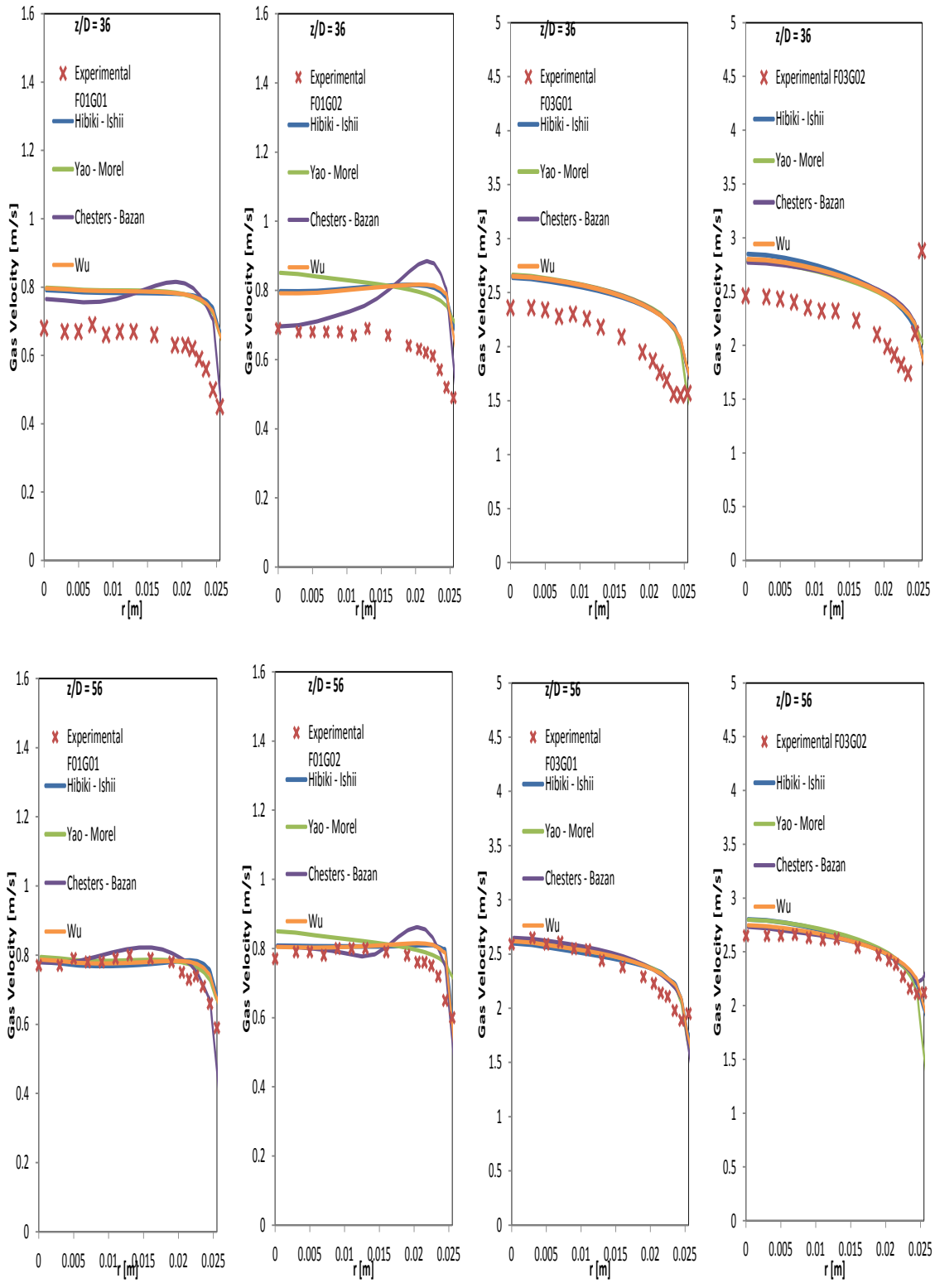

Figure 5.18. Radial gas velocity profiles for different test points at z/D: 36 and 56

5.3.3 Simulation of Bubbly-to-Slug Transition Flow using the One-group IAC Transport Equation

In order to examine the applicability of the one-group interfacial area transport equation to predict the behavior of the bubbly-to-slug transition flow, two test cases with higher void fraction, i.e., F01G03 and F03G03 have been investigated. The comparisons of the experimental and predicted flow variables radial profiles at $z/D = 56$ measurement elevation are illustrated in Figures (5.19) and (5.20). The calculated parameters by Chetsers (1991) – Bazan (1999a) models have been excluded from the comparison due to the difficulty in achieving a converged solution that affects the accuracy of the obtained results.

The void fraction profile is over-predicted in the core region with a poor ability to capture the wall peak behavior by all implemented models. With respect the interfacial area concentration profile, the Wu et al., (1998) and Hibiki and Ishii (2000a) models are providing an *over-predicted* profile in the *pipe core region* with *under estimation* in the *near wall region*, with a completely under-predicted profile by the Yao and Morel (2004) model.

This discrepancy in predicting the interfacial area profile yields a disagreement between the measured and calculated bubble Sauter mean diameter profiles, with slight differences when using Wu et al., (1998) and Hibiki and Ishii (2000a) models and an intrinsic over-prediction by Yao and Morel (2004) model. Consequently, the gas velocity radial profile shows a slight over-estimation by all models.

These discrepancies between the measured and predicted flow variables can be attributed to the bubble coalescence and breakup constitutive models that are based on the assumption of *spherical bubbles shape*s (Cheung et al., 2007), while in the flow regimes beyond bubbly flows, i.e., bubbly-to-slug transition, there are substantial differences in sizes and shapes of bubbles, which complicate the bubble interactions, requiring that the one-group IATE be extended to the two-group IATE model.

Hence, to extend the applicability of the interfacial area transport equation to a bubbly-slug transition flow, Fu and Ishii (2002) and Sun et al., (2004) developed a two-group interfacial area transport equation for a vertical air-water flow.

Moreover, as the size of the bubble increases, the transport mechanisms are further complicated due to additional bubble interaction mechanisms such as shearing-off and

surface instability that have been investigated by Sun (2001) in the inter-group (between the two-groups) and intra-group (within the same group) bubble interaction mechanisms (Wang 2010).

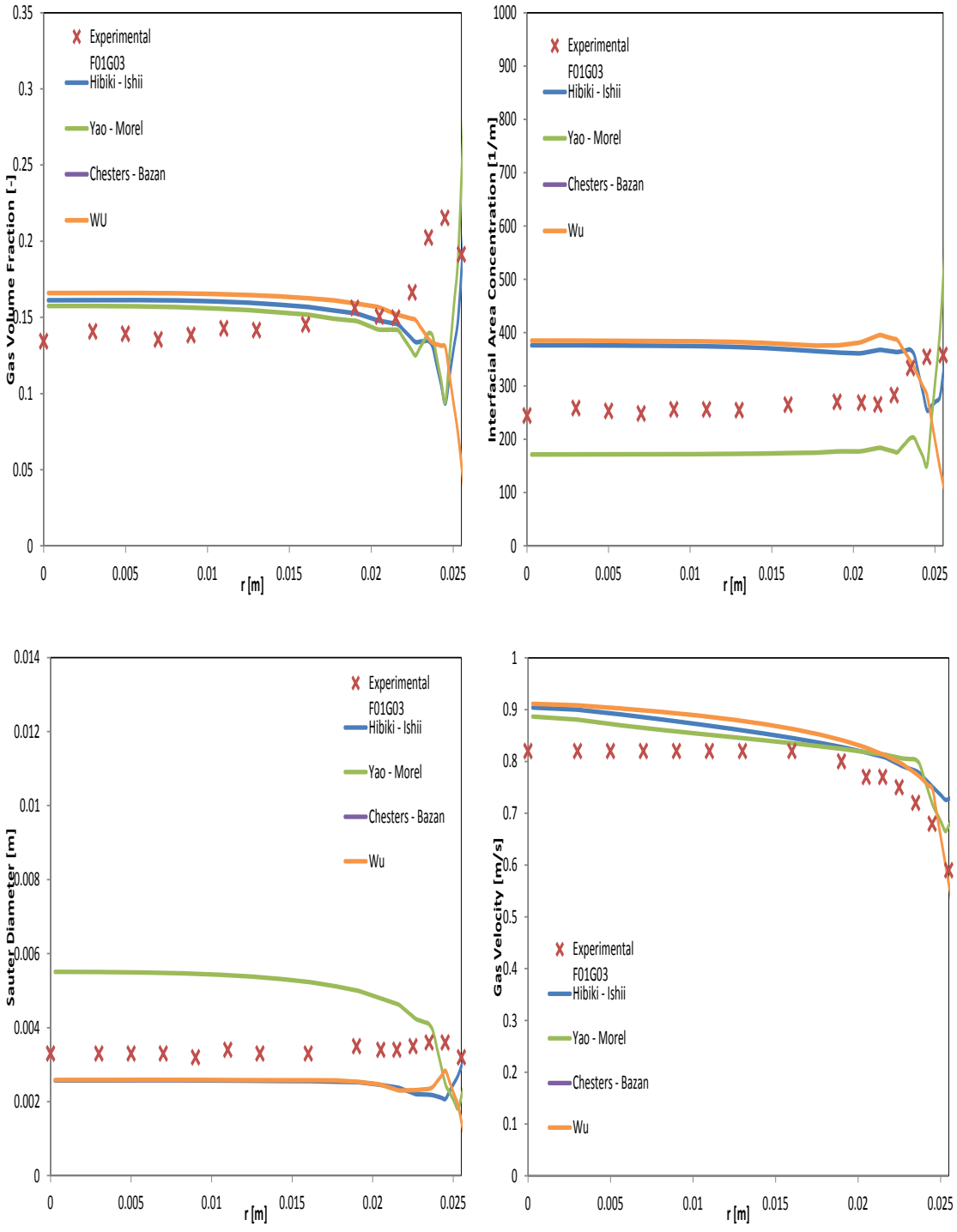

Figure 5.19. Experimental and predicted flow variables profiles for bubbly-to-slug transition case F01G03

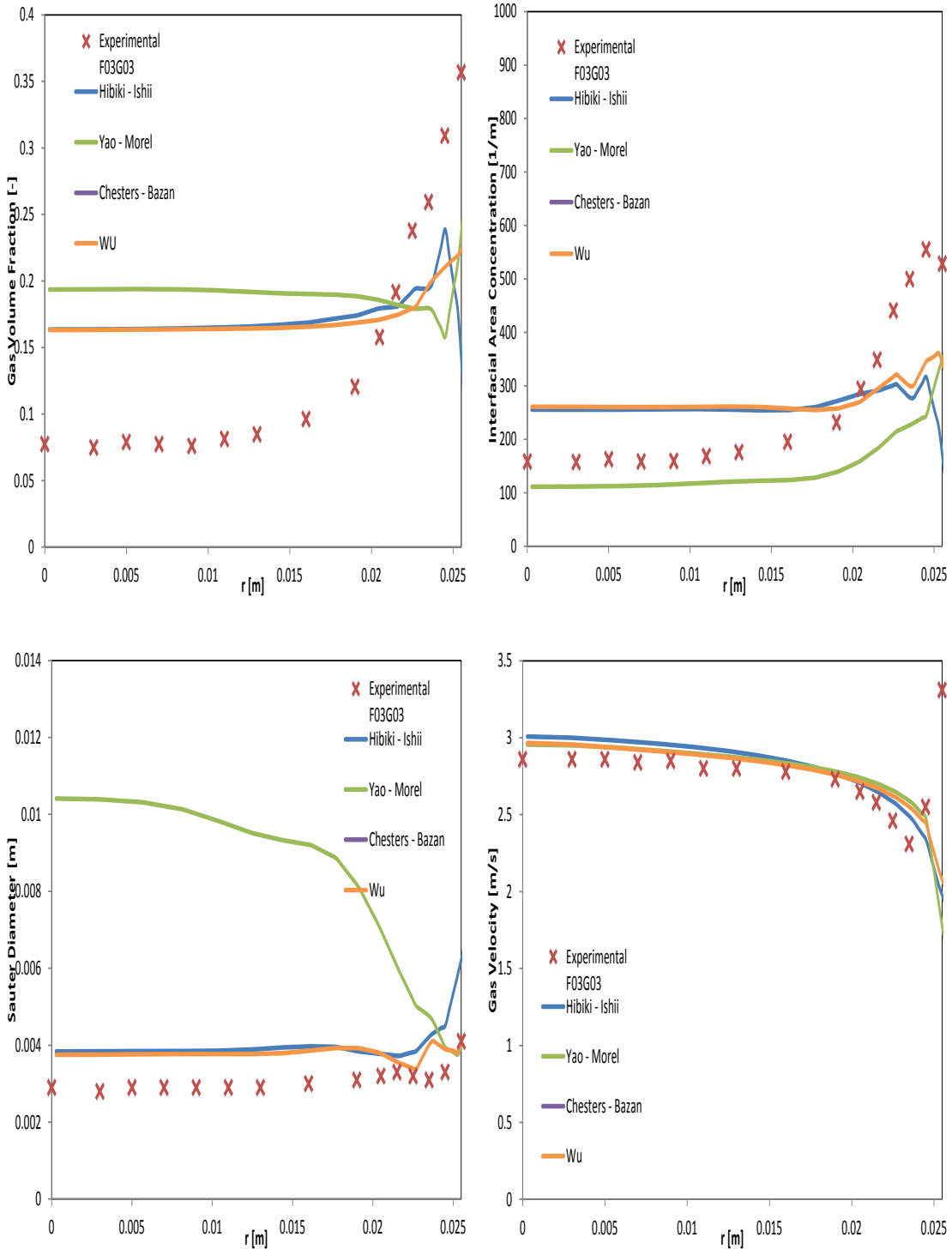

Figure 5.20. experimental and predicted flow variables profiles for bubbly-to-slug transition case F03G03

5.4 Conclusions

The one-group interfacial area transport equation coupled with Euler-Euler two-fluid model approach has been implemented in the open source CFD code OpenFOAM along with different bubble coalescence and breakup constitutive models including Wu et al., (1998), Hibiki and Ishii (2000a), Yao and Morel (2004), Prince and Blanch (1990) and Chesters (1991), and Martinez-Bazan et al., (1999a), due to the importance of the interfacial area concentration to achieve a better prediction of bubbly two-phase flow characteristics in upward pipes.

To test the validity of the implemented models, the newly developed solver has been used to simulate the upwards adiabatic bubbly flow of an air/water system in the PUMA test facility. Several test points with different combinations of gas and liquid superficial velocities are involved. Prediction of the gas volume fraction, interfacial area concentration, gas velocity and Sauter mean bubble diameter profiles are compared to the experimental data.

Results show that the four implemented models are able to reproduce the void fraction profile with a good agreement with the experimental data. The interfacial area concentration profiles are well captured by the Wu et al., (1998), Hibiki and Ishii (2000a) models, and small differences with the experimental data are observed due to the models adjustable parameters that are tuned by the authors to better approximate the 1D upward bubbly flow in pipes. The prediction of the interfacial area by Yao and Morel (2004) and Chesters (1991) - Martinez-Bazan et al., (1999a) is in relative good agreement in the core region of the pipe with large discrepancies in the near wall region. The bubble diameter profile is captured by the Wu et al., (1998), Hibiki and Ishii (2000a) models with small discrepancies in the wall region, while Yao and Morel (2004) model shows some differences with the experimental data and slight discrepancies are observed when using Chesters (1991) - Bazan et al., (1999a) models.

To estimate the adequacy of the one-group interfacial area transport equation and bubble coalescence and breakup constitutive models to predict flow variables in the flow regime beyond bubbly flow, two test cases with transitional flow conditions were investigated. The results show large differences between measured and predicted flow parameters. These discrepancies can be attributed to the spherical bubbles shape assumption in the constitutive models, where with increasing void fraction, the bubble size increases and the shape starts to deform taking the cap-shape, that complicate

the bubble interactions requiring that the one-group IAT equation be extended to the two-group IAT equation, and further interaction mechanisms such as shearing-off and surface instability that are dominant at larger bubble size be investigated.

Chapter Six

Sub-cooled Boiling

Sub-cooled boiling and the associated heat transfer are very important phenomena for the safety analysis of nuclear reactors, because they affect the neutron moderation characteristics as well as the reactivity of nuclear reactors (Koncar et al., 2005). During normal operation of pressurized water reactor (PWR), sub-cooled boiling may occur inside flow sub-channels between the heated fuel rods, when vapor bubbles are created in the micro-cavities that are distributed over the heated surface, also called nucleation sites. In BWRs takes place in the lower core region before the bulk of the coolant reaches saturation temperature and affects the neutron spectrum inside the fuel assemblies, modifying the rod burn-up conditions and the production of Plutonium. Moreover, sub-cooled boiling takes place at the downcomer during the Large Break Loss-of–Coolant Accident (LBLOCA) reflood phase where it reduces the flow rate available for core cooling (Bae et al., 2007,Song et al., 2007).

Sub-cooled boiling designates the process of evaporation of liquid flowing near a heated wall while the bulk liquid temperature is lower than the local saturation temperature. When the wall temperature exceeds the local liquid saturation temperature, the nucleation sites activate the formation of vapor bubbles. They start to grow in size as they absorb energy from the surface until they reach a critical size, at which time, in vertical flow, they slide along the heated surface and continue to increase. At one point they reach a size that forces them, through buoyancy forces, to depart from the wall migrating laterally towards the sub-cooled bulk liquid where thy condensate. The energy released by the condensing bubbles cause the bulk liquid to heat up, and can contribute to make it eventually reach saturation conditions. The lateral migration produces a radial void fraction profile decreasing from the heated wall to the sub-cooled core.
Sub-cooled boiling starts to occur at a point called the onset of nucleate boiling (ONB) and continue downstream without a significant increase in the void fraction because of the high sub-cooling of the bulk liquid condenses the steam formed. Void fraction starts to become significant at a location called the onset of significant void (OSV), at which, because of the decreased liquid bulk sub-cooling, the evaporation rate starts to exceed the vapor condensation rate (Koncar et al., 2005)(see Figure 6.1).

The sub-cooled boiling process is characterized by a large heat transfer coefficient, which is an important requirement for the efficient cooling of nuclear fuel rods. Unfortunately, there is a limit for this heat transfer. The maximum value of heat flux which can be exchanged with the fluid is called Critical Heat Flux (CHF), and it is one of the main limiting phenomena for the operating power of PWRs.

When the wall heat flux increases beyond the critical heat flux (CHF), a phenomenon called the boiling crisis takes place. In Light Water Reactors the two dominant boiling crisis mechanisms are relevant: the departure from nucleate boiling (DNB) in the subcooled or low quality regions, and the dry-out in saturated boiling high quality regions (see Figure 6.2).

In the DNB case the formation of a vapor blanket preventing the liquid to reach the heated surface causes a sudden degradation of the heat transfer coefficient. With a constant power delivered by nuclear fission, if the heat flux at the surface is such that the amount of sub-cooled boiling reaches a level in which the bubbles coalesce into the steam blanket, the clad temperature will experience a sharp increase to transfer the heat flux to the fluid. This situation leads rapidly to clad damage and the breach of the fuel rod safety barrier allowing radioactive elements to be released into the primary circuit coolant and finally lead to significant fuel failure. Hence, the nuclear reactor must be operated always at a safe margin below the CHF.

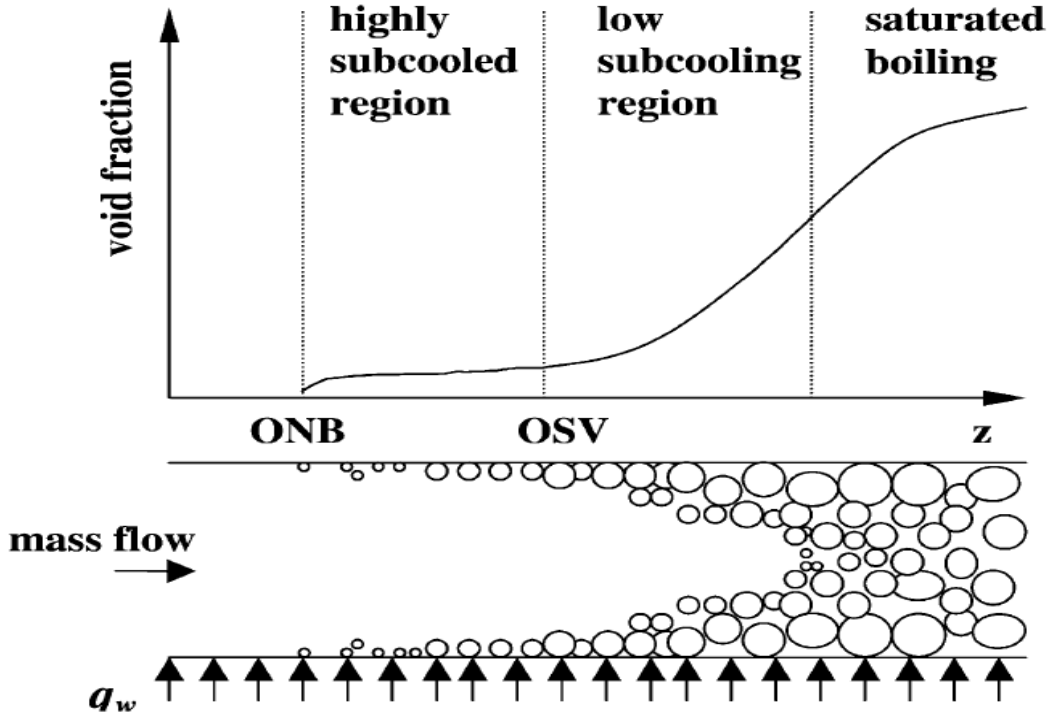

Figure 6.1. Axial void fraction profile in the sub-cooled boiling regions for upward vertical flow (Koncar et al.,2005)

Sub-cooled boiling modeling is considered as a preliminary state towards the numerical simulation of CHF and the precise prediction of the boiling crisis in CFD codes. Therefore, the accurate estimation of the radial profiles of two-phase flow parameters in the sub-cooled boiling region such as steam volume fraction, interfacial area concentration, bubble Sauter mean diameter, steam velocity and liquid temperature is essential for nuclear reactor safety.

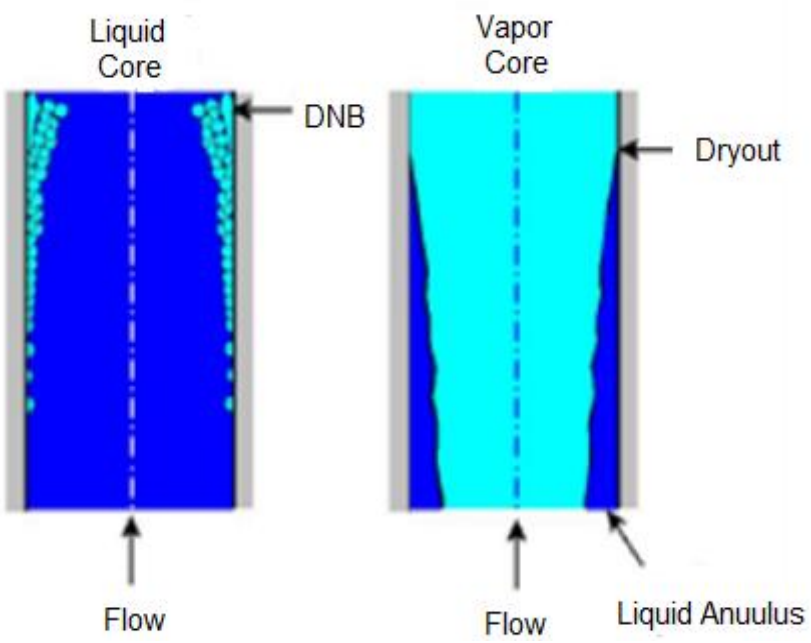

Figure 6.2. DNB and dryout mechanisms

Since the flow of phenomena associated to sub-cooled boiling have three-dimensional (3D) behavior, the one-dimensional (1D) safety analysis codes for nuclear power plants show a collateral shortcoming in predicting sub-cooled boiling related phenomena, in these 1D codes, the void fraction prediction is based on empirical correlations (Zuber et al., 1966, Zuber and Findlay 1965, Levy 1967, Kroger and Zuber 1968) that were developed and fitted to experimental data, and are only limited to the axial direction and no information regarding the radial profiles can be acquired. Moreover, the essential shortcoming of these correlations is that they are valid only for the conditions they were fitted for, i.e., fluid properties, working conditions and geometry of the test (Krepper et al., 2013).

Accordingly, the multidimensional CFD modeling of sub-cooled boiling two-phase flow is essential. The most widely used CFD approach that can analyze such a phenomenon appropriately is the Euler-Euler two-fluid model. As described in Chapter 2, this

model governs the balance of mass, momentum and energy of each phase in term of two sets of conservation equations coupled with closure relations representing the interfacial forces, as well as heat and mass transfer across the interface, these interfacial terms determine the degree of thermal and hydraulic non-equilibrium between the phases (Koncar et al., 2005). Many investigations can be found in the literature (Tu, 2002; Yeoh et al., 2005; Krepper et al., 2005 and 2007; Koncar et al., 2008; and Bae et al., 2010) for the improvement of sub-cooled boiling models for the CFD codes.

6.1 Two-Fluid Model of Sub-cooled Boiling

The two-fluid model conservation equations governing the mass, momentum and energy in diabatic flow with heat and mass transfer are

Continuity equation

$$\frac{\partial}{\partial t}(\alpha_k \rho_k) + \nabla.\left(\alpha_k \rho_k \vec{U}_k\right) = \Gamma_{ki} - \Gamma_{ik}, \tag{6.1}$$

Momentum equation

$$\begin{gathered}\frac{\partial}{\partial t}\left(\alpha_k \rho_k \vec{U}_k\right) + \nabla.\left(\alpha_k \rho_k \vec{U}_k \vec{U}_k\right) = \\ -\alpha_k \nabla P_k + \nabla.\left(\alpha_k\left(\bar{\bar{\tau}}_k + \bar{\bar{\tau}}_k^{Re}\right)\right) + \alpha_k \rho_k \vec{g} + \vec{M}_k + \Gamma_{ki}\vec{U}_i - \Gamma_{ik}\vec{U}_k\,,\end{gathered} \tag{6.2}$$

Energy equation

$$\begin{gathered}\frac{\partial}{\partial t}(\alpha_k \rho_k H_k) + \nabla.\left(\alpha_k \rho_k H_k \vec{U}_k\right) = \\ -\nabla.\left(\alpha_k\left(\bar{\bar{q}}_k + q_k^T\right)\right) + \alpha_k \frac{Dp_k}{Dt} + \Gamma_{ki}H_i - \Gamma_{ik}H_k + q_{ki}^{"}a_i + \Phi_k\,,\end{gathered} \tag{6.3}$$

In these equations $\alpha_k,\ \rho_k, \vec{U}_k$ are respectively, the void fraction, density and velocity of phase k which can be either liquid (l) or gas (g). $\bar{\bar{\tau}}_k, \bar{\bar{\tau}}_k^{Re}$ are the viscous and Reynolds (turbulent) stresses, respectively. $\vec{M}_k$ is the averaged inter-phase momentum transfer term modeled in chapter two. q_k is the diffusive flux by conduction and the subscript "T" denotes the turbulence enhanced heat flux. $q_{ki}^{"}$ is the interfacial heat flux between the two phases. a_i is the interfacial area concentration. Φ_{k} is the wall heat source.

The diffusive flux by conduction inside a phase k is given by Fourier's law of conduction as

$$q_k = -k_k \nabla T_k \ , \tag{6.4}$$

where k_k, T_k are thermal conductivity and temperature of phase k, respectively.

Sub-cooled boiling is considered as a combination of phase change due to bubble generation near the heated wall described by evaporation rate Γ_{gl}, and phase change due to condensation of the generated bubbles after departure from the wall induced by the sub-cooled liquid in the bulk and is described by condensation rate Γ_{lg}.

The mass transfer rate per unit volume due to condensation in the bulk sub-cooled liquid Γ_{lg} is given by

$$\Gamma_{lg} = \frac{h_i a_i (T_{sat} - T_l)}{h_{fg}}, \tag{6.5}$$

where h_{fg} is the latent heat of evaporation. h_i is the interfacial heat transfer coefficient, calculated according to Ranz and Marshall (1952) Nusselt number as follow

$$h_i = \frac{k_l}{D_{sm}} Nu = \frac{k_l}{D_{sm}} \left(2.0 + 0.6 Re_B^{0.5} Pr_l^{0.33}\right), \tag{6.6}$$

in which Re_B is the bubble Reynolds number, Pr_l is the surrounding liquid Prandtl number, D_{sm} is the local bubble Sauter mean diameter in the bulk domain and k_l is the liquid thermal conductivity.

The condensation of bubbles generated near the heated wall is motivated by the interfacial heat flux $q_{ki}^{"}$ that is given by

$$q_{ki}^{"} = h_i (T_{sat} - T_l), \tag{6.7}$$

Experimentally, Warrier et al., (2002) confirmed bubbles condensation in the bulk subcooled liquid using a vertical flat plate heater and high speed camera to record the bubble collapse (see Figure 6.3), which depicts the bubble collapse sequence due to condensation.

The evaporation mass transfer rate at the wall $\Gamma_{lg}$is modeled in a mechanistic way and expressed as

$$\Gamma_{gl} = \frac{\dot{q}_e''}{h_{fg}}, \tag{6.8}$$

with $\dot{q}_e''$ as the heat flux due to evaporation which is calculated by the mechanistic model for wall heat flux partitioning developed by Kurul and Podowski (1991) from the Rensselear Polytechnic Institute (RPI). This model is the most widely used one for the modeling of sub-cooled boiling flow in computational fluid dynamics (CFD) codes. It states that all wall heat energy is transformed to the liquid in the near wall region that is divided into latent heat for vapor generation and sensible heat for the bulk liquid (Yeoh and Tu, 2010). More details will be given in the next section.

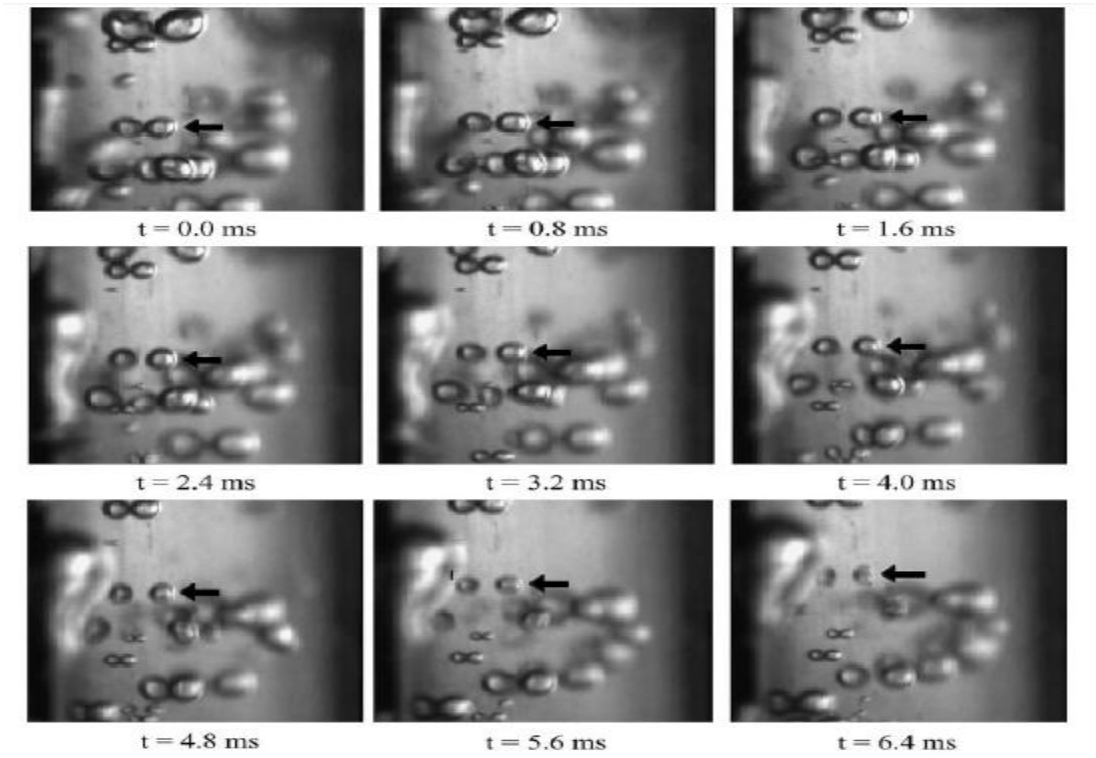

Figure 6.3. Bubble condensation sequence in the bulk sub-cooled liquid (Warrier et al., 2002)

6.2 Wall Heat Flux Partitioning Model

In the Kurul and Podowski (1991) wall partitioning model, the heat is transported from the wall to the liquid by three mechanisms (see Figure 6.4)

- Convection heat transfer $\dot{q}_c''$, directly to the sub-cooled liquid as in single phase flow.
- Evaporation heat transfer $\dot{q}_e''$, by vapor bubbles generation at the nucleation sites.
- Quenching heat transfer $\dot{q}_q''$, to the sub-cooled liquid coming from the bulk that replaces the detached bubbles from the wall cavities during the waiting

time between the bubble departure and the next bubble formation at the same nucleation site.

Accordingly, the total wall heat flux $\dot{q}_w''$ can be written as a sum of the three heat transfer mechanisms as

$$\dot{q}_w'' = \dot{q}_c'' + \dot{q}_e'' + \dot{q}_q'', \tag{6.9}$$

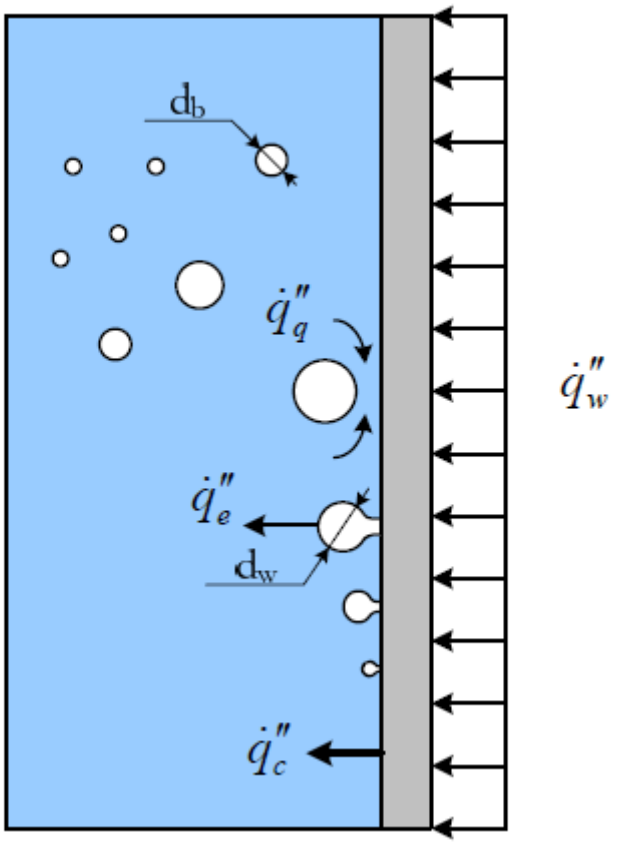

Figure 6.4. Wall heat flux partitioning (Salnikova, 2008)

Each component in the wall heat partitioning model is modeled as a function of the wall temperature and other local flow parameters.

6.2.1 Convection Heat Transfer

The single-phase turbulent convection heat transfer $\dot{q}_c''$ through the part of the wall surface that does not feel the presence of bubbles is calculated as

$$\dot{q}_c'' = h_c A_{1f}(T_w - T_l)\,, \tag{6.10}$$

where A_{1f} is the fraction of wall surface unaffected by the bubbles, and it will be modeled later. T_w is the wall temperature, T_l is the local liquid temperature in the near-wall computational cell. h_c is the single phase convection heat transfer coefficient calculated according to Dittus-Boelter (1985) Nusselt number as follow

$$h_c = \frac{k_l}{d_h} Nu = \frac{k_l}{d_h} \left(0.023 Re_l^{0.8} Pr_l^{0.4}\right), \tag{6.11}$$

in which d_h is the hydraulic diameter of the pipe.

6.2.2 Quenching Heat Transfer

The quenching heat transfer $\dot{q}_q''$ was derived analytically by Mikic and Rohsenow (1969) by assuming transient conduction from the wall to the fresh liquid that replaces the departure bubbles and is expressed as

$$\dot{q}_q'' = h_q A_{2f} (T_w - T_l), \tag{6.12}$$

where A_{2f} is the fraction of the wall area influenced by vapor bubbles given by

$$A_{2f} = N'' K \frac{\pi d_{Bw}^2}{4}, \text{ and then } A_{1f} = 1 - A_{2f}, \tag{6.13}$$

In this expression N'' and d_{Bw} are the density of active nucleation sites and the bubble departure diameter, respectively. The parameter K is the so-called bubble influence factor, which represents the ratio of the area close to the nucleation site that is affected by the heat transferred by nucleate boiling to the projected area at a bubble departure, a value of **1** is suggested by Yeoh and Tu (2005) and a value of **4** that is recommended by Kurul and Podowski (1990) is commonly used.

The quenching heat transfer coefficient h_q is written as

$$h_q = \frac{2}{\sqrt{\pi}} f \sqrt{t_{wait} k_l \rho_l C_{pl}}, \tag{6.14}$$

with C_{pl} and ρ_l as the liquid phase heat capacity and density respectively. f is the bubble departure frequency, and t_{wait} is the quenching period or *waiting time* between the departure of a bubble and the appearance of the subsequent one at the same nucleation site. Tolubinsky and Konstanchuk (1970) found that at a constant pressure, the following correlation is valid

$$\frac{t_{wait} + t_{ct}}{t_{ct}} \approx constant\,, \tag{6.15}$$

t_{ct} is the bubble contact time with the heated wall, and the cycle period can be written as $t_{cycle} = t_{wait} + t_{ct}$. A schematic description of both times is illustrated in Figure (6.5). At atmospheric pressure the constant value in the previous equation was found to be between 4 – 5. Since the bubble departure frequency f is inversely proportional to the cycle period t_{cycle}, then waiting time can be written as

$$t_{wait} = \frac{0.8}{f}, \tag{6.16}$$

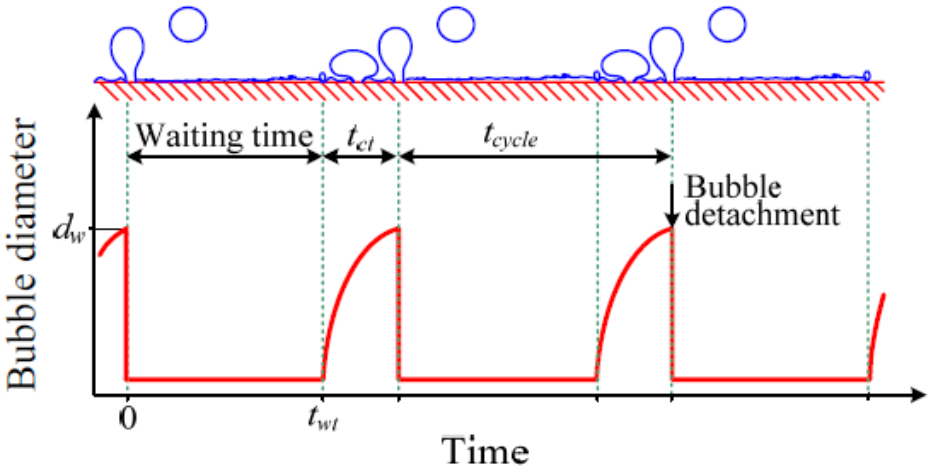

Figure 6.5. Waiting time and contact time against bubble departure diameter at single nucleation site (Salnikova, 2008)

6.2.3 Evaporation Heat Transfer

The heat flux at the wall used for bubble generation in the nucleate boiling region according to Bowring (1962) is proportional to the energy consumed for a single bubble generation, to the nucleation sites density N'' and to the bubble departure frequency f, and is given by the expression

$$\dot{q}''_e = N'' f \left(\frac{\pi}{6} d_{Bw}^3\right) \rho_g h_{fg}, \tag{6.17}$$

6.2.4 Closure Relations

The accurate modeling of bubble nucleation quantities, including the bubble departure diameter d_{Bw}, the bubble departure frequency f, and the nucleation sites density N'',

is required because they have a direct effect on the bubble generation and on the heat partitioning at the heated wall.

- **Bubble departure diameter**

Several empirical correlations have been reported in the literature for the estimation of bubble size at detachment. Tolubinsky and Konstanchuk (1970) derived a correlation by fitting the experimental data of high-pressure water boiling experiments. According to this correlation, the bubble departure diameter is evaluated as a function of the liquid sub-cooling ΔT_{sub} ,as

$$d_{Bw} = min\left(0.6[mm]exp\left(\frac{-\Delta T_{sub}}{45K}\right), 1.4[mm]\right), \tag{6.18}$$

with $\Delta T_{sub} = T_{sat} - T_l$.

Fritz (1935) proposed a model based on the assumption of static equilibrium between buoyancy force and surface tension only when bubble departures the heated wall and is given by

$$d_{Bw} = 0.208\,\theta\sqrt{\frac{\sigma}{g(\rho_l - \rho_g)}}, \tag{6.19}$$

where θ and σ are the bubble contact angle and surface tension respectively.

Kocamustafaogullari and Ishii (1995) modified the previous correlation for low pressure yielding

$$d_{Bw} = 2.5 \times 10^{-5}\left(\frac{\rho_l - \rho_g}{\rho_g}\right)\theta\sqrt{\frac{\sigma}{g(\rho_l - \rho_g)}}, \tag{6.20}$$

The bubble contact angle θ that appears in both models plays a major role in the determination of the shape of the bubble that is generated at the heated surface and it has a direct influence on the size of the detached bubble. It depends on the liquid properties like viscosity and wettability, and also depends on the surface roughness.

- **Bubble departure frequency**

Situ et al., 2007 investigated the explicit effect of the bubble departure frequency on sub-cooled boiling by studying its influence on the wall temperature and nucleation site density. Cole (1960) proposed a correlation for bubble departure frequency based on

the balance between buoyancy and drag forces for pool boiling of water (Situ et al., 2007) , expressed in term of the bubble departure diameter d_{Bw}, as

$$f = \sqrt{\frac{4g(\rho_l - \rho_g)}{3d_{Bw}\rho_l}}, \tag{6.21}$$

- **Nucleation site density**

The nucleation site density is defined as the number of active cavities per unit area (Wang et al., 2013), these cavities become nucleation sites when the surface temperature rises beyond the saturation temperature of the liquid that is in contact with it. An extensive work has been conducted during last decades to increase the number of the nucleation sites on a surface by different surface finishing methods, i.e., polishing, etching, and coating. The nucleation site density depends on the micro-roughness of the surface, liquid physical properties and wall superheat.

Benjamin and Balakrishnan (1997) conducted an experimental investigation to assess the effect of the surface-liquid interaction on the nucleation site density during nucleate pool boiling by using different surface materials polished to different grades and using different coolant liquids, and proposed the following correlation

$$N'' = 218.8Pr^{1.63}\left(\frac{1}{\gamma}\right)\Theta^{-0.4}\Delta T_w^3, \tag{6.22}$$

in which ΔT_w is the wall superheat, γ is the surface-liquid interaction parameter defined as

$$\gamma = \left(\frac{k_w\rho_w C_{pw}}{k_l\rho_l C_{pl}}\right)^{0.5}, \tag{6.23}$$

with k_w, ρ_w, C_{pw} are the wall thermal conductivity, the wall density and the wall specific heat respectively.

Θ is a dimensionless surface roughness parameter given by

$$\Theta = 14.5 - 4.5\left(\frac{R_a P}{\sigma}\right) + \left(\frac{R_a P}{\sigma}\right)^{0.4}, \tag{6.24}$$

with R_a as the surface average roughness measured using profilometer. The range of validity for the correlation is : $1.7 < Pr < 5$; $4.7 < \gamma < 9$; $0.02mm < R_a < 1.17mm$; $5K < \Delta T_w < 25K$; $13 \times 10^{-3}N/m < \sigma < 59 \times 10^{-3}N/m$; $2.2 < \Theta < 14$.

Hibiki and Ishii (2003) derived a mechanistic correlation for the nucleation site density in terms of the contact angle, liquid properties and wall superheat, as follow

$$N'' = 4.72 \times 10^5 \left\{1 - exp\left(-\frac{\theta^2}{4.17}\right)\right\}\left[exp\left\{2.5 \times 10^{-6} f(\rho^+)\frac{\Delta T_w \rho_g h_{fg}}{2\sigma T_{sat}}\right\} - 1\right], \quad (6.25)$$

with $f(\rho^+)$ a function described as

$$f(\rho^+) = -0.01064 + 0.48246\rho^+ - 0.22712\rho^{+^2} + 0.05468\rho^{+^3}, \quad (6.26)$$

and $\rho^+ = \log_{10}\left((\rho_l - \rho_g)/\rho_g\right)$.

Lemmert and Chawla (1977) expressed the nucleation site density depending on the local wall superheat as

$$N'' = [m(\Delta T_w)]^n, \quad (6.27)$$

The values of m and n are **210** and **1.805**, respectively (Kurul and Podowski, 1990).

- **Bubble diameter in the bulk domain**

The bubble Sauter mean diameter in the fluid bulk governs the interfacial area concentration as well as interfacial mass, momentum and heat transfer (e.g., see Eq. 6.6) in sub-cooled boiling. Therefore, precise modeling of local bubble size is desired. Anglart and Nylund (1996) proposed a linear function of local liquid sub-cooling ΔT_{sub}, to estimate the bubble Sauter diameter

$$D_{sm} = \begin{cases} d_{B,1} & \Delta T_{sub} > T_{sub,1} \\ \dfrac{d_{B,1}\left(\Delta T_{sub} - T_{sub,2}\right) + d_{B,2}\left(T_{sub,1} - \Delta T_{sub}\right)}{T_{sub,1} - T_{sub,2}} & T_{sub,1} \geq \Delta T_{sub} \geq T_{sub,2} \\ d_{B,2} & \Delta T_{sub} < T_{sub,2} \end{cases}, \quad (6.28)$$

Reference sub-cooling temperatures and corresponding diameters for nuclear applications are given by Anglart and Nylund (1996) to be: $d_{B,1} = 0.1\ mm$ at $T_{sub,1} = 13.5\ K$ and $d_{B,2} = 2\ mm$ at $T_{sub,2} = 5\ K$.

The dependence of the bubble diameter in the bulk domain on the liquid sub-cooling as proposed by Anglart and Nylund (1996) is illustrated in Figure (6.6).

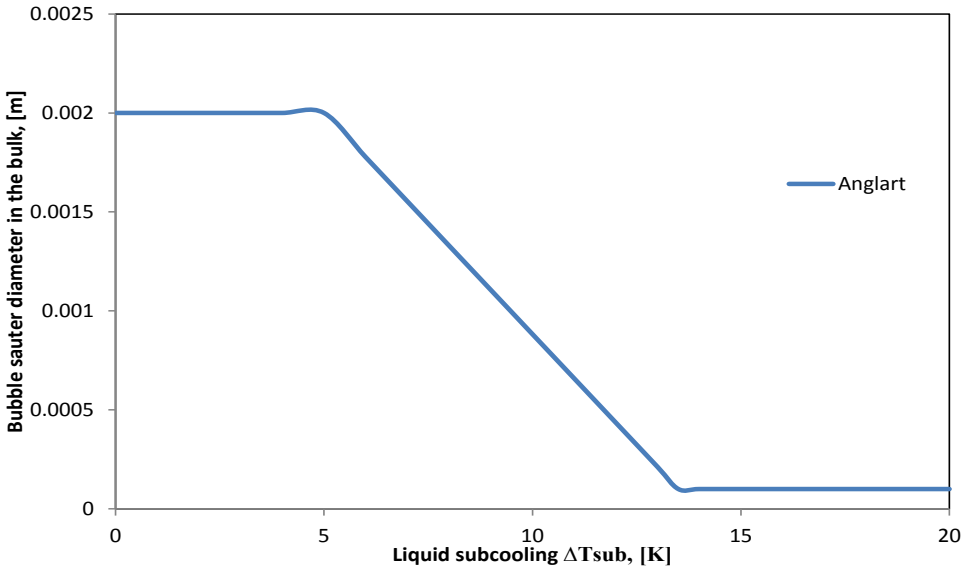

Figure 6.6. Bubble diameter as a function of the liquid sub-cooling according to Anglart and Nylund (1996)

6.3 Coupling Wall Boiling and the One-group Interfacial Area Transport Equation

The empirical correlation proposed by Anglart and Nylund (1996) depicted in Figure (6.6), predicts larger bubble sizes in the region with lower liquid sub-cooling, i.e., exactly at the heated wall, which disagree with the experimental results of Lee et al., (2002) that showed large bubble sizes away from the heated wall (Yeoh and Tu, 2004), this behavior can be attributed to the coalescence of the detached bubbles when migrating towards the bulk domain (see Figure 6.7) where a competition between bubbles coalescence and bubbles collapse due to condensation because of the increased liquid sub-cooling in the bulk domain takes place. Since the empirical correlation of Anglart and Nylund (1996) is relating the local bubble diameter profile in the bulk region to the liquid sub-cooling only and is not able to illustrate the effect of the bubble coalescence and condensation on the bubble size distribution, then the sub-cooled boiling model must be coupled to the one-group interfacial area transport equation to dynamically estimate the interfacial area concentration as well as the non-uniform bubble size distributions, and in turn enhancing the capability of two-phase sub-cooled boiling flow parameters prediction.

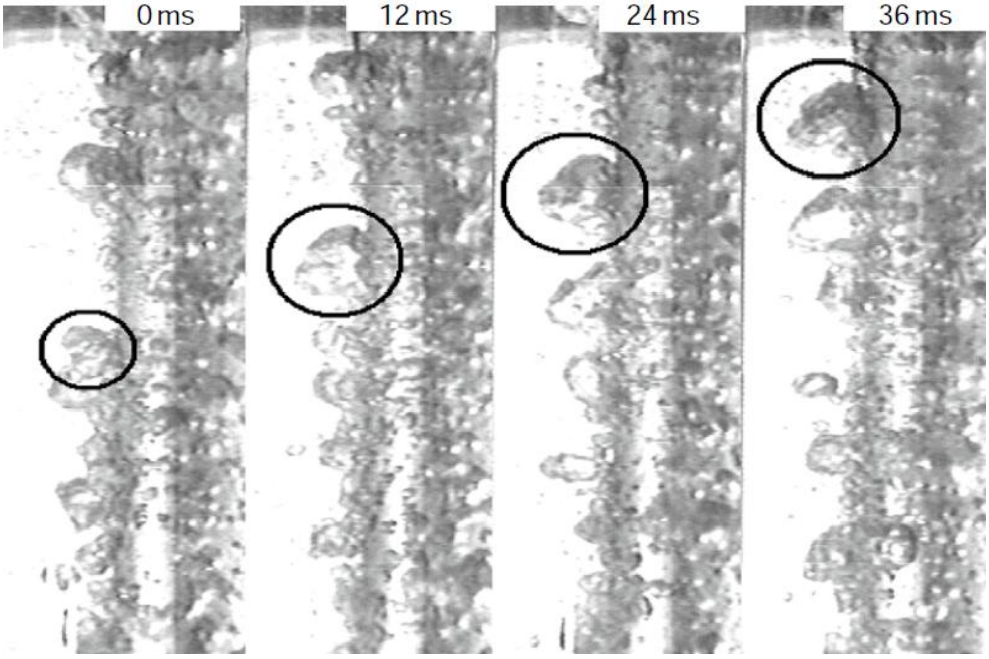

Figure 6.7. Bubble coalescence near the heated wall of an annular flow channel (Tu et al., 2005)

6.3.1 The One-group Interfacial Area Transport Equation

For the modeling of the dynamic behavior of the interfacial structure in sub-cooled boiling flow, Yao and Morel (2004) derived the one-group interfacial area transport equation that takes into account the effect of phase change, including bubble nucleation at the wall and bubble condensation in the bulk domain, on the interfacial area evolution. The transport equation is written as

$$\frac{\partial a_i}{\partial t} + \nabla.(a_i \vec{v}_i) = \frac{2}{3}\frac{a_i}{\alpha \rho_g}\left(\Gamma_{lg} - \alpha \frac{\partial \rho_g}{\partial t}\right) + \phi_{RC} + \phi_{TI} + \phi_n^{NUC}, \qquad (6.29)$$

In this equation ϕ_{RC} and ϕ_{TI} are the interfacial area density change rate by bubble coalescence due to random collision and the bubble breakup due to turbulent impact, respectively. Different models describing these two terms have been investigated in more details in Chapter 5. The Yao and Morel (2004) coalescence and breakup source terms models which are designed for flow with sub-cooled boiling in the DEBORA experiment descriped in the next chapter, are given as

$$\phi_{RC} = -12\pi\left(\frac{\alpha}{a_i}\right)^2 C_{RC1}\frac{\varepsilon^{1/3}\alpha^2}{D_{sm}^{11/3}}\frac{1}{\frac{\left(\alpha_{max}^{1/3}-\alpha^{1/3}\right)}{\alpha_{max}^{1/3}}+C_{RC2}\alpha\sqrt{We/We_{cr}}}exp\left(-C_{RC3}\sqrt{\frac{We}{We_{cr}}}\right), \quad (6.30)$$

$$\phi_{TI} = 12\pi\left(\frac{\alpha}{a_i}\right)^2 K_{B1}\frac{\varepsilon^{1/3}\alpha(1-\alpha)}{D_{sm}^{11/3}}\frac{1}{1+K_{B2}(1-\alpha)\sqrt{We/We_{cr}}}exp\left(-\frac{We_{cr}}{We}\right), \quad (6.31)$$

The description of the different parameters and the values of the used coefficients can be found in Section 4.4.3.

Γ_{lg} denotes the sink of the interfacial area by bubble condensation in the bulk domain and is modeled using Eq. (6.5). ϕ_n^{NUC} is the increase of the interfacial area by nucleation at the heated wall, modeled as the product of the bubble nucleation quantities, as

$$\phi_n^{NUC} = \pi d_{Bw}^2 f N'' A_w''' , \quad (6.32)$$

where A_w''' is the area per unit volume of the unit cell at the heated wall. The bubble diameter used in the previous equation is the bubble departure diameter calculated by Tolubinsky and Konstanchuk (1970) assuming an immediate release of the detached bubbles in the sub-cooled bulk liquid, which contradicts the experimental observations of Lee et al., (2002), Tu et al., (2005), Bonjour and Lallemand, (2001), and Prodanovic et al., (2002). These authors noticed a more complex behavior: the departing bubble from the nucleation site will not migrate directly toward the sub-cooled liquid, but it will slide along the heated wall before lifting off into the bulk domain. During bubble sliding it may collide with another detached bubble at a nucleation site downstream causing bubble enlargement due to bubble coalescence. Therefore, the bubble lift off diameter is *larger* than the bubble departure diameter (see Figure 6.8), and then a bubble lift-off diameter model is required to promote the prediction of the two-phase thermal and hydrodynamic parameters in sub-cooled boiling flows.

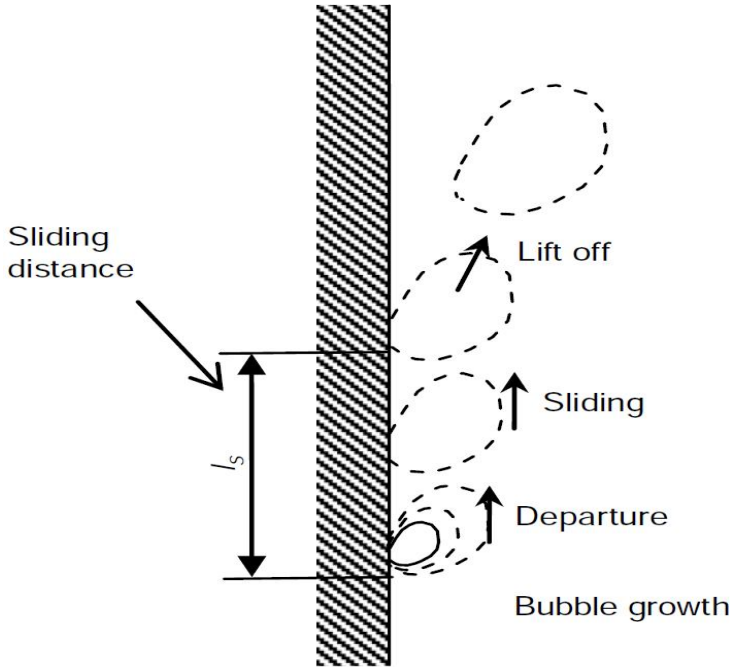

Figure 6.8. Bubble sliding and lifting off mechanism from a heated vertical wall (Yeoh and Tu, 2010)

6.3.2 Bubble Lift-off Diameter Model

The bubble lift-off or departure diameter from a heated wall can be determined by the consideration of a balance between the forces that affect the growth of the bubble at the moment of departure or lift-off. The force balance (see Figure 6.9), which is formulated by Yeoh and Tu (2005) based on the studies performed by Klausner et al., (1993) and Zeng et al., (1993) for the prediction of lift-off size under nucleate boiling conditions of refrigerant R113, is applied to the flow direction y and to the normal direction to the heated vertical x wall as follow

$$\sum F_x = F_{sx} + F_{dux} + F_{sl} + F_h + F_{cp}\,, \tag{6.33}$$

$$\sum F_y = F_{sy} + F_{duy} + F_{qs} + F_b\,, \tag{6.34}$$

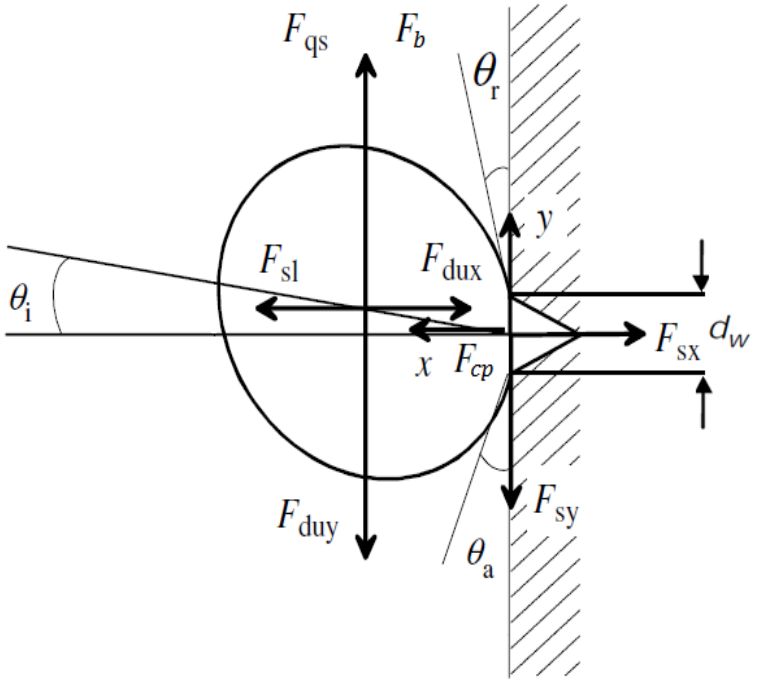

Figure 6.9. Force balance on a sliding bubble at a vertical heated wall

In the force balance F_s is the surface tension force; F_{du} is the growth force or unsteady drag force due to asymmetrical growth of a stationary bubble; F_{sl} is the shear lift force; F_h is the force due to hydrodynamic pressure; F_{cp} is the contact pressure force accounting for the bubble being in contact with a solid rather than being surrounded by liquid; F_{qs} is the quasi-steady drag force in the flow direction; F_b is the buoyancy force.

If the conditions $\sum F_x = 0$ and $\sum F_y = 0$ are satisfied, the bubble will stay attached to its nucleation site without movement, while the bubble departure directly towards the bulk domain or sliding along the heated wall depends on the violation of the aforementioned conditions. Therefore, a bubble will slide along the wall before lifting off if the condition $\sum F_y = 0$ is violated before $\sum F_x = 0$. On the other hand, if the condition $\sum F_x = 0$ is violated before $\sum F_y = 0$, the bubble will lift-off directly towards the subcooled liquid without sliding (Yeoh and Tu, 2005). For the estimation of the lift-off diameter, each force term in Eqs. (6.33) and (6.34) should be modeled.

A summary of the forces models as proposed by Klausner et al., (1993) is provided here

- **Surface tension force, F_s**

According to Klausner et al., (1993) the surface tension force in both directions can be written as

$$F_{sx} = -d_w \sigma \frac{\pi}{\theta_a - \theta_r} [cos\theta_r - cos\theta_a] , \tag{6.35}$$

$$F_{sy} = -d_w \sigma \frac{\pi(\theta_a - \theta_r)}{\pi^2 - (\theta_a - \theta_r)^2} [sin\theta_a + sin\theta_r] , \tag{6.36}$$

where θ_a and θ_r are the advancing and receding contact angles, respectively. d_w is the bubble/surface contact diameter.

- **Unsteady drag force (growth force), F_{du}**

The growth force is given by Zeng et al., (1993) as

$$F_{du} = \rho_l \pi r^2 \left(\frac{2}{3} C_s \dot{r}^2 + r\ddot{r} \right), \tag{6.37}$$

Where r is the bubble radius, $\dot{r}$ is the bubble radius derivative with respect to time, and $\ddot{r}$ is the second derivative with respect to time. The constant C_s is given by Zeng et al., (1993) to be **20/3**.

The x and y components of the growth force can be written in term of the inclination angle θ_i as

$$F_{dux} = -F_{du} cos\theta_i \quad \text{and} \quad F_{duy} = -F_{du} sin\theta_i , \tag{6.38}$$

The bubble growth rate with respect to time was derived by Zuber (1961) considering a diffusion controlled bubble growth, expressed as

$$r(t) = \frac{2b}{\sqrt{\pi}} Ja \sqrt{\eta t} , \tag{6.39}$$

where b is a constant suggested by Zeng et al., (1993) to be **1.73**. It accounts for the sphericity of the bubble, and Ja is the Jacob number defined as

$$Ja = \frac{\rho_l C_{pl} (T_w - T_{sat})}{\rho_g h_{fg}} , \tag{6.40}$$

η is the thermal diffusivity of the liquid given by

$$\eta = \frac{k_l}{\rho_l C_{pl}}, \tag{6.41}$$

- **Shear lift force, F_{sl}**

Mei and Klausner (1994) derived the shear lift force expression based on the model of Saffman (1965) for the lift force on a solid sphere and the model of Auton (1987) for the lift force on a sphere in an inviscid flow (Situ et al., 2005), yielding

$$F_{sl} = \frac{1}{2} C_L \, \rho_l \, u_r^2 \, \pi r^2 \ , \tag{6.42}$$

where u_r is the relative velocity between the bubble and the liquid phase, and C_L is the shear lift coefficient proposed by Klausner et al., (1993), obtained from

$$C_L = 3.877 G_s^{1/2} (Re_B^{-2} + 0.014 G_s^2)^{1/4}, \tag{6.43}$$

with G_s as the dimensionless liquid shear rate defined by the following formula

$$G_s = \left| \frac{du_l}{dx} \right| \frac{r}{u_r}, \tag{6.44}$$

- **Hydrodynamic pressure force, F_h** (Yun et al., 2010)

$$F_h = \frac{9}{8} \rho_l u_r^2 \frac{\pi d_w^2}{4}, \tag{6.45}$$

- **Contact pressure force, F_{cp}**

$$F_{cp} = \frac{\pi d_w^2}{4} \frac{2\sigma}{r_r}, \tag{6.46}$$

in which r_r is the bubble curvature radius defined by Klausner et al., (1993) as $r_r \sim 5r$.

- **Buoyancy force, F_b**

$$F_b = \frac{4}{3} \pi r^3 \left(\rho_l - \rho_g \right) g, \tag{6.47}$$

- **Quasi-steady drag force, F_{qs}**

$$F_{qs} = 6 C_D \, \mu_l \, u_r \, \pi r \, , \tag{6.48}$$

where the drag coefficient C_D is proposed by Klausner et al., (1993) as

$$C_D = \frac{2}{3} + \left(\left(\frac{12}{Re_B} \right)^n + 0.796 \right)^{-1/n}, \tag{6.49}$$

$$n = 0.65,$$

At the instant of bubble lift-off, the force balance in the x-direction is violated and the bubble contact diameter with the heated surface becomes **zero** (Bae et al., 2010), and hence the surface tension, hydrodynamic pressure and contact pressure forces can be neglected because they depend strongly on the contact diameter. The force balance in the x-direction yields (see Figure 6.10)

$$F_{du} + F_{sl} = 0, \tag{6.50}$$

Considering that the inclination angle of the bubble at the lift-off is **zero** and substituting the expressions for all the forces forces results in

$$10\dot{r}^2 + r\ddot{r} = \frac{1}{2} C_L \, u_r^2, \tag{6.51}$$

Substituting the bubble growth rate with respect to time (Eq. 6.39) as proposed by Zuber (1961) in the previous equation yields

$$\frac{\eta}{t_{lo}} = \frac{\pi C_L u_r^2}{9b^2 \, Ja^2}, \tag{6.52}$$

in which t_{lo} is the lift-off time (Situ et al., 2005), derived from Eq. (6.39) as

$$t_{lo} = \frac{\pi r_{lo}^2}{4b^2 \, Ja^2 \, \eta}, \tag{6.53}$$

Substituting Eq. (6.53) into Eq. (6.52) yields the bubble lift-off diameter

$$D_{lo} = \frac{12b^2}{\pi} \frac{\eta \, Ja^2}{\sqrt{C_L} u_r}, \tag{6.54}$$

Therefore, Eq. (6.32) can finally be expressed as

$$\phi_n^{NUC} = \pi D_{lo}^2 \, f \, N'' \, A_w''', \tag{6.55}$$

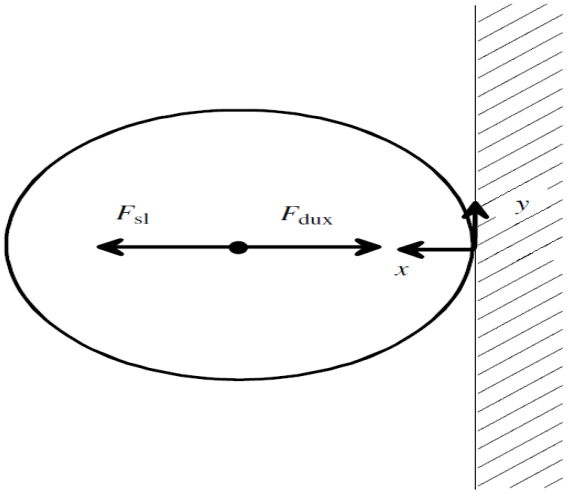

Figure 6.10. Bubble lift-off force balance (Situ et al., 2005)

6.4 Modeling of Boiling-Induced Turbulence

During the modeling of adiabatic bubbly flow in the first part of this thesis, the $k-\varepsilon$ turbulence model has been used for the calculation of the turbulent kinetic energy k and the turbulent energy dissipation rate ε and, in turn, the estimation of the shear-induced turbulent eddy viscosity υ_l^t as in Eq. (2.65). The additional turbulence generated in the wake of large bubbles, which is called bubble-induced turbulence, has been considered through two approaches. The first one is Sato's approach which involves the calculation of the bubble-induced turbulent viscosity in term of the void fraction, bubble Sauter mean diameter and the relative velocity between the phases, and then the total viscosity is linearly decomposed into the molecular viscosity and the shear-induced turbulent viscosity. The second approach has been the consideration of the bubble effect on the liquid turbulence through additional source terms in the $k-\varepsilon$ transport equations representing the turbulent effect of the drag force (Koncar and Tiselj, 2010).

In boiling flow, the liquid velocity profile in the near heated wall region was found to be influenced by the vapor bubbles generated at the wall by disordering the flow field in the laminar boundary layer. Bae et al. (2010) adopted Kataoka and Serizawa (1997) boiling-induced turbulence model that is based on the modification of the turbulence mixing length in the near-wall boiling region, where the effect of the generated bubbles

is considered by an additional source term in the turbulent kinetic energy transport equation, that can be calculated by the expression

$$\Phi_k^{boil} = \frac{N''}{t_B(^3/_2)d_B}.\frac{1}{2}v'^2_B.\frac{\pi}{6}d_B^3\,, \tag{6.56}$$

The bubble departure time t_B is defined as $^1/_f$, and v'_B is the boiling-induced fluctuating velocity predicted by Kataoka and Serizawa (1997) as $\sqrt{2}\,{}^{d_B}/_{t_B}$. Using the definition of the evaporation heat flux $\dot{q}_e''$ in Eq. (6.17) it, Eq. (6.56) yields

$$\Phi_k^{boil} = \frac{8}{9}\frac{g\Delta\rho}{\rho_l}\frac{\dot{q}_e''}{\rho_g h_{fg}}, \tag{6.57}$$

6.5 Wall Heat Flux Partitioning Algorithm implemented in OpenFOAM

The new solver developed during the work of this thesis is considered as an extension of the already included solver in OpenFOAM called twoPhaseEulerFoam. Additional interfacial forces have been implemented that were not included in the original solver, beside the one-group interfacial area concentration along with different mechanistic models to describe the bubble interaction mechanisms, i.e., bubble coalescence and breakup for the dynamic prediction of the interfacial structure leading for a better estimation of the interfacial transfer mechanisms including heat and mass transfer. For sub-cooled boiling flow modeling, the energy equation in term of specific enthalpy has been introduced and solved for the liquid phase only, while the vapor phase is assumed to be at saturation temperature. Investigations on the implementation of the complete solver are given in Appendix B.

It is worth at this moment to describe the sequence of the wall heat flux partitioning algorithm implemented in the developed solver for better understanding of the modeling process of boiling mechanism before its assessment against experimental data. In summary, the algorithm runs like this

1. Computation of the single phase convection heat transfer coefficient h_c, Eq. (6.11).

2. Initial guess of the wall superheat assuming that the total wall heat flux is consumed for single phase heat transfer. This is done by the following equation

$$T_{sup}^{w} = \frac{\dot{q}_{w}''}{h_c} - T_{sub}^{l}\,, \tag{6.58}$$

where T_{sub}^{l} is the liquid sub-cooling defined as $T_{sat} - T_{l}$, taking into consid eration that

$$T_{w} - T_{l} = T_{sup}^{w} + T_{sub}^{l}\,, \tag{6.59}$$

If the wall superheat is less than zero, then no evaporation is initiated yet.

3. If the wall superheat is larger than zero, a Newton iterative loop will start in the near-wall cells for the calculation of each heat flux component:
    a) Computation of the bubble departure diameter d_{Bw}, Eqs. (6.18), (6.19) or (6.20).
    b) Computation of the bubble detachment frequency f, Eq. (6.21).
    c) Computation of nucleation site density N'', Eqs. (6.22), (6.25) or (6.27).
    d) Calculation of the fraction of the wall area influenced by vapor bubbles A_{2f}, and the remaining fraction for single phase convection A_{1f}, Eq. (6.13).
    e) Calculation of the quenching heat transfer coefficient h_q. Eq. (6.14).
    f) Estimation of each heat flux component, convection $\dot{q}_c''$, quenching $\dot{q}_q''$ and evaporation $\dot{q}_e''$. Eqs. (6.10), (6.12) and (6.17) respectively.
    g) Computation of the total heat flux $\dot{Q}_{tot}$ from the calculated heat components.
    h) Re-estimation of the wall superheat based on the computed heat components using

$$T_{sup}^{w} = T_{sup}^{w\ *} + \frac{\dot{q}_{w}'' - \dot{Q}_{tot}}{A_{1f}h_c + A_{2f}h_q}\,, \tag{6.60}$$

where $T_{sup}^{w\ *}$ is the wall superheat calculated in the previous iteration step. This estimation equation has been also used by Michta (2011).

i) Calculation of the difference error between the actual and the computed wall heat flux which is essential for the new estimation of the wall temperature in the next iteration step.

$$error = \frac{\dot{q}_w'' - \dot{Q}_{tot}}{\dot{q}_w''}, \tag{6.61}$$

The iteration will continue until the difference error reach a limited value, i.e., 10^{-4}.

j) Final computation of the wall heat flux components.

The schematic illustration of the wall heat flux partitioning algorithm is shown in Figure (6.11).

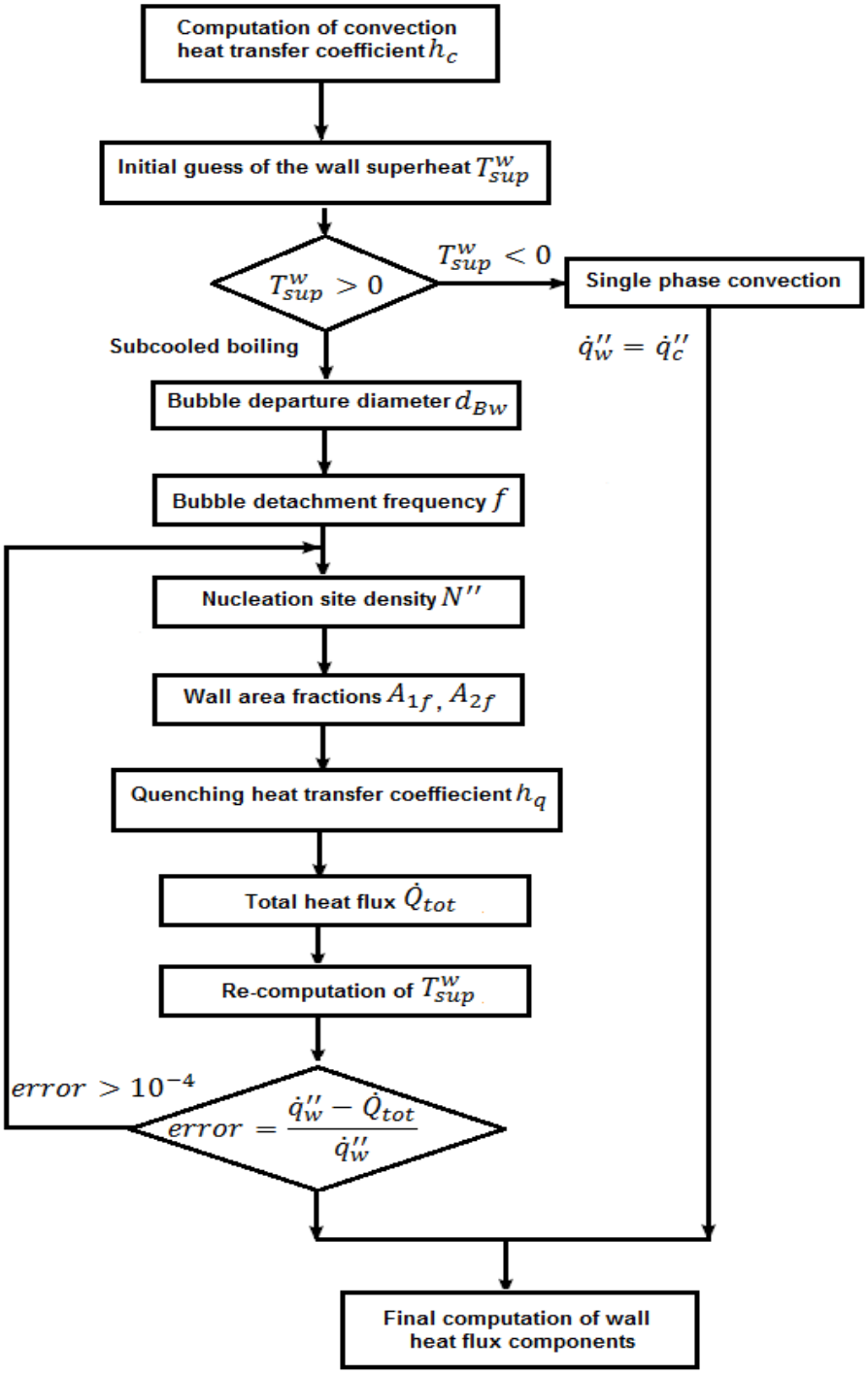

Figure 6.11. Wall heat flux partitioning algorithm for sub-cooled boiling prediction

Chapter Seven

Simulation of the DEBORA Experiment

The one-group interfacial area transport equation and bubble interaction mechanistic models coupled with the two-fluid model showed an improved potential for modeling bubbles coalescence and breakup processes and better prediction of two-phase flow parameters especially the bubble Sauter mean diameter that influences the interfacial heat and mass transfer through the interfacial area concentration (Yeoh and Tu, 2006). Sub-cooled boiling flow is associated with complex phenomena including bubble coalescence, breakup, and nucleation at the heated wall and condensation by the subcooled liquid in the bulk domain. In most of nuclear safety thermal-hydraulic system codes, the local bubble size in the bulk region is determined by empirical correlations in terms of the liquid sub-cooling only without employing the aforementioned phenomena effects that govern the bubble size distribution, which contradicts the experimental results of Lee et al.,(2002). These results have proved the occurrence of coalescence between the detached bubbles resulting in larger bubbles in the vicinity of the heated wall, and also the experimental results of Warrier et al., (2002) that confirmed gradual reduction of the bubble sizes when migrating towards the pipe center due to increasing condensation caused by the increasing liquid sub-cooling.

The one-group interfacial area transport equation serves as a suitable choice for predicting the non-uniform bubble size distribution in the sub-cooled boiling flow by the inclusion of new source terms representing bubble nucleation and condensation. Numerical investigations have been conducted to examine the capability of the newly developed OpenFOAM solver that couples the one-group interfacial area transport equation with a three dimensional two-fluid model and sub-cooled boiling models. The validation process includes the comparison of the predicted radial profiles of the local two phase flow parameters including void fraction, bubble mean Sauter diameter, interfacial area concentration, liquid temperature and bubble velocity, against the experimental data of DEBORA sub-cooled boiling Test (Manon, 2000; Garnier et al., 2001) at different pressures, heat and mass fluxes and inlet sub-cooling.

7.1 The DEBORA Test Facility

The DEBORA experiment was carried out at CEA, Grenoble (Manon, 2000; Garnier et al., 2001) to simulate sub-cooled boiling in pressurized water reactor (PWR) conditions with a simple geometry. The refrigerant R12 (Dichlorodifluoromethane) has been selected as the working fluid, the idea behind this selection is the difficulty to perform accurate local measurements at a typical flow conditions of PWR that include high pressure and temperature of water while more safe and convenient measurement can be carried out when using R12 that yields the same vapor/liquid density ratio at a lower pressure and the same Reynolds number using larger pipe diameter (Krepper and Rzehak, 2011).

The test section is a vertical heated pipe with an inner diameter equal to 19.2 mm, the pipe length is divided into three parts: the adiabatic inlet section (1m), the heated section (3.5 m) and the adiabatic outlet section (1 m) (see Figure 7.1). The R12 is injected from the bottom of the pipe and then heated up over the heated section. The gas volume fraction, interfacial area concentration, bubble size and gas velocity radial profiles are measured at the end of the heated section using an optical probes and the liquid temperature measured by means of thermocouples. The system is working under a wide range of liquid pressure (1.46 – 2.62 MPa) and mass flow rate (2000 – 3000 Kg/m²/s).

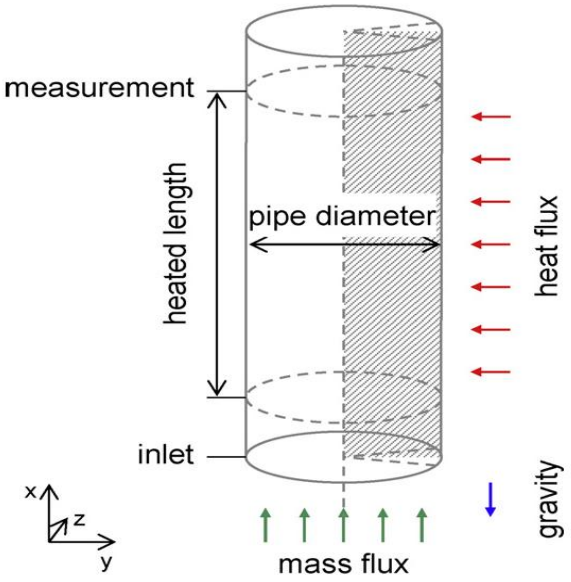

Figure 7.1. DEBORA test geometry (Krepper and Rzehak, 2011)

7.2 Numerical Conditions for the Simulation

For the modeling of sub-cooled boiling bubbly flow, the one-group interfacial area transport equation with appropriate sink and source terms representing the bubble coalescence and breakup according to Yao and Morel (2004) and bubbles nucleation and condensation based on Ranz and Marshall (1952) Nusselt number, and the wall heat flux partitioning model (Kurul and Podowski, 1991) have been coupled and solved along with the Euler-Euler two-fluid model in the open source code OpenFOAM.

Regarding the source term in the momentum equation representing the interfacial momentum exchange between the two phases, the Ishii and Zuber (1979) model is adopted for the drag force, Tomiyama et al. (2002) model for the lift force, Hosokawa et al. (2002) model for the wall lubrication force and FAD/Burns et al. (2004) model for the turbulent dispersion force.

To account for two-phase turbulence, the standard $k-\varepsilon$ model and the standard wall function that bridges the near-wall region between the wall and the turbulent core are employed for the liquid phase. In addition, the bubble-induced turbulence is taken into account by introducing appropriate source term in the $k-\varepsilon$ equations according to Morel (1997). For the gas phase, the dispersed phase zero-equation model is utilized.

For the bubble nucleation evaluation, closure relations are required for the calculation of the bubble departure diameter, bubble departure frequency and nucleation site density. The models of Tolubinsky and Konstanchuk (1970) and Fritz (1935) are used and compared for the estimation of the bubble departure diameter. The model of Cole (1960) is used for the calculation of the bubble departure frequency. For the evaluation of the nucleation site density, the models of Lemmert and Chawla (1977) and Hibiki and Ishii (2003) are employed.

The local bubble Sauter mean diameter in the bulk domain is calculated using the empirical correlation of Anglart and Nylund (1996) based on the liquid sub-cooling, and also calculated from the interfacial area concentration after the solution of the one-group interfacial area transport equation. The last approach is further modified by the inclusion of the bubble lift-off diameter calculated by the forces balance described in the previous chapter, instead of the bubble departure diameter for the calculation of the evaporative heat flux and bubble nucleation source term in the interfacial area transport equation.

The test geometry was simplified to be modeled as a quasi-2D (i.e. 5° slice of the pipe) based on the assumption of radial symmetry. A 3D simulation with 45° sector of the pipe has shown a good agreement with the simplified geometry.

At the inlet of the test section, a liquid velocity profile was set according to a typical single phase turbulent flow profile in a pipe, while the gas velocity, void fraction, bubble size and liquid enthalpy were specified uniformly. On the heated wall, a no-slip condition was used for the liquid phase and a free-slip condition for the gas phase, and a constant heat flux was adopted. Symmetry plane boundary conditions are imposed in both faces of the simplified geometry. Flow conditions for the selected test cases are summarized in Table (7.1).

Due to convergence and stability problems when using a fine mesh during the simulation, a coarse mesh has been used with a non-dimensional distance from the wall $y^+ \sim 250$, this problem was also reported by Krepper et al., (2013), which can be attributed to the nature of the Kurul and Podowski (1991) heat partitioning model which assumes that all bubbles are generated only in the cells located exactly near the wall.

Table 7.1. Flow conditions for the selected test cases

Test	*Pressure [MPa]*	*Mass flow rate [Kg/m²/s]*	*Wall heat flux [kW/m²]*	*Inlet temperature [°C]*
DEBORA1	2.62	1996	73.89	68.52
DEBORA2	2.62	1985	73.89	70.53
DEBORA5	1.46	2028	76.19	35.6
DEBORA6	1.46	2023	76.26	39.67

7.3 Assessment of Boiling Closure Models

Due to the direct impact of the bubble nucleation quantities on the bubble generation and heat partitioning at the heated wall, different boiling closure relations that model the bubble departure diameter and nucleation site density have been tested and compared against local measurements of the boiling flow parameters at the outlet of the heated pipe. Due to the tendency of the contact angle that is an essential parameter in the Fritz (1935) bubble departure diameter model and the Hibiki and Ishii (2003) nucleation site density model to accept different values depending on the application of in-

terest, then, the Lemmert and Chawla (1997) nucleation site density model will be used as a reference model during the assessment of the bubble departure diameter models, and the model of Tolubinsky and Konstanchuk (1970) for bubble departure diameter will be used as a reference model when assessing the nucleation site density models.

- **Model for the bubble departure diameter**

The comparison of the predicted radial profiles of void fraction, interfacial area concentration and bubble Sauter mean diameter calculated by the models of Tolubinsky and Konstanchuk (1970) and Fritz (1935) against the experimental data of test cases DEBORA1 and DEBORA2 is shown in Figures (7.2) and (7.3).

The void fraction profiles calculated using the Fritz (1935) model with a contact angle equal 45° show a clear under-prediction, especially in the near wall and the intermediate regions. Slight over-estimation is noticed in the bulk region for the case with higher inlet sub-cooling (DEBORA1). On the other hand, the model of Tolubinsky and Konstanchuk (1970) shows a better agreement of the predicted void fraction profiles with the measured results, with slight under-prediction in the intermediate region for the DEBORA2 test case.

The radial distributions of the interfacial area concentration estimated by both models reveal a good estimation in the bulk domain with over-prediction in the wall region for both cases. For the case of DEBORA1, a slight over-prediction is also noticed in the bulk region when using the Fitz (1935) model.

A better prediction of void fraction and interfacial area concentration profiles can be expected to yield a good estimate of the bubble Sauter mean diameters, which is the case for Tolubinsky and Konstanchuk (1970). This model shows a good agreement in general, except for the near wall region due to the over-prediction of the interfacial area in that region. On the contrary, Fritz (1935) model under-predicts the bubble Sauter mean diameter in the entire pipe section.

In conclusion, the discrepancies with respect to the experimental profiles observed when using Fritz (1935) model can be attributed to the *constant contact angle* assumed, which, in reality, evolves continuously in sub-cooled boiling flow (Tu et al. 2005). Moreover, in spite of Tolubinsky and Konstanchuk (1970) model calculating the bubble departure diameter in terms only of the liquid sub-cooling, the results show that

it is yet capable of providing acceptable predictions of sub-cooled boiling flow parameters.

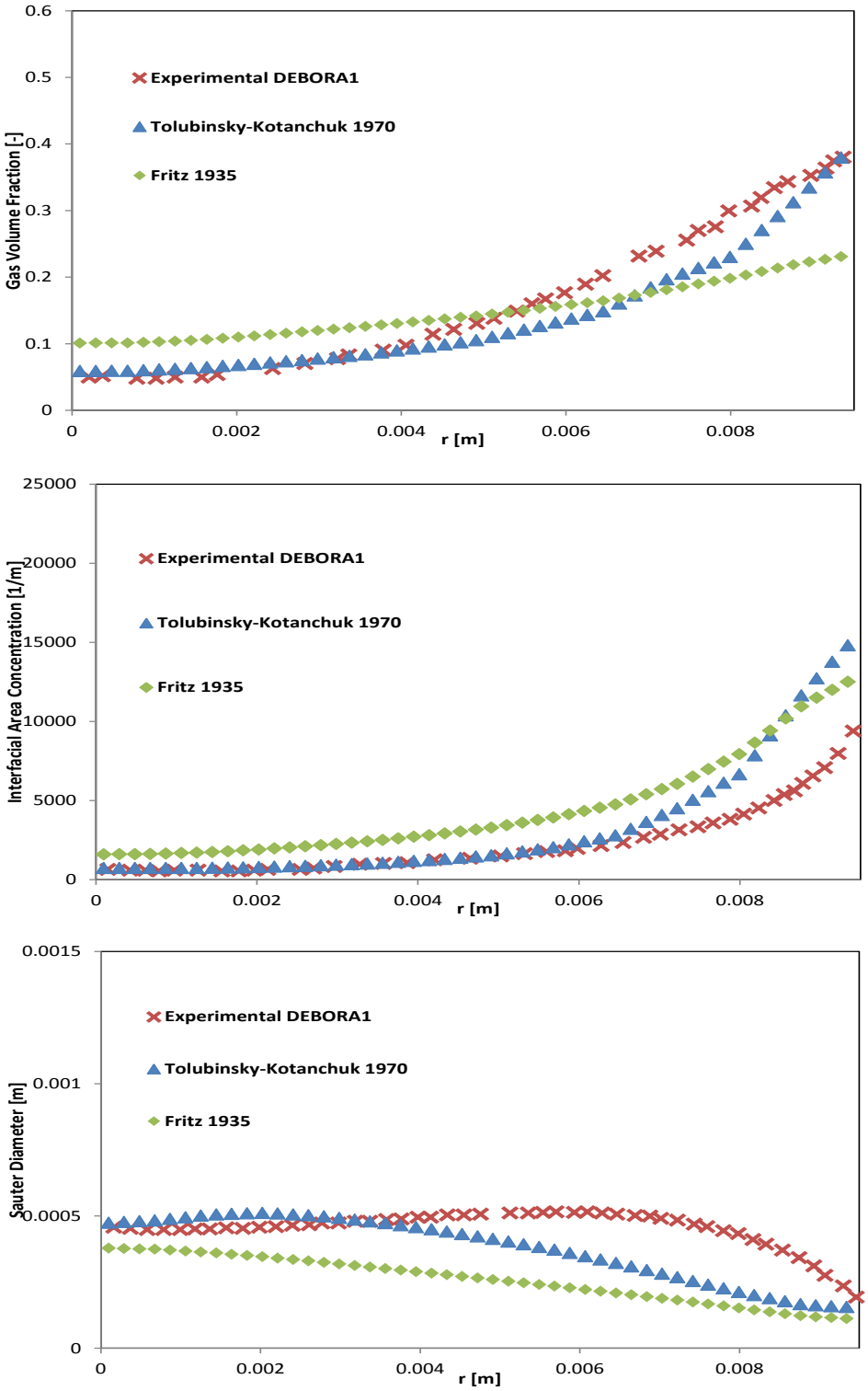

Figure 7.2. Radial profiles of void fraction, interfacial area concentration and Sauter mean diameter for DEBORA1 calculated by two different bubble departure models

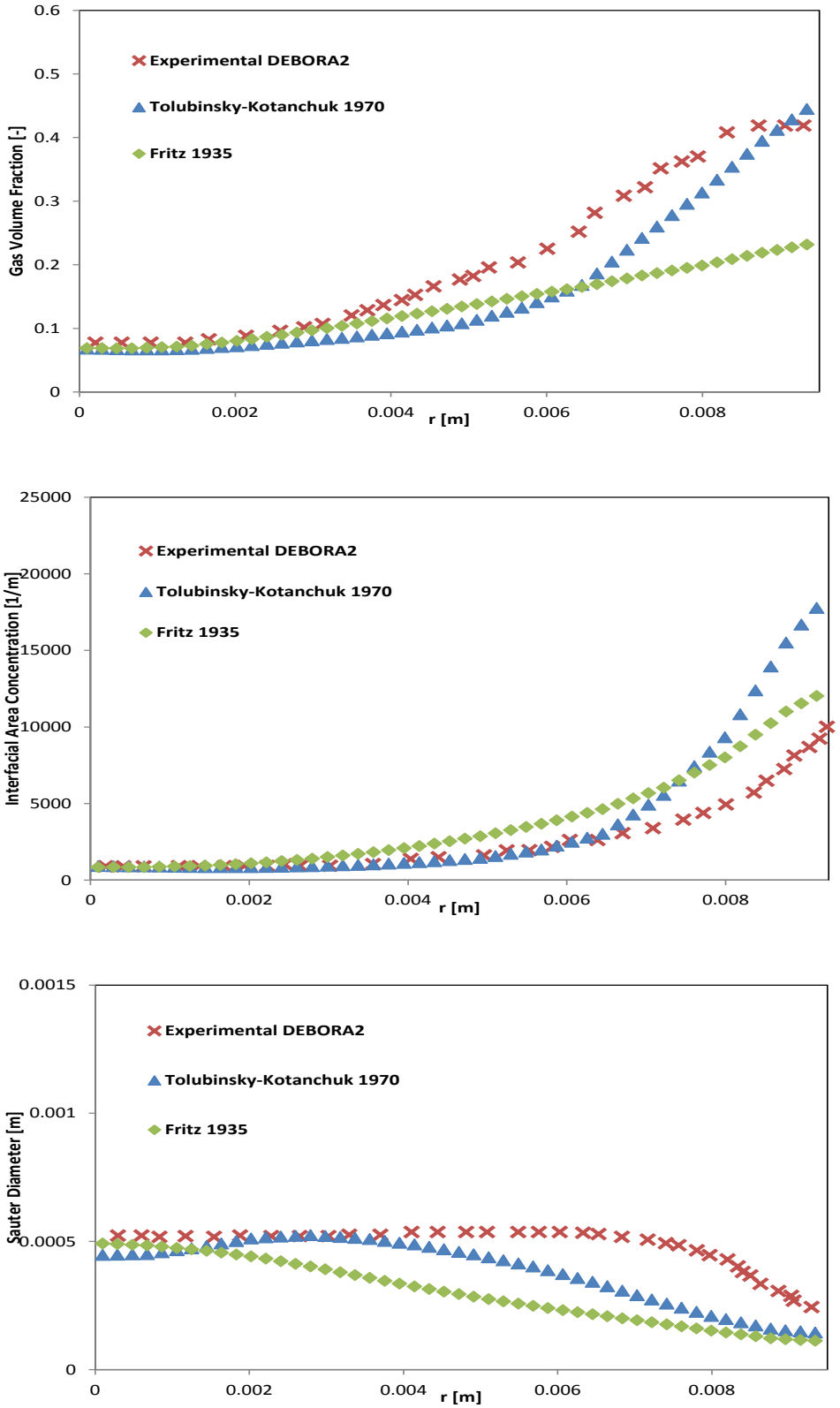

Figure 7.3. Radial profiles of void fraction, interfacial area concentration and Sauter mean diameter for DEBORA2 calculated by two different bubble departure models

- **Model for nucleation site density**

Lemmert and Chawla (1977) and Hibiki and Ishii (2003) models for nucleation site density have been implemented in the newly developed solver to examine their capability to capture the local radial profiles of boiling flow parameters as shown in Figures (7.4) and (7.5) for test cases DEBORA1 and DEBORA2 respectively.

Similar behavior is observed between the two models when predicting void fraction and interfacial area concentration profiles providing a good agreement with the experimental data especially in the bulk flow domain with slight under-prediction of the void fraction in the near-wall region by Hibiki-and Ishii (2003) model. Both models are also providing clear over-estimation of the interfacial area density in the wall region, with a slight over-prediction when using Hibiki-and Ishii (2003) model in the test case DEBORA2.

Lemmer and Chawla (1977) model shows a good agreement between the predicted and measured bubble Sauter mean bubble diameter profiles only in the center and intermediate regions, with a clear under-estimation in regions near the wall, while the Hibiki and Ishii (2003) model predicts a bubble size profile which is relatively largely under-estimated in the whole flow domain.

The similar behavior of the two models can be interpreted by the calculation of the active nucleation site density using both models in term of the wall superheat as illustrated in Figure (7.6). In the interval of wall superheat between 5K and 15K, which is the range observed during the simulation of DEBORA1 and DEBORA2 test cases, both models predict a relatively similar number of bubble nucleation sites per unit area. The very slightly higher values by the Lemmer and Chawla (1977) model can explain its predicted higher values of void fraction, interfacial area concentration in the near-wall region.

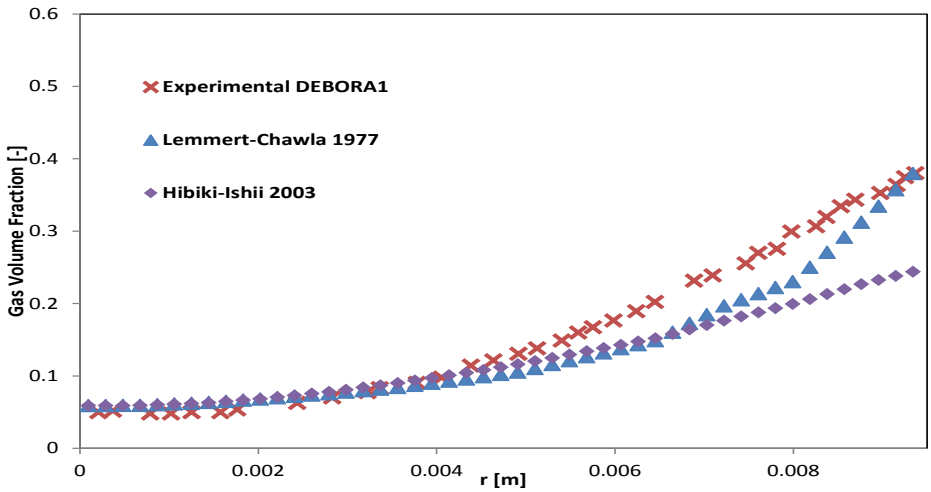

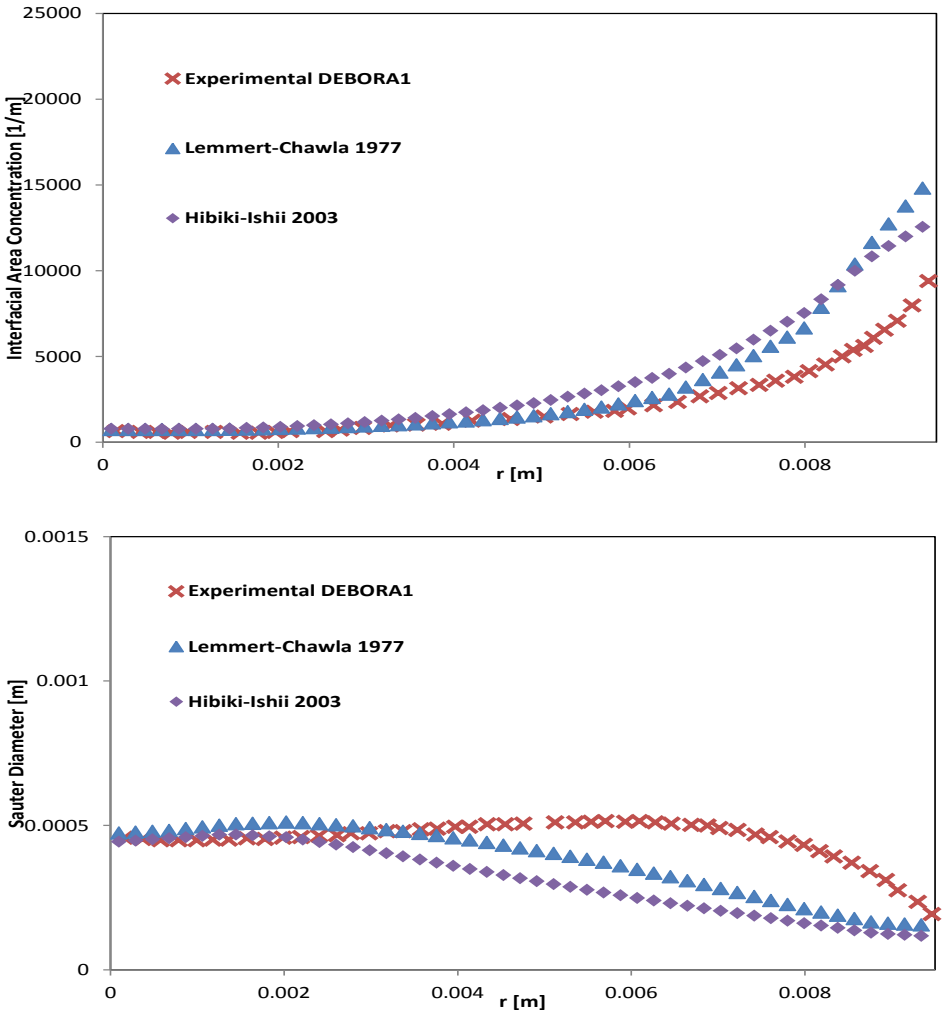

Figure 7.4. Radial profiles of void fraction, interfacial area concentration and Sauter mean diameter for DEBORA1 calculated by two different nucleation site density models

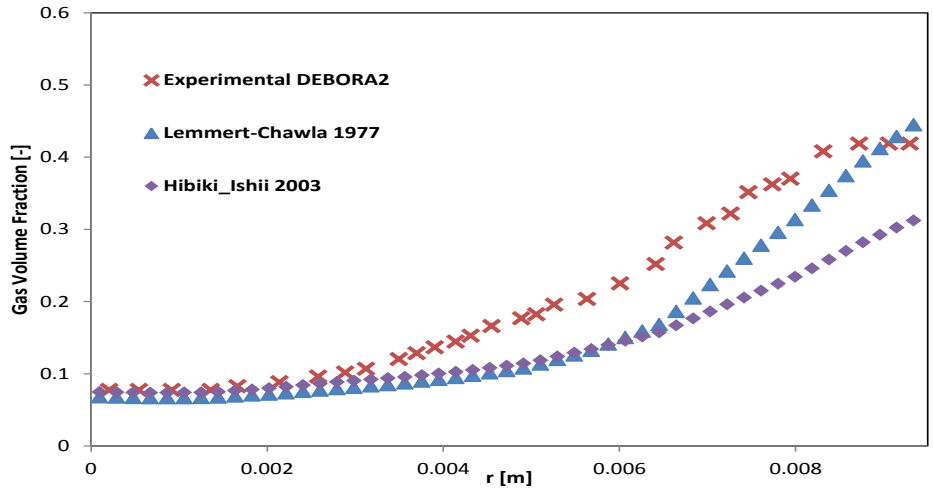

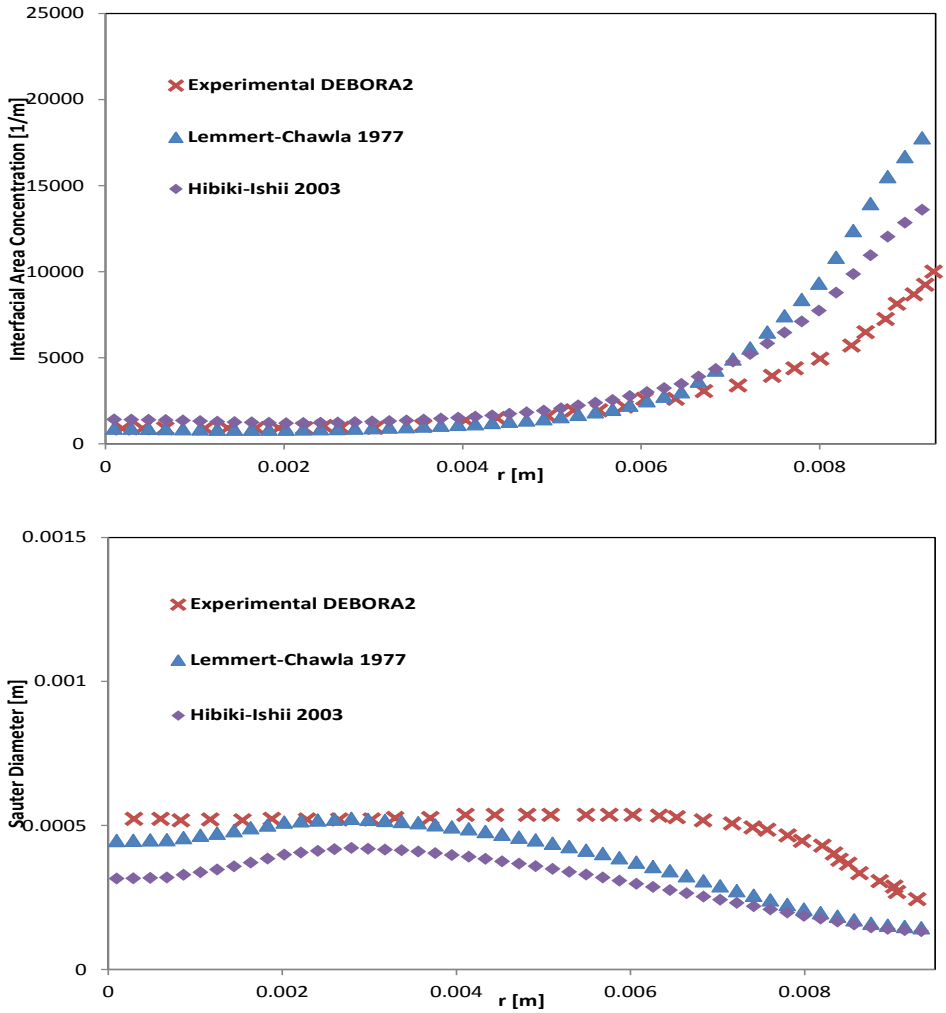

Figure 7.5. Radial profiles of void fraction, interfacial area concentration and Sauter mean diameter for DEBORA2 calculated by two different nucleation site density models

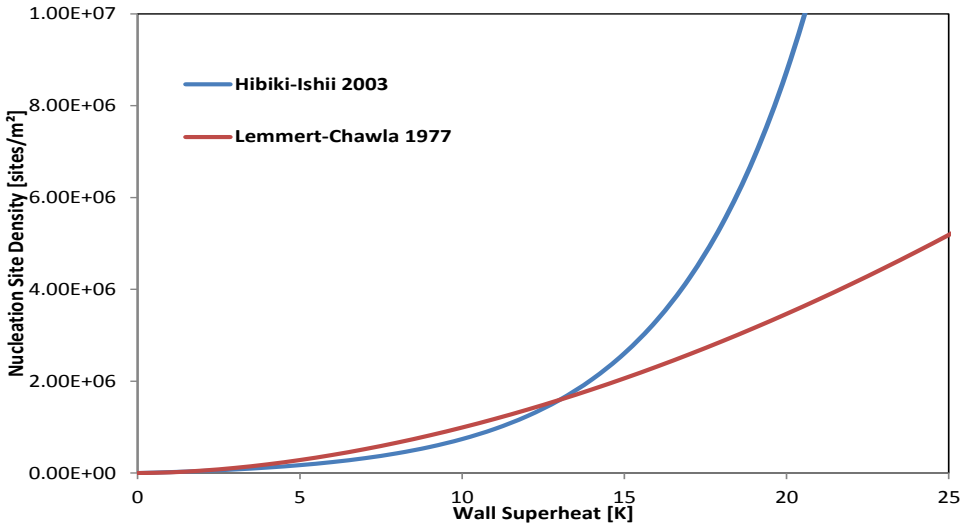

Figure 7.6. Nucleation site density calculated by Lemmert and Chawla (1977) and Hibiki and Ishii (2003) models

7.4 Evaluation of Sub-cooled Boiling Predictions with the One-group Interfacial Area Transport Equation

The accurate estimation of the local bubble diameter distribution in the bulk domain is crucial for two-phase sub-cooled boiling flow parameters prediction, where it influences the interfacial transfer process between the two phases including mass, momentum and energy. Based on the experimental observation of Warrier et al. (2002), a wide domain of bubble sizes is observed in the flow domain which prove the existence of bubbles complex interaction processes including coalescence and breakup in addition to bubble nucleation at the heated wall and bubble condensation in the bulk sub-cooled liquid. The one-group interfacial area transport equation according to Yao and Morel (2004) that incorporates the effect of phase change to enhance the modeling of dynamic behavior of the interfacial structure in sub-cooled boiling flow has been implemented in the new OpenFOAM solver that is used for the simulation of the DEBORA experiment. The predicted radial profiles of the local flow parameters calculated by the new solver including void fraction, interfacial area concentration, bubble Sauter mean diameter and gas velocity are compared against another computational results estimated by employing the empirical correlation of Anglart and Nylund (1996) which is widely used in most of the CFD codes that assumes a linear relationship between the local bubble diameter and liquid sub-cooling. In both approaches, the bubble departure diameter and nucleation sites density are calculated based on the models of Tolubinsky and Konstanchuk (1970) and Lemmert and Chawla (1977) , respectively. Both predicted results are further compared against the local measurements at the exit of the heated pipe of DEBORA experiment.

The radial distributions of void fraction for test cases DEBORA1 and DEBORA2 illustrated in figure 7.7 show that the locally predicted profile by applying the empirical relationship of Anglart and Nylund (1996) is not consistent with the measured values and it shows gross under-prediction specially in the near wall region. On the other hand, a better agreement is observed between the void fraction values determined through the application of the one-group IATE and those experimentally measured. In both approaches, the void fraction profile shows a clear increase of void fraction in the vicinity of the heated wall which agrees the nature of sub-cooled boiling phenomena, in which vapor bubbles are generated from the active nucleation sites at the wall surface (Yeoh and Tu, 2004).

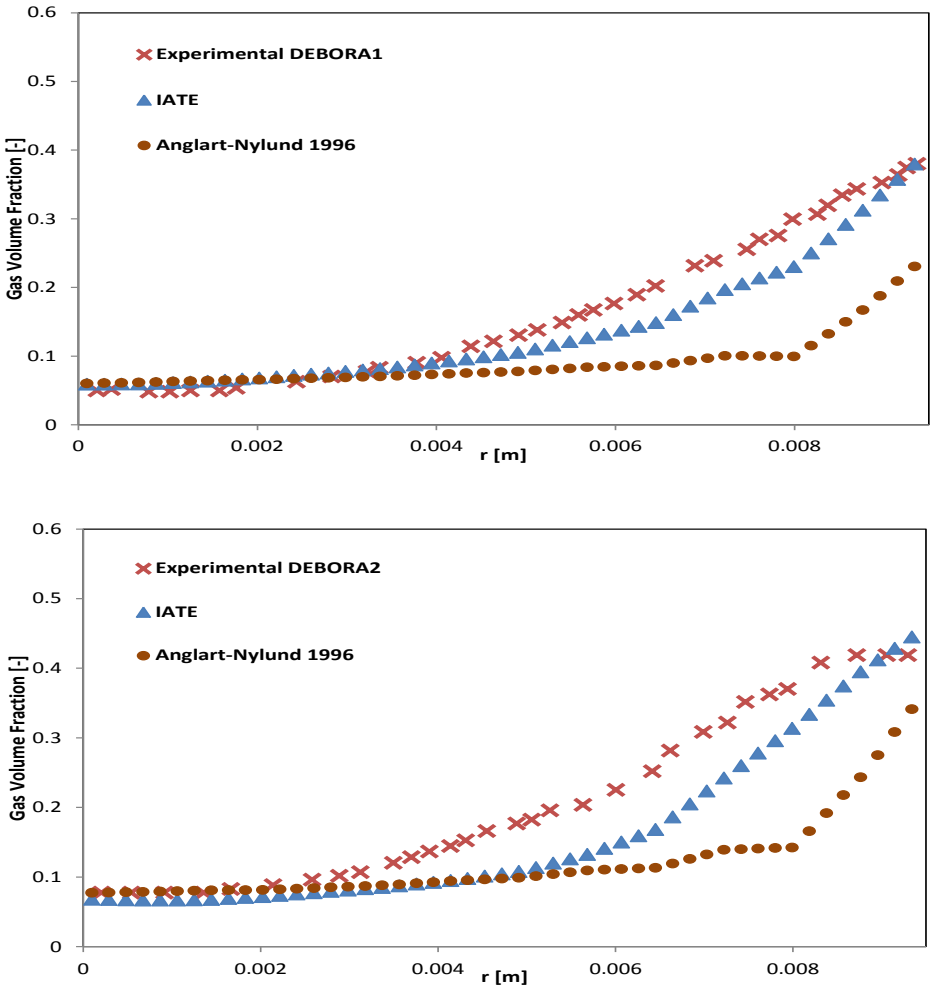

Figure 7.7. Radial distributions of void fraction for the cases DEBORA1 and DEBORA2.

The comparison of the interfacial area concentration profiles calculated by both approaches and the experimental measurements are given in Figure 7.8, where the same profile rise is also observed near the wall as in the void fraction distribution because of the presence of a large number of small bubbles. A good agreement between the predicted interfacial area profiles by both approaches and the measured one in the bulk domain is observed, while an inconsistency is noticed between the measured and predicted profiles in the near-wall region, where the Anglart and Nylund (1996) correlation under-predicts the interfacial area values and the one-group IATE model over-predicts it. According to Yeoh and Tu (2004) and based on the study of Hibiki and Ishii (2003), this discrepancy could be attributed to the fact that the used models of nucleation site density are not reliably applicable for a wide range of flow conditions including pressure, heat flux and mass flow rate, and those present in the experiments may be outside of the range of validity of the nucleation model.

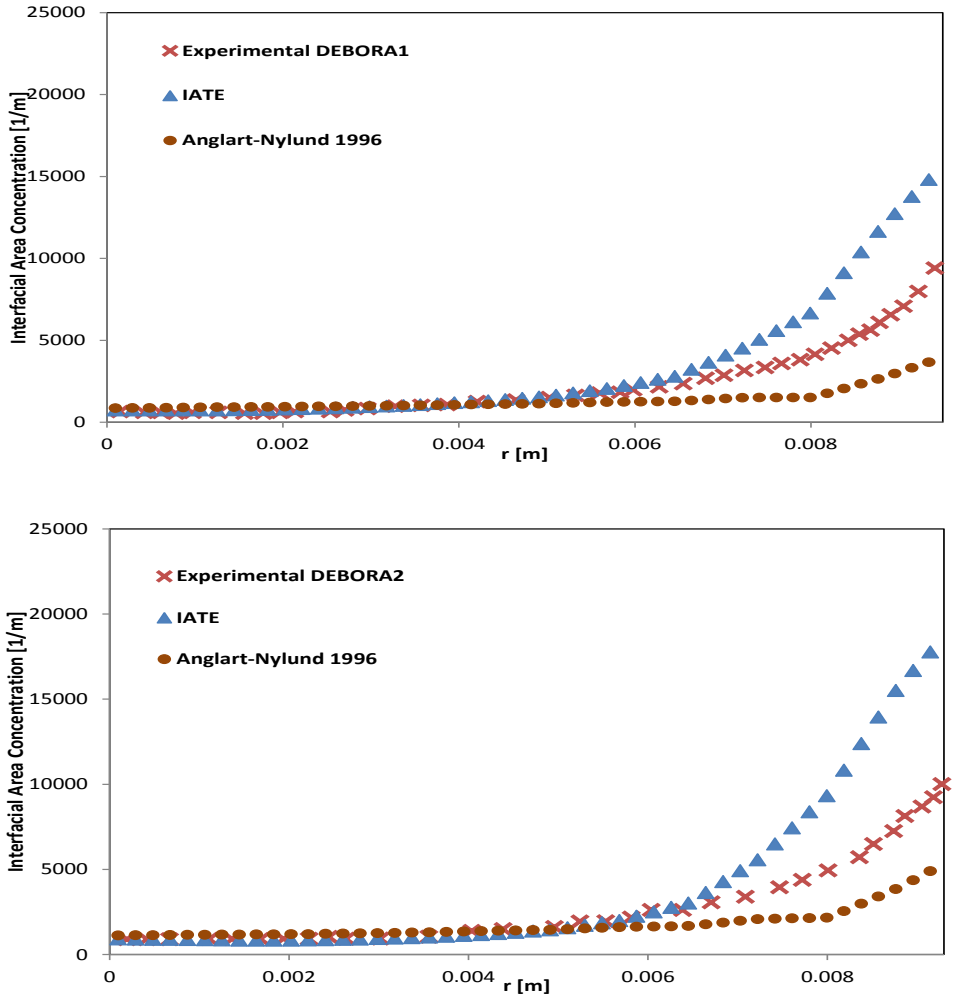

Figure 7.8. Radial distributions of interfacial area concentration for the cases DEBORA1 and DEBORA2.

Figure 7.9 depicts the prediction and measurement of the radial profile of the local bubble Sauter mean diameter. In line with Figure 6.6, the bubble size estimation by Anglart and Nylund (1996) empirical correlation shows a slight reduction of the Sauter diameter with increasing distance from the wall, with a maximum bubble diameter located at the heated wall. Such a behavior disagrees with the experimental observation of the DEBORA tests, which show a bubble size increase with increasing distance from the wall until it starts to stabilize in the bulk region following the same trend as Anglart and Nylund (1996) model. This shortcoming in the empirical correlation could be due to its inability to illustrate the effect of competition between bubble coalescence and collapse due to condensation on the bubble size distribution, which would yield the flat profile observed in Figure 7.9. The one-group IATE model adjusts the results well mainly in the core region, where the competition between bubbles coalescence and condensation takes place, while a significant bubble size under-prediction is observed

in the near-wall region that is consistent with the over-prediction of the interfacial area concentration described above: larger number of smaller bubbles for a similar void fraction.

The gas velocity profile illustrated in Figure 7.10 shows a good agreement between the vapor velocity predicted by both approaches and the measured data with a slight under-estimation by the Anglart and Nylund (1996) correlation. This result can be linked to the under-prediction of the bubble diameter in the bulk domain, which has a direct impact on the calculation of the interfacial drag (smaller bubbles result in larger drag forces) and non-drag forces. Both forces rely strongly on the estimation of the bubble diameter and play the main role in the momentum transfer between the two phases.

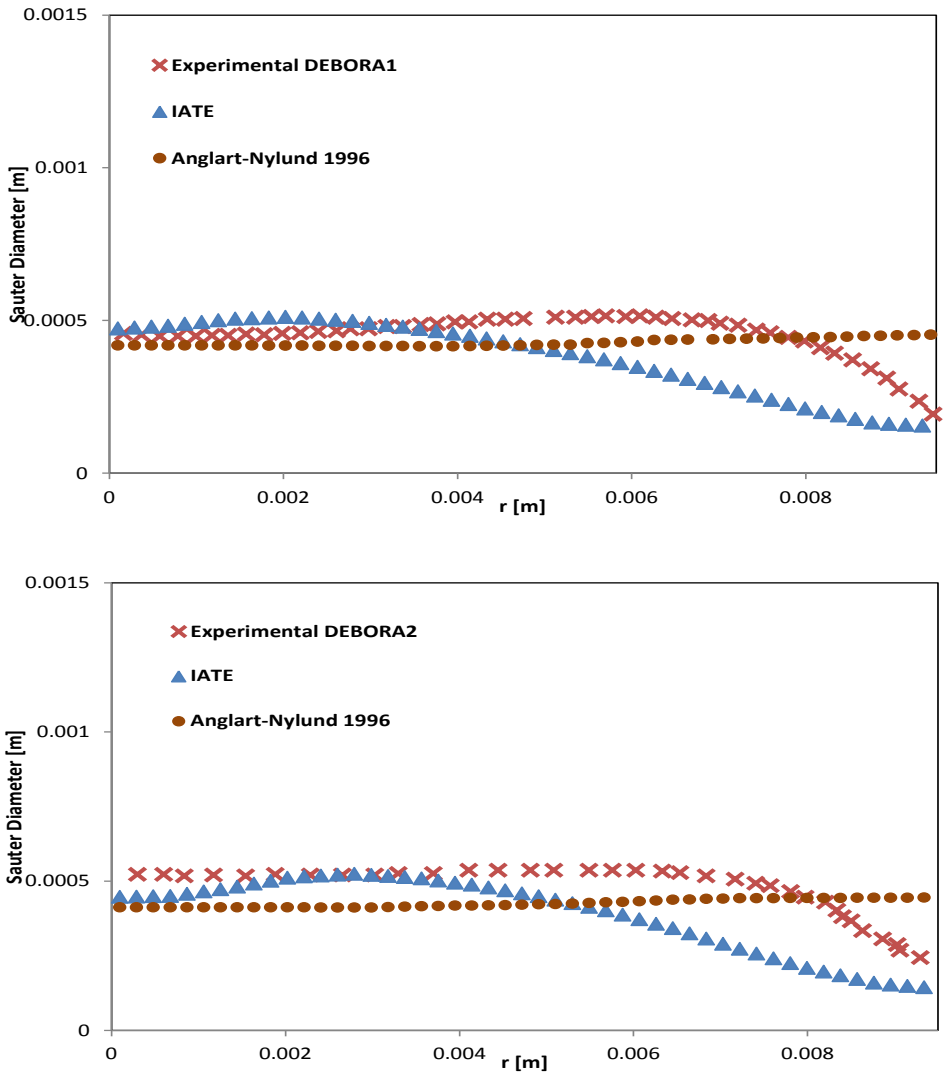

Figure 7.9. Radial distributions of bubble Suter mean diameter for the cases DEBORA1 and DEBORA2.

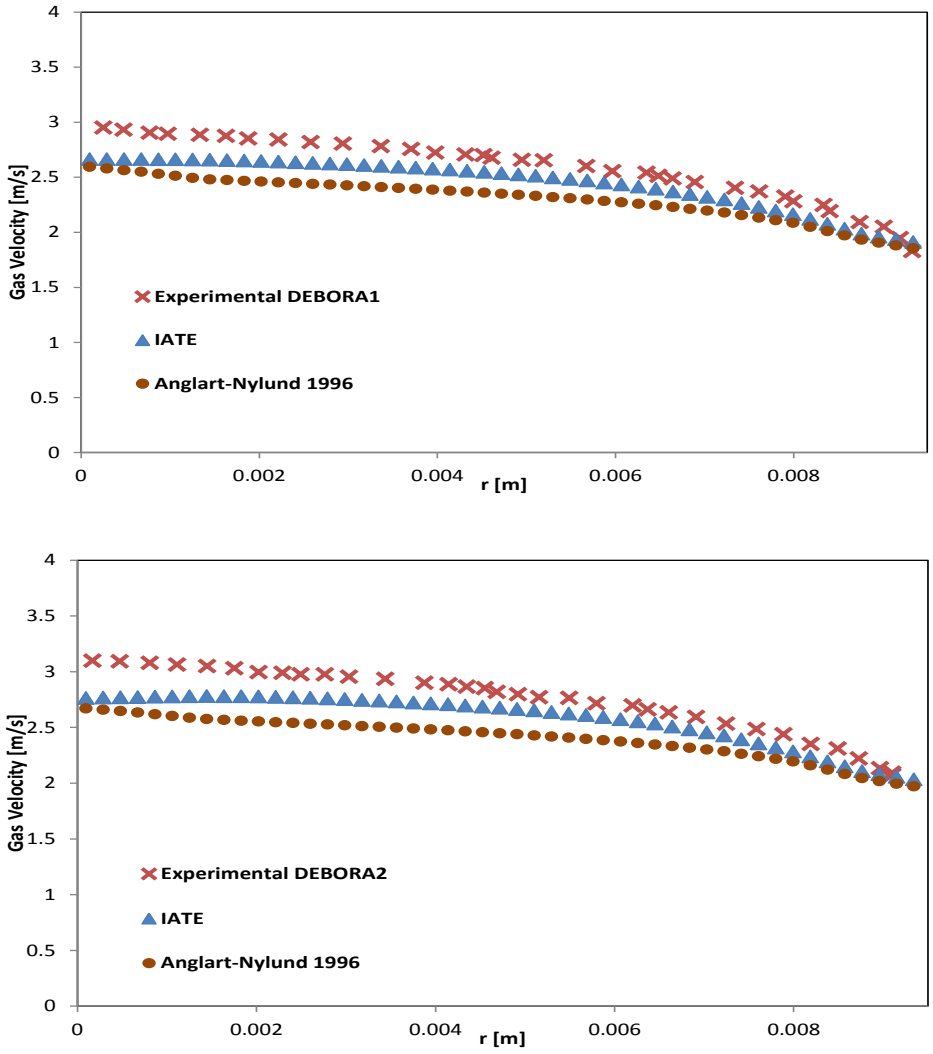

Figure 7.10. Radial distributions of gas velocity for the cases DEBORA1 and DEBORA2.

7.5 Comparison of Sub-cooled Boiling Flow Prediction by One-group IATE against that by the MUSIG Model

The inhomogeneous Multiple Size Group (MUSIG) model (Frank et al., 2008; Krepper et al., 2008) includes the division of the disperse gaseous phase into N numbers of inhomogeneous velocity groups or phases, where each group is distinguished by its own velocity. Each velocity group is divided into a number of sub-size groups which in total represent the overall bubble size distribution. Therefore, N set of momentum equations and a number of continuity equations equal to the number of the sub-size groups must be solved for the gaseous phase alongside with the conservation equations of the liquid phase. In most cases, 2 or 3 velocity groups are found enough to provide acceptable results that describe the bubbly and slug flows. Bubble coalescence and breakup

between the sub-size groups are considered through appropriate models (Frank et al., 2005).

Krepper et al. (2013) have coupled the wall boiling and the MUSIG models in the CFX code to improve the bubble size distribution prediction in sub-cooled boiling flow instead of using the Anglart and Nylund (1996) empirical correlation that yields some contradiction in the bubble diameter profile estimation. Moreover the coalescence and breakup source terms that are available in the original model used to simulate adiabatic two phase flow, Lucas and Prasser (2007), Lucas et al. (2011), Krepper et al. (2011) and Lifante et al. (2011) have included new source terms describing evaporation and condensation processes that have a major effect on the bubble size distribution in the sub-cooled boiling flow.

In the present work, the one-group IATE has been coupled to the wall boiling models in the OpenFOAM code to improve the boiling flow parameters prediction where a set of two momentum equations, one for the liquid and another for gas phase, one continuity equation for the gas phase, and one energy equation for the liquid phase (the gas phase is assumed to be at saturation) are solved, in addition to the solution of the one-group interfacial area transport equation.

To examine the merits of the one-group IATE approach implemented in this work, it has been used to simulate the sub-cooled boiling flow in the DEBORA experiment and its results compared to the simulations of the flow for the same test facility and conditions by using the MUSIG model approach by Krepper et al. (2013).

In both approaches, the wall heat flux partitioning model of Kurul and Podowski (1991) has been employed. A comparison between the predictions and the measured data at the exit of the heated pipe includes the local radial distribution of void fraction, bubble Sauter mean diameter, liquid temperature and gas velocity. Because of the unavailability of the interfacial area concentration prediction in the work of Krepper et al. (2013), it will not be included in the comparison. Details of the analysis are discussed below.

- **Void Fraction**

For test cases DEBORA1 and DEBORA2 with a system pressure of 2.62 MPa, good agreement with the measured void fraction profile is noticed for both approaches and both predicted profiles are also consistent with each other: both predict void fraction profiles which show a clear increase in the vicinity of the heated wall as illustrated in Figure 7.11. The slight increase in the void fraction values in the DEBORA2 test case

due to the decreased sub-cooling of the inlet liquid are also captured by both approaches: less sensible heat than in DEBORA1 is required to reach the liquid saturation temperature at the wall and more evaporation results in more void in the near-wall region and more void also in the intermediate-region because of less condensation as a result of a lower liquid sub-cooling.

Test cases DEBORA5 and DEBORA6 were conducted with a lower system pressure of 1.46 MPa and a higher mass flow rate and wall heat flux. In DEBORA5, with higher liquid sub-cooling at the inlet, the void fraction increase and maximum value near the wall are well captured by both approaches with a good prediction of the void fraction in the bulk region and a clear under-prediction by both models in the intermediate pipe section region. DEBORA6 with a lower liquid sub-cooling at the inlet represents an extreme case in which the generated bubbles at the wall undergo more coalescence than collapse by condensation because a higher liquid temperature in the bulk yields large bubbles which are pushed by the negative lift force towards the pipe center. This behavior was not exactly captured by the MUSIG model approach that still provides a wall peak with higher void fraction values in the bulk region than that in the DEBORA5 test case due to lower sub-cooling but still under-estimate the real profile.

On the other hand, the one-group IATE approach provides better prediction of the radial distribution of void fraction with a timid estimation of the peak in the pipe center due to the more bubble collapse caused by condensation where Warrier et al. (2002) and Yeoh and Tu (2004) also reported that the Ranz and Marshall (1952) model which is used in this work has a tendency to over-predict the condensation Nusselt number and in turn the interfacial heat transfer coefficient and the condensation rate.

- **Bubble Sauter Mean Diameter**

The comparison of the predicted and measured bubble Sauter diameter radial profile is illustrated in Figure 7.12. Contrary to the Anglart and Nylund (1996) model, the one-group IATE and the MUSIG model approaches provide a non-uniform radial distribution of the bubble size. Both predict a bubble size increases with increasing distance from the wall, in the region in which the competition between bubble coalescence and condensation plays a major role in the determination of the bubble size distribution in subcooled boiling flow.

For the test cases DEBORA1 and DEBORA2 with higher system pressure, the bubble size prediction by both approaches yields consistent results with the measured data,

while for the test cases at a lower pressure, DEBORA5 and DEBORA6, some discrepancies are observed in the prediction of the bubble size by both MUSIG and IATE.

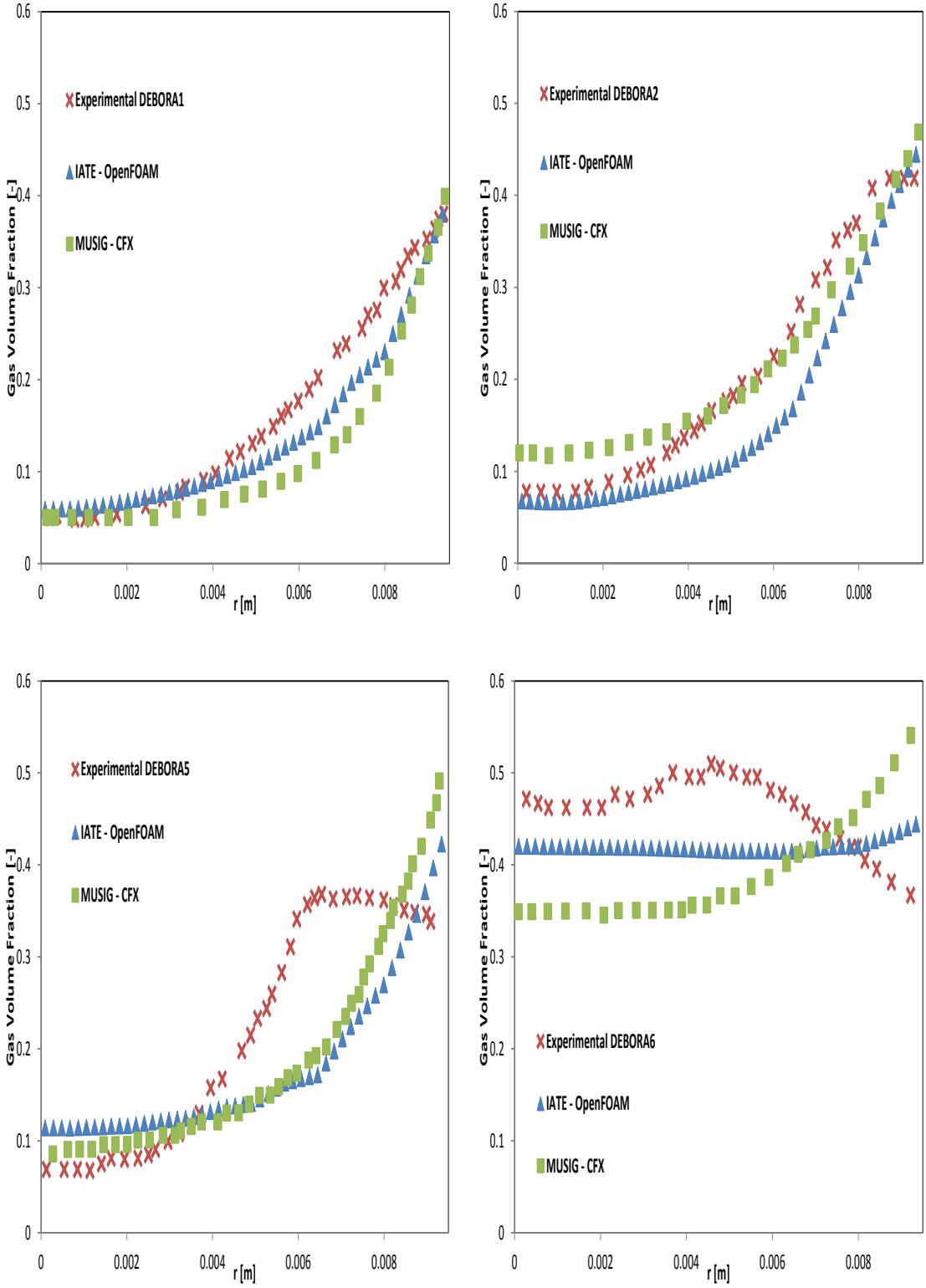

Figure 7.11. Radial gas volume fraction profiles for different DEBORA test cases at the pipe exit (MUSIG-CFX results from Krepper et al., (2013)).

The MUSIG approach shows a slight over-prediction, but still is superior to the results of the one-group IATE approach that shows under-estimation in the bubble size distribution. This superiority of the MUSIG model in predicting bubble size is attributed to the higher resolution of bubble sizes by the discretization into a larger number of bubble classes.

- **Liquid Temperature**

Due to the lack of the experimental data from other DEBORA tests, only the liquid temperatures of the high pressure cases i.e. DEBORA1 and DEBORA2 can be shown in Figure 7.13. In this Figure one can see the radial profile of the predicted and the measured liquid temperatures. The profiles calculated by both approaches are in a good agreement and also follow fairly well the experimental data. Furthermore, a large temperature gradient is predicted by both models in the near-wall region with a smoother temperature profile in the flow bulk. This can be attributed to an increased turbulent thermal diffusivity enhanced by the radial motion of vapor bubbles. A decreased temperature gradient in the vicinity of the wall is observed for the test case DEBORA2 with a lower liquid inlet sub-cooling, which results in more vapor generation at the wall and an increased turbulent thermal diffusivity due to the bubble migration towards the liquid bulk. This behavior is well captured by the one-group IATE model, while the MUSIG model shows a slight over-prediction of the liquid temperature in the near-wall region.

- **Time-averaged Gas Velocity**

As illustrated in Figure 7.14, the radial gas velocity profile predicted by both models compares favorably with the experimental data, with slight discrepancies that are attributed to the differences in predicting the bubble Sauter diameter. This variable is crucial for the proper evaluation of the interfacial momentum transfer term that appears in the momentum equations of gas and liquid phases, and therefore, influences significantly the vapor velocity. Another source of discrepancy between the two predicted gas velocity profiles is the different liquid turbulence models employed by IATE and MUSIG. Thus the $k-\varepsilon$ model is employed in the current OpenFOAM solver with the IATE implementation, while the MUSIG model in CFX uses the shear stress transport (SST) model.

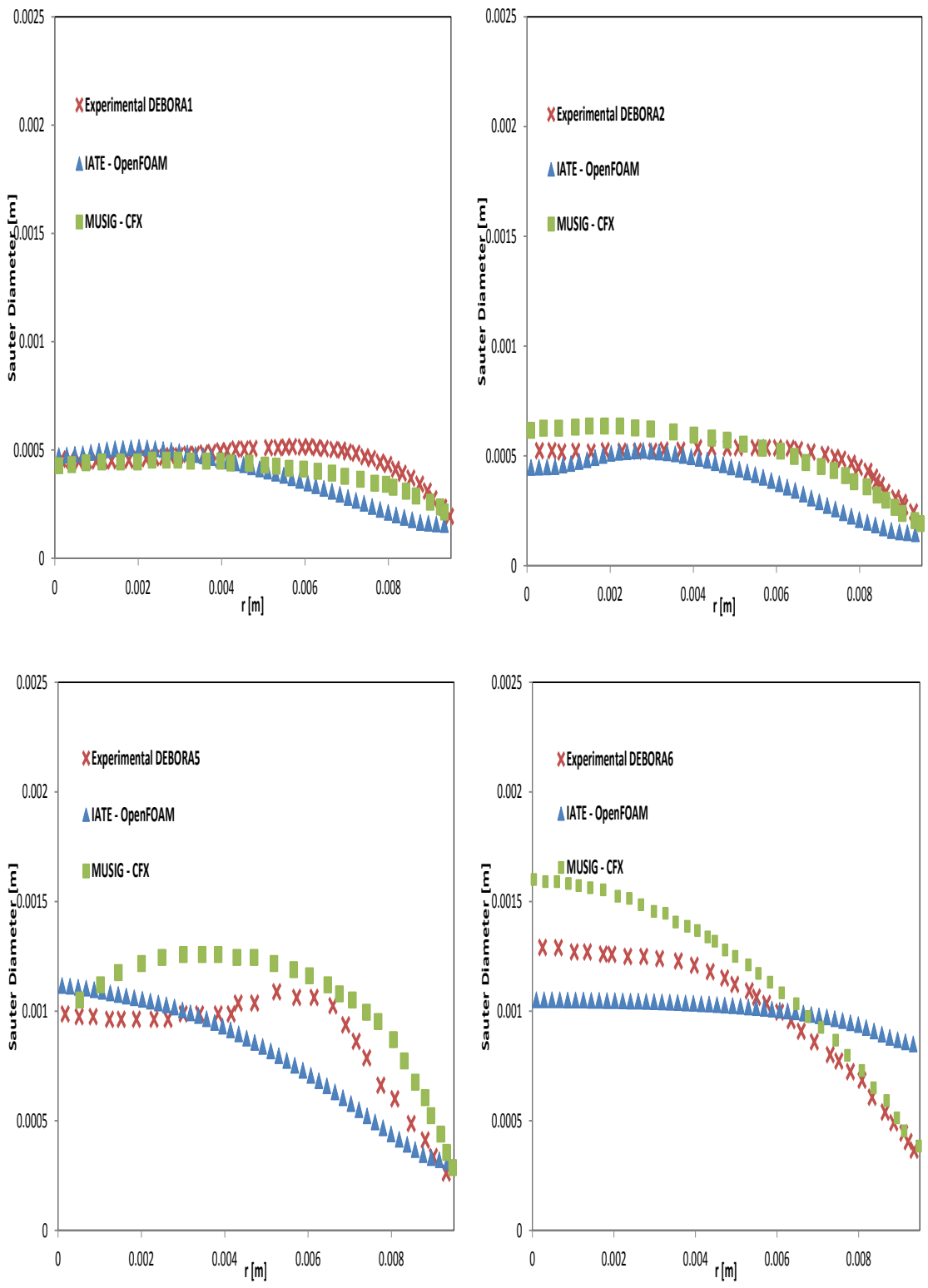

Figure 7.12. Radial bubble Sauter mean diameter profiles for different DEBORA test cases at the pipe exit (MUSIG-CFX results from Krepper et al., (2013)).

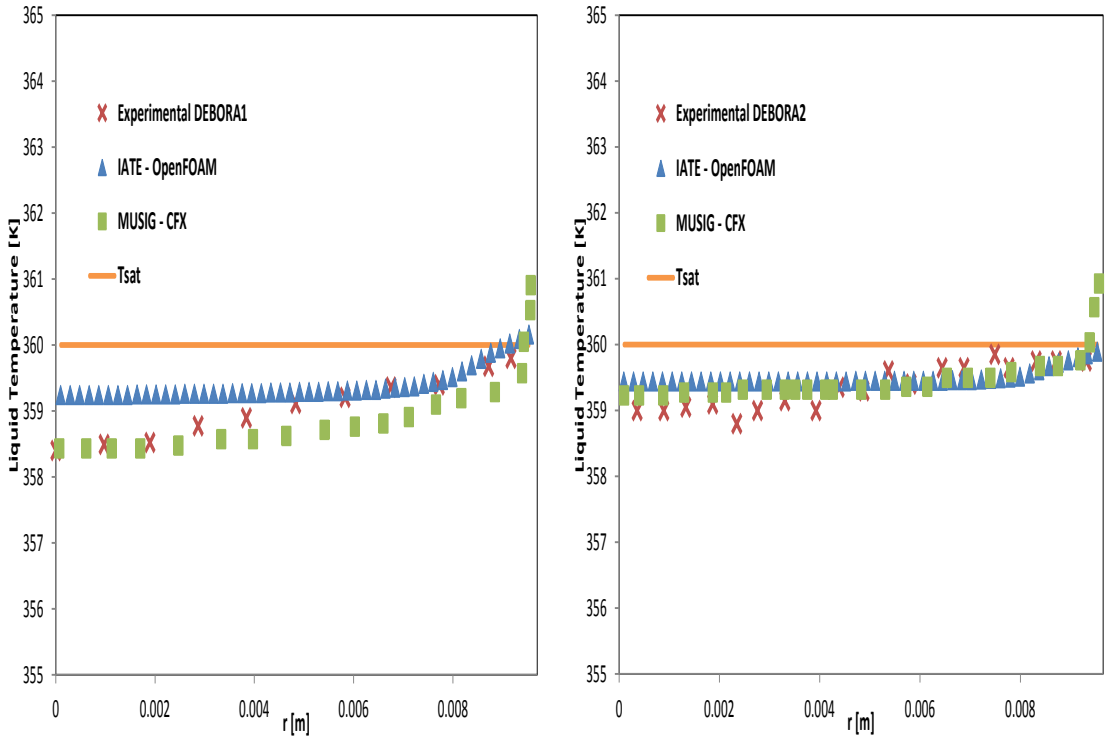

Figure 7.13: Radial liquid temperature profiles for different DEBORA test cases at the pipe exit (MUSIG-CFX results from Krepper et al., (2013)).

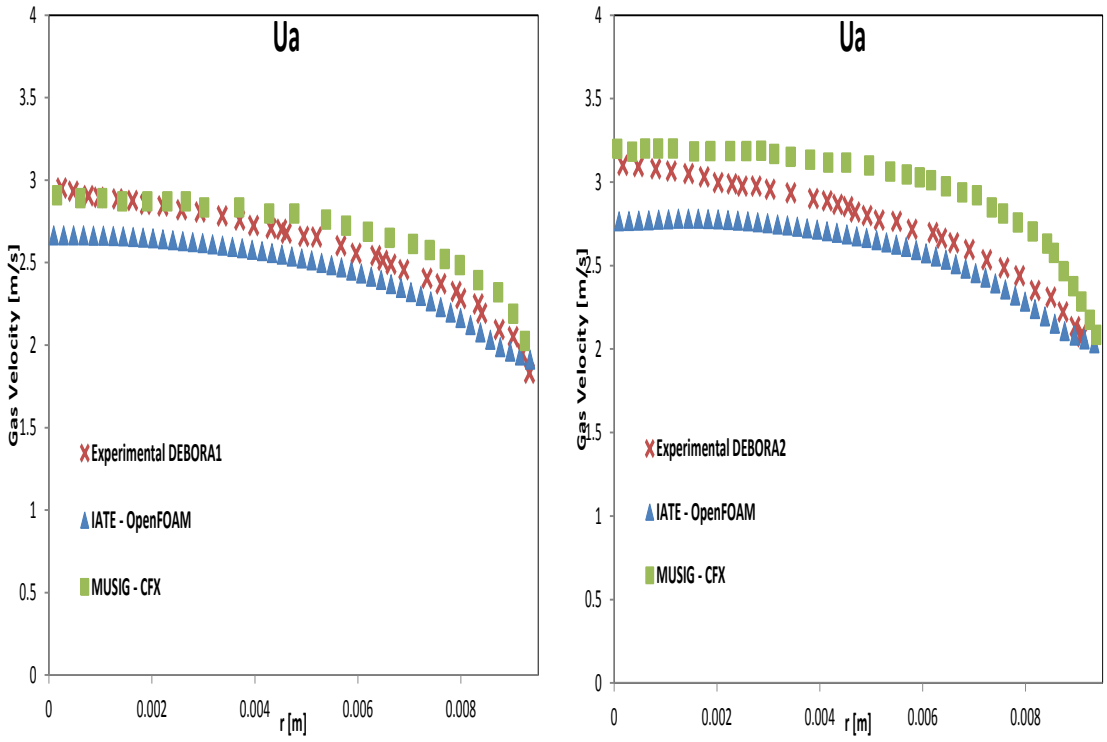

Figure 7.14. Radial gas velocity profiles for different DEBORA test cases at the pipe exit (MUSIG-CFX results from Krepper et al., (2013)).

7.6 Conclusion

The one-group interfacial area transport equation IATE coupled with the Euler-Euler two-fluid model has been implemented in the newly developed solver in the OpenFOAM code along with the wall heat flux partitioning model of Kurul and Podowski (1991) in order to enhance the prediction capability of sub-cooled boiling flow associated with complex phenomena including bubble coalescence, breakup, nucleation at the heated wall and condensation by the sub-cooled liquid in the bulk domain. Such phenomena play a major role in governing the non-uniform bubble size distribution that influences the interfacial transfer processes including heat, mass and momentum through the interfacial area concentration. The empirical correlation of Anglart and Nylund (1996) for the local bubble size determination, which is widely used in most of the CFD codes, assumes a linear relationship between the local bubble diameter and liquid sub-cooling. It has also been implemented in the new solver.

With the intention of examining the performance of the implemented models, the newly developed solver has been used to simulate the upwards sub-cooled boiling bubbly flow in the DEBORA test facility. The predictions of the gas volume fraction, gas velocity and Sauter mean bubble diameter profiles by the one-group IATE model are in good agreement with the experimental data, while the estimation of these flow parameters by the empirical correlation shows clear discrepancies. Using the one-group IATE, additional comparisons of the results obtained with different boiling closure models, including active nucleation sites density and bubble departure diameter which strongly drive bubble generation at the heated wall, has been conducted.

With the purpose of examining the relative merits of the one-group IATE approach against another population balance method, the simulation results of the DEBORA experiment simulated by using the MUSIG model implemented in the CFX code by Krepper et al. (2013) have been compared to the simulation results by the IATE model as implemented in OpenFOAM. Consistent results from both approaches have been observed for the local radial distribution of void fraction, bubble Sauter diameter, liquid temperature and gas velocity. Regarding the void fraction prediction in the extreme case DEBORA6, where a void peak is observed in the pipe center, the one-group IATE shows a slightly superior prediction than the MUSIG model, even as the higher resolution of the bubble size in the last approach consumes more computational time and resources needed for the calculation of the transport equations for each bubble size group. In the best case a minimum of15 bubble size groups for the test cases

DEBORA1 and DEBORA2 have been used by the homogeneous MUSIG model for the calculations.

In conclusion, sub-cooled boiling flow prediction by the one-group interfacial area transport equation is found to provide satisfactory results agreement with the experimental data that give it the opportunity to be a promising tool for rapid simulation of sub-cooled boiling flow with relatively low computational resources.

Chapter Eight

Conclusions and Future Work

Sub-cooled boiling flow and associated heat transfer are important phenomena for the safety analysis of nuclear reactors. It can, for instance, affect neutron moderation as well as the reactivity of the core, or it can influence the boiling characteristics along a fuel channel.

Sub-cooled boiling, compared to forced convection heat transfer, is characterized by a large heat transfer rate. The surface of the fuel rods in a nuclear reactor can transfer a large heat flux to the coolant, when this experience sub-cooled boiling. There is, nevertheless, a limit for the heat flux that can be transferred to the fluid bulk, the so-called Critical Heat Flux (CHF), which is one of the main limiting phenomena to set the operating power of LWRs. When this limit is crossed the phenomenon known as the boiling crises appears with the sudden covering of the solid surface with a film of steam that prevents the contact with liquid and results in the fast rise of the surface temperature above the damage limit for the wall material. The particular case of boiling crisis that takes place when the flow is undergoing sub-cooled boiling is called Departure from Nuleate Boiling (DNB). Because of the large heat fluxes being transferred previous to DNB under sub-cooled boiling conditions, when DNB appears, the large heat flux forces a very large temperature increase and fuel rod damage is inevitable. Therefore, precise modeling of Sub-cooled boiling is considered as an important preliminary developmental stage towards the accurate numerical simulation of CHF and the precise prediction of the boiling crises in CFD codes. Furthermore, accurate estimation of the radial profiles of two-phase flow parameters in the sub-cooled boiling region, such as gas volume fraction, interfacial area concentration, bubble Sauter mean diameter, gas velocity and liquid temperature is also very important for the prediction of physical processes, thermal-hydraulic, neutronic and mechanical, at a local level with a large impact on nuclear reactor safety.

In this work, numerical modeling of sub-cooled boiling has been conducted by using the open source code OpenFOAM framework. OpenFOAM gives the user full access to the source code, and he can add new or modify existing equations to create new numerical solvers. In the case of this thesis work the modeling of sub-cooled boiling has started with the already implemented solver in the code called “twoPhaseEulerFoam”,

which serves as a platform for two-phase flow simulation based on the solution of two sets of equations governing the conservation of the mass and momentum of the phases. The work started with the implementation of different models for the calculation of interfacial drag and non-drag force coefficients including lift, wall lubrication and turbulent dispersion forces that govern the radial distribution of the gas phase in the adiabatic bubbly flow. The implemented drag force coefficient models selected are those of Ishii and Zuber (1979), Schiller and Naumann (1933), and Tomiyama (1998a). The lift force coefficient has been modeled according to Tomiyama et al., (2002), as well as, using constant values suggested by different authors. Different models for the wall lubrication force coefficient have been implemented including Antal et al., (1991), Tomiyama (1998) and Hosokawa et al., (2002). The turbulent dispersion force coefficient has been modeled based on the models of Lopez de Bertodano (1992) and the model of Burns et al., (2004), based on the Favre average of the interfacial drag force (FAD). The bubble-induced turbulence has been modeled by implementing different corelations including the bubble-induced turbulent viscosity approach by Sato et al., (1980) and the additional source terms in the $k-\varepsilon$ equations approach by Morel (1997), Pfleger and Becker (2001), Rzehak and Krepper (2012) and Troshko and Hassan (2001). To validate the capability of the aforementioned models, the newly developed solver including these models has been used to simulate the low void fraction test cases of the air-water MT-LOOP test facility where a fixed monodisperse bubble size distribution is assumed with an average bubble size taken from the experimental data for each test point. In such a low void fraction flows, bubble interaction mechanisms like bubble coalescence and breakup are rare events but they play a major role in the determination of the bubble size distribution in high void fraction flows. For this reason these processes were not taken into consideration at this stage.

For real poly-dispersed flows with higher void fractions, the internal structure of the two -phase flow depends basically on the interfacial area concentration, which changes with the evolution of the flow due to bubble coalescence and breakup resulting from the interactions among bubbles and between bubbles and turbulent eddies. Furthermore, the closure relations representing the phasic interaction terms in the two-fluid model, express the transport of mass, momentum and energy through the interface between the phases in term of the interfacial area concentration. Based on the two-phase flow regimes and regime transition criteria, it has been shown that the empirical approach cannot describe the dynamic nature of the changes observed in the interfacial structure.

In order to obtain better predictions of the dynamic changes of the interfacial area in upward adiabatic bubbly flow, the one-group interfacial area transport equation coupled with the two-fluid model conservation equations have been implemented in the new OpenFOAM solver along with different bubble coalescence and breakup constitutive models including Wu et al., (1998), Hibiki and Ishii (2000a), Yao and Morel (2004), Prince and Blanch (1990) and Chesters (1991), and Martinez-Bazan et al., (1999a). To test the validity of the implemented models, the newly developed solver has been used to simulate the upwards adiabatic bubbly flow of an air/water system in the PUMA test facility. Prediction of the gas volume fraction, interfacial area concentration, gas velocity and Sauter mean bubble diameter profiles have been compared to the experimental data. The results have shown that the four implemented bubble coalescence and breakup models are able to reproduce the void fraction profiles in good agreement with the experimental data. The interfacial area concentration profiles are well captured by the Wu et al., (1998) and Hibiki and Ishii (2000a) models, and small differences with the experimental data are observed due to the model´s adjustable parameters, that were specially tuned by the authors to better approximate the 1D upward bubbly flow in pipes. The prediction of the interfacial area by Yao and Morel (2004) and Chesters (1991) - Martinez-Bazan et al., (1999a) is in relative good agreement in the core region of the pipe, but one can observe large discrepancies in the near wall region. The bubble diameter profile has been captured by the Wu et al., (1998) and Hibiki and Ishii (2000a) models with small discrepancies in the wall region, while Yao and Morel (2004) model shows some differences with the experimental data, and slight discrepancies are observed when using Chesters (1991) - Bazan et al., (1999a) models.

In order to complete the modeling of sub-cooled boiling flow in OpenFOAM, the wall heat flux partitioning model of Kurul and Podowski (1991) has been implemented and coupled to the two-fluid model conservation equations of mass, momentum and the energy equation newly implemented in OpenFOAM at this stage of the work. Further coupling was also made with the one-group interfacial area transport equation that was modified with the inclusion of new source terms representing the bubbles nucleation at the heated wall and the bubble condensation as they migrate into the sub-cooled liquid bulk. In addition to the default source term models representing bubble coalescence and breakup processes, all these phenomena, including bubble nucleation and condensation, were found to play a major role in governing the non-uniform bubble size distribution.

The empirical correlation of Anglart and Nylund (1996) for local bubble size determination, which is widely used in most of the CFD codes and assumes a linear relationship between the local bubble diameter and liquid sub-cooling, has also been implemented in the new solver.

With the aim of examining the performance of the full package of implemented models, the newly developed solver has been applied to the simulation of the upwards subcooled boiling bubbly flow in the DEBORA test facility. The prediction of the gas volume fraction, gas velocity and Sauter mean bubble diameter profiles by the one-group IATE model are in a good agreement with the experimental data, while the estimation of these flow parameters by the empirical correlation shows clear discrepancies. Using the one-group IATE, additional analysis of the performance of different boiling closure models, including active nucleation sites density and bubble departure diameter, that strongly govern bubble generation at the heated wall, has been conducted. Of these models, that of Tolubinsky and Konstanchuk (1970) for bubble departure diameter and the model of Lemmert and Chawla (1977) for nucleation site density have been found to provide the best fit to the experimental results.

The simulation results of the DEBORA experiments by the MUSIG model implemented in ANSYS-CFX by Krepper et al. (2013) have been compared to the simulation results by the IATE model implemented in OpenFOAM. This has been carried out with the intention of testing the capability of the one-group IATE of providing good prediction of sub-cooled boiling flow parameters. Both approaches, IATE and MUSIG, have been found to provide comparable results for the local radial distribution of void fraction, bubble mean Sauter diameter, liquid temperature and gas velocity. Regarding the void fraction prediction in the extreme case DEBORA6 in which a void peak is observed in the pipe center, the one-group IATE has shown a better prediction than the MUSIG model, even of the higher resolution of the bubble size in the last approach that consumes more computational time and resources needed for the solution of the transport equations for each bubble size group.

The capability of the one-group interfacial area transport equation newly implemented in OpenFOAM in the course of this thesis work to provide satisfactory prediction of sub-cooled boiling flow parameters in vertical up-flow conditions, is a promising sign for further development of this computer platform to accurately simulate local physical processes of importance for nuclear safety applications, such as CFH on-set and progression.

Finally, the summary of the conclusions and achievements of this work are the following

1. A new solver for the numerical simulation of sub-cooled boiling in flow channels and pipes has been developed, implemented in OpenFOAM and validated against experimental data from three facilities, which provided data specific for the assessment of the main physical processes modelled by the solver.
2. A combination of the following closure models to address the balance of forces acting on bubbles implemented in the new OpenFOAM solver was found to provide the best agreement between the measured and the predicted radial void fraction profiles of different MT-LOOP test cases
    - **Drag force**: Ishii and Zuber (1979).
    - **Lift force**: Tomiyama et al. (2002).
    - **Wall lubrication force**: Hosokawa et al. (2002).
    - **Turbulent dispersion force**: FAD/Burns et al. (2004).
    - **Bubble-induced turbulence**: Morel (1997).
3. The one-group interfacial area transport equation implemented in the solver to calculate interfacial area density in the computational volumes was found to provide the best predictiona of the dynamic changes of the interfacial area in upward adiabatic bubbly flow when coupled to the Wu et al., (1998) or Hibiki and Ishii (2000a) coalescence and breakup models.
4. The wall heat flux partitioning model of Kurul and Podowski (1991) implemented to calculate subcooled bouiling was found to provide better predictions of the boiling flow parameters when coupled to the one-group IATE rather than coupling to the imperical correlation of Anglart and Nylund (1996).
5. Of a number of different boiling closure models, the Tolubisky and Konstanchuk (1970) model for bubble departure diameter and the model of Lemmert and Chawla (1977) for nucleation site density were found to provide the best fit to the experimental data.
6. The comparison of the simulation carried out with the complete solver and the best performing models described above, of the sub-cooled boiling flow in the DEBORA experiment by the one-group IATE using OpenFOAM against that by the MUSIG models implemented in ANSYS-CFX by Krepper et al., (2013) showed that both approaches providing comparable results with the advantage of the one-group IATE approach regarding the less amount of computational time and resources required.

An area for future work is the extension of the one-group IATE to the two-group IATE, where with increasing void fraction, the bubble size starts to increase and the shape starts to deform taking the cap-shape which make the spherical bubble shape assumption invalid that complicates bubble interactions and impose new interaction mechanisms such as shearing-off and surface instability that are dominant at large bubble size.

Additional work is also recommended for the improvement of the interfacial area concentration prediction in sub-cooled boiling by the consideration of a lift-off frequency reduction factor that should be incorporated in the nucleation source term of the interfacial area transport equation. This is consistent with the experimental observations that point to the occurrence of bubble coalescence processes between a sliding bubble after departing from its nucleation site and another bubble at another nucleation site thus reducing the number of actual bubbles lifted off from the wall and, in turn, reducing the values of the predicted interfacial area concentration in the near-wall region to acceptable levels.

APPENDIX A

Gauss' Theorem

Scalar function

$$\int_V \nabla f dV = \int_A f n dA, \tag{A1}$$

Vector function

$$\int_V \nabla . f dV = \int_A f . n dA, \tag{A2}$$

Tensor function

$$\int_V \nabla . \bar{\bar{f}} dV = \int_A \bar{\bar{f}} . n dA, \tag{A3}$$

Leibniz's Theorem

$$\frac{d}{dt}\int_{V_k(t)} f(r,t)\, dV = \int_{V_k(t)} \frac{\partial f}{\partial t} dV + \int_{A_k(t)} f(U_I . n_k) dA, \tag{A4}$$

APPENDIX B

Implementation of the solver in OpenFOAM

The formulation of the two-phase conservation equations in the new solver is based on the work of Rusche (2002).

- **Momentum Equation**

The momentum conservation equation for both phases is written as

$$\frac{\partial}{\partial t}\left(\alpha_k \rho_k \vec{U}_k\right) + \nabla.\left(\alpha_k \rho_k \vec{U}_k \vec{U}_k\right) = -\alpha_k \nabla P_k + \nabla.\left(\alpha_k\left(\bar{\bar{\tau}}_k + \bar{\bar{\tau}}_k^{Re}\right)\right) + \alpha_k \rho_k \vec{g} + \vec{M}_k + \Gamma_{ki}\vec{U}_i - \Gamma_{ik}\vec{U}_k, \tag{B1}$$

This equation is implemented in OpenFOAM in a phase-intensive form by dividing it by α_k as suggested by Rusche (2002) to avoid singularity of the equation when one of the phases approaches zero, that yields the phase-intensive form of the momentum equation

$$\frac{\partial}{\partial t}\left(\vec{U}_k\right) + \nabla.\left(\vec{U}_k \vec{U}_k\right) = -\frac{\nabla P_k}{\rho_k} + \nabla.\bar{R}_k^{eff} + \vec{g} + \frac{\vec{M}_k}{\rho_k \alpha_k} + \frac{\Gamma_{ki}\vec{U}_i}{\alpha_k \rho_k} - \frac{\Gamma_{ik}\vec{U}_k}{\alpha_k \rho_k}, \tag{B2}$$

Where

$$\bar{R}_k^{eff} = \frac{\bar{\bar{\tau}}_k + \bar{\bar{\tau}}_k^{Re}}{\rho_k} = -\upsilon_k^{eff}\left(\nabla \vec{U}_k + \nabla \vec{U}_k{}^T - \frac{2}{3} I \nabla.\vec{U}_k\right) + \frac{2}{3} I k_k, \tag{B3}$$

Rusche (2002) decomposed the Reynolds stress $\bar{R}_k^{eff}$ into a diffusive component and a correction as

$$\bar{R}_k^{eff} = \bar{R}_k^{effD} + \bar{R}_k^{effC}, \tag{B4}$$

Where

$$\bar{R}_k^{effD} = -\upsilon_k^{eff} \nabla \vec{U}_k, \tag{B5}$$

And from B3

$$\bar{R}_k^{effC} = -\upsilon_k^{eff}\left(\nabla \vec{U}_k{}^T - \frac{2}{3} I \nabla.\vec{U}_k\right) + \frac{2}{3} I k_k = \bar{R}_k^{eff} + \upsilon_k^{eff} \nabla \vec{U}_k, \tag{B6}$$

Using the definition of total phase velocity

$$\vec{U}_k^{\tau} = \vec{U}_k - \upsilon_k^{eff} \frac{\nabla \alpha_k}{\alpha_k}, \tag{B7}$$

The discretized form of the momentum equation reads

$$\frac{\partial \overline{U}_k}{\partial t} + \nabla.(\phi_k^{\tau}\overline{U}_k) - \nabla.\left(\upsilon_k^{eff}\nabla\overline{U}_k\right) + \nabla.\bar{R}_k^{effC} + \frac{\nabla\alpha_k}{(\alpha_k+\delta)}.\bar{R}_k^{effC} = -\frac{\nabla P_k}{\rho_k} + \vec{g} + \frac{\vec{M}_k}{\rho_k\alpha_k} + \frac{\Gamma_{ki}\vec{U}_i}{(\alpha_k+\delta)\rho_k} - \frac{\Gamma_{ik}\vec{U}_k}{(\alpha_k+\delta)\rho_k}, \quad \text{(B8)}$$

Where ϕ_k^{τ} denotes the total phase flux calculated by interpolating the total phase velocity in equation (B7) to the phase centers as

$$\phi_k^{\tau} = \phi_k - \upsilon_k^{eff}\frac{\nabla_f^{\perp}\alpha_k}{(\alpha_k+\delta)}, \quad \text{(B9)}$$

Implementation of the interfacial momentum exchange term $\vec{M}_k$ need special treatment because it contains the void fraction in the denominator. Therefore, the Weller (2002) approach is adopted where for a gas phase (a) dispersed in liquid phase (b), the interfacial momentum transfer term writes

$$\begin{aligned} \bar{M}_a = & -\tfrac{3}{4}\alpha_a\alpha_b f_a\tfrac{C_D\rho_b}{d_a}|\overline{U}_r|\overline{U}_r, && \text{Drag} \\ & -\alpha_a\alpha_b f_a\rho_b C_L\overline{U}_r\times(\nabla\times\overline{U}_b), && \text{Lift} \\ & +\alpha_a\alpha_b f_a\rho_b C_W|\overline{U}_r|^2\vec{n}_w, && \text{Wall lubrication} \end{aligned} \quad \text{(B10)}$$

Because every force term contains the product of $\alpha_a\alpha_b$ then, it can be divided by α_a or α_b to avoid the singularity problem (Rusche 2002). The modifier function f_a is a function of α_a where Weller (2002) proposed that $f_a = \alpha_a$.

The lift and wall lubrication forces are treated explicitly while a semi-implicit treatment was conducted for the drag force. Due to numerical oscillations caused by the gradient of the void fraction, the turbulent dispersion force is treated in the coupling algorithm of the pressure equation.

At the beginning, the momentum equation is discretized without the pressure gradient term, the buoyancy term, the explicit part of the drag force and the turbulent dispersion force yielding system of linear algebraic equations that can be expressed in a matrix form as

$$[A][\phi] = [R], \quad \text{(B11)}$$

Where $[A]$ is the coefficient matrix, $[\phi]$ is the column vector of the dependent variable and $[R]$ is the source vector.

Therefore, for the gas phase (a) solution of the algebraic equation $[A]$ yields the predicted flux

$$\phi_a^* = \left(\frac{(A_a)_H}{(A_a)_D}\right)_f .S, \tag{B12}$$

This flux is corrected by the inclusion of the buoyancy and the explicit term of the drag force and the turbulent dispersion force

$$\phi_a^{*'} = \phi_a^* + \left(\frac{1}{(A_a)_D}\right)_f g.S + \left(\frac{\alpha_b A_d}{\rho_a (A_a)_D}\right)_f \phi_b - \left(\frac{C_{TD} k \rho_b}{\rho_a(\alpha_a + \delta)} . \frac{1}{(A_a)_D}\right)_f S\nabla_f^{\perp} \tag{B13}$$

Where A_d of the drag force is calculated as $A_d = \frac{3}{4}\frac{C_d \rho_b}{d_a}$, and ϕ_b is the flux of the liquid phase. The operators $(A_a)_D$ and $(A_a)_H$ are the diagonal and the "H" elements of the coefficient matrix A_a, respectively.

Using the last calculated flux $\phi_a^{*'}$, the pressure equation is solved to get the value of the pressure gradient that is used to make the final correction of the flux as

$$\phi_a = \phi_a^{*'} - \left(\frac{1}{\rho_a (A_a)_D}\right)_f S\nabla_f^{\perp}\bar{p}, \tag{B14}$$

Finally, this calculated flux is reconstructed to calculate the gas velocity.

- **Continuity Equation**

The phase fraction is obtained from the solution of the continuity equation that is written for the conservation of volume instead of mass as

$$\frac{\partial}{\partial t}(\alpha_k) + \nabla.\left(\alpha_k \vec{U}_k\right) = \frac{\Gamma_{ki} - \Gamma_{ik}}{\rho_k}, \tag{B15}$$

To get more conservative and bounded results of the void fraction, Weller (2002) rearranged the continuity equation of the gas phase as

$$\frac{\partial}{\partial t}(\alpha_a) + \nabla.\left(\alpha_a \vec{U}\right) + \nabla.\left(\alpha_a \alpha_b \vec{U}_r\right) = \frac{\Gamma_{gl} - \Gamma_{lg}}{\rho_a}, \tag{B16}$$

Where $\vec{U} = \alpha_a \vec{U}_a + \alpha_b \vec{U}_b$ and $\vec{U}_r = \vec{U}_a - \vec{U}_b$. The presence of the relative velocity helps to couple the two phase fluxes implicitly.

The discretized form of the continuity equation that is implemented in the solver reads

$$\frac{\partial}{\partial t}(\alpha_a) + \nabla.\left((\alpha_a)_f \phi\right) + \nabla.\left((\alpha_a \alpha_b)_f \phi_r\right) = \frac{\Gamma_{gl} - \Gamma_{lg}}{\rho_a}, \tag{B17}$$

For more details see Rusche (2002).

- **Interfacial Area Transport Equation**

The interfacial area transport equation is treated implicitly as in the continuity equation where the discretized form reads

$$\frac{\partial}{\partial t}(a_i) + \nabla.\left((a_i)_f \phi\right) = \frac{2}{3}\left(\frac{a_i}{\alpha_a}\right)\left(\frac{\partial \alpha_a}{\partial t} + \nabla.\left((\alpha_a)_f \phi_a\right)\right) \quad \text{(B18)}$$

$$+12\pi\left(\frac{\alpha_a}{a_i}\right)^2 (Coalescnce + Breakup) + \frac{2}{3}\left(\frac{a_i}{\alpha_a \rho_a}\right)\Gamma_{lg} + Nucleation,$$

Modeling of $Coalescnce$, $Breakup$, Γ_{lg}, $Nucleation$ are found in chapters 4 and 6.

- **Energy Equation**

The energy equation is solved for the liquid phase only while the gas phase is assumed to be at saturation conditions. The energy equation is written in term of the specific enthalpy with a phase intensive form as in the momentum equation as

$$\frac{\partial}{\partial t}(H_b) + \nabla.(H_b \phi_b) + H_b \nabla.\phi_b =$$
$$-\frac{1}{\alpha_b \rho_b}\nabla.\left(\alpha_b\left(\bar{\bar{q}}_b + q_b^T\right)\right) + \frac{1}{\rho_b}\frac{Dp_k}{Dt} + \frac{\Gamma_{lg}H_{a,sat} - \Gamma_{gl}H_b}{\alpha_b \rho_b} + \frac{q_{li}^{"} a_i}{\alpha_b \rho_b} + \frac{\Phi_w}{\alpha_b \rho_b}.APV, \quad \text{(B19)}$$

Where APV is the area per unit volume of the near wall cells. The evaporation term Γ_{gl} is calculated using the wall heat flux partitioning algorithm described in figure 6.11.

- **Solution Sequence**

The sequence of the solution of the implemented solver is summarized as:

1. Calculation of the condensation rate Γ_{lg}.
2. Calculation of the evaporation rate Γ_{gl} using the wall heat flux partitioning algorithm.
3. Solution of the void fraction equation.
4. Solution of the interfacial area transport equation.
5. Computation of the interfacial forces coefficients.
6. Assembling the $U_a$and U_b equations and computation of flux predictors.
7. Solution of the pressure equation using the predicted flux.
8. Correction of the flux using the pressure gradient and reconstruction to get the value of velocities.
9. Re-computation of the void fraction and the interfacial area concentration.
10. Solution of the $k - \varepsilon$ equations.
11. Solution of the energy equation.

Bibliography

Anglart, H. and O. Nylund (1996). "CFD application to prediction of void distribution in two-phase bubbly flows in rod bundles." Nuclear Engineering and Design 163(1-2): 81-98.

ANSYS CFX User Manual, Release 12.1, ANSYS Inc, 2009.

Antal, S. P., et al. (1991). "Analysis of Phase Distribution in Fully-Developed Laminar Bubbly 2-Phase Flow." International Journal of Multiphase Flow 17(5): 635-652.

Auton, T. R. (1987). "The Lift Force on a Spherical Body in a Rotational Flow." Journal of Fluid Mechanics 183: 199-218.

Bae, B. U., et al. (2008). "Computational analysis of a subcooled boiling flow with a one-group interfacial area transport equation." Journal of Nuclear Science and Technology 45(4): 341-351.

Bae, B. U., et al. (2010). "Analysis of subcooled boiling flow with one-group interfacial area transport equation and bubble lift-off model." Nuclear Engineering and Design 240(9): 2281-2294.

Batehelor, G. K. (1956). "*The theory of homogeneous turbulence.*" London: Cambridge University Press.

R.J. Benjamin, A.R. Balakrishnan (1997). "Nucleation site density in pool boiling of saturated pure liquids: effect of surface micro-roughness and surface and liquid physical properties, Exp. " Thermal Fluid Sci. 15: 32–42.

Bonjour, J., & Lallemand, M. (2001). "Two-phase flow structure near a heated vertical wall during nucleate pool boiling. " *International Journal of Multiphase Flow*, *27*, 1789–1802.

Bowring, R. W. (1962). "Physical model based on bubble detachment and calculation of steam voidage in the subcooled region of a heated channel. " *Report HPR-10*. Halden, Norway: Institute for Atomenergi.

Burns, A. D., Frank, T., Hamill, I., & Shi, J. (2004). "The Favre averaged drag model for turbulent dispersion in Eulerian multiphase flow. " In Proceedings of the fifth international multiphase flow, Yokohama, Japan.

Chen, P., et al. (2005). "Numerical simulation of bubble columns flows: effect of different breakup and coalescence closures." Chemical Engineering Science 60(4): 1085-1101.

Chesters, A. K. (1991). "The Modeling of Coalescence Processes in Fluid Liquid Dispersions - a Review of Current Understanding." Chemical Engineering Research & Design 69(4): 259-270.

Cheung, S. C. P., et al. (2007). "On the numerical study of isothermal vertical bubbly flow using two population balance approaches." Chemical Engineering Science 62(17): 4659-4674.

Cheung, S. C. P., et al. (2007). "On the modelling of population balance in isothermal vertical bubbly flows - Average bubble number density approach." Chemical Engineering and Processing 46(8): 742-756.

Cole, R. (1960). "A photographic Study of Pool Boiling in the Region of the Critical Heat Flux." Aiche Journal 6(4): 533-538.

Coulaloglou, C. A. and L. L. Tavlarides (1977). "Description of Interaction Processes in Agitated Liquid-Liquid Dispersions." Chemical Engineering Science 32(11): 1289-1297.

Dittus, F. W. and L. M. K. Boelter (1985). "Pioneers in Heat-Transfer in Automobile Radiators of the Tubular Type (reprinted from university of california publications in engineering, Vol 2, PG 443-461, 1930." International Communications in Heat and Mass Transfer 12(1): 3-22.

Drew, D. A., & Lahey, R. T., Jr. (1979). "Application of general constitutive principles to the derivation of multi-dimensional two-phase flow equation." *International Journal ofMultiphase Flow*, *5*, 243–264.

Enwald, H., et al. (1996). "Eulerian two-phase flow theory applied to fluidization." International Journal of Multiphase Flow 22: 21-66.

Th. Frank, J.-M. Shi, A.D. Burns. "Validation of Eulerian multiphase flow models for nuclear reactor safety applications. " 3rd International Symposium on Two-phase Flow Modeling and Instrumentation, Pisa, 22.-24. Sept. 2004, pp. 1-9.

Th. Frank. "Advances in Computational Fluid Dynamics (CFD) of 3-dimensional gas liquid multiphase flows. "NAFEMS Seminar "Simulation of Complex Flows (CFD). " Wiesbaden, Germany, April 25-26, 2005, pp. 1-18.

Frank, T., et al. (2008). "Validation of CFD models for mono- and polydisperse air-water two-phase flows in pipes." Nuclear Engineering and Design 238(3): 647-659.

Fritz, W. (1935). "Berechung des Maximalvolumes von Dampfblasen. " *Zeitschrift Für Physik*, *36*, 379–384.

Fu, X. Y. and M. Ishii (2003). "Two-group interfacial area transport in vertical air-water flow I. Mechanistic model." Nuclear Engineering and Design 219(2): 143-168.

Fu, X. Y. and M. Ishii (2003). "Two-group interfacial area transport in vertical air-water flow II. Model evaluation." Nuclear Engineering and Design 219(2): 169-190.

Garnier, J., Manon, E., Cubizolles, G. (2001). "Local measurements on flow boiling of refrigerant 12 in a vertical tube." Multiphase Sci. Technol. 13, 1–111.

Gharaibah, E. (2008). "Entwicklung und Validierung eines Modells polydisperser Zweiphasenströmungen unter Berücksichtigung von Koaleszenz und Dispersion. " Ph.D. Thesis, Technische Universität München.

Hawkes, J. (2004). "The Simulation and Study of Conditions Leading to Axial Offset Anomaly in Pressurized Water Reactors." Master Thesis, Georgia Institute of Technology.

Hibiki, T. and M. Ishii (2000). "One-group interfacial area transport of bubbly flows in vertical round tubes." International Journal of Heat and Mass Transfer 43(15): 2711-2726.

Hibiki, T., et al. (2001). "Axial interfacial area transport of vertical bubbly flows." International Journal of Heat and Mass Transfer 44(10): 1869-1888.

Hibiki, T. and K. Mishima (2001). "Flow regime transition criteria for upward two-phase flow in vertical narrow rectangular channels." Nuclear Engineering and Design 203(2-3): 117-131.

Hibiki, T. and M. Ishii (2002). "Development of one-group interfacial area transport equation in bubbly flow systems (vol 45, pg 2351, 2002)." International Journal of Heat and Mass Transfer 45(17): 3679-3680.

Hibiki, T. and M. Ishii (2003). "Active nucleation site density in boiling systems." International Journal of Heat and Mass Transfer 46(14): 2587-2601.

Hill, D. (1998). "The Computer Simulation of Dispersed Two-Phase Flow." Ph.D. Thesis, University of London.

Hosokawa, S., Tomiyama, A., Misaki, S., Hamada, T. (2002). "Lateral migration of single bubbles due to the presence of wall." In Proc. ASME Joint U.S.–European Fluids Engineering Division Conference, FEDSM2002, Montreal, Canada, p. 855.

Ishii, M. (1975). "*Thermo-fluid dynamic theory of two phase flow*." Paris, Byrolles.

Ishii, M. and Chawla, T. "Local drag laws in dispersed two-phase flow." Technical report, ANL-79-105, Argonne National Laboratory, Chicago, 1979.

Ishii, M. and N. Zuber (1979). "Drag Coefficient and Relative Velocity in Bubbly, Droplet or Particulate Flows." Aiche Journal 25(5): 843-855.

Ishii, M. and Mishima, K. (1984). "Two-fluid Model and Hydrodynamic Constitutive Relations. " *Nucl. Eng Des.* 82: 107-126.

Ishii, M., et al. (2002). "Interfacial area transport equation: model development and benchmark experiments." International Journal of Heat and Mass Transfer 45(15): 3111-3123.

Ishii, M., and Hibiki, T. (2006). "*Thermo-fluid dynamics of two-phase flow*." Berlin: Springer-Verlag.

Ivey, H. (1967). "Relationship Between Bubble Frequency, Departure Diameter and Rise Velocity in Nucleate Boiling." *International Journal of Heat and Mass Transfer*, Vol. 10, pp. 1023-1040.

Jo, D. and S. T. Revankar (2011). "Investigation of bubble breakup and coalescence in a packed-bed reactor - Part 1: A comparative study of bubble breakup and coalescence models." International Journal of Multiphase Flow 37(9): 995-1002.

Kataoka, I., Serizawa, A. (1997). "Turbulence characteristics and their application to multi-dimensional analysis of two-phase flow." Proceedings of the 8th International Topical Meeting on Nuclear Reactor Thermal-Hydraulics,Kyoto, Japan, Vol. 3, 1677–1683.

Kim, J. and Lee, W. (1987). "Coalescence behavior of two bubbles in stagnant liquids." Journal of Chemical Engineering of Japan, vol. 20, no. 5, pp. 448–453.

Kim, S. (1999). "Interfacial Area Transport Equation and Measurement of local interfacial Characteristics." PhD Thesis, Purdue University.

Kim, S., et al. (2003). "Interfacial area transport and evaluation of source and sink terms for confined air-water bubbly flow." Nuclear Engineering and Design 219(1): 61-75.

Kirkpatrick, R. and Lockett, M. (1974). "The influence of approach velocity on bubble coalescence." Chem. Eng. Sci. 29 , 2363.

Klausner, J. F., et al. (1993). "Vapor Bubble Departure in Forced-Convection Boiling." International Journal of Heat and Mass Transfer 36(3): 651-662.

Kocamustafaogullari, G. and M. Ishii (1995). "Foundation of the Interfacial Area Transport-Equation and its Closure Relations." International Journal of Heat and Mass Transfer 38(3): 481-493.

Koncar, B., Mavko, B., Hassan, Y.A. (2005). "Two-phase wall function for modeling ofturbulent boundary layer in subcooled boiling flow." In Proceedings NURETH-11, Avignon, France, Oct. 2005, Paper 443.

Koncar, B. and E. Krepper (2008). "CFD simulation of convective flow boiling of refrigerant in a vertical annulus." Nuclear Engineering and Design 238(3): 693-706.

Koncar, B. and I. Tiselj (2010). "Influence of near-wall modelling on boiling flow simulation." Nuclear Engineering and Design 240(2): 275-283.

Krepper, E., et al. (2005). "On the modelling of bubbly flow in vertical pipes." Nuclear Engineering and Design 235(5): 597-611.

Krepper, E., et al. (2007). "CFD modelling of subcooled boiling - Concept, validation and application to fuel assembly design." Nuclear Engineering and Design 237(7): 716-731.

Krepper, E., et al. (2008). "The inhomogeneous MUSIG model for the simulation of polydispersed flows." Nuclear Engineering and Design 238(7): 1690-1702.

Krepper, E. and R. Rzehak (2011). "CFD for subcooled flow boiling: Simulation of DEBORA experiments." Nuclear Engineering and Design 241(9): 3851-3866.

Krepper, E., et al. (2013). "CFD for subcooled flow boiling: Coupling wall boiling and population balance models." Nuclear Engineering and Design 255: 330-346.

Kroeger, P. and Zuber, N. (1968). "An Analysis of the Effects of Various Parameters on the Average Void Fractions in Subcooled Boiling." *International Journal of Heat Mass Transfer,*11, 211-233.

Kurul, N., Podowski, M.Z. (1990). "Multidimensional effects in forced convection subcooled boiling." In Proceeding of the Ninth International Heat Transfer Conference, Jerusalem, August 1990, pp. 21–26.

Kurul, N. and Podowski, M. (1991). "On the Modeling of Multidimensional Effects in Boiling Channels." Proc. of the 27th National Heat Transfer Conference, Minneapolis, MN.

Lahey, R. T., et al. (1993). "Phase Distribution in Complex-Geometry Conduits." Nuclear Engineering and Design 141(1-2): 177-201.

Lasheras, J. C., et al. (2002). "A review of statistical models for the break-up of an immiscible fluid immersed into a fully developed turbulent flow." International Journal of Multiphase Flow 28(2): 247-278.

Launder, B. and Spalding, D. (1974). "The numerical computation of turbulent flows." *Computer Methods in Applied Mechanics and Engineering*, *3*, 269–289.

Lee, T. H., et al. (2002). "Local flow characteristics of subcooled boiling flow of water in a vertical concentric annulus." International Journal of Multiphase Flow 28(8): 1351-1368.

Lehr, F., et al. (2002). "Bubble-size distributions and flow fields in bubble columns." Aiche Journal 48(11): 2426-2443.

Lemmert, M., & Chwala, J. M. (1977). "*Influence of flow velocity on surface boiling heat transfer coefficient*." New York and Washington: Academic Press and Hemisphere.

Levich, V. (1962). "*Physicochemical hydrodynamics*." Englewood Cliffs, NJ: Prentice-Hall.

Liao, Y. and D. Lucas (2009). "A literature review of theoretical models for drop and bubble breakup in turbulent dispersions." Chemical Engineering Science 64(15): 3389-3406.

Liao, Y. et al. (2011). "Development of a generalized coalescence and breakup closure for the inhomogeneous MUSIG model." Nuclear Engineering and Design 241(4): 1024-1033.

Liao, Y. and D. Lucas (2012). "Investigations on Bubble-Induced Turbulence Modelling for Vertical Pipe Bubbly Flows." Proc. of the 20th International Conference on Nuclear Engineering, Anaheim, California, 2012.

Lifante, C., Reiterer, F., Frank, Th., Burns, A. (2011). "Coupling of wall boiling with discrete population balance model." In: The 14th International Topical Meeting on Nuclear Reactor Thermal Hydraulics, NURETH-14, Toronto, Ontario, Canada, September 25–30, NURETH14-087.

Loeb, L. (1927). "The Kinetic Theory of Gases." Dover, New York, USA.

Lopez de Bertodano, M. (1992). "Turbulent bubbly two-phase flow in a triangular duct." Ph.D. Dissertation, Rensselaer Polytechnic Institute.

Lucas, D., et al. (2005). "Development of co-current air-water flow in a vertical pipe." International Journal of Multiphase Flow 31(12): 1304-1328.

Lucas, D. and H. M. Prasser (2007). "Steam bubble condensation in sub-cooled water in case of co-current vertical pipe flow." Nuclear Engineering and Design 237(5): 497-508.

Lucas, D. et al. (2010b). "Experimental investigations on the condensation of steam bubbles injected into sub-cooled water at 1 MPa." Multiphase Science and Technology, accepted, (2010b).

Luo, H. (1993). "Coalescence, break-up and liquid recirculation in bubble column reactors." Ph.D. Dissertation, Norwegian Institute of Technology.

Manon, E. (2000). "Contribution a l'analyse et a la modelisation locale des ecoulements boillants sous-satures dans les conditions des Reacteurs a Eau sous Pression." Ph.D. Thesis. Ecole Centrale Paris.

Martinez-Bazan, C. (1999a). "On the break-up of an air bubble injected into a fully developed turbulent flow. Part 1. Break-up frequency. " Journal of Fluid Mechanics, 401, 157–182.

McDonough, J. " Introductory Lectures on Turbulence. Physics, Mathematics and Modeling. " Department of Mechanical Engineering and Mathematics. University of Kentucky.

Mei, R. W. and J. F. Klausner (1994). "Shear Lift Force on Spherical Bubbles." International Journal of Heat and Fluid Flow 15(1): 62-65.

Michta, E. (2011). "Modeling of Subcooled Nucleate Boiling with OpenFOAM." Master Thesis, Royal Institute of Technology, Stockholm.

Mikic, B. and Rohsenow, W. (1969). "A new correlation of pool-boiling data including the fact of heating surface characteristics." ASME J. Heat Transfer 91, 245–250.

Mishima, K. and Ishii, M. (1984). "Flow Regime Transition Criteria for Upward Two-phase Flow in Vertical Tubes." Int. J. Heat Mass Transfer 11:123-131.

Morel, C. (1997). "Turbulence Modeling and first Numerical Simulations in Turbulent Two-Phase Flows." Proc. 11th Symp. on Turbulent Shear Flows, Grenoble, France, pp. P3-10, 1997.

Oolman, T. and Blanch, H. (1986a). "Bubble coalescence in air-sparged bioreactor." Biotechnology and Bioengineering, 28, 578–584.

Oolman, T. and Blanch, H. (1986b). "Bubble coalescence in stagnant liquids." Chemical Engineering Communications, 43, 237–261.

OpenFOAM user guide, http://www.foamcfd.org/Nabla/guides/UserGuide.html.

Pellacani, F. (2012). "Development and validation of bubble breakup and coalescence constitutive models for the one-group interfacial area transport equation." Ph.D. Thesis, Technische Universität München.

Pfleger, D. and S. Becker (2001). "Modelling and simulation of the dynamic flow behaviour in a bubble column." Chemical Engineering Science 56(4): 1737-1747.

Politano, M. S., et al. (2003). "A model for turbulent polydisperse two-phase flow in vertical channels." International Journal of Multiphase Flow 29(7): 1153-1182.

Politis, S. (1989). "Prediction of two-phase solid-liquid turbulent flow in stirred vessels." Ph.D. Thesis, University of London.

Prasser, H. et al. (2003). "Flow maps and models for transient two-phase flows." Forschungszentrum Dresden, FZR-379.

Prince, M. J. and H. W. Blanch (1990). "Bubble Coalescence and Break-up in Air-Sparged Bubble-Columns." Aiche Journal 36(10): 1485-1499.

Prodanovic, V., et al. (2002). "Bubble behavior in subcooled flow boiling of water at low pressures and low flow rates." International Journal of Multiphase Flow 28(1): 1-19.

Ranz, W. and Marshall, W. (1952). "Evaporation from droplets: Parts I and II." Chemical Engineering Progress, 48, 141–148.

Rusche, H. (2002). "Computational uid dynamics of dispersed two-phase ows at high phase fractions." Ph.D. Thesis, Imperial College, London.

Rzehak, R., et al. (2012). "Comparative study of wall-force models for the simulation of bubbly flows." Nuclear Engineering and Design 253: 41-49.

Rzehak, R. and E. Krepper (2013). "Bubble-induced turbulence: Comparison of CFD models." Nuclear Engineering and Design 258: 57-65.

Saffman, P. (1965). "The lift on small sphere in slow sphere flow. *Journal of Fluid Mechanics*. " *22*, 385–400.

Salnikova, T. (2008). "Two-Phase CFD Analyses in Fuel Assembly Sub-Channels of Pressurized Water Reactors Under Swirl Conditions." Ph.D. Thesis, Technischen Universität Dresden.

Sato, Y., et al. (1981). "Momentum and heat transfer in two-phase bubble flow." International Journal of Multiphase Flow, 7, pp.167-177.

Santos, M.(2008). "Medida Experimental de la Concentración de Área Interfacial en Flujos Bifásicos Finamente Dispersos y en Transición." Ph.D. Thesis, Universidad Politécnica de Valencia.

Schiller, L. and Naumann, A. (1933). "Über die grundlegenden Berechungen beider Schwer kraftaufbereitung." Duetscher Ingenieure, 77, pp.318.

Schmidtke, M. (2008). "Investigation of the dynamics of fluid particles using the Volume of Fluid Method." PhD Thesis, University Paderborn.

Shinnar, R. and Church, J. (1960). "Predicting particle size in agitated dispersions." Industrial and Engineering Chemistry, 52, pp.253-256.

Situ, R., et al. (2005). "Bubble lift-off size in forced convective subcooled boiling flow." International Journal of Heat and Mass Transfer 48(25-26): 5536-5548.

Situ, R., et al. (2007). "Assessment of Effect of Bubble Departure Frequency in Forced Convection Subcooled Boiling." Proc. 16th Australasian Fluid Mechanics Conference, Gold Coast, Australia, 2007.

Song, C. H., et al. (2007). "Thermal-hydraulic tests and analyses for the APR1400's development and licensing." Nuclear Engineering and Technology 39(4): 299-312.

Sun, X., (2001). "Two-group interfacial area transport equation for a confined test section." Ph. D Thesis. Purdue University.

Sun, X. et al. (2004). "Modeling of bubble coalescence and disintegration in confined upward two-phase flow." Nuclear Engineering and Design 230(1-3): 3-26.

Sun, X., (2007). "Overview of Interfacial Area Transport in Multiphase Flow Systems." Presentation at the Annual Meeting of the Chemical Reaction Engineering Laboratory (CREL), Washington University.

Taitel, Y., et al. (1980). "Modeling Flow Pattern Transitions for Steady Upward Gas-Liquid Flow in Vertical Tubes." Aiche Journal 26(3): 345-354.

Talley, J. D., et al. (2011). "Implementation and evaluation of one-group interfacial area transport equation in TRACE." Nuclear Engineering and Design 241(3): 865-873.

Tolubinsky, V. and Kostanchuk, D. (1970). "Vapor bubbles growth rate and heat transfer intensity at subcooled water boiling." In: Fourth international heat transfer conference, 5, Paper No. B-2.8, Paris, France.

Tomiyama, A., et al. (1998). "Drag coefficients of single bubbles under normal and micro gravity conditions." Jsme International Journal Series B-Fluids and Thermal Engineering 41(2): 472-479.

Tomiyama, A., et al. (2002). "Transverse migration of single bubbles in simple shear flows." Chemical Engineering Science 57(11): 1849-1858.

Troshko, A. A. and Y. A. Hassan (2001). "A two-equation turbulence model of turbulent bubbly flows." International Journal of Multiphase Flow 27(11): 1965-2000.

Tsouris, C. and L. L. Tavlarides (1995). "Breakage and Coalescence Models for Drops in Turbulent Dispersions (vol 40, pg 395, 1994)." Aiche Journal 41(8): 1851-1851.

Tsuchiya, K., et al. (1989). "Visualization of Bubble Wake Interactions for a Stream of Bubbles in a Two-Dimensional Liquid Solid Fluidized-Bed." International Journal of Multiphase Flow 15(1): 35-49.

Tu, J. Y., et al. (2005). "On population balance approach for subcooled boiling flow prediction." Journal of Heat Transfer-Transactions of the Asme 127(3): 253-264.

Wallis, G. B. (1969). "One-dimensional two-phase flow." New York: McGraw-Hill.

Wang, S., et al. (1987). "3-D turbulence structure and phase distribution measurements in bubbly two-phase flows." International Journal of Multiphase Flow, 13, 327–343.

Wang, S. M. , et al. (2013). "Population balance modelling for subcooled boiling flow of liquid nitrogen in a vertical tube." International Journal of Heat and Mass Transfer 60: 632-645.

Wang, X. (2010). "Simulations of Two-phase Flows Using Interfacial Area Transport Equation." Ph.D. Thesis, The Ohio State University.

Warrier, G. R., et al. (2002). "Interfacial heat transfer during subcooled flow boiling." International Journal of Heat and Mass Transfer 45(19): 3947-3959.

Wellek, R. et al. (1966). "Shapes of liquid drops moving in liquid media." AIChE Journal, 12, 854–862.

Wu, Q., et al. (1998). "One-group interfacial area transport in vertical bubbly flow." International Journal of Heat and Mass Transfer 41(8-9): 1103-1112.

Wu, Q. et al. (1998b). "Framework of two-group model for interfacial area transport in vertical two-phase flows." Transactions of the American Nuclear Society, 79, pp. 351 352.

Yao, W. and Morel, C. (2004). "Volumetric interfacial area prediction in upwards bubbly two-phase flow." International Journal of Heat and Mass Transfer, 47, 307–328.

Yeoh, G. H. and J. Y. Tu (2004). "Population balance modelling for bubbly flows with heat and mass transfer." Chemical Engineering Science 59(15): 3125-3139.

Yeoh, G. H. and J. Y. Tu (2005). "A unified model considering force balances for departing vapour bubbles and population balance in subcooled boiling flow." Nuclear Engineering and Design 235(10-12): 1251-1265.

Yeoh, G. H. and Tu, J. Y. (2005). "Thermal-hydrodynamics modelling of bubbly flows with heat and mass transfer." AIChE Journal, 51, 8–27.

Yeoh, G. H. and J. Y. Tu (2006). "Two-fluid and population balance models for subcooled boiling flow." Applied Mathematical Modelling 30(11): 1370-1391.

Yeoh, G.H. and Tu, J.Y. (2010). "Computational Techniques for Multiphase Flows—Basics and Applications." Elsevier Science and Technology, Butterworth-Heinemann.

Yun, B.J., Splawski, A., Lo, S., Song, C.-H., (2010). " Advanced wall boiling model for the subcooled boiling flow with CFD code. " In: The 7th Korea-Japan Symposium on Nuclear Thermal Hydraulics and Safety (NTHAS7), Chuncheon, Korea, November 14–17.

Zeng, L. Z., et al. (1993). "A unified Model for the Prediction of Bubble Detachment Diameters in Boiling Systems .2. Flow Boiling." International Journal of Heat and Mass Transfer 36(9): 2271-2279.

Zuber, N. (1961). "The dynamics of vapor bubbles in nonuniform temperature fields." International Journal of Heat and Mass Transfer, 2, 83–98.

Zuber, N. and Findlay, J. (1965). "Average volumetric concentration in two-phase flow systems." J. Heat Trans. 87 (1965) 453.

Zun, I. (1980). "The transverse migration of bubbles influenced by walls in vertical bubbly flow." Int. J. Multiphase Flow 6, 583.